Energy

GEOTHERMAL

DOE/ET/27111-11
(DE84014825)

MICROSEISMIC MONITORING OF CHOCOLATE BAYOU, TEXAS THE PLEASANT BAYOU NO. 2 GEOPRESSURED/GEOTHERMAL ENERGY TEST WELL PROGRAM

By
Frederick J. Mauk
Billie Kimball
Robert Alan Davis

Work Performed Under Contract No. AC08-79ET27111

The University of Texas at Austin
Austin, Texas

Technical Information Center
Office of Scientific and Technical Information
United States Department of Energy

DISCLAIMER

DISCLAIMER

This report has been reproduced directly from the best available copy.

Available from the National Technical Information Service, U. S. Department of Commerce, Springfield, Virginia 22161.

Price: Printed Copy A08
Microfiche A01

Codes are used for pricing all publications. The code is determined by the number of pages in the publication. Information pertaining to the pricing codes can be found in the current issues of the following publications, which are generally available in most libraries: *Energy Research Abstracts (ERA); Government Reports Announcements* and Index (*GRA* and I); *Scientific and Technical Abstract Reports (STAR);* and publication NTIS-PR-360 available from NTIS at the above address.

DOE/ET/27111-11
(DE84014825)
Distribution Category UC-66a

Technical Report

MICROSEISMIC MONITORING OF CHOCOLATE BAYOU, TEXAS

THE PLEASANT BAYOU NO. 2 GEOPRESSURED/GEOTHERMAL

ENERGY TEST WELL PROGRAM

by

Frederick J. Mauk
Billie Kimball
Robert Alan Davis

Prepared for
U.S. Department of Energy
Division of Geothermal Energy

under Contract Number DE-AC08-79ET27111

Bureau of Economic Geology
The University of Texas at Austin
Austin, Texas 78712

W. L. Fisher, Director

1984

CONTENTS

FIGURES

FIGURES Continued

TABLES

ABSTRACT

Seismological monitoring of the Chocolate Bayou region of Brazoria County, Texas, in the vicinity of the DOE Pleasant Bayou geopressured/geothermal design well has resulted in significant improvement in assessing the potential seismological hazards and risks associated with the development of this alternative energy resource. Since the inception of the monitoring program in 1978, there have been four periods during which significant volumes of brine have been produced from the Pleasant Bayou No. 2 well and subsequently reinjected into the Pleasant Bayou No. 1 well. Continuous seismic monitoring and analyses of the data through September 1983 have resulted in the following observations and conclusions. (1) The temporal distribution of seismic events from 1978 through 1983 is not uniform. There is a pronounced increase in the frequency of occurrence of microearthquakes in the latter half of 1981. (2) Because the increased seismicity follows the Phase I short-term flow test with a delay of over two hundred days and occurs both during and following the aborted Phase II long-term flow test, the exact causality relationship between brine production and/or disposal and induction of microearthquakes is unclear. The coincidence of onset of seismicity and times of brine production and the absence of seismicity in 1982 following a fourteen-month shut-in strongly suggest the existence of a correlation, however. Seismic activity resumed late March 1983 following the re-initiation of the Phase II long-term flow test in September 1982, therefore adding support for a hypothesized delayed strain-release response of the local geologic column to the stress perturbation induced by the design well production. (3) Microearthquakes occurring in the Gulf Coast region have previously been divided into two separate groups of events. Type I event is typical microearthquake in character, composed of well-defined body waves and surface waves. These events are observed to propagate across the monitoring array at P-wave velocity. Type II events propagate at very low velocities (<400 m/sec) and contain no identifiable body phases. Since the increase in frequency of occurrence of both event types during and following well production indicates that they are in some way production related, it is important to determine their origin and mode of propagation. To resolve some of the uncertainties associated with these events, in particular the question of focal depth, synthetic seismograms were calculated by modal summation based on a Gulf Coast earth model. Comparison of time domain and frequency domain observed and synthetic signals has offered strong evidence that focal

Keywords: Microseismic monitoring, geopressured/geothermal energy, Chocolate Bayou, Texas

depth is one distinguishing factor between these two event types. Type II events originate at depths less than 800 m; type I events apparently have source depths greater than 800 m. Depths of type II and hypocenter locations calculated for the majority of observed type I events are less than that of the production reservoir. (4) Spectral analysis of observed type II signals and synthetic seismograms also provide substantial evidence of trapped modes rather than simple Rayleigh propagation. (5) The spatial distribution of the seismic epicenter at Pleasant Bayou from 1979 through September 1983 cluster in the vicinity of proposed locations of growth faults at depths of 15,000 feet west and northwest of the Pleasant Bayou No. 2 well.

These data combined with the few unambiguously recorded first P-wave motions suggest that these microearthquakes occur as dip slip events along growth faults above the production horizon. The sense of block motion is dilitational (downward) at the seismograph stations. Because of the poor depth resolution, it is uncertain whether the events are more likely associated with brine production or brine injection. The preponderance of events have depths more strongly favoring brine injection than brine production as the causality agent; however, this evidence is extremely weak. (6) The characteristics of the observed seismicity do not indicate a high seismic risk associated with these events. No events with magnitudes greater than 2.0 have been observed. All events range in magnitude from 0.0 to 1.5. There is no obvious relationship between events which would suggest a normal foreshock, mainshock, or aftershock sequence as observed in active tectonic regions. Even when event frequency was high, the total number of events was low ($\leq$20 events/5-day period). Although the number and size of these microearthquakes constitute a low seismic risk due to ground accelerations, the integrated displacement from many events along a single growth fault may constitute a subsidence hazard. The greatest benefit to be derived from microseismic monitoring of such production regions may be to identify which local faults display the greatest instability to slipping and thus constitute the regions which should be monitored most closely by other techniques for subsidence effects.

INTRODUCTION

Commercial utilization of Gulf Coast geopressured/geothermal brines as an alternative energy source requires production and disposal of these environmentally hazardous fluids at rates exceeding 10,000 barrels per day per well. Fluid volume withdrawal and injection at these rates alters the state of subsurface stress, thereby potentially resulting in induced microearthquake activity and ground subsidence. To investigate the potential seismic risks associated with the production of brines from the Pleasant Bayou No. 2 design well in Brazoria County Texas, Teledyne Geotech, with the authorization of the Texas Bureau of Economic Geology, conducted a seismic monitoring program at Chocolate Bayou from September 1978 through September 1983. The primary objective of the Brazoria seismic monitoring program was to determine if production from the Pleasant Bayou geopressured/geothermal energy well resulted in enhanced seismicity which would constitute a risk in itself or would indicate the longer term hazard of accelerated subsidence.

The results of this study have demonstrated that seismicity is enhanced by the brine production; however, neither the increased number of events, nor the size of the induced microearthquakes constitute a serious hazard or risk due to ground accelerations. Whether or not these microearthquakes cumulatively constitute a long-term subsidence risk is not answered by these data.

This is the final technical report of the Chocolate Bayou seismic monitoring program. It is intended to define the experimental procedures, summarize the observations from 1978 through 1983, and discuss the results and conclusions drawn from analyses of the data. Although we believe the principal objective of the program has been accomplished, we also believe that many more questions have been raised than answered by this study. Additional research in the areas of seismic energy propagation through Gulf Coast sediments, growth fault mechanics, and the interaction of fluid transport and mechanical characteristics of faulted aquafers in the Gulf Coast is strongly indicated.

THE BRAZORIA SEISMIC NETWORK, INSTRUMENTATION, DESIGN, AND SPECIFICATIONS

The Brazoria County seismic array consisted of five seismograph stations in the Chocolate Bayou area of Brazoria County, Texas. The locations of these stations, local cultural features, and projected locations of growth faults at a depth of 16,000 feet are illustrated on figure 1. The aperture of the array is four kilometers. The latitudes, longitudes and elevations of the sensors are listed in table 1. Figure 2 is a block diagram illustrating the operation of the array. Each station consisted of a Teledyne Geotech S-500 seismometer which was locked in a borehole at a depth of one hundred feet. The signal from the seismometer was magnified using a Teledyne Geotech 42.50 amplifier and then FM multiplexed to a voice-band carrier frequency for transmission to a common data collection point at Liverpool, Texas. Data transmission was via telephone telemetry circuits. At Liverpool, the signals from the five stations were amplitude conditioned and multiplexed together for transmission via AT&T long lines to the Teledyne Geotech laboratory at Garland, Texas.

TABLE 1. BRAZORIA COUNTY TEXAS SEISMIC ARRAY

Site	Latitude(N) Deg	Min	Sec	Longitude(W) Deg	Min	Sec	Elevation Feet	Magnification X 1000 @ 5 Hz	VCO Hz
BEG1	29	17	28	95	16	53	-87	147	1360
BEG2	29	17	32	95	14	01	-87	138	2380
BEG3	29	16	54	95	15	22.5	-97	140	1020
BEG4	29	15	54	95	14	45.2	-90	164	2040
BEG5	29	15	53.4	95	16	10.3	-84	159	1700

In Garland, the five station signals were demultiplexed from their respective carriers using Teledyne Geotech 46.12 discriminators. The signals and precise time code then were recorded on magnetic tape and on 16-mm film using a Teledyne Geotech develocorder. The unity-gain velocity response of the system is illustrated in figure 3. The magnification at a frequency of five hertz of the individual stations is given in table 1. Variations in effective magnification reflect the variability of the ambient noise at the different sites.

Typical power spectra densities of ambient noise conditions at four sites in Chocolate Bayou are illustrated in figure 4. These noise sites do not correspond with the final array sites but are given to illustrate the typical ambient conditions.

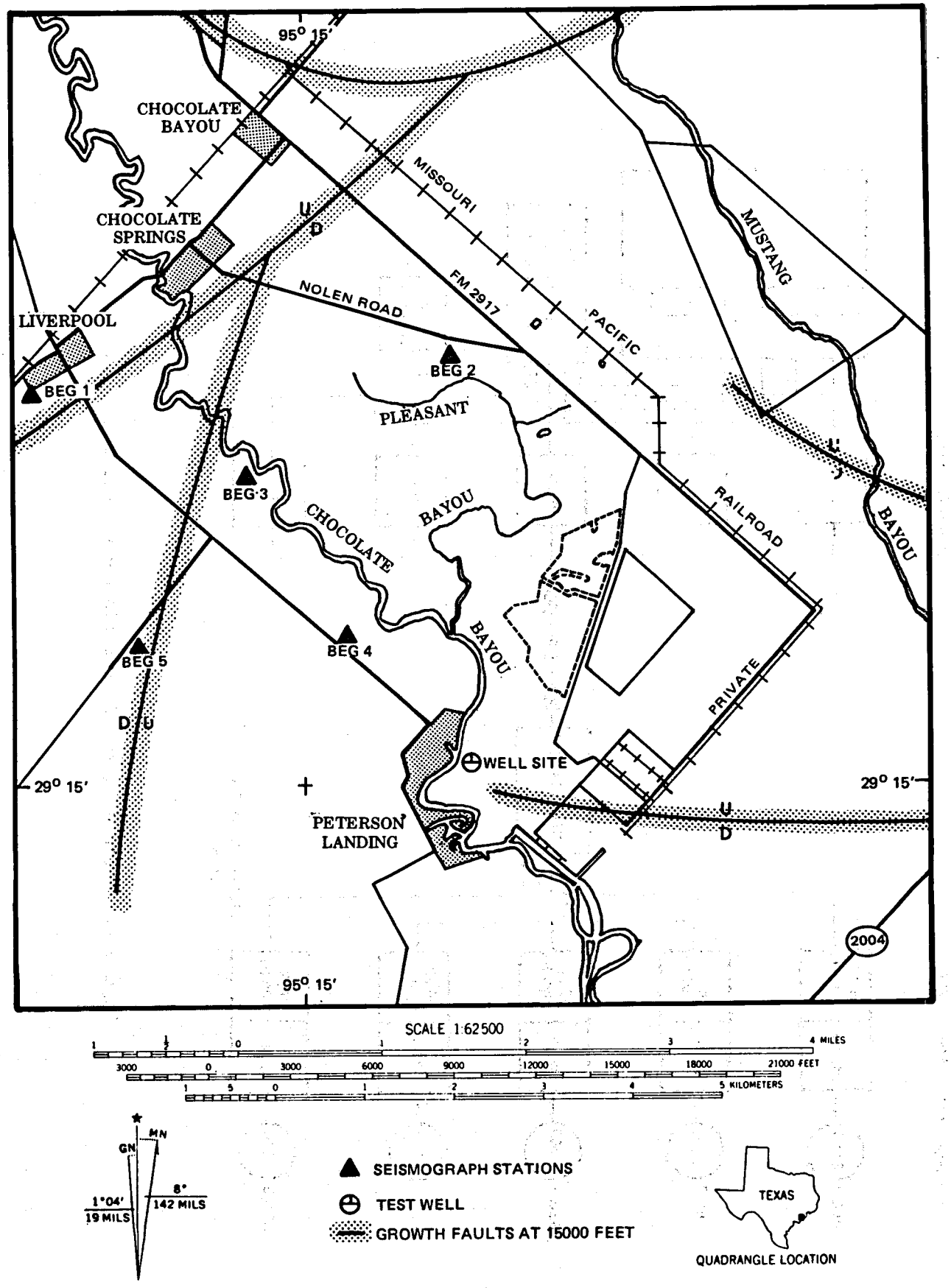

Figure 1. Brazoria County Texas seismic array.

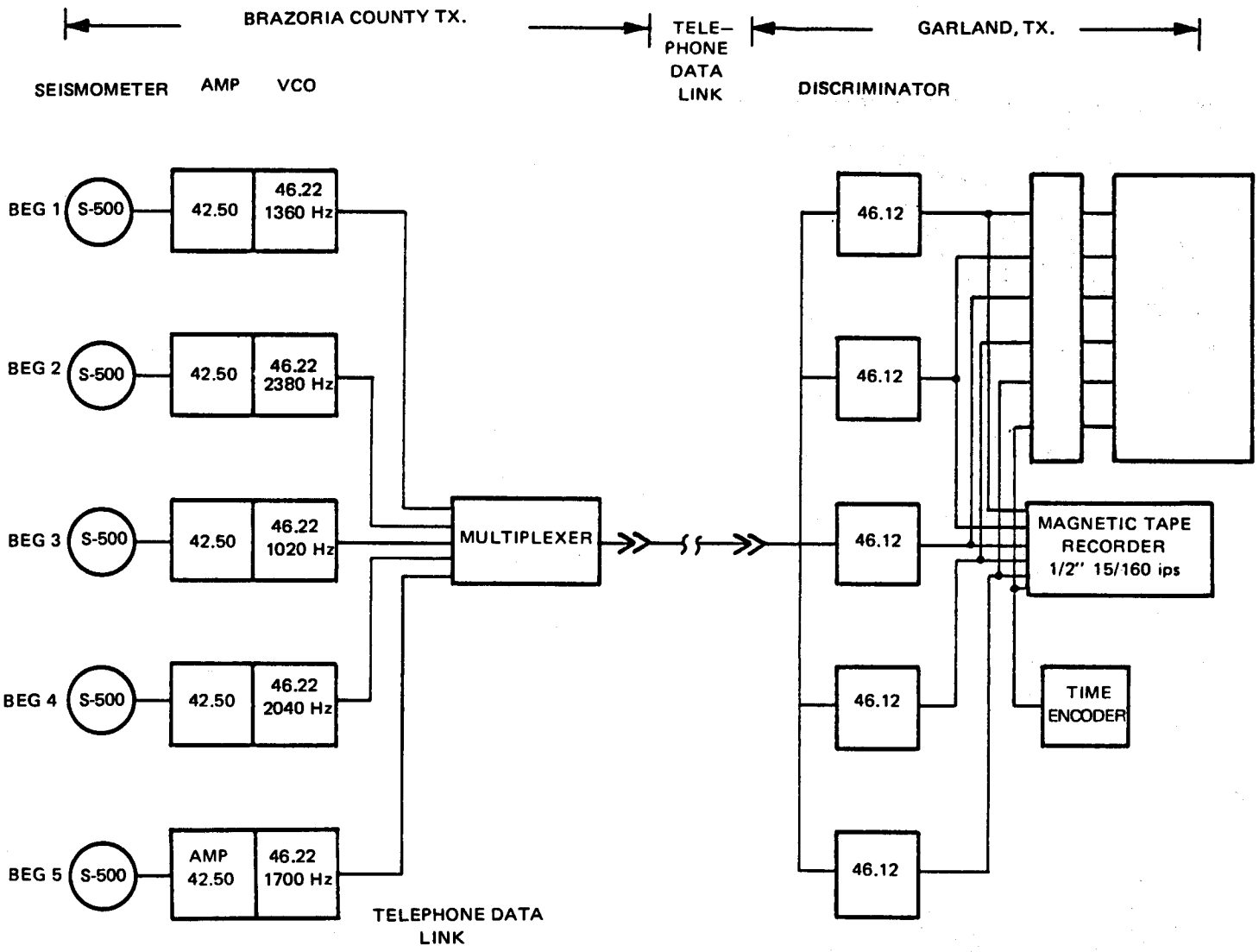

Figure 2. Block diagram of Brazoria County seismic array.

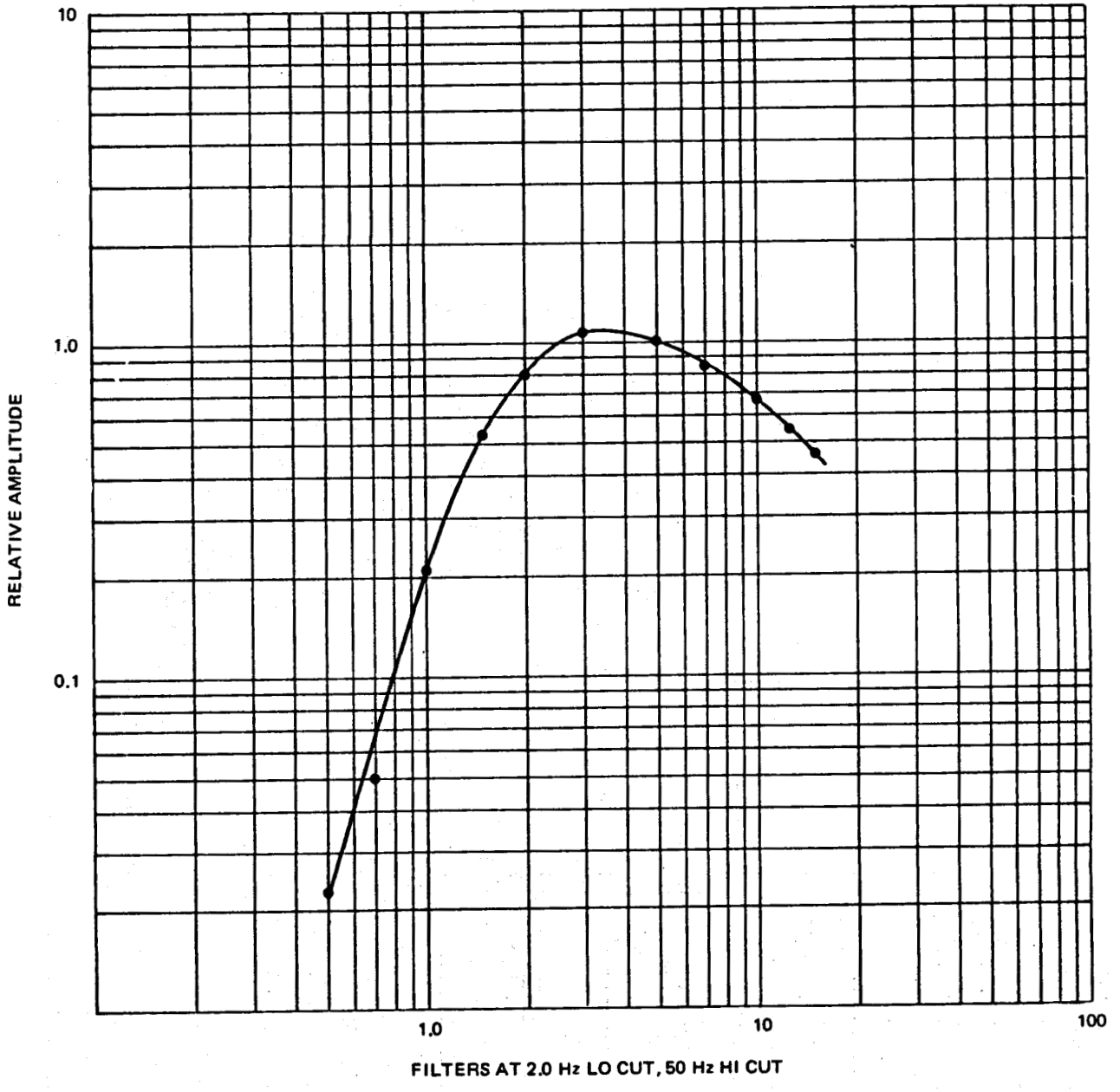

Figure 3. System velocity response at Brazoria.

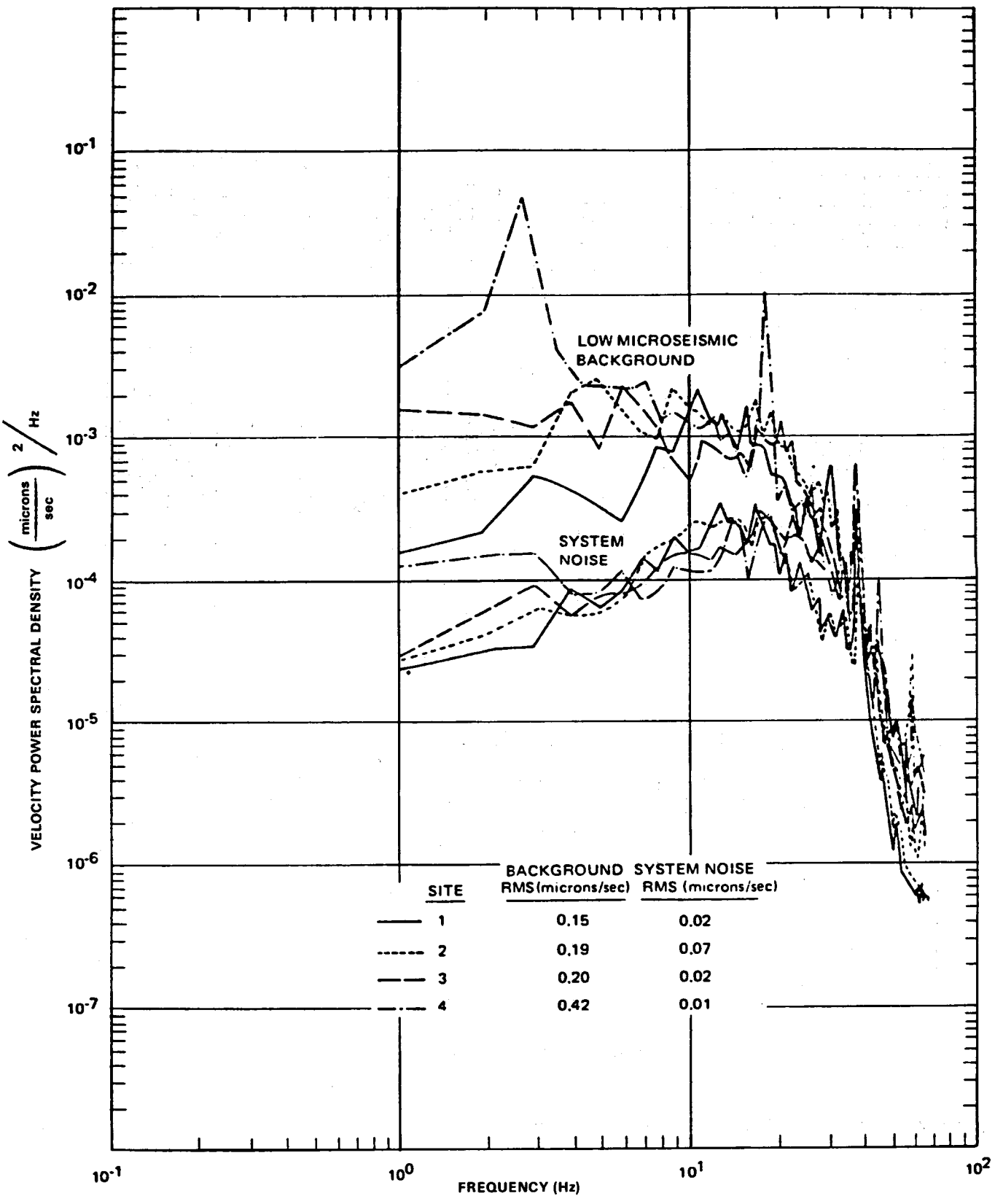

Figure 4. A comparison of representative system noise and calm period spectral estimates.

In general, the maximum (0-P) ground displacements observable with the Brazoria seismograph instrumentation without significant distortion or clipping at one, five and ten hertz are respectively $7.4 * 10^{-5}$, $2.6 * 10^{-6}$, and $1.2 * 10^{-6}$ meters. The minimum (0-P) ground displacements observable are between $1 * 10^{-9}$ and $5 * 10^{-9}$ meters depending upon ambient ground noise conditions. These observation limitations correspond to events with seismic moments between 10^{17} and 10^{20} dyne-cm or approximate local magnitudes between -0.5 and 2.5 (see figure 5).

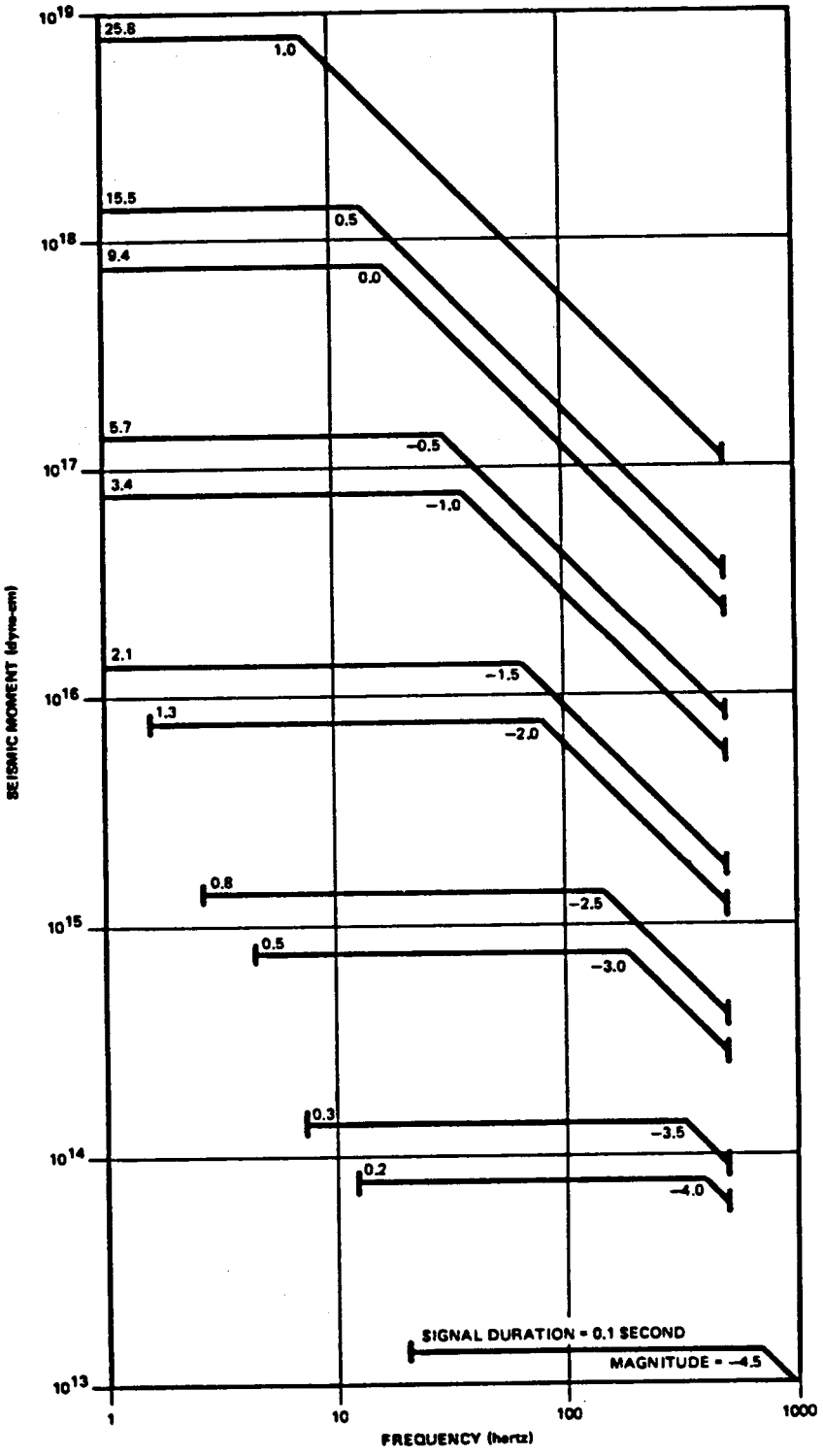

Figure 5. Corner frequency versus seismic moment for central United States earthquakes (after Street, Herrmann, and Nuttli, 1975).

DATA ANALYSIS PROCEDURES

Two general types of signals were recorded by the Brazoria seismic array, and each required specific data processing procedures. Type I events were signals which traversed the array with apparent velocities more nearly like body waves (that is, P-waves and S-waves). The analysis procedures for phase arrival timing and locating these events are discussed under the heading Body Wave Data. Type II events were signals which traversed the array with apparent velocities more nearly like surface waves. The analysis procedures for locating these events are discussed under the heading Surface Wave Data. Finally, the methodology for computing event magnitude is discussed under the heading of Magnitude Determination.

Body Wave Data

The data generated by the Brazoria seismic array were analyzed using standard procedures to yield basic information about origin times, locations and magnitudes of observed events. The 16-mm film seismograms were reviewed carefully to detect any microseismic events that may have occurred. When an event was detected, the analyst measured the amplitude, period, and arrival times of the P (compressional), S (shear), and L_R (surface) wave of the event. The amplitude, period and arrival time data are stored for subsequent input into a computer code (MEHYPO) which estimates the origin times, source coordinates and local magnitudes of the observed events. The estimation algorithm is similar to that described (Lee and Lahr, 1972) in that it finds the origin time and set of source coordinates which minimizes the mean square difference between observed and predicted arrival times at the various sensor locations. The code also provides various location uncertainty estimates which are based upon the assumption that the arrival time errors are normally distributed and that the seismic velocity structure is known without error. The sensor frequency response data, the P-wave amplitude and period data are used to compute the local magnitudes of the observed events.

A generalized P-wave velocity structure for the Gulf Coast is illustrated in figure 6. The actual velocity structures used in the event location procedure are listed in tables 2a and 2b. Two different velocity structures were necessary because of sharp velocity inversions in shallow layers. These velocity inversion layers can be included in the location computational schemes for array-interior events because the wave incidence angles are sufficiently high to permit transmis-

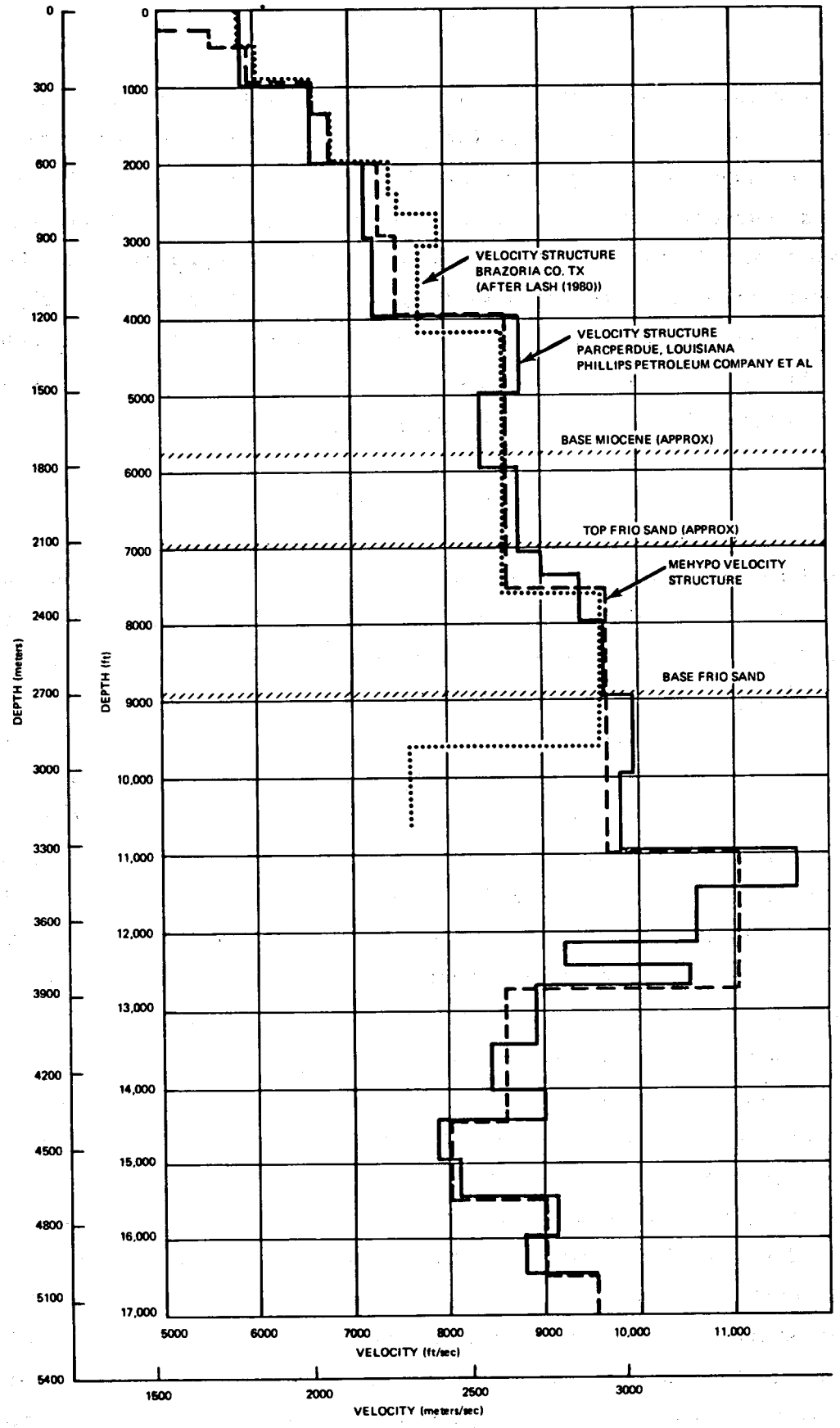

Figure 6. P-wave velocity structure.

TABLE 2A. VELOCITY STRUCTURE FOR EVENTS INSIDE THE ARRAY

Layer Parameters	P-Wave Vel. (Km/sec)	S-Wave Vel. (Km/sec)	Thickness (Km)
1	0.6100	.352	0.0091
2	1.7070	.986	0.1000
3	1.7500	1.010	0.0400
4	1.8000	1.039	0.1500
5	2.0120	1.162	0.1220
6	2.0730	1.197	0.2140
7	2.2550	1.302	0.2900
8	2.2860	1.320	0.3100
9	2.6210	1.513	1.036
10	2.9260	1.689	1.0500
11	3.3530	1.936	0.5500
12	2.6210	1.513	0.5200
13	2.4380	1.403	0.3100
14	2.7430	1.584	0.3100
15.	2.9260	1.689	0.3000
16	3.1700	1.830	0.3000
17	3.5000	2.021	0.3000
18	3.8000	2.194	1000.0000

TABLE 2B. VELOCITY STRUCTURE FOR EVENTS OUTSIDE THE ARRAY

Layer Parameters	P-Wave Vel. (Km/sec)	S-Wave Vel. (Km/sec)	Thickness (Km)
1	0.8000	0.4619	0.0600
2	1.1000	0.6351	0.0710
3	1.3910	0.8031	0.3270
4	2.2000	1.2702	0.2650
5	2.3500	1.3568	0.4500
6	3.5400	2.0439	1.6680
7	3.9600	2.2864	1.8140
8	4.2500	2.4538	0.6000
9	4.7000	2.7136	1.0000
10	4.9000	2.8291	5.0000
11	5.1000	2.9446	200.0000
12	5.3000	3.0600	1000.0000

sion of the waves through the layers. However, array exterior events can have wave incidence angles to the low velocity layers which do not permit theoretical transmission of the energy as a normal refracted wave and thus fail to converge to a location solution. Solutions exterior to the array can be obtained by smoothing these velocity inversions out of the structure as in table 2b. Comparisons of known and computed locations of explosions outside the array demonstrated that this smoothing procedure does not jeopardize the accuracy of the location. On the other hand, including the velocity inversion layers for array interior events improves both the precision and accuracy of the locations obtained.

The S-wave velocity structure was derived from the P-wave velocity structure using the formulation:

$$V_S = V_P \frac{1}{/(1 + 1-2\sigma)^{1/2}}$$

where: V_S = Shear wave velocity
V_P = Compressional wave velocity
σ = Poisson ratio

Water has a Poisson ratio of 0.5, and most competent rock has a Poisson ratio of 0.25. Lash (1980) has determined the Poisson ratio for surficial Gulf Coast sediments to be greater than 0.45 with the ratio decreasing with increasing depth. To utilize S-waves for hypocenter location, a fixed V_P/V_S ratio of 1.732 was used. Epicenters were computed only for events observed at four or more stations because of possible ambiguities of solutions based on data from fewer stations.

Surface Wave Data

Signals consisting entirely of surface (Rayleigh) waves and/or leaking modes were recorded commonly by the Brazoria, Parcperdue, Sweet Lake, and Rockefeller Refuge seismic arrays. Hypocenters of events generating these signals cannot be determined using standard Geiger least-squares inversion procedures. It is possible to determine approximate epicenters of these events, however, if an appropriate wave velocity for the observed phase arrivals can be determined.

The excitation of surface waves, particularly in an environment characterized by significant variations in velocity in three dimensions, is more complex than excitation of primary body waves. Surface waves, unlike body waves, propagate not only as fundamental mode oscillations, but also as higher mode oscillations. These higher modes are analagous to overtones produced by musical instruments. Both the

velocities and amplitudes of the Rayleigh modes excited are critically dependent on the body wave (both P- and S-waves) velocity structure. Figure 7 illustrates the relative excitation of the first four vertically-oriented, two-hertz Rayleigh modes as a function of depth for a location near Apache, Oklahoma, (Douze, 1964). Also illustrated are the density, P-wave, and S-wave profiles for the upper 3,000 meters of geological section. The relative amplitudes of the higher modes generally decline significantly as mode number increases when the velocity structure is free of low-velocity zone energy traps. If, on the other hand, the depth of a particular model maximum occurs in a low-velocity zone (LVZ), that mode will display an anomalous amplitude compared with that which would be excited if the LVZ were not present. The observed Rayleigh-wave energy at any particular frequency is dependent upon the depth of observation and the total energy integrated over all possible modes. Thus, for example, a seismogram from a location at a depth of 2,000 meters in the structure of figure 6 would display Rayleigh waves dominated by first, second and third higher mode arrivals with very little contribution by the fundamental mode.

The Gulf Coast sedimentary column is significantly more complex than the one illustrated in figure 7, and the relative importance of higher mode contributions, particularly at wave frequencies greater than two hertz, should not be underestimated. Figure 8 illustrates the computed and observed Rayleigh group velocities as a function of period for six Rayleigh modes in Gulf Coast sediments for Refugio County, Texas (Ebeniro and others, 1983). Note that fundamental third-, fourth-, and fifth-order harmonics are observed, and that first and second higher modes are not. The higher modes are strongly, normally dispersed (that is, phase and group velocities are inversely related to wave frequency). The fundamental mode, on the other hand, is relatively nondispersed, or slightly inversely dispersed, in the frequency range from one to five hertz. This accounts for why the Rayleigh wave train frequently appeared as an impulsive arrival in the time domain. Since the density, bulk and shear moduli are all low for Gulf Coast sediments, the fundamental mode Rayleigh wave velocities are also low, ranging from 150 m/sec to 350 m/sec. Unfortunately, the velocity range also is occupied by acoustical transmissions through air, and significant coupling of atmospheric acoustic and earth Rayleigh waves is highly probable. Thus, it is very important to determine if observed signals are of atmospheric or earth origin. This discrimination is not necessarily obvious as will be shown in a later section.

Unfortunately, strong evidence exists that the mode of propagation of type II

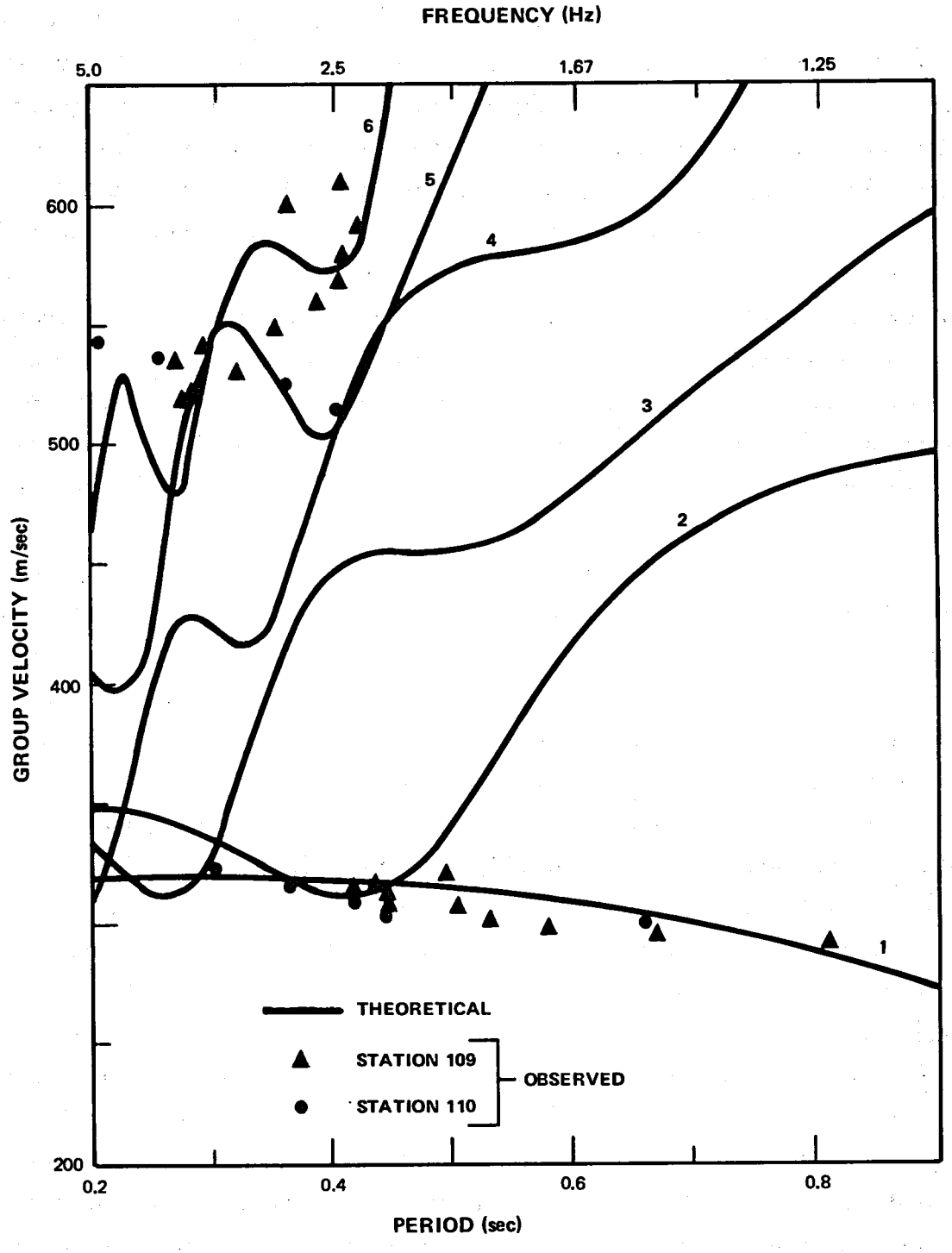

Figure 7. Rayleigh wave group velocity for six modes in Texas Gulf Coast sediments (after Ebeniro, Wilson and Dorman, 1982).

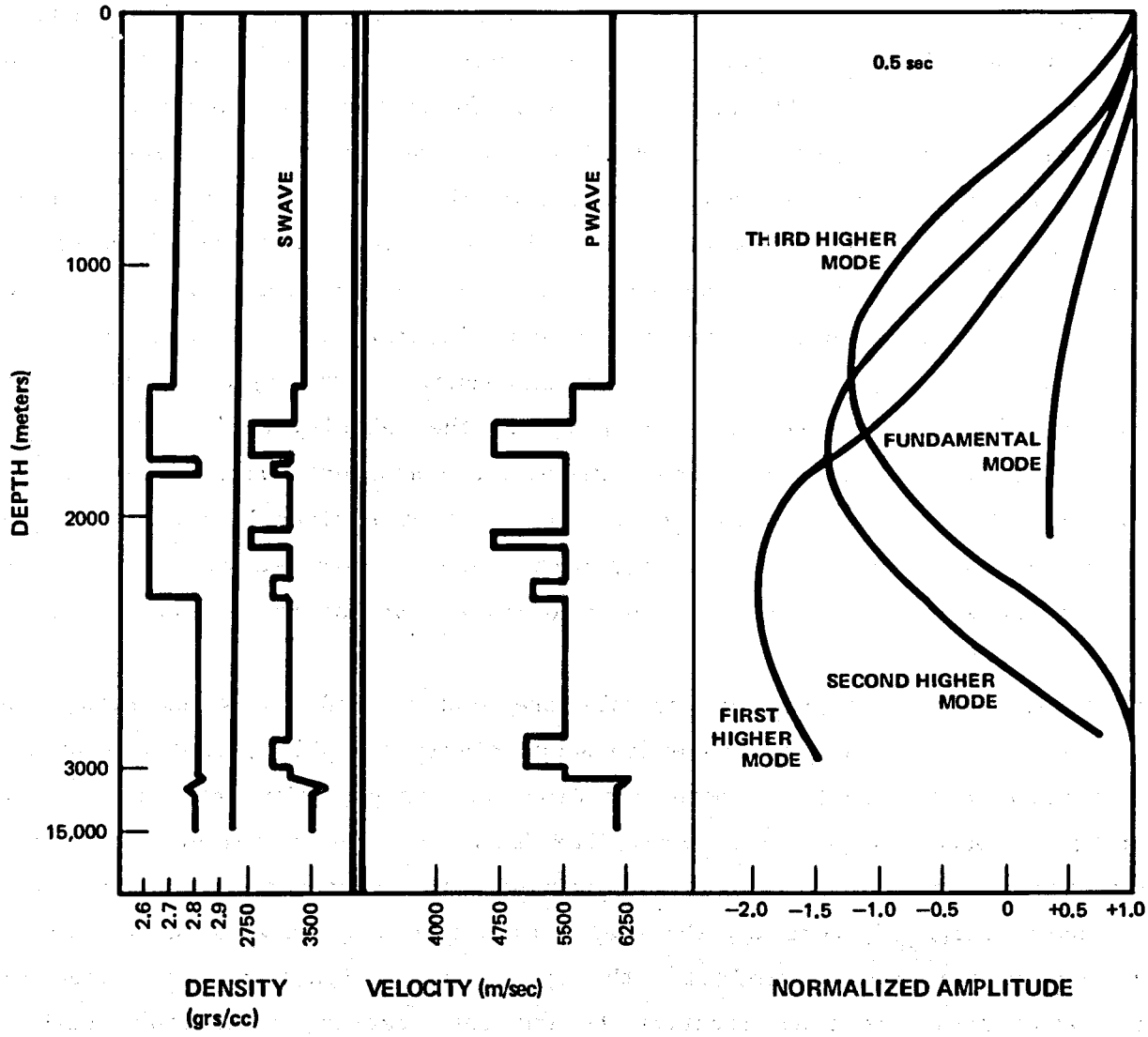

Figure 8. Velocities, density, and theoretical Rayleigh wave amplitude-depth curves at 2.0 Hz, Apache, Oklahoma (after Douze, 1964).

events is not a simple surface wave. There are several energy traps (low velocity in the Pleasant Bayou velocity structure at depths layers) between zero and one and a half kilometers, and the potential effect of these traps requires some explanation. In general, the propagation of energy across a discontinuity in velocity physically obeys Snell's law as illustrated in figure 9a. If there exists in the velocity structure one or more layers with velocities significantly less than the velocities of their bounding layers, then the conditions are ideal to create a wave guide or trapping layer as illustrated in figure 9b by the layer identified as V_2. If the velocity contrast between the bounding layers and the trapping layer is sufficiently large, the energy can never escape from the layer and continues to propagate down the layer as a series of reflected waves. Perfect traps, however, are exceedingly difficult to create, and more often the case is that, at each reflection, a little energy leaks off into the adjacent layers. This "leaked" energy can be observed as a leaking mode arrival on seismograms. If the type of wave trapped is S_V, in a poorly consolidated water-rich layer, the velocity could be exceedingly low (S-wave velocity in water is zero). Because the apparent surface velocity (V_a) is the surface distance between the source and receiver divided by the total travel time rather than the sum of the real ray path distances divided by the sum of the real ray segment velocities, the apparent velocity can appear to be much slower than it is in actuality.

If these observed impulsive arrivals are leaking mode S_V waves rather than surface waves (a subtle distinction which seems highly probable), then the location scheme utilized can result in both location and origin time biases. If the microearthquake occurs within the array, the bias would be as follows. Since the real velocity and real path length are unknown, the computed origin time would always be underestimated, that is, the real origin time would always be earlier than the apparent origin time. Similarly, the apparent location would be biased in a direction away from the real location toward the station or stations with the fastest velocities.

Because of the complexities in Gulf Coast modal excitation and propagation, type II event epicenters computed from described apparent velocities must be regarded with a greater caution than more complete body wave solutions. The procedure we follow to locate these events is to solve iteratively for the least-squares error associated with both the location and wave velocity simultaneously. The functional relationship between epicentral area uncertainty and half-space velocity typically assumes approximately hyperbolic shape (see figure 10).

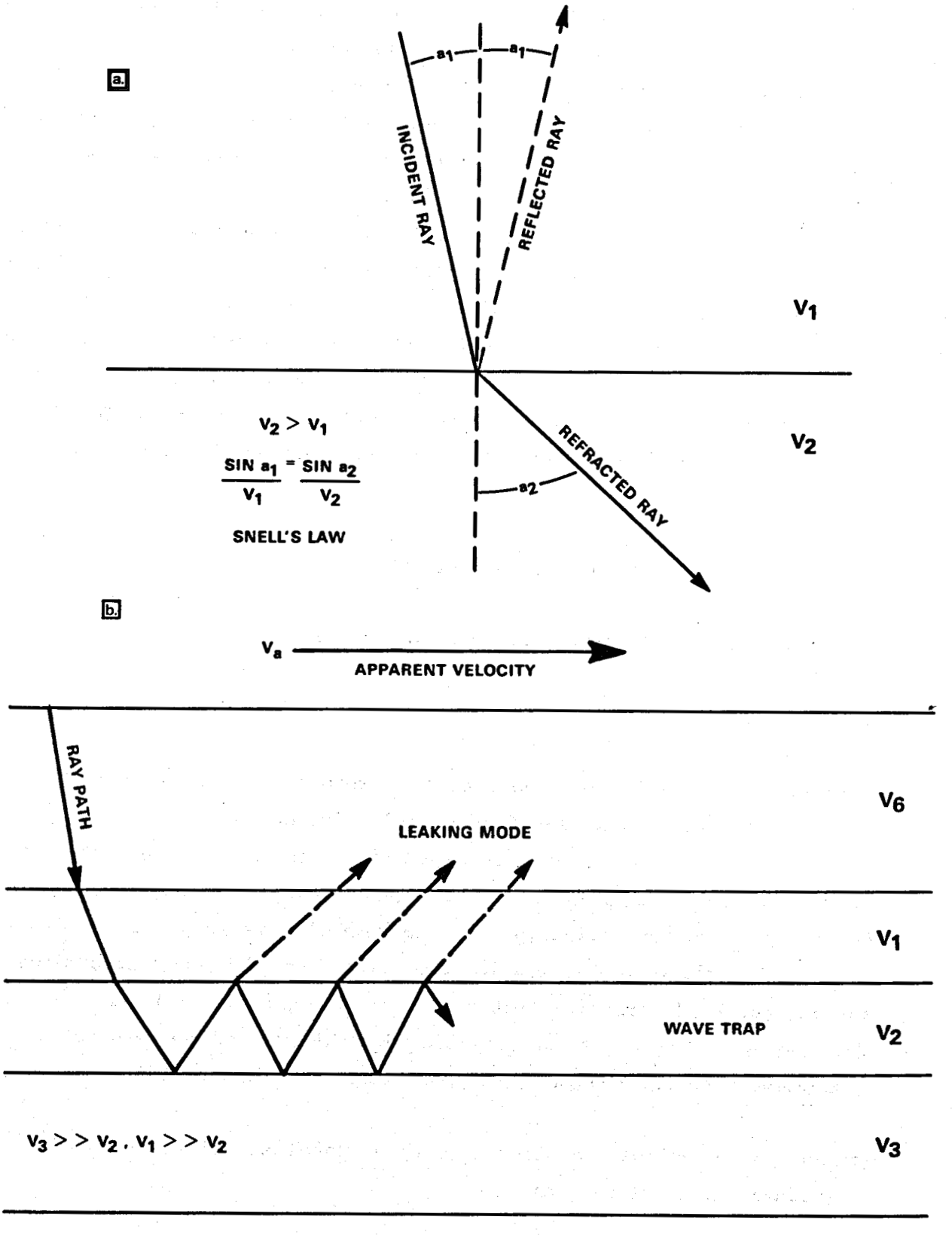

Figure 9. a. Diagram illustrating transmission of an energetic ray across a velocity interface. b. The propagation of a leaking mode from a trapping layer (V_2).

We assume that the hyperbolic vertex corresponds with the best half-space velocity and that the computed location using this velocity is the best approximation of the epicenter. Depth is not resolved by this technique.

In principal, this location analysis technique permits the simultaneous determination of the best-fit velocity and location; however, a word of caution is appropriate here. When few arrival time observations (<10) exist with which to invert iteratively for an epicenter solution, it is possible to produce an intra-array alias location from an extra-array source by fixing an appropriate half-space velocity. The extreme example of this possibility is that the arrival times from a distant teleseism can yield a location solution within the array, if the interior velocity used for location is set sufficiently low. For this reason, epicenters of events located using this least-squares inversion technique, particularly when best-fit velocities are less than 350 meters/second, should be viewed with appropriate caution. Where possible, we have attempted to identify such suspect event locations in a later section.

Magnitude Determination

Magnitudes have primarily been calculated using duration as

$$MD = -2.22 + 2.28 \log (D)$$

where D is duration in seconds from onset of P to return of coda to ambient noise level. It has been shown by (Aki and Chouet, 1975; Chouet and others, 1978; Aki, 1981) that the duration of seismic coda is dependent on the number and distribution of potential back scattering sources. For this reason, coda duration magnitude formulations must be tailored specifically for each region where they were used. The duration magnitude formula we use is one for the Mississippi Embayment determined by the Tennessee Earthquake Information Center. Since a magnitude scale has not been developed for the Gulf Coast, it is possible that all quoted magnitudes are in error. The magnitudes quoted should agree approximately with normal Richter magnitudes.

Magnitudes may be calculated alternatively as local seismic magnitudes based upon maximum surface wave amplitude as

$$ML = \log10\ (a/2) - 1.15 + 0.8\ \log10\ (x)2$$

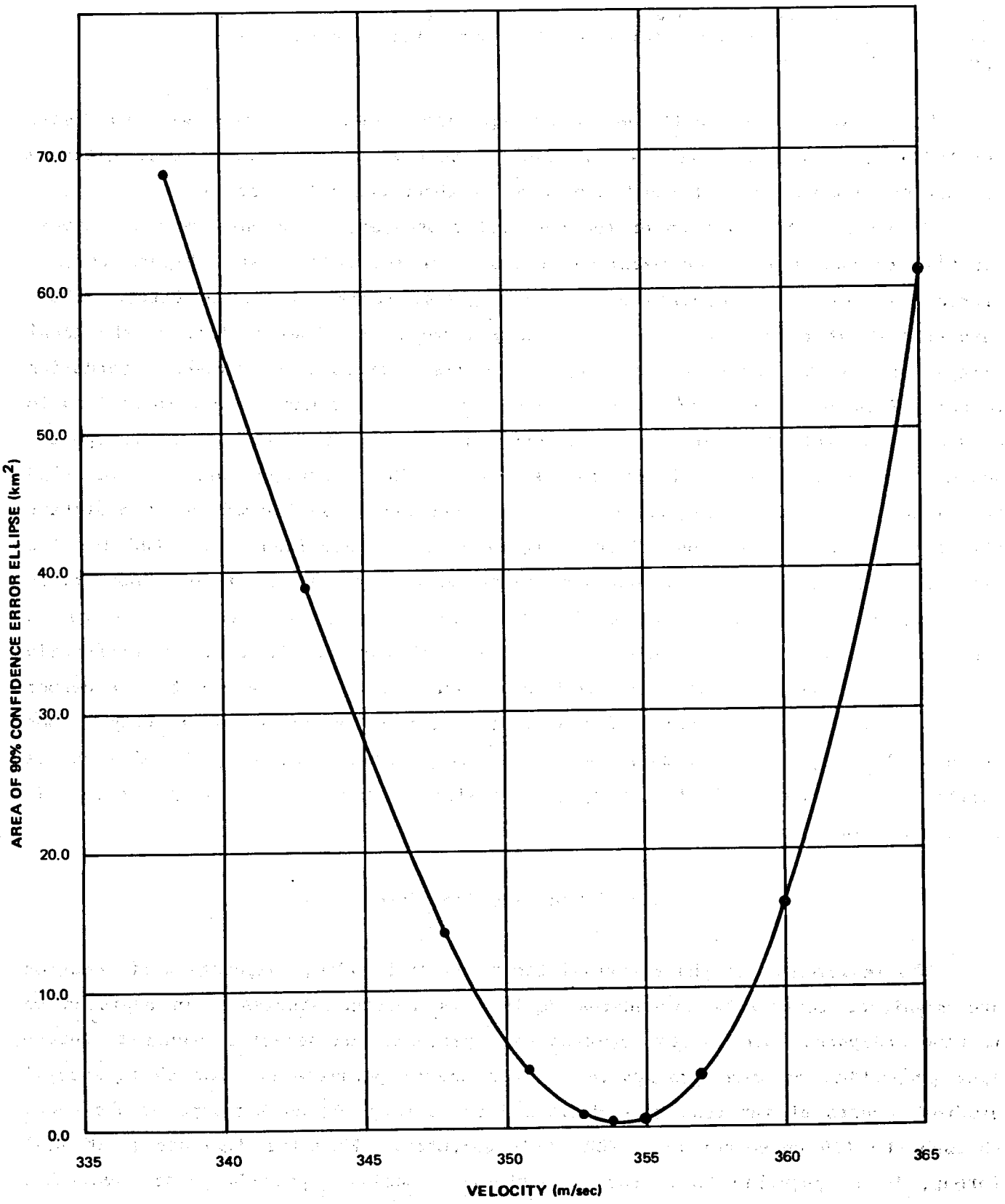

Figure 10. Velocity analysis of Rayleigh/leaking mode event 22 August 1982 at 18:52:28.7 UTC time.

where ML is the local magnitude
and A is the peak-to-peak surface wave amplitude in millimicrons
and X = [(epicentral distance) 2 + (hypocentral depth) 2]1/2
and X > 1.0

The constant -1.5 in the magnitude equation assumes a surface wave to P-wave amplitude ratio of 10. Thus, a magnitude 0 event at 1 km distance would generate surface waves with a peak-to-peak amplitude of about 2.8 millimicrons.

Throughout the duration of the monitoring program, there have been few opportunities to subtantiate the magnitude formulas of the Gulf Coast. Figure 11 is a microearthquake which occurred near Lake Charles, Louisiana, on 16 October 1983. This Gulf Coast earthquake was sufficiently large to be observed both on the local arrays and distant seismograph stations of the Tennessee Earthquake Information Center. This event provided a critical tie for Gulf Coast magnitude computations to adjacent regions. The duration magnitude computed from the data of the Parcperdue seismic array stations illustrated is 3.02. This compares with an Mb (Lg) (magnitude based on the amplitude of the Lg, scattered wave) computed from distant stations of 3.8. This comparison suggests that the magnitudes reported for the Brazoria array may be underestimated by approximately half a magnitude. However, it is equivalently important to realize that the majority of events observed at Brazoria had focal depths apparently less than a kilometer. These are significantly less deep than the Lake Charles earthquake, and, thus, the tie may be for deeper events only. The exact "size" of the events recorded by the Brazoria array is not known. The reported magnitudes are internally consistent, and, if alternative calibration becomes available, it will be possible to rescale these magnitudes if it is of importance.

Special Analyses Procedures

The measurement of phase arrival times and amplitudes, computation of location and magnitude constitute procedures defined as routine studies. In addition to routine analyses, some special studies were performed on selected events to determine properties of wave propagation and/or source parameters. For these special studies, events of interest were digitized by playing the analog tape of the event through the A/D converter of a PDP 11-24 computer. When the data are in digital format, it is possible to perform a variety of analyses procedures not available with analog data. We have emphasized procedures to help understand the propagation

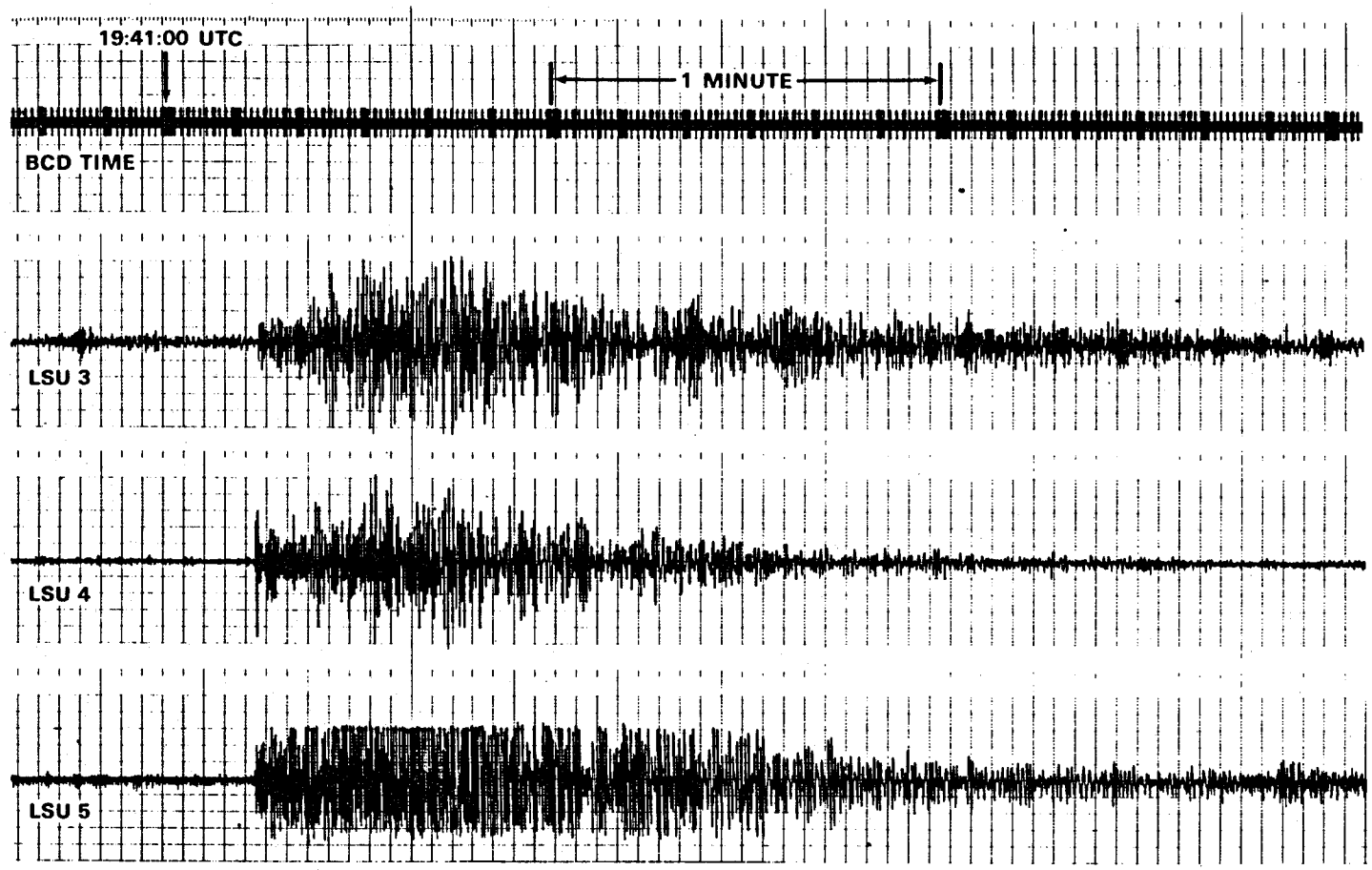

Figure 11. Microearthquake from the Lake Charles, Louisiana, area. OT = 19:40:46.1 UTC (CST + 5 hrs) on 16 October 1983.

of seismic energy and source depth of events. The results of these analyses are presented in a later section.

SEISMICITY AND THE PLEASANT BAYOU PRODUCTION HISTORY

Microseismic monitoring of the Pleasant Bayou geopressured/geothermal test well area began in September 1978 and continued through September 1983. During that time period, there were four brief episodes of production from the Pleasant Bayou No. 2 well. These episodes are identified in table 3. More detailed descriptions of the three principal production periods are given in the following sections.

Phase I Production Test

A short-term brine production test of the Pleasant Bayou No. 2 well (Phase I test) extended from 16 September through 31 October 1980. Analyses of the data to determine reservoir characteristics have been reported by Hartsock (1981) and Garg, Riney, and Fwu (1981). The production histories published by these two analysis groups are mutually inconsistent. Since the test monitoring was performed by Gruy and Associates, we have included only the published bottomhole pressure and production rate history of Hartsock, 1981, (figure 1) to illustrate the Phase I production characteristics. Specific perturbations to the pressure log are numerically identified and keyed to table 4. Figure 12 illustrates that there were essentially three significant pressure declines and two pressure increases during the performance period. These correspond to times when flow rate was altered dramatically. Thus, for example, the production rate reduction from 15,324 barrels per day to 13,386 barrels per day did not constitute a significant bottomhole pressure perturbation.

The total volume of brine produced during the Phase I test was 537,300 barrels. Prior to this short-term (47 days) test, 274,000 barrels of brine had been produced from the Pleasant Bayou No. 2 well between 15 November and 3 December 1979.

July 1981 Phase II Production Test

On 2 July 1981, brine production was reinitiated in what was expected to be the Phase II long-term flow test. Because of a variety of problems with instrumentation and the Pleasant Bayou wells, the high-volume, long-term flow test was aborted on 18 July 1981.

The total volume of brine produced in the Phase II test of 2-18 July 1981 was 220,904 barrels. A plot of the brine and gas production versus flow time is illus-

TABLE 3. PLEASANT BAYOU PRODUCTION HISTORY

Test No.	Flow Test Identification	Flow Initiation	Flow Cessation	Volume Produced (* 10^5 bbl)	Average Rate bbl/d
1	Pre Phase I	15 November 1979	3 December 1979	2.74	15,222
2	Phase I (Short Term)	16 September 1980	31 October 1980	5.37	Variable 6,600-19,200
3	Phase II (Long Term) Aborted	2 July 1981	18 July 1981	2.21	Variable 14,000-28,000
4	Phase II (Long Term)	27 September 1982	13 April 1983	35.2	19,000

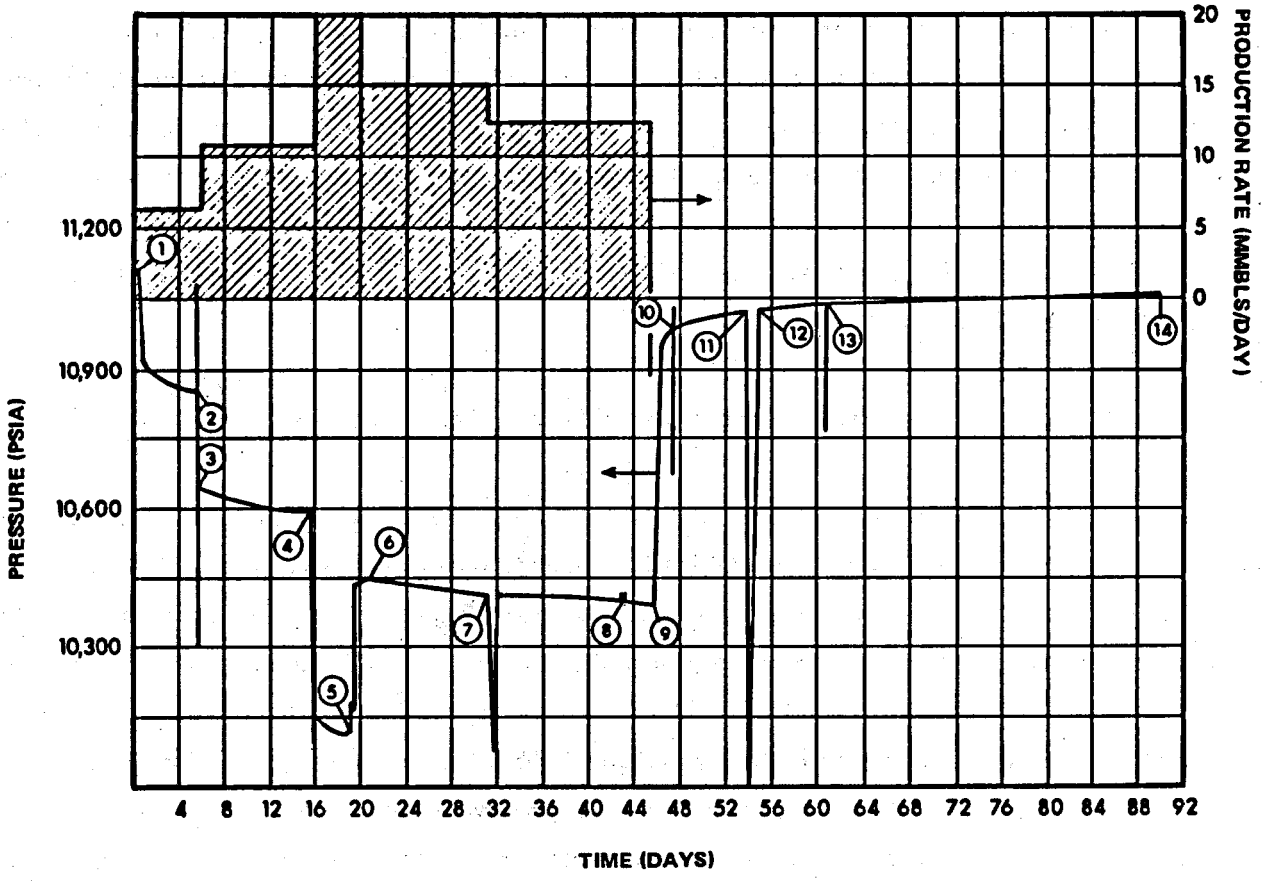

Figure 12. Bottomhole pressure versus time, Phase I test, Pleasant Bayou No. 2 well.

TABLE 4. SEQUENCE OF EVENTS IN PHASE I TESTING, PLEASANT BAYOU NO. 2 WELL

Event no.*	Date	Time hrs	Event
1	9-16-80	1130	Opened well for Phase I test at 6,624 B/D
2	9-21-80	1710	Well shut in to repair adjustable choke
3	9-21-80	1932	Opened well for second flow rate at 10,896 B/D
4	10-01-80	1102	Increased flow rate to 19,200 B/D
5	10-05-80	0632	Reduced rate to 15,324 B/D to reduce injection pressure
6	10-08-80	1230	Reduced rate to 13,386 B/D to reduce injection pressure
7	10-17-80	1550	Lost signal in surface recording system
8	10-29-80	2240	Abnormal pressure-production response
9	10-31-80	1532	Well shut in to monitor pressure buildup
10	11-02-80	0940	Lost signal from HP gauge. Moved gauge and regained signal
11	11-08-80	1700	Lost signal from HP gauge. Pulled gauge, repaired, and re-ran.
12	11-10-80	0511	Gauge on bottom
13	11-15-80	1800	Erratic pressure readings for one hour
14	12-15-80	1304	Pulled Hewlett-Packard bottomhole pressure gauge

*Refer to Fig. 1.

trated in figure 13. The actual production rate history for the Phase II test is illustrated in figure 14. This figure clearly demonstrates the difficulties encountered during the test which required four significant shut-ins before the test was aborted. The corresponding production well and disposal well bottom hole pressure histories are illustrated in figures 15 and 16 respectively. Although the Phase II test of July 1981 was not successful, forty-one percent as much brine was produced in the 254 hours of flow time as was produced in the 1116 hours of Phase I flow time. Thus, the Phase II test may be more significant as a formation strain perturbation than the Phase I test.

September 1981 Phase II Long-Term Flow Test

The Phase II, long-term flow test of the Pleasant Bayou No. 2 geopressured/geothermal design well was reinitiated approximately 27 September 1982 following a shut-in of over fourteen months. In anticipation that some aspect of the production history may display a causality relationship with induced seismicity, we maintain a computer log of wellhead tubing pressure and approximate withdrawal rate from the Pleasant Bayou No. 2 well and the wellhead injection pressure for the Pleasant Bayou No. 1 well. Data for this computer log are provided by Gruy Federal Corp. Data are entered at hourly increments from 1 October through 23 October 1982. All subsequent data are entered at daily increments because more detailed logs were no longer provided to us by Gruy Federal. Graphs of the production wellhead tubing pressure and approximate brine withdrawal rate and the wellhead brine injection pressure as a function of time for the period from 1 October through 13 April 1983 are illustrated in figure 17. Specific times when flow rate has been altered are indicated by the alphabetic markers at the bottom of figure 17. Except for seven shut-ins, all other entries indicate times when choke adjustments were made. Although alteration of choke settings and shut-ins result in some short-term perturbations of the production and disposal histories, the production pressure curve generally displays a long-term exponential pressure decline typically observed for confined aquifers. Similarly, the injection pressure curve displays a long-term logarithmic increment in injection pressure as a function of time commonly observed at other injection wells.

Basically, there are two distinct types of signals which have been recorded by the Brazoria seismic array throughout the operational period: (1) events with distinguishable P and/or S phases (type I), and (2) events without body phase arri-

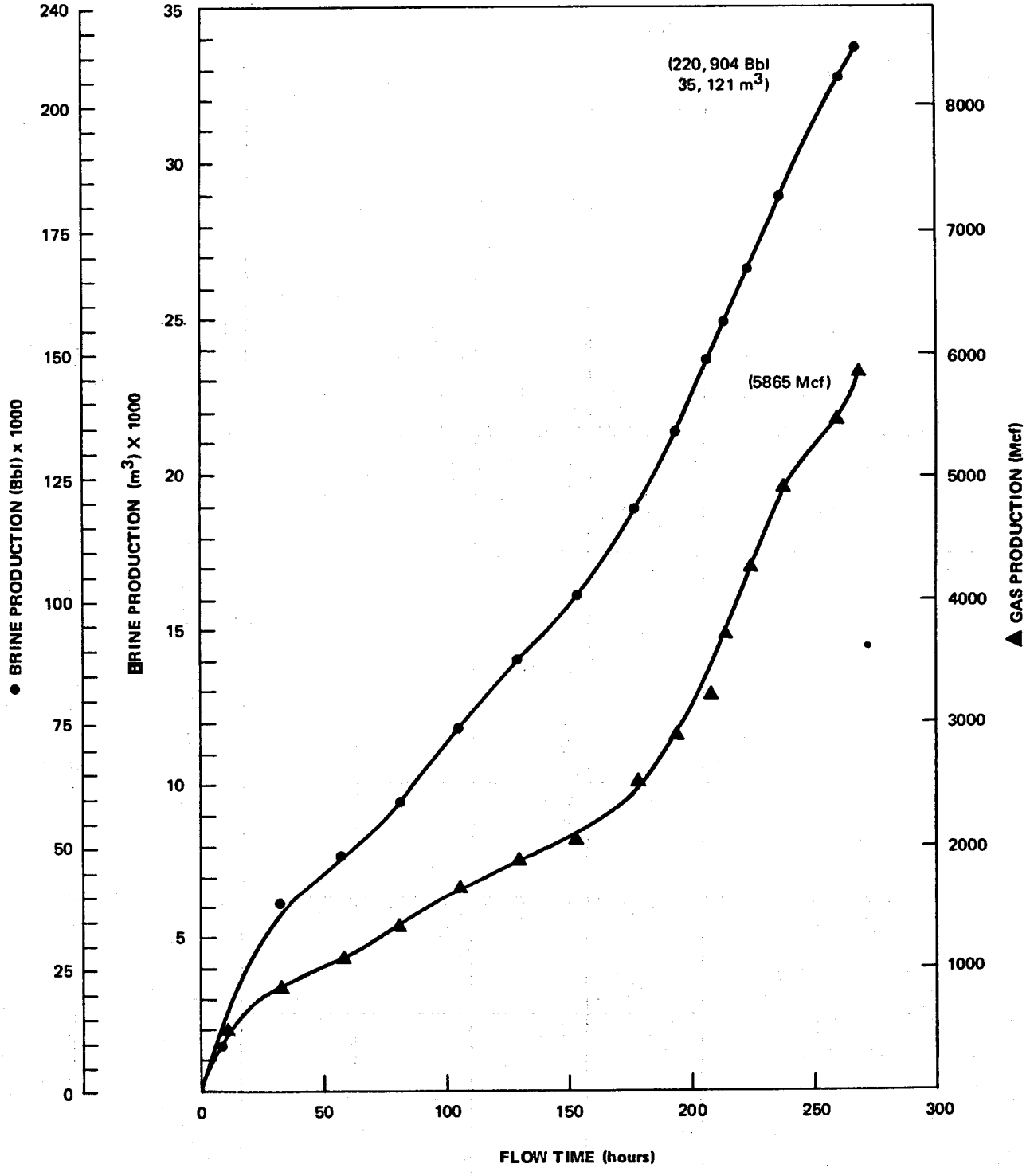

Figure 13. Phase II production from Pleasant Bayou No. 2 for the period 2-18 July 1981.

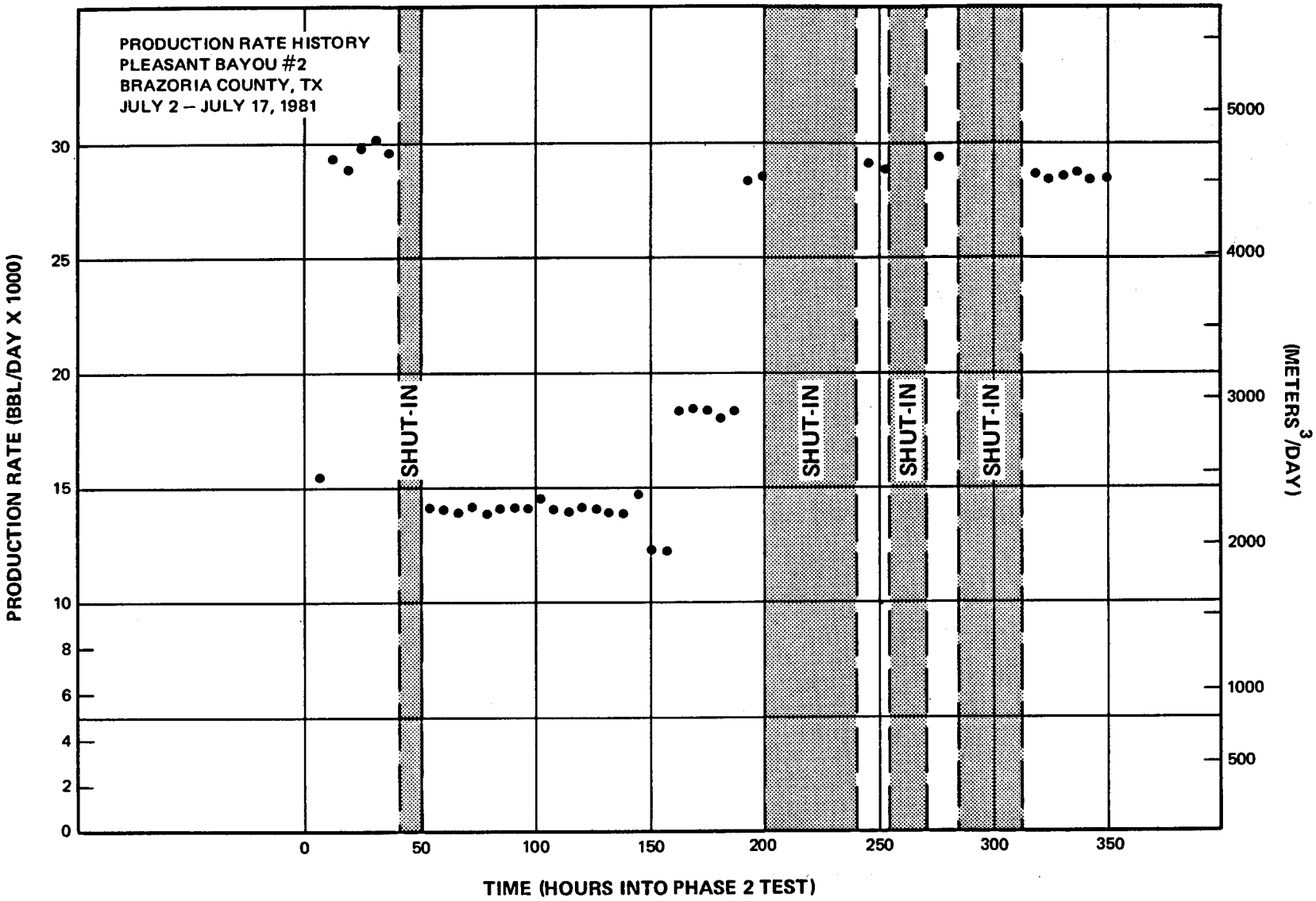

Figure 14. Pleasant Bayou Phase II test production rate history.

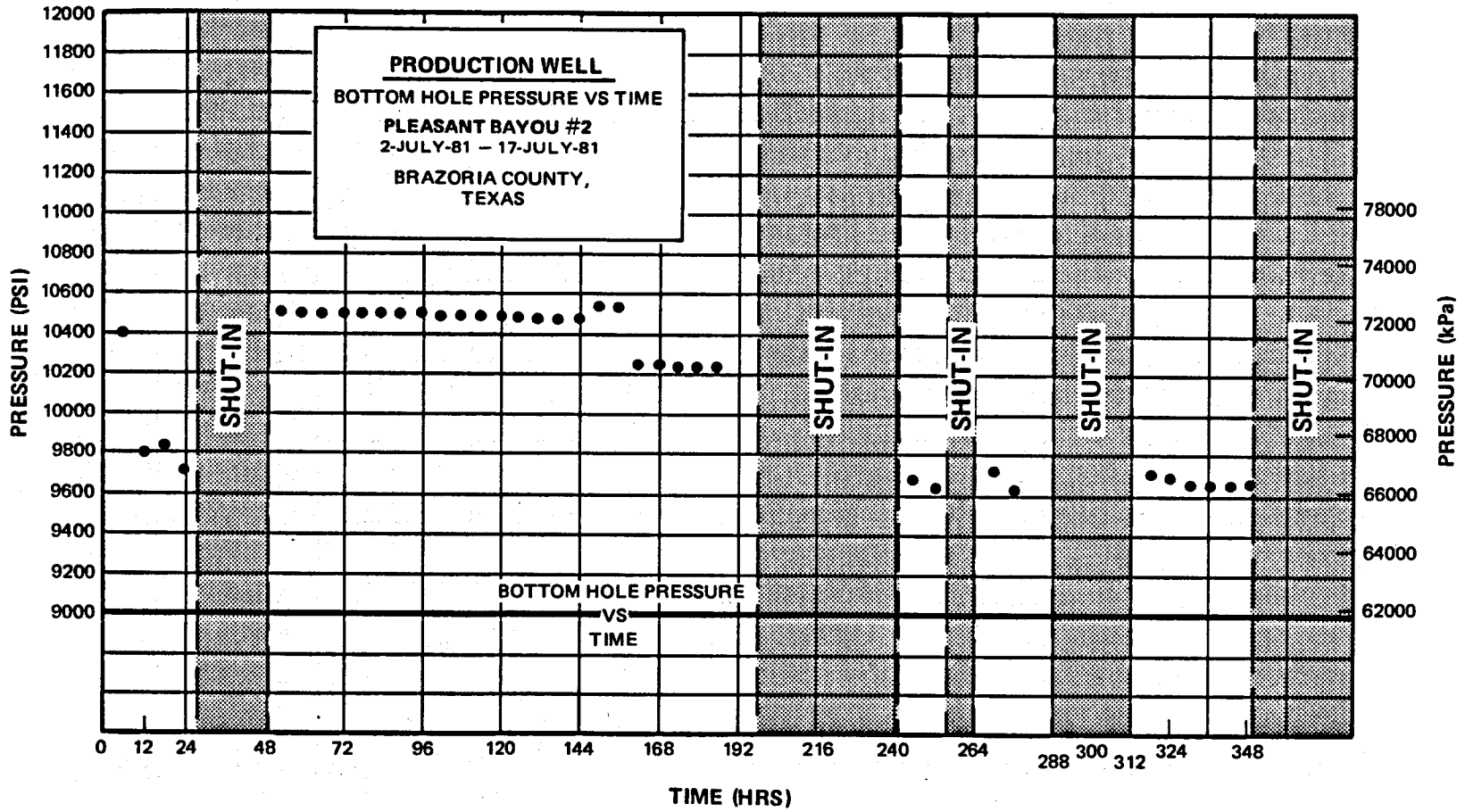

Figure 15. Pleasant Bayou Phase II test production well bottomhole pressure versus time.

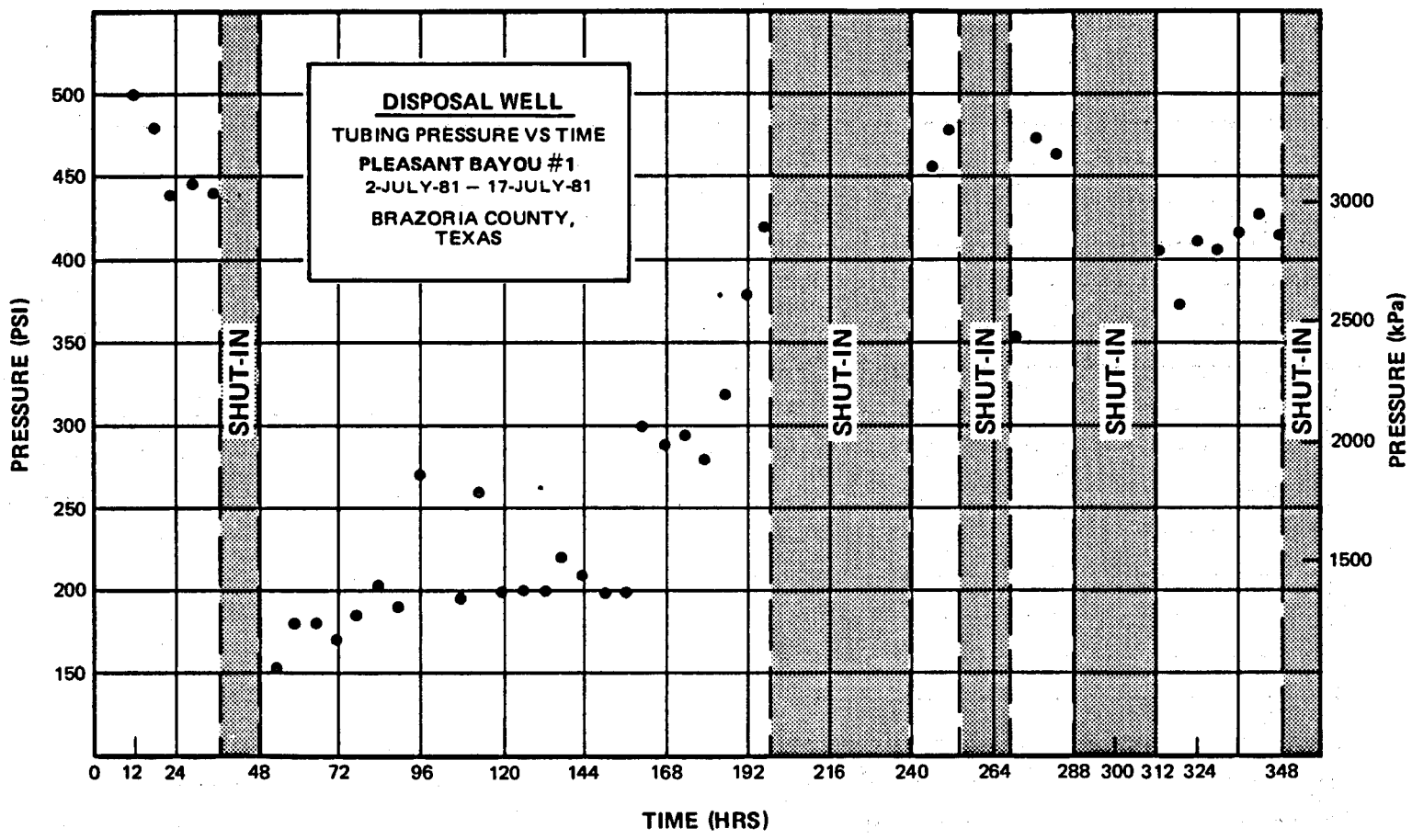

Figure 16. Pleasant Bayou Phase II test disposal well injection pressure versus time.

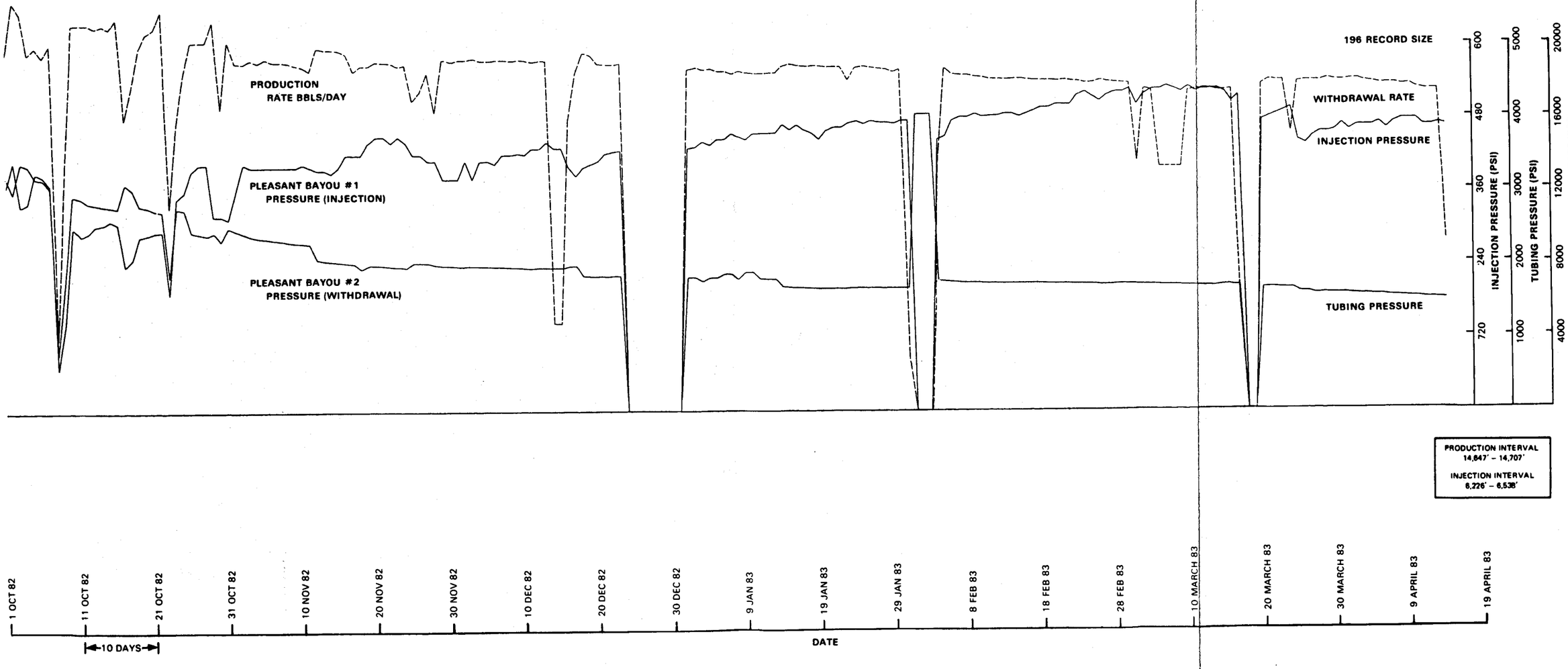

Figure 17. Injection pressure, tubing pressure and flow rate history of the Phase II testing of the Pleasant Bayou No. 2, geopressured/geothermal test well from 1 October, 1982 to September 1983.

vals, but with impulsive Rayleigh/leaking mode signatures (type II). Additional details about the propagation of these events are given in the section on special studies of the signals. A complete listing of the phase arrival data and computed event location for all natural local events is given in appendix A.

The events with identifiable P and/or S phase arrivals which are either unquestionably or suspected to be microearthquakes and not explosives have many common characteristics. P- and S-waves from these events usually are rich in frequencies greater than five hertz, and the seismogram coda tails commonly display exponential amplitude decay similar to those of microearthquakes observed at other locations. (See figure 11). Two examples of this type of event are included as figures 18 and 19.

Determination of P-wave first motions is not unambiguous but appears to be predominantly dilitational (downward) on most seismograms when discrimination is possible. This is a characteristic consistent with a downward local geological block movement. All of type I events yield hypocentral solutions which suggest a depth of origin generally between two and six kilometers. No events have been observed which locate deeper than six kilometers.

Epicenters of the type I events cluster within one and a half kilometers of the projected 15,000-feet deep locations of growth faults on the west and northwest edge of the reservoir (see figure 20, locations indicated by large asterisks). Although a few events appear to associate with the northeast trending fault near Liverpool and Chocolate Springs, the majority of the epicenters appear to associate with a north-south trending growth fault which passes near seismograph stations BEG 1 and BEG 3, and terminates near Chocolate Springs. Furthermore, the majority of epicenters since 1979 which have computed locations near this proposed fault are the east (up-dip) side of the fault. Since the location precision of most of these events is poor and the location accuracy of the growth fault and the epicenter is unknown, little significance can be placed on the relative position of the epicenters to the growth fault.

The magnitude of type I events are all small, between 0.0 and 1.5, and there is no obvious functional relationship between the frequency of occurrence and the magnitude of these events. In fact, the occurrence of this type of event is relatively rare. The largest number (10) occurred in 1981, one was recorded in 1982, and one in 1983.

Events identified as Rayleigh or leaking mode type II signals far outnumber the microearthquakes with P-wave or S-wave phase arrivals. An example of this type

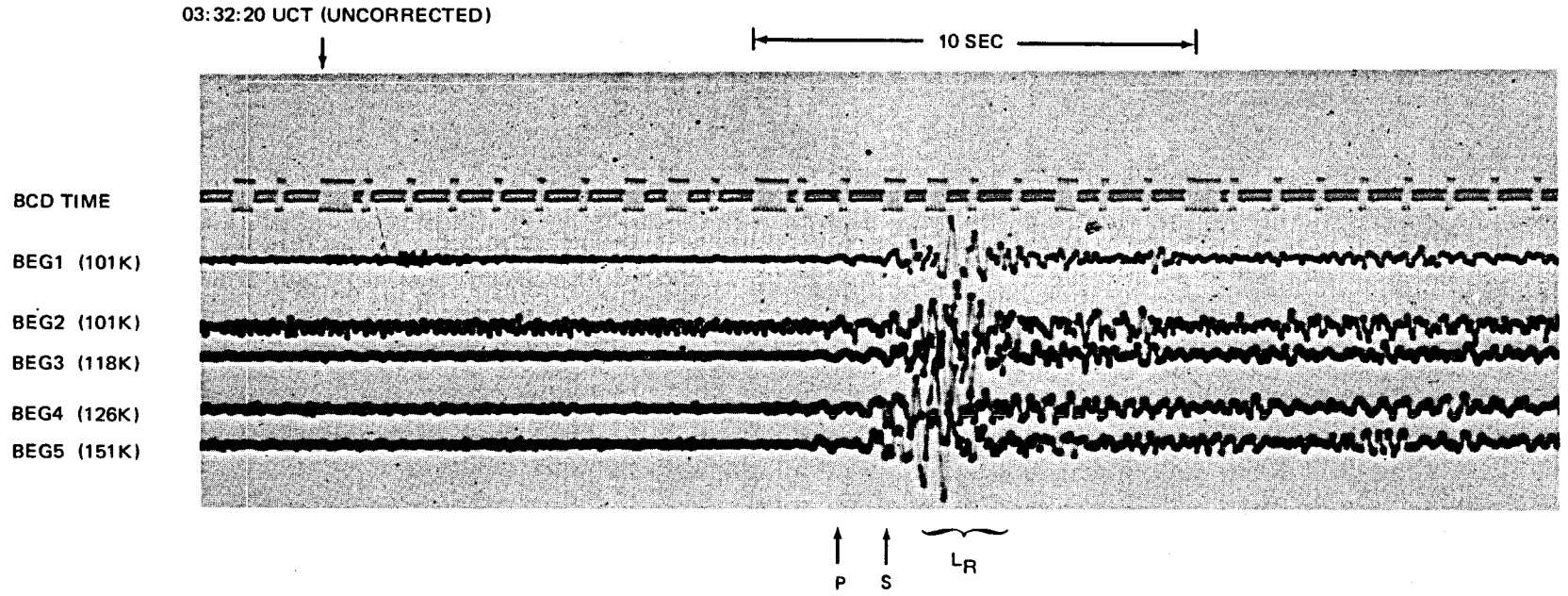

Figure 18. Earthquake 1 January 1981, 03:32:29.3 UTC.

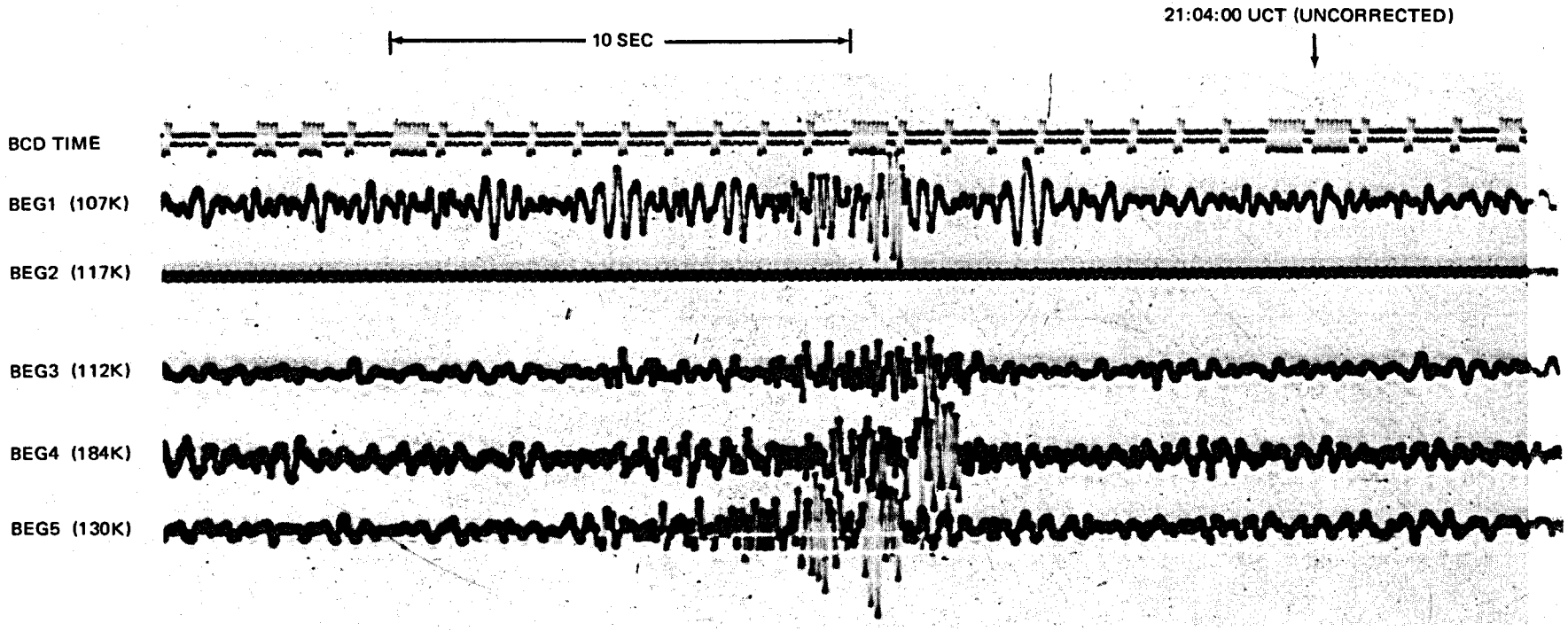

Figure 19. Earthquake 12 May 1981, 21:03:42.9 UTC, depth 5 km.

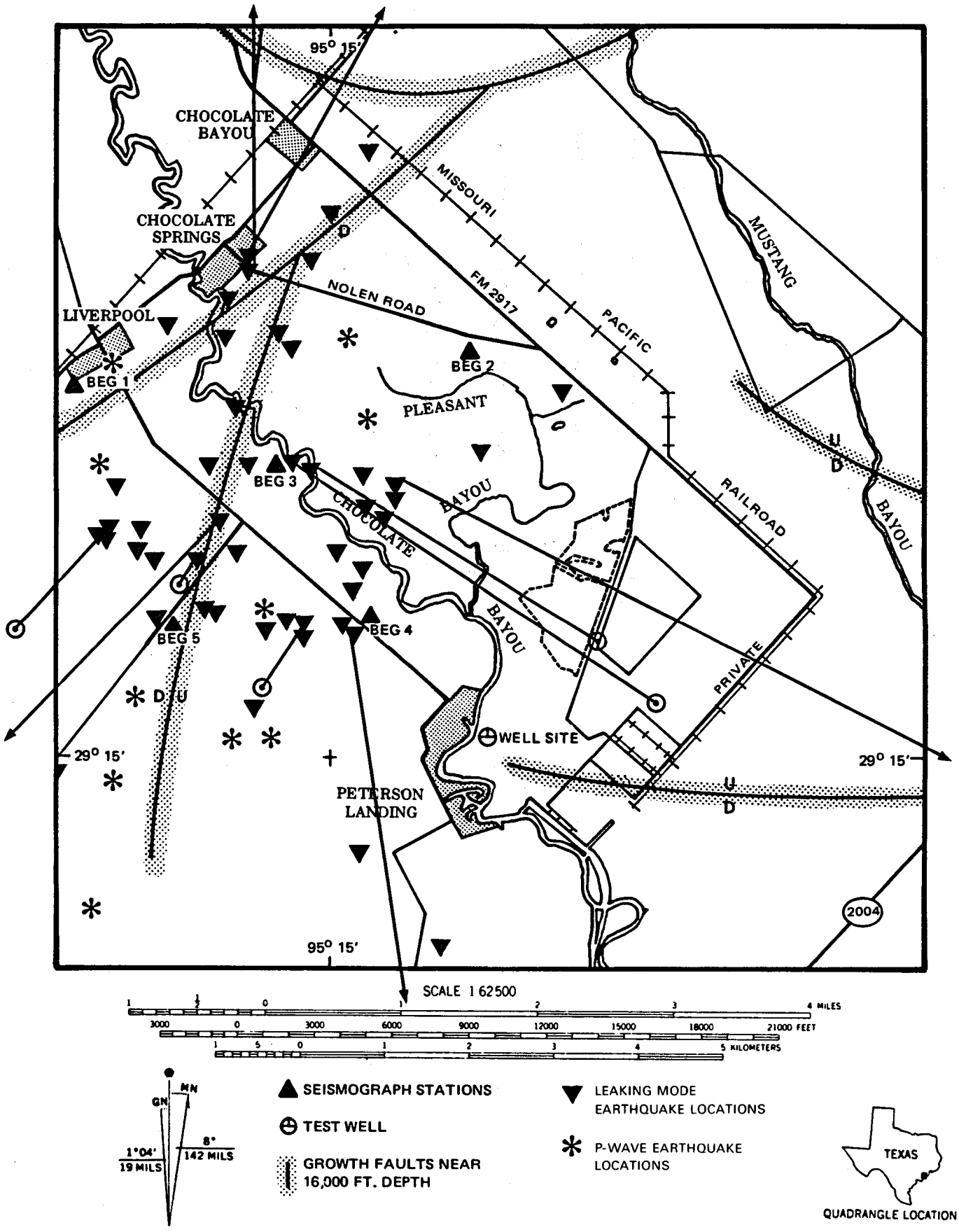

Figure 20. Location of microearthquake activity (presumed to be of natural origin) occurring in the vicinity of the Pleasant Bayou monitoring array 1981 - 1983.

of signal is illustrated in figure 21. Since most of the signals observed throughout the seismic monitoring period at Chocolate Bayou were of this type, most of the special analyses have concentrated on understanding these events. These special studies will be described later in this report.

The epicenters of events identified as Rayleigh or leaking mode propagations are illustrated in figure 20 as inverted triangles. In general, these events have been located using the least-squares error/best velocity method described previously. Eleven of the events located with smallest errors using velocities less than 300 m/sec. Although these locations may be correct, it is difficult to accept as physically meaningful velocities which are significantly less than acoustic velocities in air. Alternative epicenters for these eleven events were calculated using a fixed velocity of 400 m/sec. The rationale for using this particular wave propagation speed is that it is a dominant Rayleigh wave velocity appearing on the forward modelled synthetic seismograms. The events on figure 20 with alternate epicenters are illustrated as inverted triangles with lines terminated at open circles. The inverted triangle is the epicenter associated with the best-fit velocity, the open circle is the location with the velocity fixed at 400 m/sec. If the alternate epicenter did not remain on the map using the 400 m/sec velocity, the line is terminated by an arrow in the direction of moveout. Because of the uncertainties associated with both location procedures, it is only possible to say that the actual epicenter lies somewhere along the illustrated line between the two end points.

Regardless of the uncertainty associated with the location of these eleven events, the general spatial distribution of seismicity remains relatively fixed. Why the seismicity clusters in the vicinity of the growth faults northwest of the test wells is unknown. We have no reason to believe that this distribution is an artifact of the array configuration since events also locate near the chemical plant east of the Pleasant Bayou well. Furthermore, since the spatial distribution of seismicity prior to and post test production essentially is identical, production of brine enhanced the seismicity but did not change its character.

Duration magnitudes of the type II events range from near -2.0 Md to .5 Md; therefore, as a group, they are smaller than type I events. Type II events are observed as single events or in 'swarms', with multiple observations within a short time span.

The temporal distribution of all seismic events which have been recorded since the beginning of the Phase I short-term flow test in 1980 are illustrated in figure 22. Both type I and type II events are embodied in the solid bars of the histogram.

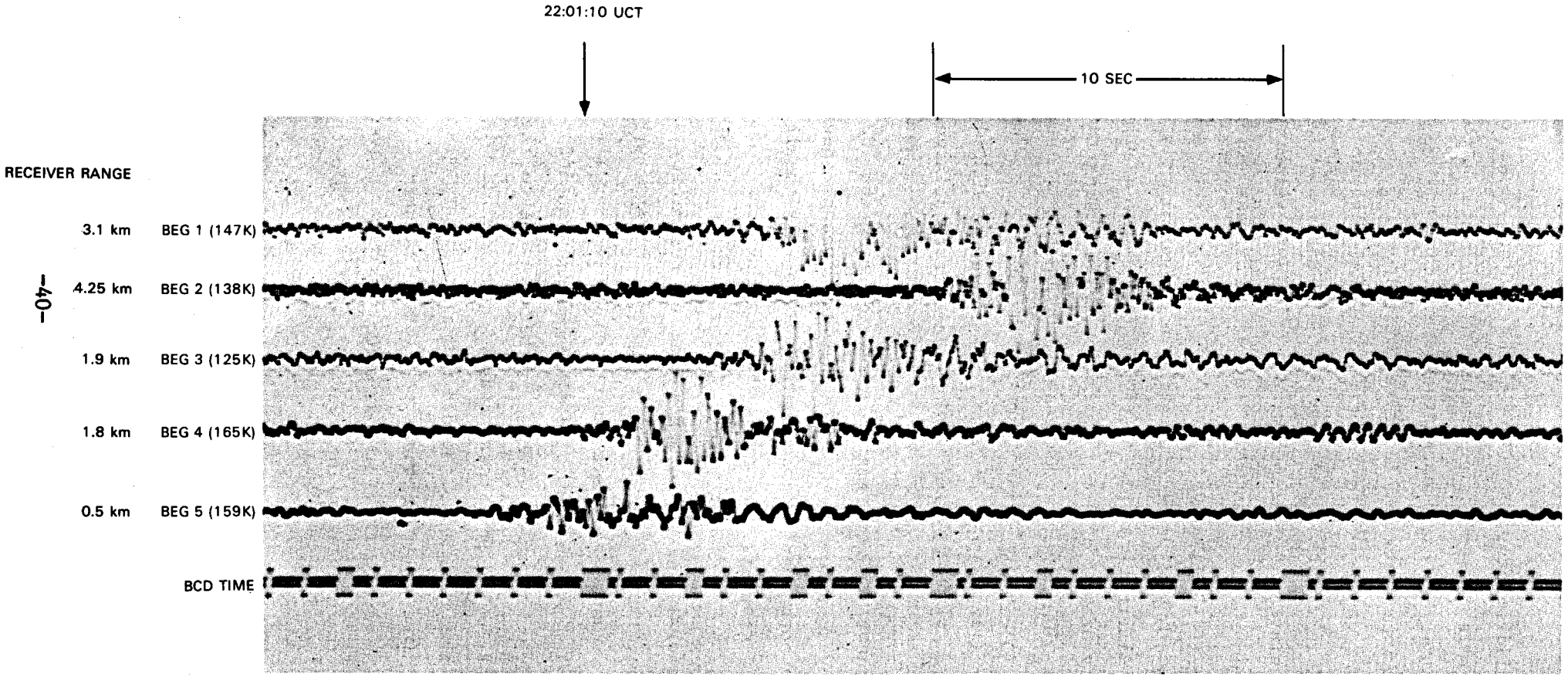

Figure 21. Event 25 January 1983 at 22:01:05.66 UTC.

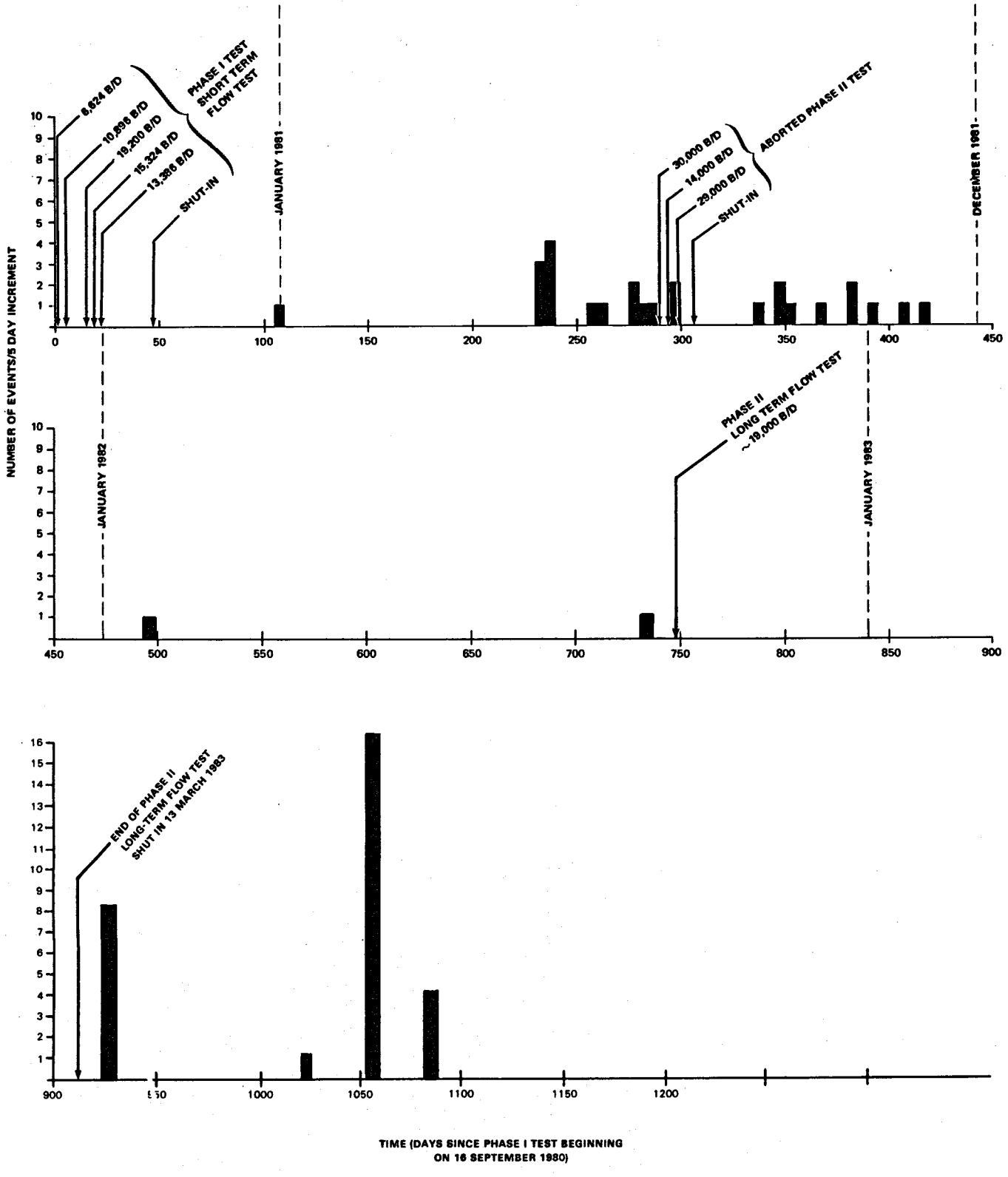

Figure 22. Temporal distribution of seismicity at Pleasant Bayou 1981 and 1982 through September, 1983.

In addition to the temporal distribution of seismicity, the production activity at the test wells is indicated by arrows along the time line. Although it is not possible to relate the occurrence of seismicity to particular aspects of either Phase I, the aborted Phase II or long-term Phase II production tests, it is obvious that increases in seismic activity occurred one hundred and fifty to two hundred days after the end of both the Phase I and Phase II production periods. The reason for the delay between the production periods and enhanced seismicity is unknown but may relate to a diffusion process.

SEISMICITY ORGINATING NEAR THE CHEMICAL PLANT EAST OF THE GEOPRESSURED/GEOTHERMAL ENERGY WELL

During the Brazoria seismic monitoring program, episodes of seismicity have been recorded that locate near the chemical complex east of the well. Seismic activity occurring in this region exhibits unusual characteristics that are not observed elsewhere. Locatable Rayleigh/leaking mode events with epicenter solutions near the chemical plant are often accompanied by periods of high-frequency rumble and some by harmonic tremor of time duration up to several hours in length. This unusual rumble and harmonic tremor activity is not observed from other azimuths at the Pleasant Bayou site, and is not observed at other Gulf Coast monitoring sites. The uncharacteristic nature of these events and the proximity of the estimated epicenter locations to the chemical complex leads us to believe they are associated with industrial processes and not related to the geopressured/geothermal energy well. They are, therefore, addressed as a group in this special section of the technical report.

Table 5 documents dates and times of occurrences of this group of events. An example of a rumble sequence accompanying a Rayleigh/leaking mode event locating near the chemical plant is illustrated in figure 23. Figure 24 illustrates harmonic tremor associated with another event locating near the plant.

Two forms of effluent disposal from industrial complexes potentially can result in the types of seismic signals observed. These are high-pressure effluent flares and high-volume subsurface injections. Both of these disposal methods are known to be practiced by the chemical plant where the seismic episodes appear to originate.

Model I Hypothesis: The observed seismic episodes are related to unusual flare conditions at one or more industrial stacks.

Under normal circumstances, the flaring of industrial gases should not result in noticeable seismic signals at moderate distances. If the ignition of the flare was erratic, however, it could result in repeated ignitions and extinctions which might generate acoustic signals. The amplitude and dominant period of the acoustic signals would correlate with fireball dimensions, and the temporal separation would relate to the time between reignitions. The seismometers in the far-field would record these signals as impulsive, acoustic-coupled Rayleigh waves with variable amplitude and spacing, and each episode would appear to originate from a single source. Due to changing atmospheric conditions, different episodes might appear to

TABLE 5. SEISMICITY EPISODES LOCATED NEAR THE CHEMICAL COMPLEX EAST OF THE GEOPRESSURED/GEOTHERMAL WELL

1. 81-12-06
   08:49:48.72
   Impulsive Rayleigh event and rumble event sequence

BEG1	iLR	08:50:09.65;
BEG2	iLR	08:50:00.65;
BEG3	iLR	08:50:02.27;
BEG5	iLR	08:50:04.00

Description of event series on 05 December 1981:

22:57:00 - High-frequency rumble event begins and continues until 08:47:30 on 06 December 1981

Description of event series on 06 December 1981:

00:01:00 - A very slight harmonic tremor was recorded at this time with a duration of approximately 8 minutes

08:47:30 - The high-frequency rumble event subsides to the normal noise level for this site

08:49:28 - Low-amplitude Impulsive Rayleigh event listed above

08:50:00 - Low-level rumble activity begins and intermittently occurs during the times listed below:

08:50:00 - 09:43:10
09:46:37 - 09:43:10
09:48:10 - 09:47:20
09:49:33 - 09:50:10
09:51:00 - 09:51:30
09:52:12 - 09:53:00
09:53:40 - 09:54:15
09:54:55 - 09:55:40
09:56:15 - 09:57:00
09:57:35 - 09:58:10
09:58:50 - 09:59:30
10:00:10 - 10:00:50
10:01:32 - 10:02:20
10:02:50 - 10:03:22
10:04:10 - 10:04:50
10:05:30 - 10:06:10
10:07:00 - 10:07:40
10:09:50 - 16:00:00

TABLE 5. SEISMICITY EPISODES LOCATED NEAR THE CHEMICAL COMPLEX EAST OF THE GEOPRESSURED/GEOTHERMAL WELL (continued)

09:46:25.32 - Impulsive Rayleigh event/G13216

BEG1	iLR	09:46:46.55;
BEG2	iLR	09:46:37.50;
BEG3	iLR	09:46:39.08;
BEG5	iLR	09:46:40.80

2. 82-01-05
09:49:16.9
Impulsive Rayleigh event

BEG1	iLR	09:49:39.08, A=5, D=4;
BEG2	iLR	09:49:29.70, A=4, D=4;
BEG3	iLR	09:49:31.18, A=3, D=4;
BEG4	iLR	09:49:26.40, A=8, D=5;
BEG5	iLR	09:49:32.93, A=4, D=4

Description of event series on 05 January 1982:

04:50:13 - A series of eleven impulsive Rayleigh arrivals ending at 04:51:36, followed by a slight rumbling.

04:51:40 - A high-amplitude rumble begins (A=8mm) which decreases to normal ambient noise levels at 05:04:07.

05:04:17 - A weak set of impulsive Rayleigh arrivals.

05:05:20 - More high-amplitude rumbling occurs (A=8mm), which remains a constant 8-10 hertz rumble with higher frequencies of noise present. This rumble persists with very few harmonic episodes until 09:49:00, when an emergent ending occurs in the same order in which the impulsive Rayleigh waves arrive.

09:49:27 - A very prominent impulsive Rayleigh event occurs, which apparently indicates a shutting down of some type, and is the last sign of any activity from the area southeast of the array for this date.

3. 82-01-10
07:20:17.3
Impulsive Rayleigh event

BEG1	iLR	07:20:39.10;
BEG2	iLR	07:20:29.70;
BEG3	iLR	07:20:31.50;
BEG4	iLR	07:20:26.50;
BEG5	iLR	07:20:33.35

TABLE 5. SEISMICITY EPISODES LOCATED NEAR THE CHEMICAL COMPLEX EAST OF THE GEOPRESSURED/GEOTHERMAL WELL (continued)

Description of event series on 10 January 1982:

00:02:20 - An emergent, high-amplitude rumble with a five-second duration.

00:03:25 - A harmonic tremor occurs and sustains a constant amplitude on A=8 for approximately 20 minutes. The amplitude is nearly half (A=4) for the next 60 minutes and even lesser for the next 6 hours, although the tremor is still noticeable.

02:02:40 - An impulsive Rayleigh arrival with a different type of sinuous coda forming the tail of the event.

06:07:00 - The harmonic tremor mentioned above ends in a rumble type of ending which is emergent in nature.

06:13:01 - An impulsive Rayleigh arrival which precedes another rumble episode which lasts for 90 seconds.

06:17:05 - An impulsive Rayleigh arrival precedes another rumble episode of numerous high frequencies which has an emergent ending at 07:09:30.

07:20:25 - An impulsive Rayleigh arrival precedes a harmonic tremor episode which lasts until 08:11:25, where a rumble type of ending occurs.

08:14:37 - An impulsive Rayleigh arrival occurs with another sinuous coda tailing the arrival. These tails are 4-8 seconds in duration and are closely followed by a rumble episode at 08:16:05 which lasts for 30 seconds.

08:17:10 - An impulsive Rayleigh arrival with the same type of rumble activity following until 08:33:30, when the rumble activity ceases with a surge of rumble activity.

08:33:40 - An impulsive Rayleigh arrival precedes more rumble activity which diminishes at 08:39:10, and progressively builds up to a peak in rumble activity at 09:17:40. The rumble continues with few noticeable harmonic episodes until a severe rumble episode occurs at 10:43:23 which lasts for over 2 minutes and ends abruptly in the same order of arrival as the impulsive Rayleigh events.

10:46:48 - An impulsive Rayleigh arrival followed by a low-level rumble episode with slight harmonics noted.

11:27:00 - A high-frequency rumble episode occurs which lasts to 11:45:00 where a 10-second, noise-free interval exists. The rumble episode continues

TABLE 5. SEISMICITY EPISODES LOCATED NEAR THE CHEMICAL COMPLEX EAST OF THE GEOPRESSURED/GEOTHERMAL WELL (continued)

until another noise-free interval of 7 seconds is present at 12:00:00.

12:00:07 - A very small, impulsive Rayleigh arrival precedes another high-frequency rumble episode which remains at a very low amplitude and contains increasingly more harmonics over the next 10 hours.

19:56:30 - The amplitude of the harmonic tremor nearly quadruples for the next few minutes. The harmonic tremor continues until indistinguishable from the ambient noise nearly 17 hours later.

4. 82-04-18
03:25:38.5
Impulsive Rayleigh event

BEG1	iLR	03:26:01.05;
BEG2	iLR	03:25:53.00;
BEG3	iLR	03:25:53.68;
BEG4	iLR	03:25:48.20;
BEG5	iLR	03:25:54.40

Description of event series on 18 April 1982:

01:47:00 - A harmonic tremor begins which lasts until 02:33:00.

02:40:40 - The harmonic tremor begins approximately 30-second bursts at 02:42:40, 02:46:20, 02:55:00, 02:56:50, and another 3-minute burst at 03:08:00.

02:58:53 - A series of six impulsive Rayleigh events ending at 03:00:08.

03:18:03 - A large amplitude harmonic tremor begins, and ends at 03:21:40 with a series of approximately ten impulsive Rayleigh events (see figure 16). The ground motion in nanometers for this event has been calculated to be as follows: BEG 1-83 nm, BEG 2-103 nm, BEG 3-140 nm, BEG 4-144 nm, BEG 5-83 nm. This clearly shows that BEG 2,3 and 4 are the closest stations to the source of the event. The decrease in ground motion at BEG 5 can be explained by interference from a major growth fault situated near the station.

03:25:53 - A series of four impulsive Rayleigh events ending at 03:27:20.

03:40:49 - Two impulsive Rayleigh events which are followed by a rumble event with very few harmonics noted. The rumble activity continues to diminish steadily over the next six hours.

TABLE 5. SEISMICITY EPISODES LOCATED NEAR THE CHEMICAL COMPLEX EAST OF THE GEOPRESSURED/GEOTHERMAL WELL (continued)

10:04:31 - A single impulsive Rayleigh event.

11:10:18 - The beginning of a series of at least twenty impulsive Rayleigh events which last periodically up until 12:24:18.

Description of additional events on 19 April 1982:

03:15:00 - A harmonic tremor begins which lasts approximately 3 minutes.

03:48:00 - A high-frequency rumble event occurs which lasts for 11.5 minutes.

5. 82-05-03
05:00:36.0
Impulsive Rayleigh event

BEG2	iLR	05:00:49.87;
BEG3	iLR	05:00:50.60;
BEG4	iLR	05:00:45.24;
BEG5	iLR	05:00:51.49

Description of event series on 03 May 1982:

04:03:23 - A rumble episode begins which lasts until 04:04:42. This rumble episode contains a slight harmonic tremor from 04:04:10 to 04:04:24.

04:53:00 - A series of multiple impulsive Rayleigh arrivals begins which precedes a high-frequency rumble episode which is nearly three times the amplitude of the normal ambient noise. This rumble episode lasts until 05:00:38, when an emergent ending occurs in the same order of arrival as the impulsive Rayleigh events.

05:00:45 - An impulsive Rayleigh event precedes another high-frequency rumble episode which is also much higher in amplitude than the normal ambient noise character of the record. This rumble eipsode contains few harmonics and has an emergent ending at 05:25:00.

05:28:00 - A high-frequency rumble episode begins emergently and continues until 09:25:15. A noted peak in activity was recorded from 07:38:00 to 07:50:00.

Additional Harmonic tremor episodes on 03 May 1982:

17:12:00, D=20 minutes
17:42:00, D=13

TABLE 5. SEISMICITY EPISODES LOCATED NEAR THE CHEMICAL COMPLEX EAST OF THE GEOPRESSURED/GEOTHERMAL WELL (continued)

Additional Harmonic tremor episodes on 04 May 1982:

01:25:00, D=15 minutes
01:46:00, D=5
02:37:00, D=7
03:34:00, D=67
05:54:00, D=26
08:35:00, D=11
11:21:00, D=8
11:40:00, D=2

6. 82-05-18
00:35:35.3
Impulsive Rayleigh event

BEG1	iLR	00:35:58.10;
BEG2	iLR	00:35:48.77;
BEG3	iLR	00:35:50.71;
BEG4	iLR	00:35:45.47;
BEG5	iLR	00:35:52.27

7. 82-06-12
11:35:49.0
Impulsive Rayleigh event and rumble event sequence

BEG1	iLR	11:36:10.00;
BEG2	iLR	11:36:01.90;
BEG3	iLR	11:36:02.63;
BEG4	iLR	11:35:57.30;
BEG5	iLR	11:36:03.70

Additional activity on 12 June 1982:

08:26:00 - Emergent beginning of a rumble event

08:51:00 - Decrease in amplitude until 09:02:00

09:26:00 - Increase in amplitude to 40 millimeters peak-to-peak which lasts until 10:28:00

10:28:00 - Rumble continues with slightly noticeable harmonics

11:33:00 - Rumble event ends emergently

11:35:58 - Impulsive Rayleigh event listed above

11:37:52 - Impulsive Rayleigh event listed below

TABLE 5. SEISMICITY EPISODES LOCATED NEAR THE CHEMICAL COMPLEX EAST OF THE GEOPRESSURED/GEOTHERMAL WELL (continued)

BEG1	iLR	11:38:05.40;
BEG2	iLR	11:37:57.38;
BEG3	iLR	11:37:58.38;
BEG4	iLR	11:37:52.78;
BEG5	iLR	11:37:59.30

13:16:00 - Small rumble event lasting until 13:18:30

8. 82-08-22
18:52:28.7
Impulsive Rayleigh event and rumble sequence

BEG1	iLR	18:52:51.25;
BEG2	iLR	18:52:43.14;
BEG4	iLR	18:52:38.71;
BEG5	iLR	18:52:44.79

Additional events on 82-08-22

GROUP I - 18:52:38 to 19:21:52

21 impulsive Rayleigh events followed by a rumble episode containing no events (D=22 mins.)

18:52:42, 18:53:34, 18:54:30, 18:54:32, 18:54:39, 18:55:53, 18:56:46, 18:56:49, 18:56:52, 18:57:32, 18:57:35, 18:57:36, 18:57:40, 18:57:42, 18:57:45, 18:57:48, 18:57:52, 18:58:10, 18:58:16, 18:59:00, 18:59:04, 18:59:06, 18:59:21, 18:59:25, 18:59:38, 18:59:56

GROUP II - 19:21:52 to 20:20:10

An uncounted number of impulsive Rayleigh events occurring almost continually during this period. Separation between most events is less than one second.

GROUP III - 20:20:10 to 20:34:42

Harmonic tremor (D=9 mins) begins at 20:20:10, with a series of 23 impulsive Rayleigh events beginning 7 minutes later. These 23 events are followed by 5 minutes of no recorded seismic activity.

20:27:10, 20:27:44, 20:27:58, 20:28:04, 20:29:06, 20:29:11, 20:29:36, 20:30:02, 20:30:26, 20:30:48, 20:31:00, 20:31:17, 20:31:24, 20:31:40, 20:32:11, 20:32:18, 20:32:20, 20:32:32, 20:33:38, 20:33:45, 20:33:53, 20:34:37, 20:34:42

TABLE 5. SEISMICITY EPISODES LOCATED NEAR THE CHEMICAL COMPLEX EAST OF THE GEOPRESSURED/GEOTHERMAL WELL (continued)

GROUP IV - 20:40:37 to 20:46:10

Harmonic tremor (D=6 mins.) begins with an impulsive Rayleigh event at 20:40:37. Three other similar events occur during this tremor at 20:41:13, 20:41:30 and 20:41:51.

GROUP V - 20:54:03 to 20:59:20

Another harmonic tremor (D=5 mins.) begins with an impulsive Rayleigh event at 20:54:03. Approximately 35 other impulsive Rayleigh events were recorded during this short-duration tremor.

GROUP VI - 22:13:27 to 22:13:42

Three smaller impulsive Rayleigh events were recorded during this fifteen-second period at 22:13:27, 22:13:34 and 22:13:42.

9. 82-09-25
00:47:38.2
Impulsive Rayleigh event and rumble event sequence

BEG1	iLR	00:47:59.56;
BEG2	iLR	00:47:51.60;
BEG3		Inoperative
BEG4	iLR	00:47:47.02;
BEG5	iLR	00:47:53.20

00:44:00 - Emergent beginning of the rumble event. Amplitude and frequency begin to increase steadily from approximately 5 hertz to approximately 7 hertz

00:47:40 - Amplitude diminishes to 4 millimeters peak-to-peak on BEG 4

00:47:47 - Impulsive Rayleigh event occurs which is listed above. The high-frequency portion of the wave is of duration approximately 2 seconds

00:48:30 - Seismic traces return to the normal ambient noise level

10. 83-03-07
15:50:00 UTC (D = 10 mins.)

11. 83-03-22
22;34:00 UTC (D = 26 mins.)
Harmonic Tremor

TABLE 5. SEISMICITY EPISODES LOCATED NEAR THE CHEMICAL COMPLEX EAST OF THE GEOPRESSURED/GEOTHERMAL WELL (continued)

12. 83-05-03
    09:10:40 UTC
    Rumble Episode

13. 83-05-25
    01:05:33 UTC
    Rayleigh event followed by small rumble sequence (D = 2 mins.)

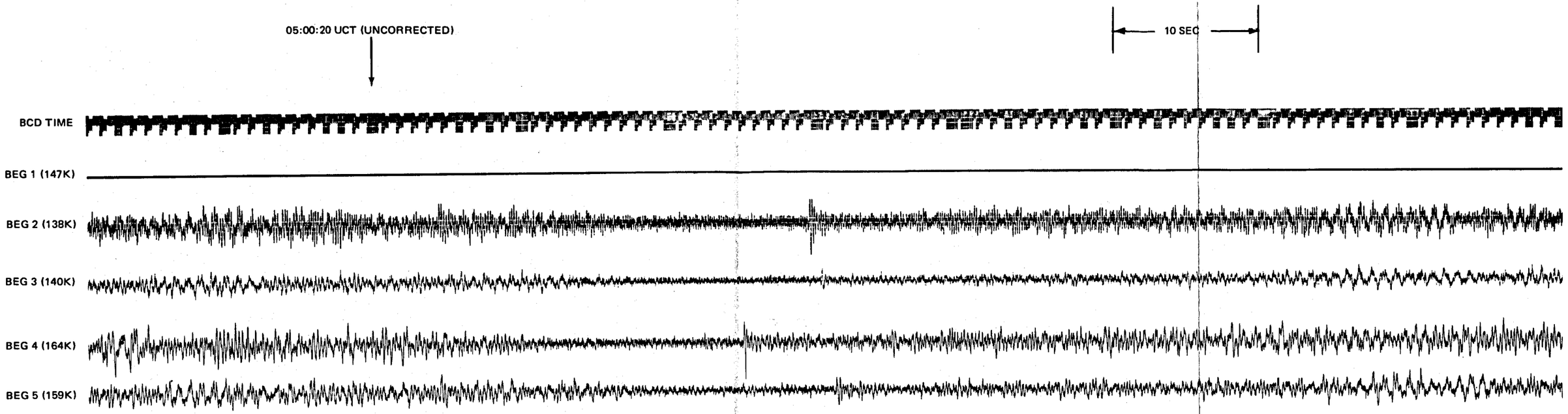

Figure 23. Rayleigh/leaking mode event originating near the chemical plant east of the geothermal test well site. OT = 05:00:36.0 UTC on 3 May 1982, velocity = 348 meters/second. Note associated high-frequency rumble activity ten seconds before and immediately following the event.

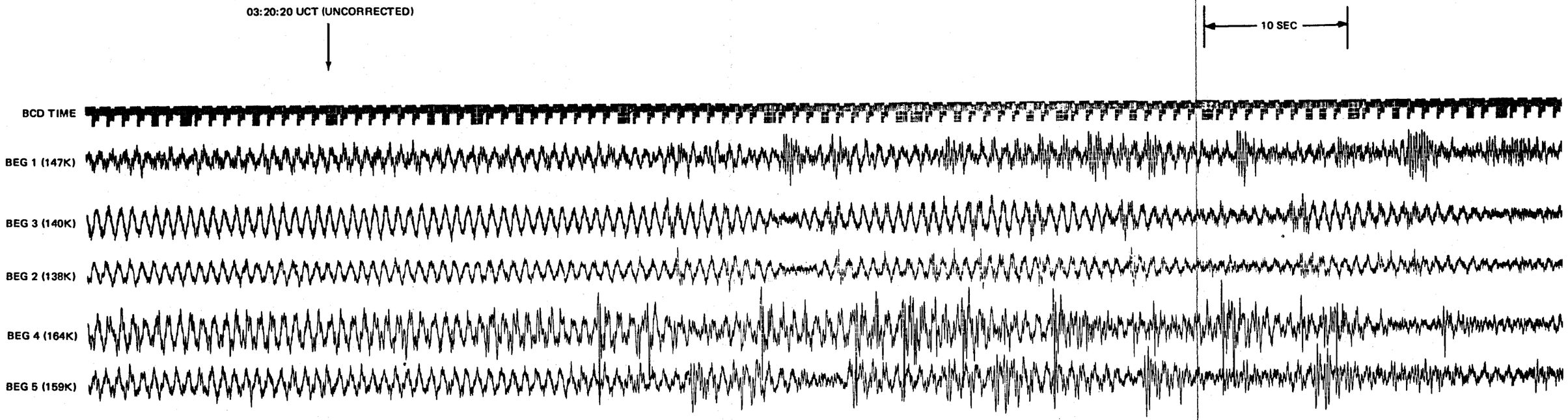

Figure 24. Rayleigh/leaking mode event originating near the chemical plant east of the geothermal test well site. OT = 03:25:38.5 UTC on 18 April 1982, velocity = 347 meters/second. Associated harmonic tremor activity is approximately 1.35 Hz.

originate from different sources because of variations in acoustic velocity and atmospheric refractive conditions. The occurrences of rumble-type events could correspond with episodic turbulent flow from the stack which might result in additional acoustic signals. The harmonic tremor possibly might be the result of "organ pipe" resonance of the stacks under high-volume flow conditions or, alternatively, a pipe hammer induced in a valved feed pipe. Essentially, this hypothetical model could rationalize all of the seismic phenomena observed.

Model II Hypothesis: The observed seismic episodes are related to subsurface waste injection at one or more disposal wells.

There are many documented cases where subsurface injection of fluids resulted in induced microearthquakes. Perhaps the best documented case is that of injections at the Rocky Mountain Arsenal Well and the Denver earthquakes (Hollister and Weimer, 1968). It is possible to interpret the ensemble of seismic event characteristics exhibited by the complex episodes from 6 December 1981 and 25 September 1982 by a hypothetical model which involves intermittent flow of injected fluids controlled by stress-sensitive asperities along a system of formational discontinuities. This hypothesis would require the impulsive Rayleigh events to be of earth rather than atmospheric origin. Since body waves are not observed for these events, a mechanism to justify their absence is required (see Data Analysis Procedures Surface Wave Data section). The fact that events of this type, that is, impulsive Rayleigh events, have been recorded previously at all geopressured/geothermal design well sites and that a suite of such events at the Brazoria site appears to collocate with microearthquakes located using body phases would support the theory that these are also microearthquakes.

In conclusion, two alternative models have been presented which could rationalize the data equally well. Model I associates the seismicity with effluent from industrial flare stacks. Model II associates the seismicity with effluent fluids injected into a geological formation. Other models not presented also may account for the observations, and it should not be assumed that either model presented is necessarily the correct solution.

In summary, excluding the events which locate at the chemical complex east of the Pleasant Bayou wells which are suspected to relate to activities at the chemical plant rather than the production from the geopressured/ geothermal well, there are several important observations from routine analyses of the seismic data. (1) Two types of events are commonly recorded, one has identifiable body phase arrivals, the other is characterized by only surface wave propagation. The second type of event

far outnumbers the first. (2) The spatial distribution of epicenters for both event types overlaps and clusters approximately four kilometers west-northwest of the Pleasant Bayou well. Although there is a growth fault projected at a depth of 15,000 feet at this location, all hypocenters occur at considerably shallower depths (less than three kilometers). Unless this growth fault is nearly vertical, it is difficult to relate the seismicity to that particular structure. (3) Hypocenters for type I events are poorly constrained, and hypocenters for type II events are unconstrained using routine least-squares location inversion procedures. Alternative techniques are required to better constrain the focal depths. This will be discussed in the Special Studies section. (4) The magnitudes of events are all smaller than 2.0 but may be underestimated by as much as 0.5 magnitude units. (5) Seismicity is not uniformly distributed in time but tends to occur in relatively isolated segments one hundred fifty to two hundred days following shut-in of the geopressured/geothermal well. The intensity of induced seismicity appears to relate to the number of days production exceeded 15,000 barrels/day in the test period.

Special Studies

In addition to the routine analyses of the microearthquakes at Chocolate Bayou, it became obvious that some special studies would be required to understand the wave propagation mechanism and source characteristics of the events, particularly the mode II signals. To address these problems, we chose two directions of approach. The first was to use the known velocity structure to forward model synthetic seismograms with which to compare the observed time-series signals. The second was to digitize some of the better defined signals, transform them to the frequency domain and perform comparative analyses in the frequency domain of the observed and synthetic signals. These studies proved to be quite valuable in both defining wave propagation characteristics and depth of sources.

The absence of identifiable body phases for the type II events was a particularly distressing observation. Without body-phase arrivals, nearly all routine analyses schemes fail to define either source or transmission path characteristics. There are at least three alternative, physically plausible reasons for the absence of body phases. (1) All body phases are very high frequency. Thus, the combination of low Q (highly attenuating) sediments and incorrect instrumental passband might result in poorly recorded or totally missed body phases. We believe that this explanation is the least attractive because some events with body phases are

recorded. Furthermore, the frequency content of the body and surface waves for these events is not significantly different. (2) A second possibility is that there are no body phases because the events are acoustic coupled from atmospheric sources. Such observations have been reported previously (Jardetsky and Press, 1952; Cook and Goforth, 1967; Espinosa and others, 1968). This is a very tenable explanation for some of the events such as the chemical plant process overturns and sonic booms and must, therefore, be examined carefully. (3) A third possible explanation for the absence of body phases is that the events are generated at some particular depth in which the body waves become trapped by low-velocity layers and only appear as leaking modes. This is a particularly attractive explanation because the sources become ground based rather than atmospheric in origin and is very likely, given the Chocolate Bayou structure. In fact, we have observed events propagated by both the second and third methods. Furthermore, we believe that the analyses procedures we have followed permit separation of the two mechanisms as well as identifying the depth of the buried sources.

The first step in our analysis procedure has been to generate a suite of synthetic surface wave seismograms with which to compare the observed signals. Two principal alternative methods exist for generating synthetic seismograms through a known velocity structure, the generalized ray technique, and the modal excitation technique. Theoretically, both methods yield identical solutions (duplicate seismograms) given an infinite number of rays in the former case or an infinite number of frequencies in the latter. There are specific cases, however, when one or the other method is computationally more practical. Given a simple velocity structure in which there are few inversions to produce multiple reflections, a generalized ray approach to produce synthetic seismograms is much faster and simpler to compute. When significant energy traps exist in the velocity structure, however, the number of rays which need to be summed to yield a meaningful representation of what must happen in reality becomes untractable. In these circumstances, a modal approach to structural resonance characteristics produces the more representative seismogram with fewer computations required. The number of modes which needs to be considered for summation depends upon the complexity of the velocity structure, the degree of accuracy with which the fit between synthetic and observed data is desired, and the cost of computing the synthetics which increases nonlinearly with the number of modes. In order to model body waves into the synthetics, higher order modes must be included, thus substantially increasing cost.

Because there are several energy traps in the Pleasant Bayou velocity struc-

ture at depths between zero and one and a half kilometers, synthetic seismograms were computed using a modal summation approach. The apparent frequency content of the observed signals indicated that limiting the bandwidth between zero hertz and fourteen hertz would likely yield a reasonably representative synthetic. Although adding frequencies to at least fifty hertz would yield a more accurate synthetic, the cost of computing the synthetics becomes prohibitive. In addition, the recorded data are band limited, so there is no particular necessity for higher resolution data. The chosen parameters exclude modes necessary for modelling body waves; however, type II events contain no identifiable body waves.

The first step in computing synthetic seismograms through modal summation is to determine the structural excitation phase velocities for the bandwidth of interest. The crustal structure used for these analyses is illustrated in the appendix in figure B1, and the actual layer compressional and shear velocities used are listed in table B1. For simplicity in computation, the Poisson ratio was fixed at 0.25. The computed modal phase velocities as a function of frequency are illustrated in figure B2. The amplitudes of the waves traveling with these phase velocities attenuate as a function of distance from the source because of geometrical spreading and anelastic earth properties. Although Gulf Coast sediments undoubtedly have an attenuation coefficient (Q) which is less than one hundred, the transmission paths of interest are so short that the anelastic attenuation, even at a frequency of fourteen hertz, is not particularly significant. For our calculations, we assumed Q to be infinite (the case for a perfectly elastic body).

Given the phase velocity and amplitude excitation characteristics for the Pleasant Bayou region (Appendix figures B1 and B2) in the bandwidth of interest, synthetic displacement seismograms, or Green's functions, can be computed for given source receiver separations given specific source characteristics.

We have computed synthetic seismograms for two particular sources. We have assumed the sources to be normal dip-slip, double-couple events with dip angles of 45 degrees or 90 degrees to be most likely for the Pleasant Bayou region. The displacement is assumed to be a step (Heaviside function) in time with a static moment equal to 6.28 x 10**20 dyne-cm (roughly equivalent to a magnitude 2.0 earthquake). Synthetic seismograms were computed for source depths of 0.0, 0.3, 0.8, 1.3, 1.8, 2.8 and 3.8 kilometers and receiver epicentral distances from one to ten kilometers. The suite of synthetic seismograms for 45-degree dip-slip sources as a function of depth and distance are illustrated in the appendix in figures B3 through B18. The synthetics for 90-degree dip-slip sources are illustrated in

figures B19 through B34. Each of the ten traces in figures B3 to B34 is scaled to its own maximum value. The first figure of each set (of two) vertically oriented displacement Green's functions is not corrected for instrument response. Convolution of the synthetic records with the instrument response of the Pleasant Bayou seismometers was performed, and response corrected seismograms are shown as the second figure of each set.

One of the most striking features of the suites of seismograms is the high degree of variability of modal excitations as a function of source depth. The relationship of the source depths to the velocity structure is illustrated in figure B1. Note that the first two source depths (0.0, 0.3 km) are above the region of low-velocity layering; the next two (0.8, 1.0 km) are bounded above and below by low-velocity layers; the next three (1.3, 1.8, 2.8 km) are within a region of normal velocity gradient; and the last (3.8 km) is in the region of velocity inversion associated with the geopressured zone. The synthetics generated for surface sources have characteristics similar to observed exploration shots. The principal difference is that an explosion is not a double-couple, dip-slip source. The seismograms are relatively uncomplicated by multiple phase arrivals, and the arrival time moveout as a function of distance is large (greater than twenty-three seconds over an epicentral distance span of ten kilometers). At a source depth of three hundred meters, the seismograms have become significantly more complex than those at the surface. The surface waves are inversely dispersed (that is, higher frequency arrivals precede lower frequency arrivals), and the coda tails for both source depths end with a 1.2-1.3 hertz resonance. Interestingly, this resonant frequency is not observed on synthetic seismograms with a source depth of eight hundred meters. Since this is the dominant frequency of the harmonic tremors which are observed periodically, we conclude that the source depths of these events must be less than eight hundred meters. In addition, since the signals locating near the chemical plants southeast of the Pleasant Bayou test wells frequently have associated resonances at this frequency, it is concluded that these sources also are at depths less than eight hundred meters (2,625 feet). Since the fluid injections at these chemical complexes are known to be at a depth greater than 1524 meters (5000 feet), it seems less likely that the signals observed are related to injections into the disposal horizon. The sources of these events, however, remain unresolved.

Synthetic seismograms produced by sources in the depth range from eight hundred meters (2625 feet) through 1,800 meters (5906 feet) have very distinct, high-amplitude resonances with a period of approximately 3.5 seconds (0.286 hertz).

These are particularly large for a source depth of 1300 meters (4265 feet) and an epicentral distance of five kilometers. Given the apparent velocity of this wave (416 m/sec), the length would be 1456 m (4777 feet) or a half wave length of 728 m (2388 feet). With these characteristics, the observed wave is an energy resonance trapped between the surface and the depth of the last significant low-velocity zone. Unfortunately, this resonance frequency is outside the passband of the instruments deployed in the Pleasant Bayou array and thus would not be observed. If the passband were wider, however, the relative excitation of this trapped mode could be useful as an event depth discriminant.

The synthetic seismograms for events at depths of 2.8 and 3.8 kilometers display low-frequency (0.222 Hz) waves on the seismograms. The corresponding half-wave length indicates that these waves correspond to energy channeled in the low-velocity zone at a depth of approximately 4.5 kilometers. These waves would not be observable on the current Pleasant Bayou array because of the limited passband, however. Finally, note the very low arrival time moveout for the epicentral distance span from one to ten kilometers for events with depths greater than 2.8 kilometers.

The next analysis procedure to help understand the wave propagation characteristics was to perform multiple-filter (moving-window) transformations of the time series data into frequency-versus-velocity space. This technique, developed by Landisman and others, 1969, is particularly lucidating for separation of individual wave propagations in complex surface wave and/or guided wave time series data set. Basically, the time series data are passed through a series of very narrow bandpass filters which are centered at particular windows of the data dependent upon the propagation velocity. Envelope amplitudes are computed for each window, and the amplitudes then are normalized and contoured as a function of energy in a velocity-versus-logarithm of frequency space. The resulting plot is a contour mapping of the mechanism of energy propagation. Regions of the space characterized by energy maxima are contoured in high numbers (99), whereas regions of the space with energy transmission minima are contoured as low numbers. By examining the plots, it is immediately obvious if energy is propagated as distinct packets as is the case with trapped modes or as continuously dispersed energy as is the case for typical surface wave transmissions. In addition, the distribution of energy in the space frequently can be used as a diagnostic for some source characteristics such as depth of the source.

To provide a known source data set with which to compare similar analyses of

observed signals, moving window transforms were produced for the synthetic seismograms in appendix B. The results of these analyses have been included at the end of appendix B. Multiple filter plots have been calculated from instrument-response-corrected synthetic waveforms for both 45-degree and 90-degree source dips, depths 0.3, 0.8, 2.8 and 3.8 km at receiver ranges 2, 5 and 8 km. Multiple filter plots for the 45-degree source dip are shown in figures B35 through B46. Plots calculated for the 90-degree source dip are shown in figures B47 through B58. Plot amplitudes are normalized to a maximum value of 99, and have been contoured at increments of ten units.

There is an enormous quantity of information embodied in these plots, and careful comparative study of them likely will reveal additional details not described below. Our intention here is to illustrate some of the important conclusions which can be derived from such analyses. Comparing figures B35, B36, and B37, for example, illustrates both the general characteristics of sources at shallow depths and the effects of increasing distance. Note that all contoured energy essentially is velocity bound between 300 and 650 m/sec. The most prominent velocity is approximately 400 m/sec. In addition, note that the predominant excitation frequency is distance dependent. For example, at a distance range of two kilometers (B35), there is a single energy maximum at a frequency of 3 hertz. At a distance of five kilometers (B36), however, there are two energy lobes which are apparent, one at approximately 2.7 hertz and one at 4.5 hertz. At a distance of eight kilometers, several frequency lobes are present. This clearly demonstrates that the energy is being propagated as a trapped or guided wave. The particular frequency which is observed at any given distance is a function of the angles of reflection at the top and bottom of the waveguide. Thus, any given distance will "tune" to a particular frequency or frequencies. By comparing figures B47, B48, and B49 with B35, B36, and B37, it is obvious that the source mechanism orientation also plays a role in frequency selectively of the waveguide as well as the apparent velocity of propagation. In general, events at source depths less than 500 meters have energy propagated in a velocity band between 300 and 650 m/sec. The number of eigen frequencies excited is dependent upon the distance from the source.

The effects on the moving window analyses of increasing the source depth are illustrated by comparing figures B35 (300 m), B38 (800 m), B41 (2800 m), and B44 (3800 m). The relationship between these source depths and the velocity traps in the structure are shown in figure B1. Essentially, the same type of behavior can be seen at greater epicentral distances but is more complex because of the increased

number of eigen frequencies excited. The source depth effect on these plots is very dramatic and clearly demonstrates these analyses are quite sensitive methods for depth evaluation. Comparing figures B35 and B44, for example, illustrates that the same eigen frequencies are excited by sources with depth differences of 2500 meters, but the distribution of velocities is radically different. In addition, given a specific source displacement, that is, 45° or 90° dip slip, there is a spectral hole which is related to source depth apparent on each of the plots. The primary frequency of the hole lowers with increased depth (for example, 3 hertz on B41 versus 2.7 hertz on B44). Note, however, that the positions of the holes are also dependent on the orientation of the source displacement. Using these analyses of synthetic events as templates for comparison with similar analyses of observed signals therefore provides a powerful tool for interpreting these complex signals.

It is important to understand that the observed signals will be complicated additionally because of scattering, attenuation, and body wave reflection interference. Nevertheless, the data appear to be remarkably consistent with these forward models. Several type I and type II signals were digitized and analyzed using the multiple filter analysis technique. These examples of the type II signals and their corresponding multiple filter analyses are illustrated in figures 25, 26, and 27. Although the source depths of these events were indeterminant from the routine location procedures, the general character of the moving window analyses clearly demonstrates all have source depths less than 800 meters. Throughout the monitoring program, we maintained a position that the sources of these type II events had to be very shallow. These moving window analyses finally demonstrate that this position was correct. The similarity of the moving window analyses of the local events (figures 25 and 26) to the synthetics in appendix B are very remarkable. The third event (figure 27), however, demonstrates that attenuation in the real earth can play an important role in defining the observed eigen frequencies. Attenuation effects have been neglected in the synthetics.

For comparison, a multiple filter analysis was performed on a digitized sonic boom and is illustrated in figure 28. The time series signal of this event is roughly similar to those of figures 25 and 26, suggesting that discrimination of this source type might be difficult. There is, however, a distinct multimodality of the signals in figures 25 and 26 which is missing in the sonic boom, and the overall character of the moving window analyses are distinctly different.

Two examples of multiple filter analysis of type I (P-wave) signals are illustrated in figures 29 and 30. In these cases, the velocity window has been

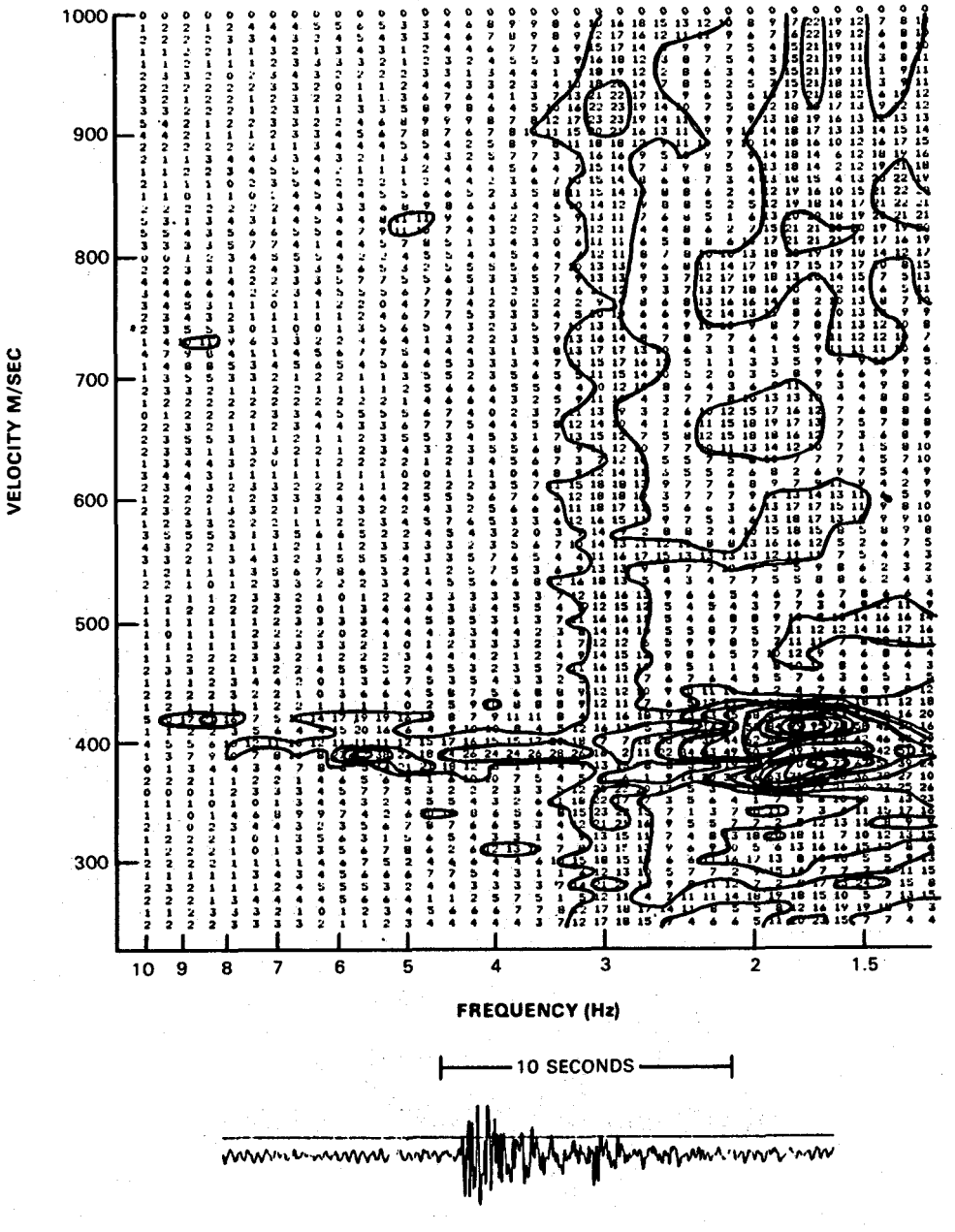

Figure 25. Multiple filter analysis of a type II signal with epicentral distance of 3.04 km.

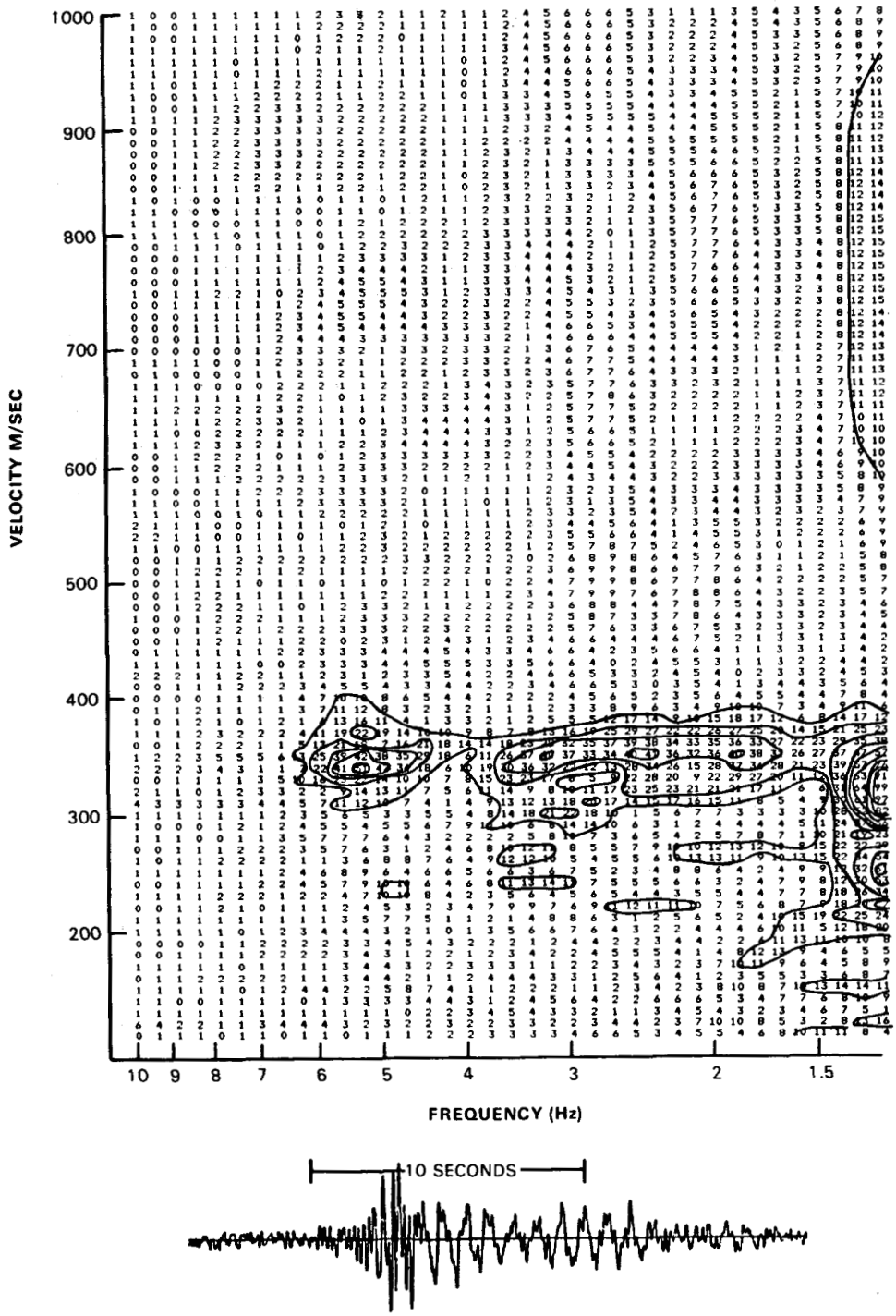

Figure 26. Multiple filter analysis of a type II signal with epicentral distance of 7.11 km.

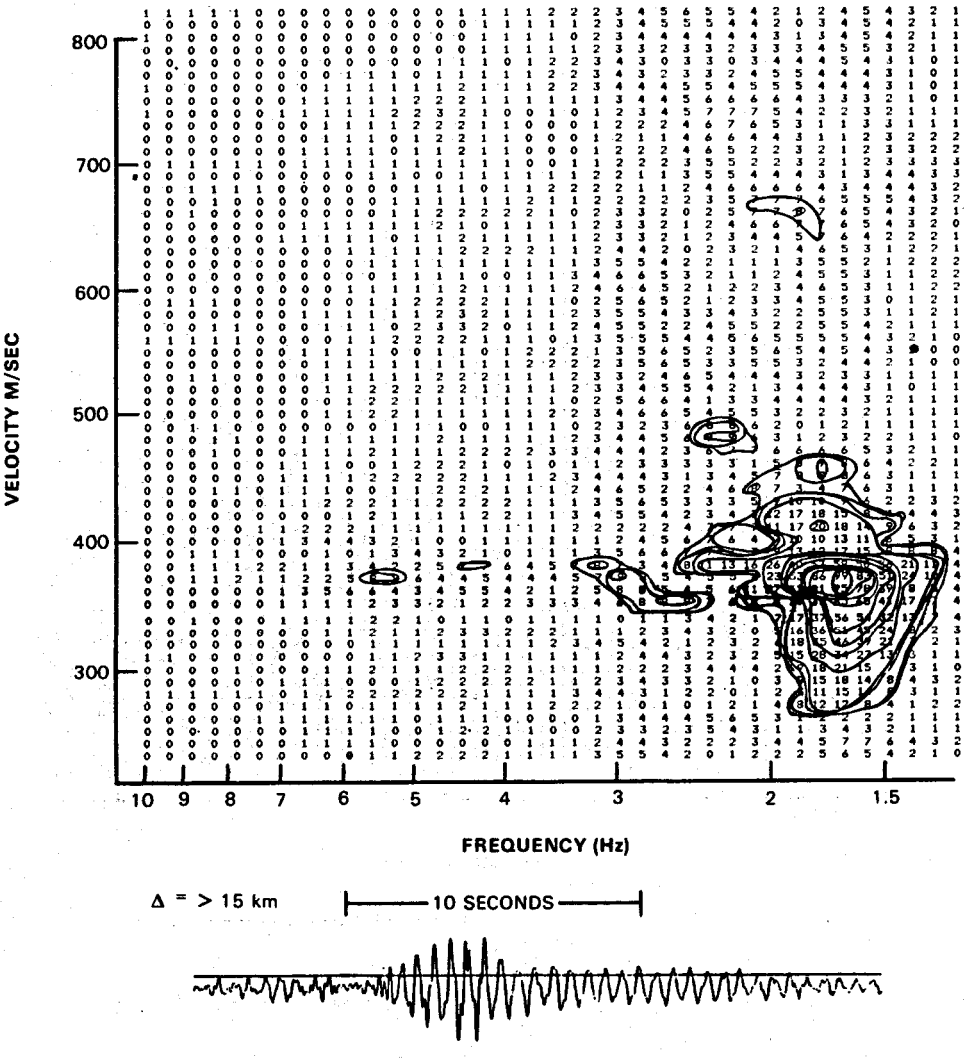

Figure 27. Multiple filter analysis of a type II signal with epicentral distance greater than 15 km.

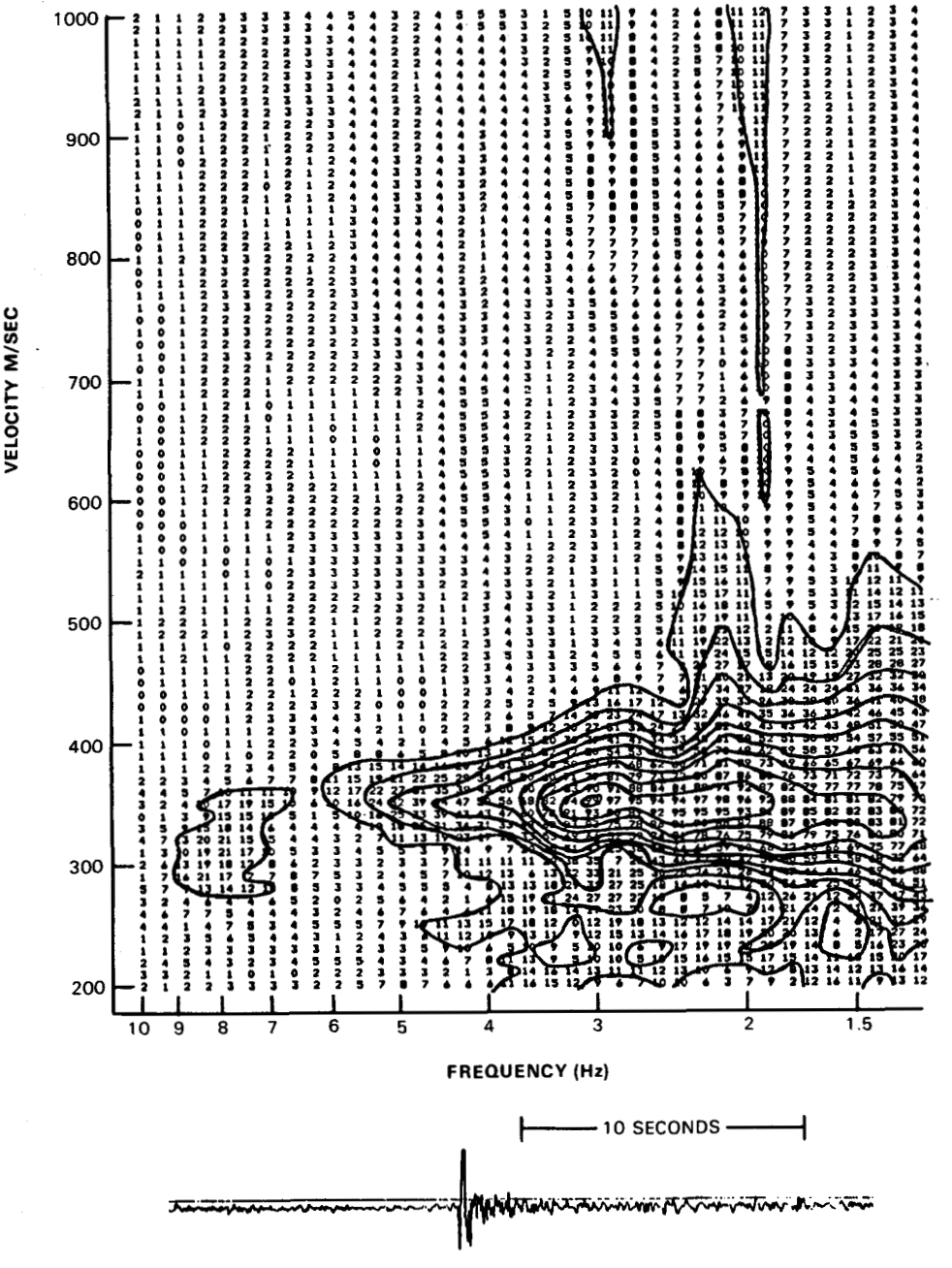

Figure 28. Multiple filter analysis of a sonic boom generated by an aircraft at a distance of 2.56 km.

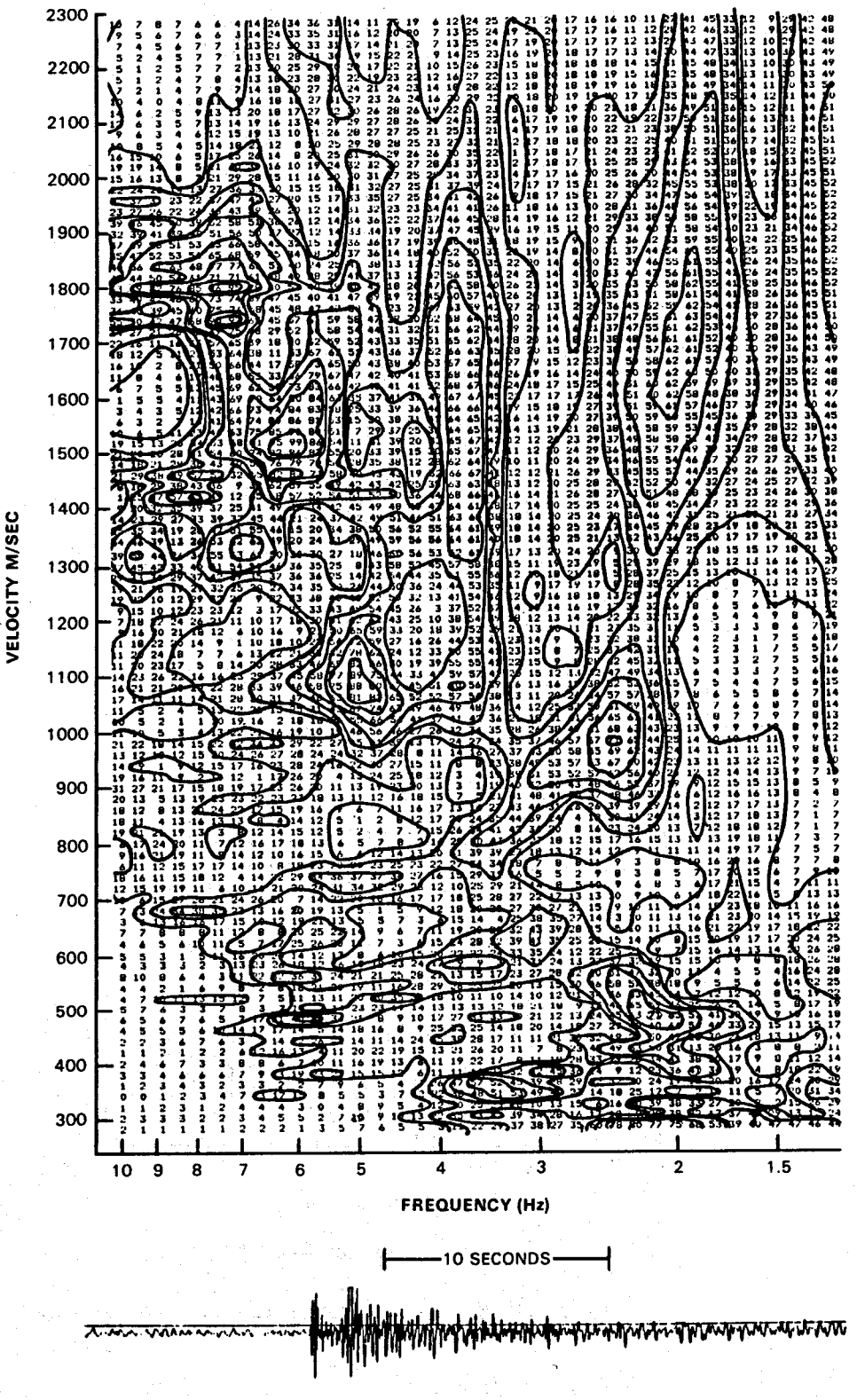

Figure 29. Multiple filter analysis of a type I (P-wave) signal, epicentral distance = 8.44 km, depth = 1.5 km.

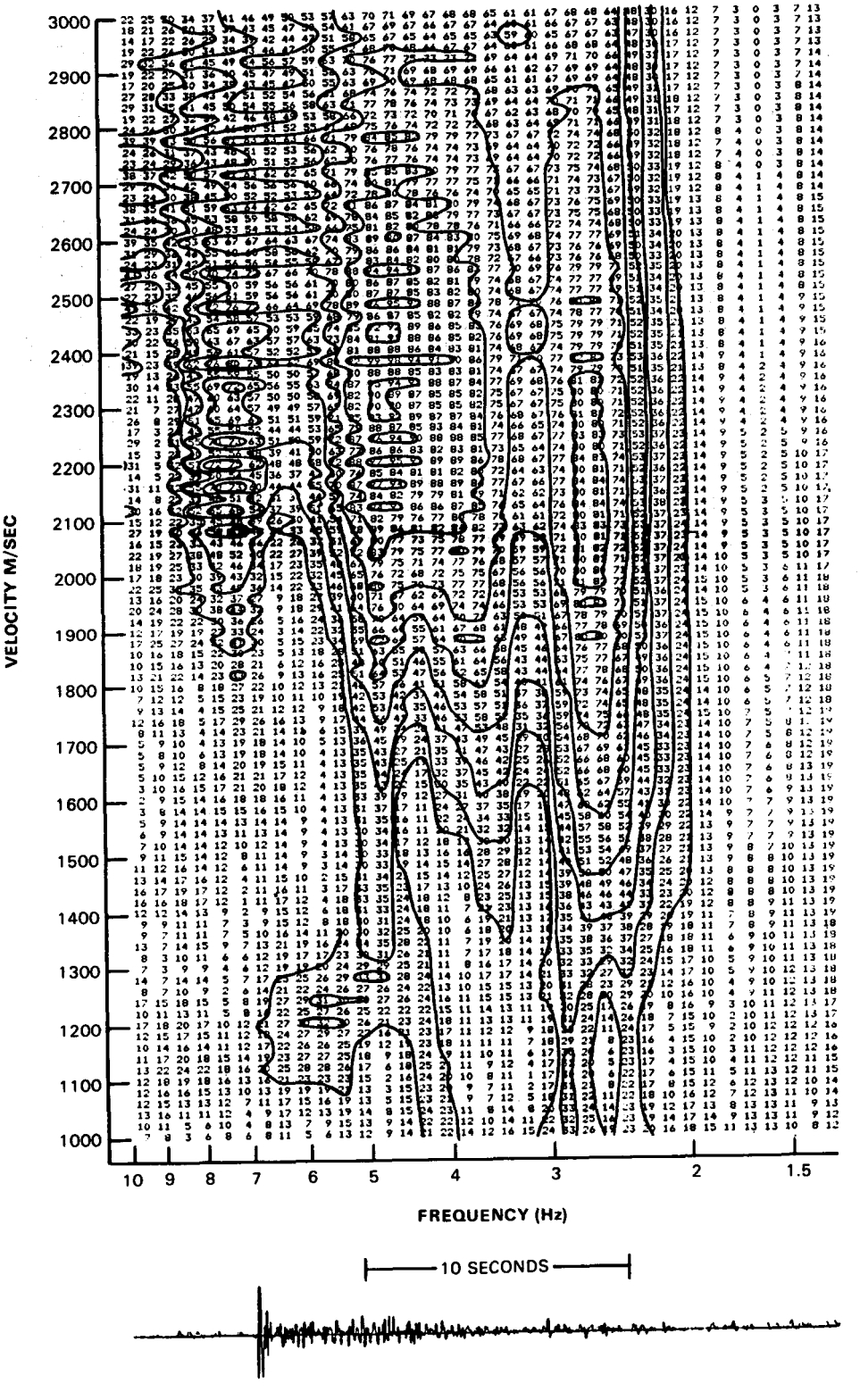

Figure 30. Multiple filter analysis of a type I (P-wave) signal, epicental distance = 3.7 km, depth = 1.5 km.

expanded to permit viewing of the region occupied by the body phase arrivals. In figure 29, for example, the P-wave energy is located at a frequency band between seven and eight hertz with a velocity of 1700 to 1800 m/sec. The corresponding S-wave energy appears at a frequency of approximately five hertz with a velocity between 1000 and 1150 m/sec. Other prominent energy arrivals occur at a frequency between six and seven hertz with a velocity of 1500 m/sec, nine to ten hertz with a velocity of approximately 1300 m/sec, and 2.5 hertz with a velocity of approximately 950 m/sec. These arrivals cannot be identified positively and are possibly secondary reflections and/or converted phases. Note that there is little energy allocated to the surface waves compared with the body waves. This is typical for a source depth/dimension ratio of this order. The character of surface wave energy distribution in frequency and velocity is comparable to the deeper sources for the synthetics, confirming that this is deeper source event and not one less than 1000 meters deep. The second type I event (figure 30) is even more dramatic. There is virtually no energy allocated to the surface waves in this example, and the body wave velocities are significantly higher. In this case, it is likely that the event is deeper than the hypocenter program solution yielded. To produce an average P-wave velocity of 2400 m/sec requires the event to be approximately three kilometers deep. In addition, there is significant ringing of the P energy indicating a large amount of multipath propagation.

In conclusion, microseismic monitoring of the Chocolate Bayou region in the vicinity of the Pleasant Bayou geopressured/geothermal energy well has resulted in the following observations.

1. Ambient seismicity occurs at a very low rate of a few events per year. The spatial distribution of these events suggests association with a few specific growth faults.

2. Two types of events were recorded, one with identifiable body phase arrivals, and one which has only surface wave arrivals. The latter event type occurs more frequently than the former. Both event types range in magnitude between -0.5 and 2.0.

3. Events with identifiable body phases are generated by surface explosions and events with depths greater than one kilometer. Events which propagate as apparent surface waves have depths of origin between 300 and 800

meters.

4. Following periods of pumping from the Pleasant Bayou well, seismic activity was enhanced from ambient conditions. There was an apparent delay of 150-200 days between onset of activity and initiation of pumping at a rate exceeding 18,000 barrels/day. This delay may be related to stress diffusion rate.

5. All seismicity observed had focal depths less than the production depth. Most events had focal depths less than the disposal depth. It is, therefore, unknown whether the enhanced seismicity is related to withdrawal or injection of the brine.

6. It is unknown whether the increased seismicity is related to ground subsidence since there was no independent method of evaluating subsidence simultaneously with seismic monitoring.

7. The increased level of seismic activity does not constitute a significant seismic risk in terms of ground accelerations; however, it is unknown whether the cumulative effects of these events may constitute a potential subsidence risk.

8. Increased understanding of these seismic observations will not be accomplished by deploying standard microseismic arrays at future sites. The sites are too structurally heterogeneous to generate simple, meaningful results using standard methodologies; however, alternative technology to address these issues does exist.

9. An important goal for future studies is to determine if and how these seismic events relate to subsidence and whether commercial scale productions would constitute a significant subsidence hazard comparable to the documented Houston aquifer problem.

REFERENCES

Aki, K., 1981, Source and scattering effects on the spectra of small local earthquakes: Bull. Seis. Soc. Amer., v. 71, no. 5, pp. 1687-1701.

Aki, K., and Chouet, B., 1975, Origin and coda waves: source attenuation and scattering effects, Jour. Geophys. Res., v. 80, no. 23, pp. 3322-3342.

Aki, K., Fehler, M. and Das, S., 1977, Source mechanism of volcanic tremor: fluid driven crack models and their application to the 1963 Kilauea eruption: Jour. Volcanol. Geotherm. Res., v. 2, pp. 259-287.

Chouet, B., 1981, Ground motion in the near field of a fluid driven crack and its interpretation in the study of shallow volcanic tremor: Jour. Geophys. Res., v. 86, no. B7, pp. 5985-6016.

Chouet, B., Aki, K., and Tsujiura, M., 1978, Regional variation of the scaling law of earthquake source spectra: Bull. Seis. Soc. Amer., v. 68, no. 1, pp. 49-79.

Cook, J. C. and Goforth, T., 1967, Seismic effects of sonic booms: Teledyne Geotech Technical Note 3/67, 19 p.

Das, S., and Scholz, C. H., 1981, Theory of time dependent rupture in the earth: Jour. Geophys. Res., v. 86, no. B7, pp. 6039-6051.

Douze, E. J., 1964, Rayleigh waves in short period seismic noise: Bull. Seis. Soc. Amer., v. 54, no. 4, pp. 1197-1212.

Ebeniro, J., Wilson, C. R., and Dorman, J., 1983, Propagation of dispersed compressional and Rayleigh waves on the Texas Coastal Plain, Geophys., v. 48, no. 1, pp. 27-35

Espinosa, A. F., Sierra, P. J., and Mickey, W. V., 1968, Seismic waves generated by sonic booms: a geoacoustical problem: Jour. Acoust. Soc. Amer., v. 44, no. 4, pp. 1024-1082.

Ferrick, N., Qamar, A., and St. Lawrence, W. F., 1982, Source mechanism of volcanic tremor: Jour. Geophys. Res., v. 87, no. B10, pp. 8675-8633.

Garg, S. K., Riney, T. D., and Fwu, J. M., 1981, Analysis of phase I flow data from Pleasant Bayou No. 2 geopressured well, in Bebout, D. G., and Bachman, A. L., eds., Proceedings of the Fifth Conference Geopressured-Geothermal Energy: U.S. Gulf Coast, Louisiana State University, Baton Rouge, Louisiana, pp. 97-100.

Hartsock, J. H., 1981, Test prognosis and actual test performance of the Pleasant Bayou No. 2 Well, in Bebout, D. G., and Bachman, A. L., eds., Proceedings of the Fifth Conference Geopressured-Geothermal Energy: U.S. Gulf Coast, Louisiana State University, Baton Rouge, Louisiana pp. 91-95.

Hollister, J. C., and Weimer, R. J., 1968, Denver earthquakes and the arsenal well: Quarterly of the Colorado School of Mines, v. 63, no. 1, January 1968, 251 p.

Jaeger, J. C., 1969, Elasticity, fracture and flow, Methuen's monographs on physical subjects: Barnes and Noble Publishers, 268 p.

Jardetsky, W. S. and Press, F., 1952, Rayleigh wave coupling to atmospheric compression waves: Bull. Seis. Soc. Amer., v. 42, no. 2, pp. 135-144.

Landisman, Dziewonski, M. A., and Sato, Y., 1969, Recent improvements in the analysis of surface wave observations: Geophys. Jour., v. 17, pp. 369 -403.

Lash, C. C., 1980, Shear waves, multiple reflections, and converted waves found by a deep vertical wave test (vertical seismic profiling): Geophys. v. 45, no. 9, pp. 1373-1411.

Lee, W.H.K., and Lahr, J.C., 1975, HYPO71 (Revised): A computer program for determining hypocenter, magnitude, and first motion patterns of local earthquakes: U.S. Geological Survey Open File Report 75-311, 113 p.

Mauk, F., 1982, Microseismic monitoring of Chocolate Bayou, Texas, the Pleasant Bayou No. 2 geopressured/geothermal energy test well program 1981 annual progress report: Teledyne Geotech Technical Report No. 82-2, 74 p.

Nuttli, O., 1979, The relation of sustained maximum ground acceleration and velocity to earthquake intensity and magnitude, state-of-the-art for assessing earthquake hazards in the United States: Report 16, U.S. Army Corps of Engineers Miscellaneous Papers S-73-I, 74 p.

Zoback, M. L., and Zoback, M., 1980, State of stress in the conterminous United States: Jour. Geophys. Res., v. 85, no. B11, pp. 6113-6156.

APPENDIX A

PHASE ARRIVAL DATA FOR EARTHQUAKES 1981 - SEPTEMBER 1983

Entries for the data log utilize the following notation conventions:

Station Identification

BEG1, BEG2, BEG3, BEG4, BEG5

Phase Identification

P - compressional wave

S - shear wave

LR - Rayleigh surface wave

i - impulsive first motion

e - emergent first motion

c - compressional first motion

d - dilatational first motion

? - ambiguity of designation

pP - P-wave reflected at the crust near the epicenter

sS - S-wave converted to P-wave at reflection like pP

Airy - Airy phase (minimum group velocity) of Rayleigh wave.

Phase Timing

Times are designated in Universal Coordinated Time (UTC) which is equivalent to Central Standard Time + six hours. Explosions in a sequence may be designated by hour and minute only.

Phase Amplitude and Period

A_m = maximum 0-peak amplitude of the phase in mm observed on develocorder review (20 x magnification)

A = sustained 0-P amplitude in mm observed on develocorder review (20 x magnification) of a train of waves.

T = period of the wave in seconds.

D = duration of signal in seconds from onset of P to code = ambient noise.

C = number of cycles in a wave train.

Example Data Entry

BEG1 iPC 04:24:15.1, T = 0.5, A_m = 20.0, A = 13.0;
eS 04:24:20.3, T = 1.0, D = 35

Station BEG1 recorded an impulsive-compressional P-wave at 04:24:15.1 UTC. The sustained amplitude was 13 mm zero to peak, the maximum amplitude was 20 mm, the period of the wave was 0.5 seconds. An emergent S-wave was recorded at 04:24:20.3 UTC with a period of 1.0 seconds. The total event duration was 35 seconds.

1. 81-01-01
   03:32:29.3 ±0.04
   29°15'26"N
   95°15'36.3"W
   H = 6.0, M_D =
   90% confidence error ellipse Az = 17°, a = 0.5 km, b = 0.3 km

BEG1	ePd	03:32:31.80 ±0.03,
	S	03:32:33.35,
	LR	03:32:34.82;
BEG2	ePc	03:32:31.95 ±0.05,
	eS	03:32:33.61,
	LR	03:32:34.87;
BEG3	ePc	03:32:31.61 ±0.02,
	LR	03:32:34.57;
BEG4	eP	03:32:31.44 ±0.02,
	iS	03:32:32.79 ±0.02,
	LR	03:32:34.46;
BEG5	ePd	03:32:31.38 ±0.02,
	iS	03:32:32.77 ±0.02,
	LR	03:32:34.46

2. 81-05-12
   21:03:42.9 ±0.02
   29°15'38.2"N
   95°16'04.5"W
   H = 5.0, M_D =
   90% confidence error ellipse Az = 138°, a = 3.4 km, b = 3.2 km

BEG3	iPd	21:03:44.95;
BEG4	P	21:03:44.9;
BEG5	P	21:03:44.7;
	S	21:03:45.9;
	?	21:03:46.45;
	LR	Am = 19

3. 81-05-13
   16:14:12,8 ±0.19
   29°15'12.6"N
   95°16'12.0"W
   H = 1.0, M_D =
   90% confidence error ellipse Az = 26°, a = 0.9 km, b = 0.5 km

BEG3	P	16:14:14.7;
BEG4	P	16:14:14.5;
	S	16:14:15.55;

BEG5	P	16:14:14.0;
	LR	Am = 12

4. 81-05-13
16:23:33.05 ±0.44
29°14'20.5"N
95°16'21.6"W
H = 0 km, M_D =
90% confidence error ellipse Az = 133°, a = 1.8 km, b = 1.5 km

BEG3	eP	16:23:36.1,
	S	16:23:37.95;
BEG4	P	16:23:35.55;
	S	16:23:37.35;
BEG5	iP	16:23:35.3
	S	16:23:36.65

5. 81-05-28
13:39:02.5 ±0.13
29°17'09.7"N
95°14'56.0"W
H = 0 km, M_D =
90% confidence error ellipse Az = 148°, a = 0.6 km, b = 0.3 km

BEG2	iPc	13:39:03.95;
BEG3	iPc	13:39:03.6,
	S	13:39:04.5;
BEG4	iP	13:39:04.4,
	S	13:39:05.45;
	D	4.5
BEG5	iP	13:39:04.75
	S	13:39:06.0

6. 81-06-20
20:57:20.2 ±0.47
29°16'59.8"N
95°16'16.5"W
H = 0.0 km, M_D =
90% confidence error ellipse Az = 37°, a = 2.7 km, b = .7 km

BEG1	P	20:57:21.07,
	S	20:57:21.55;
BEG2	P?	20:57:23.15;
BEG3	P	20:57:22.1,
	S	20:57:22.5;
BEG4	LR	20:57:23.5;
BEG5	P?	20:57:21.75

7. 81-06-21
16:23:02.7

29°17'42.8"N
95°15'03.4"W
H = 0.0, M_D =
90% confidence error ellipse Ax = 155°, a = 3.7 km, b = 1.5 km

BEG1	iP	16:23:04.9;
BEG2	iP	16:23:03.95;
BEG3	iP	16:23:03.95;
BEG4	iP	16:23:05.28;
BEG5	iP	16:23:05.3

8. 81-10-02
07:27:32.9 ±0.28
29°16'03.7"N
95°15'26.2"W
H = 0.0 km, M_D =
90% confidence error ellipse Az = 0°, a = 1.3 km, b = 0.5 km

BEG1	iP	07:27:35.7,
	iS	07:27:36.4,
	LR	07:27:37.9;
BEG3	eS?	07:27:35.4,
	LR	07:27:37.35;
BEG4	eP	07:27:34.0,
	iS	07:27:34.7,
	LR	07:27:36.2;
BEG5	iP	07:27:33.95,
	iS	07:27:34.8,
	LR	07:27:36.15, Am = 4.5

9. 81-10-02
07:27:43.9
29°15'22.4"N
95°15'26.6"W
H = 0.0L, M_D =
90% confidence error ellipse Az = 179°, a = 3.0 km, b = 0.5 km

BEG1	eP	07:27:46.7,
	S	07:27:47.6,
	LR	07:27:48.9;
BEG2	iP	07:27:46.85;
BEG3	iP	07:27:46.4,
	LR	07:27:48.5;
BEG4	iP	07:27:45.4,
	iS	07:27:45.9,
	LR	07:27:47.55;
BEG5	iP	07:27:45.1,
	iS	07:27:46.1
	LR	07:27:47.4, Am = 4.5

10. 82-01-09
10:37:07.6 UTC

29 29 26.7 N
95 09 16.7 W
Velocity=339 meters/second
90% confidence error ellipse Az=30 , a=4.4 km, b=0.1 km

BEG1	iLR	10:38:33.10;
BEG2	iLR	10:38:25.30;
BEG3	iLR	10:38:31.85;
BEG4	iLR	10:38:35.40;
BEG5	iLR	10:38:38.60

11. 82-01-23
14:10:51.4 UTC
29 17 30.2 N
95 16 14.1 W
H = 0.92 Kilometers
90% confidence error ellipse Az=51 , a=1.6 km, b=1.3 km

BEG1	iP	16:31:27.30;
BEG2	eP	16:31:27.45;
BEG3	iP	16:31:27.10;
BEG4	P	16:31:24.50;
BEG5	eP	16:31:24.75

12. 82-06-08
00:49:29 UTC
No epicenter determined

BEG1	LR	00:49:41.30;
BEG2	iLR	00:49:32.20;
BEG3	eLR	00:49:33.92;
BEG4	iLR	00:49:29.15;
BEG5	eLR	00:49:37.50

13. 82-07-16
17:52:59 UTC
No epicenter determined

BEG1	iLR	17:53:01.00;
BEG2	iLR	17:52:53.70;
BEG3	Inoperative	
BEG4	iLR	17:52:59.40;
BEG5	iLR	17:53:05.45

14. 83-01-17
17:56:57 UTC
Teleseism from Guatemala
OT=17:52:21.8, H=138 km., mb=4.8

15. 83-01-17

21:31:03 UTC
Impulsive Rayleigh event from outside the array

BEG1	iLR	21:31:10.00;
BEG2		Inoperative
BEG3	iLR	21:31:09.57;
BEG4	iLR	21:31:05.22;
BEG5	iLR	21:31:03.00

Additional events on 82-01-17: 21:35:40 (unclear arrivals)

16. 83-01-17
22:12:31 UTC
Explosion shot series from outside the array

Additional events:

83-01-17:	22:18:55, 23:17:26, 23:21:55
83-01-18:	23:27:10
83-01-25:	17:52:12, 17:57:18, 18:57:48, 20:54:50
83-01-26:	17:07:18, 17:10:00, 17:13:15, 17:16:50, 18:06:30
83-01-28:	16:21:50, 16:29:03, 16:55:22, 17:02:38, 17:12:04,
	17:18:22, 17:47:20, 17:53:40, 18:00:25, 18:07:12,
	18:26:23, 19:06:28, 19:19:54, 19:26:46

17. 83-01-25
22:01:05.66 UTC, Velocity=255 m/sec
Impulsive Rayleigh event

BEG1	iLR	22:01:16.25;
BEG2	iLR	22:01:21.75;
BEG3	iLR	22:01:15.50;
BEG4	iLR	22:01:11.60;
BEG5	iLR	22:01:09.10

Additional events on 82-01-25: 17:28:38 and 21:54:46 (unclear arrivals)

18. 83-02-03
17:32:48.07 UTC, Velocity=330 m/sec
Impulsive Rayleigh event from outside the array

BEG1	iLR	17:33:44.72;
BEG2		Inoperative
BEG3	iLR	17:33:44.05;
BEG4	iLR	17:33:40.15;
BEG5	iLR	17:33:37.30

19. 83-02-04
05:22:21.66 UCT, Velocity=335 m/sec
Impulsive Rayleigh event

BEG1	iLR	05:22:52.30;

BEG2 iLR 05:22:42.49;
BEG3 iLR 05:22:44.48;
BEG4 iLR 05:22:39.07;
BEG5 iLR 05:22:45.40

Additional events on 83-02-04:

04:22:40 - First event of a series of three (D=3 seconds).
05:22:54 to 05:34:30 - Thirty-seven (37) events were recorded with an average peak-to-peak amplitude of _millimeters.
05:34:30 to 05:38:13 - Sixty-five (65) events were recorded with an average peak-to-peak amplitude of 10 millimeters.
05:47:43 - Ap-p=14 mm
05:48:15 - Ap-p=11 mm
05:48:18 - Ap-p=14 mm
05:49:17 - Ap-p=12 mm
05:49:26 - Ap-p= 7 mm
05:50:25 - Ap-p=14 mm
05:51:26 to 06:08:26 - Two hundred and sixty-five (265) events were recorded with an average peak-to-peak amplitude of 15 millimeters.
06:12:07 - Ap-p= 5 mm
08:00:17 - Ap-p= 7 mm
08:01:08 - Ap-p= 4 mm
08:01:16 - Ap-p= 5 mm
08:06:26 - Ap-p= 7 mm

20. 83-02-04
17:06:42 UTC
Exploration shot series from outside the array

Additional events:

83-02-04: 17:10:00, 17:14:08, 17:24:50, 17:28:12, 20:00:43
83-02-16: 20:38:40, 20:44:30, 20:51:10, 20:55:30, 20:59:15, 21:06:47, 21:15:48, 21:37:00, 21:46:32
83-02-22: 22:45:09, 22:47:53, 22:54:30, 23:00:08, 23:04:30, 23:08:35, 23:12:25, 23:15:55, 23:20:25, 23:26:13, 23:30:26, 23:35:50, 23:38:05, 23:44:35, 23:52:40
83-02-23: 15:22:42, 15:51:52, 16:06:00, 16:12:08, 16:19:30, 16:25:30, 16:33:30, 16:54:47, 17:05:20, 18:05:10, 18:41:00, 18:47:03, 18:52:38, 19:15:52, 19:28:30, 19:41:40, 19:54:12, 20:00:22, 20:57:15, 21:24:50, 21:58:22, 22:16:40, 22:22:48, 22:33:42, 22:39:56, 23:05:27
83-02-24: 23:36:40, 23:42:00
83-03-04: 15:52:55, 15:59:02, 16:06:00, 16:12:16, 16:18:20, 16:25:04, 16:42:38, 16:53:31, 17:07:10, 17:19:23, 17:31:32, 17:40:06, 17:45:15, 17:49:17

21. 83-02-15
15:01:15.30 UTC, Velocity=350 m/sec

Impulsive Rayleigh event from south of the array

BEG1	iLR	15:01:41.85;
BEG2	iLR	15:01:39.50;
BEG3	iLR	15:01:36.50;
BEG4	iLR	15:01:30.65;
BEG5	iLR	15:01:33.00

Additional events on 83-02-04:

04:22:40 - First event of a series of three (D=3 seconds)

22. 83-03-08
19:01:45 UTC
Rayleigh event from distant quarry blast to the northwest

Additional blasts:

83-03-09: 01:12:29

23. 83-03-23
12:27:54.29 UTC, Velocity=345 m/sec
Impulsive Rayleigh events from southeast of the array center

BEG1	iLR	12:28:11.90;
BEG2		Inoperative
BEG3	iLR	12:28:04.25;
BEG4	eLR	12:28:01.20;
BEG5		Inoperative

Additional events:

83-03-22: 03:30:43, 03:41:59, 03:42:13, 03:44:00 (possibly 5 others)

24. 83-03-23
17:02:10.22 UTC, Velocity=140 m/sec
Impulsive Rayleigh event

BEG1	iLR	17:02:23.70;
BEG2		Inoperative
BEG3	iLR	17:02:25.20;
BEG4	LR	17:02:32.55;
BEG5	iLR	17:02:19.30

25. 83-03-23
17:10:07 UTC
Impulsive Rayleigh event from outside the array

BEG1	iLR	17:10:07.00;
BEG2		Inoperative

BEG3		Inoperative
BEG4	iLR	17:10:11.70;
BEG5	iLR	17:10:16.00

Additional Impulsive Rayleigh events:

83-03-23: 17:22:16, 17:44:10, 18:03:03, 18:45:40, 18:49:29, 19:13:12, 19:15:26, 19:18:32, 19:28:49, 19:29:43, 19:32:53

26. 83-03-23
19:34:11.92 UTC, Velocity=175 m/sec
Impulsive Rayleigh event

BEG1	iLR	19:34:25.22;
BEG2		Inoperative
BEG3	iLR	19:34:22.30;
BEG4	iLR	19:34:26.75;
BEG5	iLR	19:34:16.60

Additional Impulsive Rayleigh events:

83-03-23: 19:40:18, 19:42:50, 19:44:45

27. 83-03-23
19:48:30.54 UTC, Velocity=135 m/sec
Impulsive Rayleigh event

BEG1	iLR	19:48:44.70;
BEG2		Inoperative
BEG3	iLR	19:48:46.70;
BEG4	iLR	19:48:54.10;
BEG5	iLR	19:48:39.98

Additional Impulsive Rayleigh events:

83-03-23: 19:49:48, 19:52:24, 19:53:27

28. 83-03-23
19:59:17.64 UTC, Velocity=155 m/sec
Impulsive Rayleigh event

BEG1	iLR	19:59:31.80;
BEG2		Inoperative
BEG3	iLR	19:59:29.75;
BEG4	iLR	19:59:35.30;
BEG5	iLR	19:59:23.70

29. 83-03-23
20:28:06.49 UTC, Velocity=195 m/sec

Impulsive Rayleigh event

BEG1	iLR	20:28:20.00;
BEG2		Inoperative
BEG3	iLR	20:28:13.70;
BEG4	iLR	20:28:16.90;
BEG5	iLR	20:28:11.10

30. 83-03-25
16:18:57.59 UTC, Velocity=185 m/sec
Impulsive Rayleigh event

BEG1	iLR	16:18:59.50;
BEG2		Inoperative
BEG3	iLR	16:19:06.80;
BEG4	iLR	16:19:09.00;
BEG5	iLR	16:19:07.30

31. 83-03-28
16:33:43.15 UTC, Velocity=225 m/sec
Impulsive Rayleigh event

BEG1	iLR	16:34:03.00;
BEG2		Inoperative
BEG3	iLR	16:34:08.00;
BEG4	iLR	16:34:03.40;
BEG5	iLR	16:33:56.60

32. 83-03-29
13:42:30.02 UTC, Velocity=225 m/sec
Impulsive Rayleigh event

BEG1	iLR	13:42:36.80;
BEG2		Inoperative
BEG3		Inoperative
BEG4	iLR	13:42:44.60;
BEG5	iLR	13:42:41.90

33. 83-03-29
20:47:45 UTC
Impulsive Rayleigh event from outside the array

BEG1	iLR	20:47:49.00;
BEG2		Inoperative
BEG3		Noisy
BEG4	iLR	20:47:45.30;
BEG5		Noisy

Additional events:

83-03-30: 17:15:04, 17:46:53, 17:48:25, 17:49:10, 17:53:40, 17:55:20

34. 83-05-02
23:47:45 UTC
Teleseism from Coalingua, California
OT=23:42:37.9 UTC, H=12 Km., mb=6.2

83-05-03
04:53:21.01 UTC, Velocity = 349 meters/sec
Impulsive Rayleigh event from the chemical plant southeast of the array

BEG1	iLR	04:53:47.50;
BEG	iLR	04:53:40.10;
BEG3	iLR	04:53:40.40;
BEG4	iLR	04:53:34.60;
BEG5		Inoperative

Additional Impulsive Rayleigh events:

83-05-03: 13:42:19, 13:42:23, 13:42:40, 13:42:51, 13:43:21, 13:43:42, 13:44:04, 13:44:22, 13:45:02, 13:45:19, 13:45:53, 13:46:16, 13:48:48, 13:48:49, 13:48:51, 13:49:06

35. 83-05-05
07:39:27 UTC
Teleseism from south of Panama
OT=07:33:46.3 UTC, H=11 km., mb=5.5

36. 83-05-05
18:57:46 UTC
Impulsive Rayleigh event from outside the array

BEG1	iLR	18:57:47.50;
BEG2		Noisy ;
BEG3	iLR	18:57:47.00;
BEG4	iLR	18:57:53.50;
BEG5		Inoperative

Additional Impulsive Rayleigh events:

83-05-05: 20:59:23, 23:37:14

37. 83-05-09
15:58:20 UTC
Teleseism from the Panama-Costa Rica border region
OT=15:53:02.7 UTC, H=36 Km., mb=5.7

83-05-09
21:02:05 UTC
Explosion shot series from northeast of the array

Additional Explosion shots:

83-05-09:	21:07:00, 21:12:50, 21:17:20, 21:25:30, 21:30:50, 21:35:40, 21:40:02, 21:57:40, 22:03:00
83-05-10:	13:35:20, 22:03:00
83-05-11:	16:42:37, 17:13:50, 17:20:52, 18:55:30, 18:59:40, 19:04:20, 23:31:08, 23:35:30
83-05-12:	21:06:44, 21:17:40, 21:21:35, 21:39:40, 21:45:02, 21:49:30, 21:54:54, 22:06:00, 22:08:51, 22:12:00, 22:14:50, 22:37:37, 22:44:01, 22:47:18

38. 83-05-09
21:55:52.72 UTC, Velocity = 347 meters/sec
Impulsive Rayleigh event from near the geopressured/geothermal well

BEG1	iLR	21:56:11.80;
BEG2	iLR	21:56:05.75;
BEG3	iLR	21:56:04.70;
BEG4	iLR	21:55:58.80;
BEG5		Inoperative

39. 83-05-09
23:51:00 UTC
Impulsive Rayleigh event from outside the array

BEG1	iLR	23:51:12.50;
BEG2	iLR	23:51:14.00;
BEG3	iLR	23:51:11.30;
BEG4	iLR	23:51:09.75;
BEG5		Inoperative

Additional Impulsive Rayleigh events:

83-05-09:	23:57:00

40. 83-05-10
00:24:10 UTC
Impulsive Rayleigh event from outside the array

BEG1	iLR	00:24:14.00;
BEG2	iLR	00:24:24.20;
BEG3	iLR	00:24:17.50;
BEG4	iLR	00:24:18.30;
BEG5		Inoperative

41. 83-05-10
00:31:00 UTC

Impulsive Rayleigh event from outside the array

BEG1	iLR	00:31:16.10;
BEG2	iLR	00:31:16.15;
BEG3	iLR	00:31:12.30;
BEG4	iLR	00:31:11.60;
BEG5		Inoperative

Additional Impulsive Rayleigh events:

83-05-10: 13:16:01

42. 83-05-19
15:36:11 UTC
Explosion shot series from outside the array

Additional Explosion shots:

83-05-19: 15:41:58, 15:47:28, 15:52:59, 15:59:02, 16:04:19, 16:17:59, 16:26:16, 16:32:01, 16:41:20, 16:54:16, 17:05:20, 17:12:09, 17:30:52, 19:39:45, 20:10:38, 20:31:59, 21:01:00, 21:27:46, 22:50:45, 22:54:23, 23:37:13, 23:55:58, 23:59:58

43. 83-05-20
06:12:31.14 UTC, Velocity = 355 meters/sec
Impulsive Rayleigh event from the chemical plant southeast of the array

BEG1	iLR	06:12:49.90;
BEG2	iLR	06:12:40.90;
BEG3	iLR	06:12:42.48;
BEG4	iLR	06:12:38.30;
BEG5		Inoperative

44. 83-06-01
01:55:45 UTC
Teleseism from Mindoro, Philippine Islands
OT=01:37:00.7 UTC, H=260 Km., mb=5.5

45. 83-06-02
20:20:28 and 20:21:56 UTC
Teleseism from the Peru-Brazil border region
OT=20:12:51.3 UTC, H=607 Km., mb=5.9

46. 83-06-20
14:57:42 UTC
Explosion shot series from outside the array

Additional Explosion shots:

83-06-20: 15:03:31, 15:08:09, 15:13:31, 17:21:43, 17:25:59, 18:49:41,
19:20:08, 19:27:50, 19:29:10, 20:53:00, 21:03:43, 21:29:49,
21:43:43, 21:55:18, 22:03:01, 22:14:28, 22:19:59, 22:36:31,
22:49:38, 22:54:39, 22:58:55, 23:03:51, 23:08:21, 23:13:04,
23:17:51, 23:22:44, 23:36:33, 23:41:45, 23:47:44, 23:57:03
83-06-21: 00:03:37, 00:08:54, 00:15:35, 00:21:20, 00:32:20, 00:36:07,
14:36:36, 14:42:15, 14:47:55, 15:40:18, 15:56:44
83-06-27: 19:39:37, 19:46:31, 19:48:07, 19:53:37, 19:55:35, 20:02:23,
20:08:50, 20:20:39, 21:28:09, 21:27:20, 21:30:51, 21:32:56,
21:32:47, 21:36:34, 21:40:35, 21:48:54, 21:53:10, 21:56:14,
22:01:39, 22:02:46, 22:08:42, 22:10:35, 22:23:19, 22:38:39,
22:58:16, 23:01:04, 23:04:21, 23:13:39
83-06-28: 00:59:51, 01:04:50, 01:09:12, 01:28:17, 17:15:01, 17:27:59,
17:31:01, 17:50:34, 17:57:15, 18:01:15, 18:06:16, 18:13:26,
19:24:47, 20:26:45, 21:01:35, 21:09:10, 21:20:16, 22:12:24,
22:15:35, 22:19:13, 22:22:58, 22:55:37, 23:01:04, 23:05:44
83-06-29: 00:52:58, 00:57:28, 01:07:38, 01:11:00, 01:14:42, 01:17:39,
01:20:42, 01:28:24
83-06-30: 17:05:57, 18:05:52, 18:31:13, 18:29:49, 18:48:00, 18:55:04

47. 83-07-06
00:06:50 UTC
Explosion shot series from outside of the array

Additional Explosion shots:

83-07-06: 00:13:55, 00:18:55, 02:58:30
83-07-07: 19:34:02, 19:52:11, 19,55,44, 19,58:51, 20:13:11, 20:19:40,
20:47:12, 21:28:01, 21:35:25, 21:44:45, 21:47:28, 21:54:40,
22:06:23, 22:08:51, 22:12:46, 22:16:21, 22:29:54, 22:33:39,
22:40:28, 22:43:26, 22:46:36, 22:56:27, 22:56:40, 23:01:10,
23:04:30, 23:08:30, 23:39:08, 23:43:02, 23:50:12, 00:03:32,
00:06:50, 00:10:15, 00:42:15, 00:45:48, 00:49:45, 00:52:15,
00:58:10, 01:01:00, 01:03:17, 01:37:50

48. 83-07-07
19:36:05.8 UTC
Large Impulsive Rayleigh event, Velocity = 500 meters/second
Md = 0.5

BEG1	iLR	19:36:17.60;
BEG2	iLR	19:36:08.30;
BEG3	iLR	19:36:12.80;
BEG4		Inoperative;
BEG5	iLR	19:36:13.10

49. 83-07-07
22:54:49.2 UTC
Impulsive Rayleigh event from inside the array, Velocity = 400
meters/second

BEG1	iLR	22:55:06.00;
BEG2	iLR	22:54:57.00;
BEG3	iLR	22:54:59.50;
BEG4		Inoperative;
BEG5	iLR	22:55:01.50

50. 83-07-11
20:16:20 UTC
Explosion shot series from outside of the array

Additional Explosion shots:

83-07-11:	20:16:42, 20:32:49, 20:59:50, 21:04:40, 21:07:36, 21:11:50, 21:11:57, 21:13:08, 21:26:58, 21:51:53, 21:59:43, 22:42:12, 22:45:39, 23:07:39, 23:11:00, 23:14:54, 23:17:52, 23:25:46, 23:50:25, 23:55:56
83-07-12:	00:01:05, 00:06:17, 00:09:10, 00:13:20, 00:17:33, 00:24:05, 00:27:04, 00:30:01, 00:33:04

51. 83-07-26
15:30:41 UTC
Explosion shot series from outside of the array

Additional Explosion shots:

83-07-26:	15:42:46, 15:50:16, 16:16:28, 16:24:11, 16:38:40, 16:45:23, 17:55:16, 17:55:45, 18:09:05, 18:15:03, 18:48:25, 19:22:21, 19:30:02, 19:34:12
83-07-27:	17:20:50, 18:54:35, 19:24:39, 19:42:23, 19:48:31, 22:08:28, 22:12:03, 22:20:15, 22:29:16, 22:42:51, 23:27:28, 23:38:44, 23:41:58, 23:57:57
83-07-28:	00:09:09, 00:17:57, 00:20:59, 00:23:55, 00:34:47, 00:34:53, 00:40:34, 00:40:31, 00:49:51, 00:58:52, 01:34:28, 01:58:08

52. 83-07-26
18:16:20 UTC
Emergent Rayleigh event from outside the array

BEG1	iLR	18:16:32.20;
BEG2	iLR	18:16:33.50;
BEG3	iLR	18:16:27.10;
BEG4	iLR	18:16:27.10;
BEG5		Inoperative

53. 83-07-26
18:19:36 UTC
Emergent Rayleigh event from outside the array

BEG1	iLR	18:19:41.60;
BEG2	iLR	18:19:44.50;

BEG3	iLR	18:19:44.50;
BEG4	iLR	18:19:27.30;
BEG5		Inoperative

54. 83-07-26
19:13:38.8 UTC
Emergent Rayleigh event from outside the array

BEG1	iLR	19:13:47.40;
BEG2	iLR	19:13:41.45;
BEG3	iLR	19:13:38.00;
BEG4	iLR	19:13:41.30;
BEG5		Inoperative

55. 83-07-26
19:14:31.1 UTC
Emergent Rayleigh event from inside the array, Velocity = 250 meters/second

BEG1	iLR	19:14:45.60;
BEG2	iLR	19:14:39.20;
BEG3	iLR	19:14:39.45;
BEG4	iLR	19:14:37.00;
BEG5		Inoperative

56. 83-07-26
19:20:40 UTC
Emergent Rayleigh event from outside the array

BEG1	iLR	19:20:49.50;
BEG2	iLR	19:20:42.20;
BEG3	iLR	19:20:42.80;
BEG4	iLR	19:20:40.50;
BEG5		Inoperative

57. 83-08-02
20:38:51 UTC
Explosion shot series from outside of the array

Additional Explosion shots:

83-08-02:	21:09:11, 21:22:32, 21:54:00, 22:28:40, 23:25:29, 23:54:12, 23:58:58, 00:09:57, 00:14:56, 00:19:06, 00:23:33, 00:28:05, 00:32:31, 00:38:48, 00:48:58, 00:55:18
83-08-03:	14:28:53, 14:36:38, 14:49:09, 15:10:42, 15:20:26

58. 83-08-04
03:09:57.8 UTC

Impulsive Rayleigh event from outside the array

BEG1	iLR	03:10:18:15;
BEG2	iLR	03:10:16.00;
BEG3	iLR	03:10:20.50;
BEG4		Inoperative;
BEG5	iLR	03:10:26.10

59. 83-08-04
03:13:11.1 UTC
Impulsive Rayleigh event, Velocity = 125 meters/second

BEG1	iLR	03:13:33.30;
BEG2	iLR	03:13:32.40;
BEG3	iLR	03:13:36.20;
BEG4		Inoperative;
BEG5	iLR	03:13:41.90

60. 83-08-04
03:32:58.7 UTC
Impulsive Rayleigh event, Velocity = 350 meters/second

BEG1	iLR	03:33:06.80;
BEG2	iLR	03:33:08.80;
BEG3	iLR	03:33:02.10;
BEG4		Inoperative;
BEG5	iLR	03:33:02.40

61. 83-08-04
03:33:41.6 UTC
Impulsive Rayleigh event, Velocity = 275 meters/second

BEG1	iLR	03:33:56.00;
BEG2	iLR	03:33:55.20;
BEG3	iLR	03:33:49.70;
BEG4		Inoperative;
BEG5	iLR	03:33:48.10

62. 83-08-04
03:34:21.1 UTC
Impulsive Rayleigh event, Velocity = 350 meters/second

BEG1	iLR	03:34:28.00;
BEG2	iLR	03:34:29.50;
BEG3	iLR	03:34:22.00;
BEG4		Inoperative;
BEG5	iLR	03:34:27.40

63. 83-08-04
03:35:02.7 UTC
Impulsive Rayleigh event, Velocity = 350 meters/second

BEG1	iLR	03:35:08.50;
BEG2	iLR	03:35:12.20;
BEG3	iLR	03:34:04.90;
BEG4		Inoperative;
BEG5	iLR	03:35:08.40

64. 83-08-04
03:36:05.1 UTC
Impulsive Rayleigh event, Velocity = 350 meters/second

BEG1	iLR	03:36:18.10;
BEG2	iLR	03:36:19.20;
BEG3	iLR	03:36:13.60;
BEG4		Inoperative;
BEG5	iLR	03:36:09.50

65. 83-08-04
19:22:26.6 UTC
Impulsive Rayleigh event, Velocity=325 meters/second

BEG1	iLR	19:22:40.75;
BEG2	iLR	19:22:35.10;
BEG3	iLR	19:22:38.90;
BEG4	iLR	19:22:44.20;
BEG5		Inoperative

66. 83-08-04
20:01:32.8 UTC
Impulsive Rayleigh event, Velocity = 375 meters/second

BEG1	iLR	20:01:45.50;
BEG2	iLR	20:01:42.90;
BEG3	iLR	20:01:33.40;
BEG4	iLR	20:01:33.40;
BEG5		Inoperative

67. 83-08-04
21:07:49.7 UTC
Impulsive Rayleigh event, Velocity = 100 meters/second

BEG1	iLR	20:08:11.20;
BEG2	iLR	20:08:23.50;
BEG3	iLR	20:08:16.25;
BEG4		Inoperative;
BEG5		Inoperative

68. 83-08-04
21:51:46.5 UTC
Impulsive Rayleigh event, Velocity = 100 meters/second

BEG1	iLR	21:52:07.15;
BEG2	iLR	21:52:14.00;
BEG3	iLR	21:52:07.20;
BEG4	iLR	21:52:04.20;
BEG5		Inoperative

69. 83-08-05
06:30:00 UTC
Teleseism from western Brazil
OT = 06:21:42.4 UTC, H = 21 Km., mb = 5.5

70. 83-08-09
11:44:50.4 UTC
Impulsive Rayleigh event, Velocity = 250 meters/second

BEG1	iLR	11:44:57.00;
BEG2	iLR	11:45:05.70;
BEG3	iLR	11:45:02.30;
BEG4	iLR	11:45:06.45;
BEG5		Inoperative

71. 83-08-09
11:53:42.3 UTC
Impulsive Rayleigh event, Velocity = 100 meters/second

BEG1	iLR	11:54:18.80;
BEG2	iLR	11:54:15.80;
BEG3	iLR	11:54:13.10;
BEG4	iLR	11:54:07.80;
BEG5		Inoperative

72. 83-08-09
16:32:38 UTC
Impulsive Rayleigh event from outside the array

BEG1	iLR	16:32:45.60;
BEG2	iLR	16:32:43.70;
BEG3	iLR	16:32:48.00;
BEG4	iLR	16:32:52.30;
BEG5		Inoperative

73. 83-08-10

17:19:24.5 UTC
Impulsive Rayleigh event, Velocity = 300 meters/second

BEG1	iLR	17:19:37.30;
BEG2	iLR	17:19:32.10;
BEG3	iLR	17:19:36.10;
BEG4	iLR	17:19:41.00;
BEG5		Inoperative

74. 83-08-11
16:12:15.2 UTC
Impulsive Rayleigh event, Velocity = 375 meters/second

BEG1	iLR	16:12:33.10;
BEG2	iLR	16:12:31.60;
BEG3	iLR	16:12:28.10;
BEG4	iLR	16:12:22.60;
BEG5		Inoperative

75. 83-08-11
16:12:56.9 UTC
Impulsive Rayleigh event, Velocity = 350 meters/second

BEG1	iLR	16:13:20.00;
BEG2	iLR	16:13:17.10;
BEG3	iLR	16:13:14.40;
BEG4	iLR	16:13:08.20;
BEG5		Inoperative

76. 83-08-11
16:13:43.3 UTC
Impulsive Rayleigh event, Velocity = 350 meters/second

BEG1	iLR	16:13:59.50;
BEG2	iLR	16:13:56.10;
BEG3	iLR	16:13:53.40;
BEG4	iLR	16:13:48.20;
BEG5		Inoperative

77. 83-08-11
16:15:00 UTC
Impulsive Rayleigh event from outside the array

BEG1	iLR	16:15:11.55;
BEG2	iLR	16:15:07.80;
BEG3	iLR	16:15:05.80;
BEG4	iLR	16:14.59.50;

BEG5		Inoperative

78. 83-08-11
17:04:03.9 UTC
Impulsive Rayleigh event from outside the array, Velocity = 350 meters/second

BEG1	iLR	17:04:42.60;
BEG2	iLR	17:04:54.40;
BEG3	iLR	17:04:47.20;
BEG4	iLR	17:04:47.60;
BEG5		Inoperative

79. 83-08-11
17:13:55.1 UTC
Impulsive Rayleigh event, Velocity = 350 meters/second

BEG1	iLR	17:14:08.40;
BEG2	iLR	17:14:14.90;
BEG3	iLR	17:14:07.80;
BEG4	iLR	17:14:06.50;
BEG5		Inoperative

80. 83-08-16
12:56:20 UTC
Acoustic-coupled Rayleigh event or Sonic Boom

BEG1	iLR	16:12:33.10;
BEG2	iLR	16:12:31.60;
BEG3	iLR	16:12:28.10;
BEG4	iLR	16:12:22.60;
BEG5		Inoperative

Additional acoustic-coupled Rayeigh events:

83-09-06: 21:02:00

81. 83-08-17
11:07:28 UTC
Teleseism from near the coast of Kamchatka
OT = 10:55:52.8 UTC, H = 55 Km., mb = 6.5

82. 83-08-24
22:18:10 UTC
Explosion shot series from outside the array

Additional Explosion shots:

83-08-24:	21:29:15,	22:30:50,	22:59:50,	23:13:05,	23:14:50,	23:17:30,
	23:20:00,	23:23:30,	23:31:40,	00:12:50,	00:16:30,	00:19:50,
	00:20:30,	00:31:15,	00:34:20,	00:38:00,	00:44:05,	00:47:20
83-08-25:	14:29:12,	14:47:00,	14:50:50,	14:57:40,	15:00:50,	15:08:35,
	15:12:50					

83. 83-08-29
14:35:04 UTC
Explosion shot series from outside the array

Additional Explosion shots:

83-08-29:	14:54:47,	15:02:12,	15:19:04,	15:53:14,	16:00:40,	16:29:50,
	16:39:30,	17:02:20,	17:10:20,	17:19:35,	17:21:18,	17:24:20,
	17:27:12,	17:27:30,	17:30:30,	17:40:38,	17:50:10,	17:55:33,
	18:02:10,	18:06:09,	18:17:40,	18:20:25,	18:22:52,	18:23:20,
	18:30:40,	19:33:10,	19:36:06,	19:39:39,	19:41:12,	20:19:14,
	20:21:32,	20:22:13,	20:26:23,	20:30:40,	20:35:01,	20:42:30
83-08-30:	21:13:53,	21:40:55,	21:48:50,	22:16:20,	22:20:40,	22:26:30,
	22:36:00,	22:50:45,	22:54:32,	22:59:06,	23:00:20,	23:02:20,
	23:04:30,	23:10:45,	23:14:12,	23:18:32		
83-08-31:	14:48:09,	15:06:44,	15:24:22,	15:31:10,	15:50:55,	15:57:00,
	15:59:34,	16:02:45,	16:06:00,	16:34:30,	16:43:20,	16:58:30,
	18:31:40,	19:14:55,	19:20:23,	19:23:00,	20:59:00,	21:05:10,
	21:09:10					
83-09-01	16:38:50,	16:46:16,	16:50:56,	16:56:20,	17:01:00,	17:11:40,
	17:59:40,	18:02:05,	19:02:32,	19:40:48,	19:45:30,	19:47:00,
	19:51:00,	19:56:50,	20:23:30,	20:28:15,	20:34:50,	20:36:50,
	20:39:40,	20:41:20,	20:51:50,	21:37:50,	21:41:50,	21:43:20
83-09-02	16:10:10,	16:17:02,	16:22:40,	16:28:50,	16:38:05,	16:44:40,
	17:07:50,	17:35:26,	17:59:40,	18:14:30,	18:21:10,	18:30:15,
	18:37:10,	19:01:25,	19:10:00,	19:24:15,	19:33:10,	19:45:50,
	19:59:00,	29:04:02,	20:24:30,	20:34:10,	20:59:50,	21:06:50

84. 83-09-06
20:46:53.5 UTC
Impulsive Rayleigh event, Velocity = 275 meters/second

BEG1	iLR	20:47:08.80;
BEG2	iLR	20:47:07.90;
BEG3		Inoperative;
BEG4	iLR	20:47:01.30;
BEG5	iLR	20:46:59.50

85. 83-09-07
01:14:44.2 UTC
Impulsive Rayleigh event, Velocity = 200 meters/second

BEG1	iLR	01:15:05.40;
BEG2	iLR	01:14:52.90;
BEG3		Inoperative;
BEG4	iLR	01:15:05.40;
BEG5	iLR	01:14:53.10

86. 83-09-07
19:30:35 UTC
Teleseism from southern Alaska
OT = 19:22:04.8 UTC, H = 42 Km., mb = 6.2

87. 83-09-08
22:26:13 UTC
Teleseism from the Ionian Sea
OT = 22:04:51.0 UTC, H = 10 Km., mb = 5.1

88. 83-09-09
01:34:43.7 UTC
Impulsive Rayleigh event, Velocity = 325 meters/second

BEG1	iLR	01:35:03.40;
BEG2	iLR	01:34:54.60;
BEG3		Inoperative;
BEG4		Inoperative;
BEG5	iLR	01:34:51.40

89. 83-09-08
01:35:48.3 UTC
Impulsive Rayleigh event, Velocity = 100 meters/second

BEG1	iLR	01:36:19.50;
BEG2	iLR	01:36:10.40;
BEG3		inoperative;
BEG4	iLR	01:36:13.80;
BEG5	iLR	01:36:07.20

90. 83-09-09
02:51:04.8 UTC
Impulsive Rayleigh event, Velocity = 100 meters/second

BEG1	iLR	02:51:36.20;
BEG2	iLR	02:51:27.25;
BEG3		Inoperative;
BEG4	iLR	02:51:30.00;
BEG5	iLR	02:51:24.10

91. 83-09-09
03:00:56.0 UTC
Impulsive Rayleigh event, Velocity = 100 meters/second

BEG1	iLR	03:01:26.70;
BEG2	iLR	03:01:18.80;
BEG3		Inoperative;
BEG4	iLR	03:01:21.80;
BEG5	iLR	03:01:15.20

92. 83-09-09
10:34:20 UTC
Teleseism from near the coast of Nicaragua
OT = 10:29:56.1 UTC, H = 73 Km., mb = 4.9

APPENDIX B

SYNTHETIC SEISMOGRAMS BASED ON THE PLEASANT BAYOU EARTH MODEL

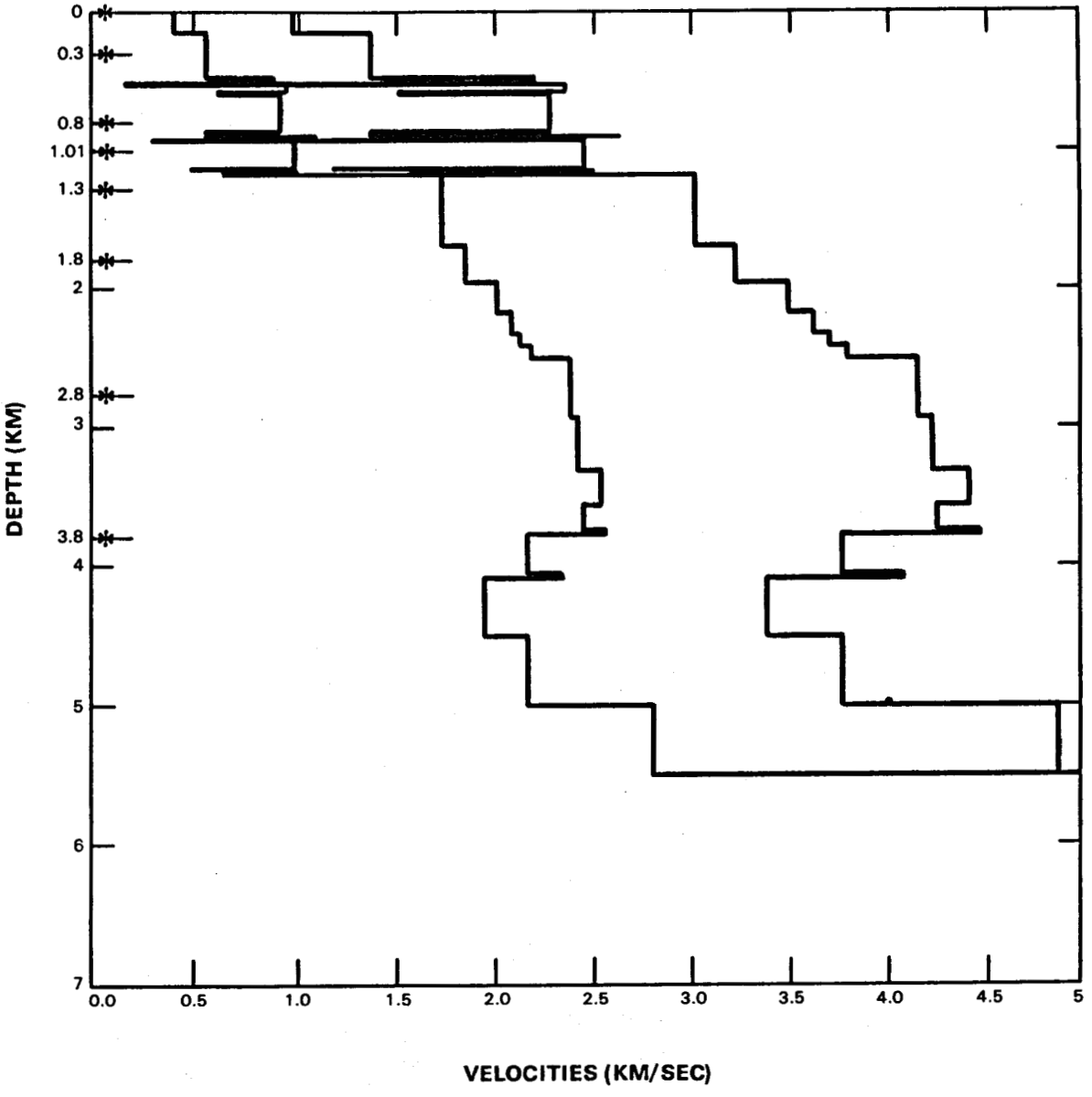

Figure B1. Crustal structure model used to calculate synthetic seismograms for the Pleasant Bayou vicinity. Asterisks indicate source depths used for modeling.

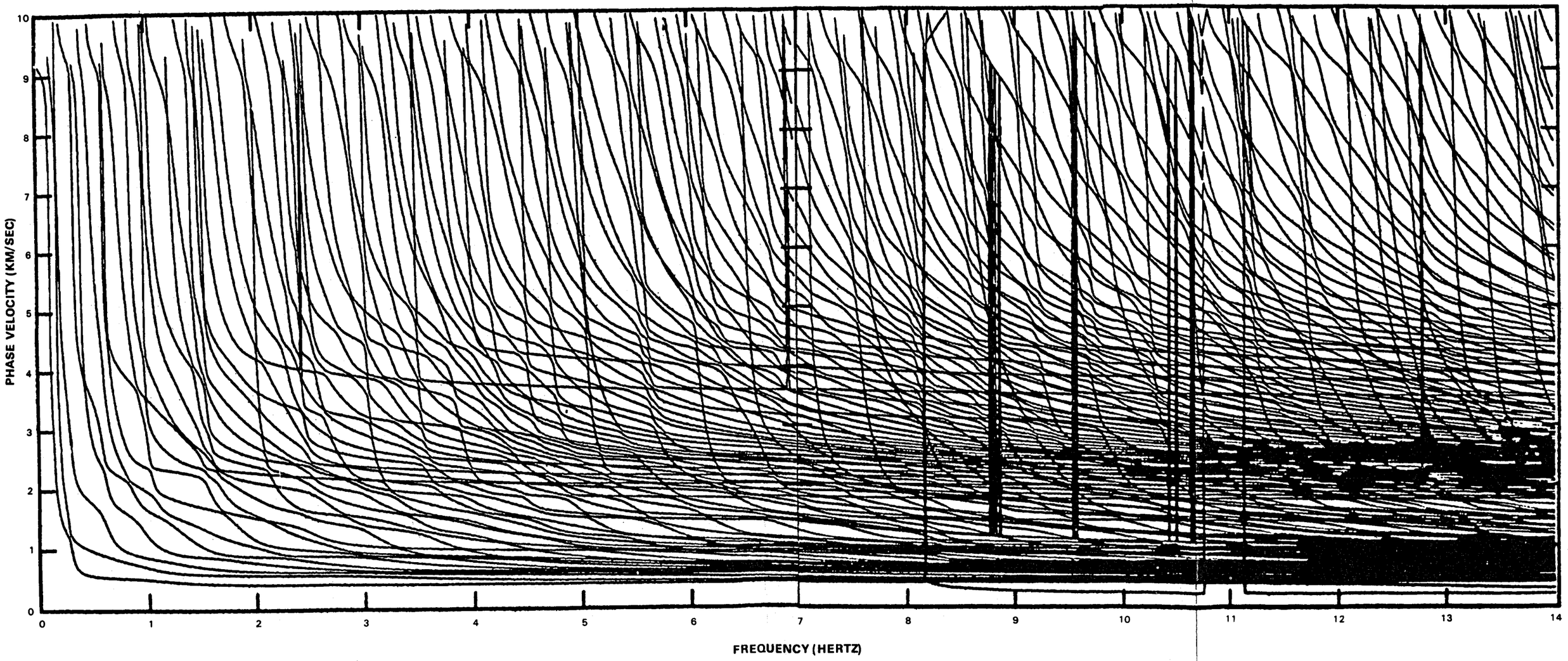

Figure B2. Phase velocities by frequency of the calculated modes.

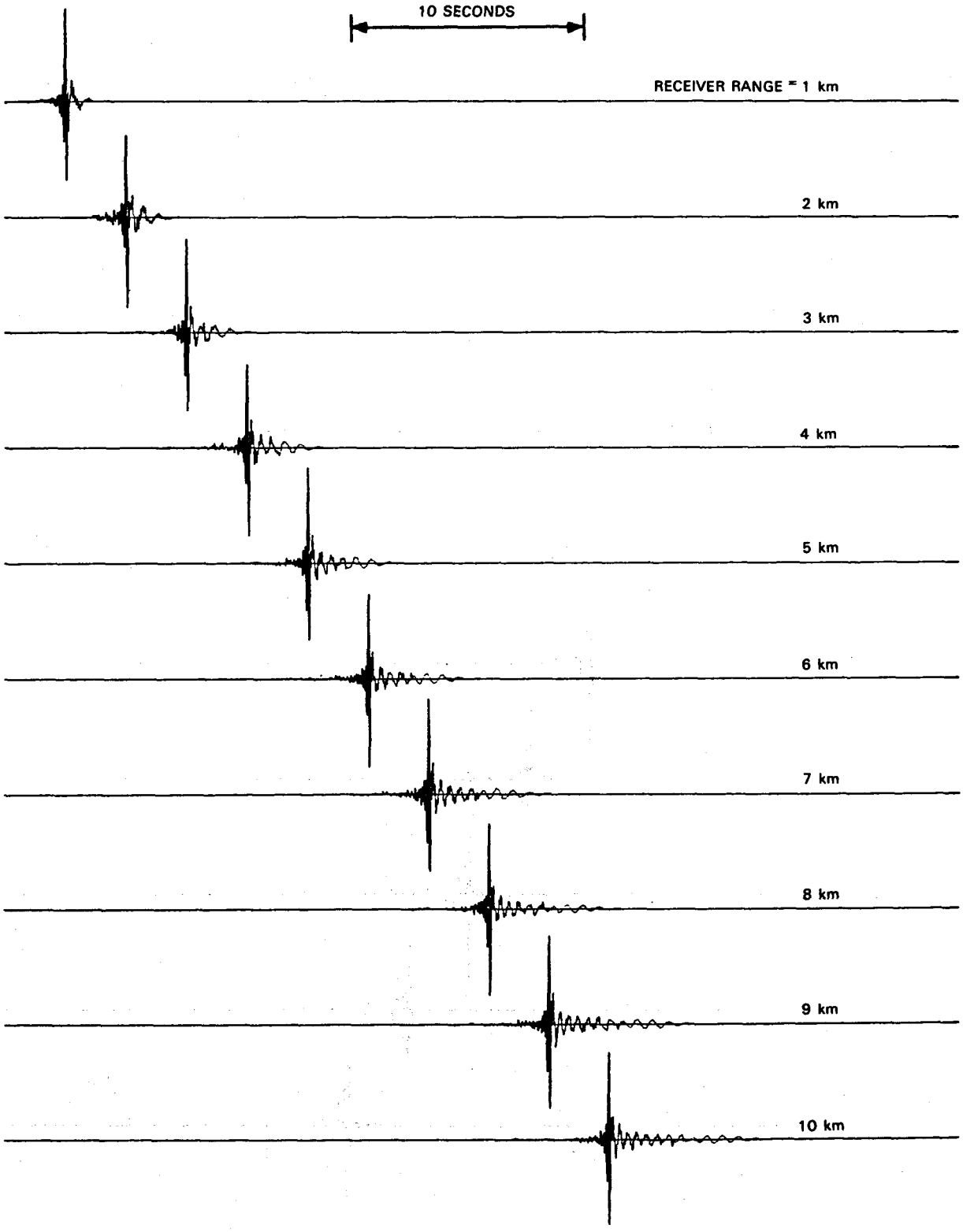

Figure B3. Synthetic seismogram calculated for source dip 45°, source depth 0.0 km.

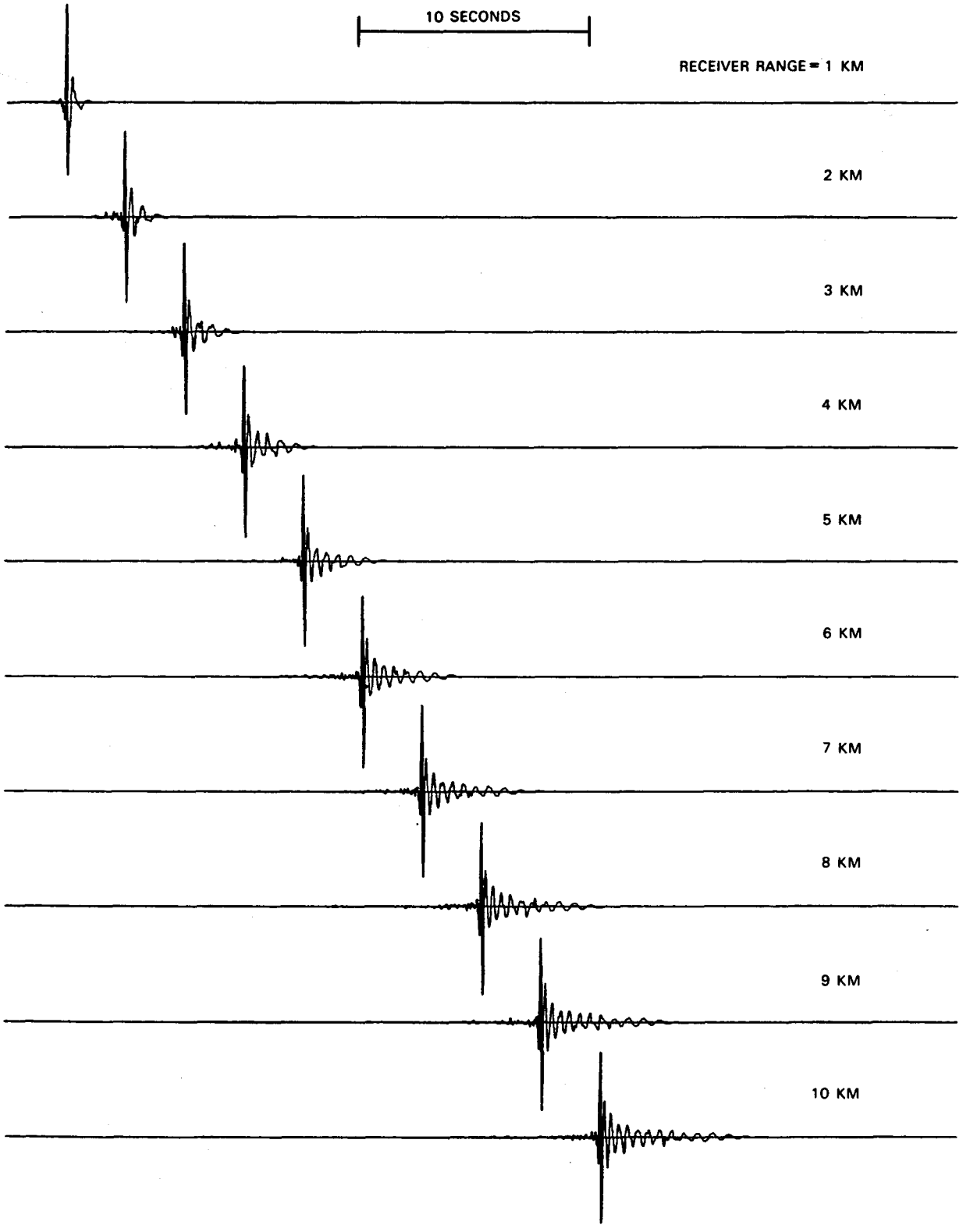

Figure B4. Synthetic seismogram calculated for source dip 45°, source depth 0.0 km and convolved with instrument transfer function.

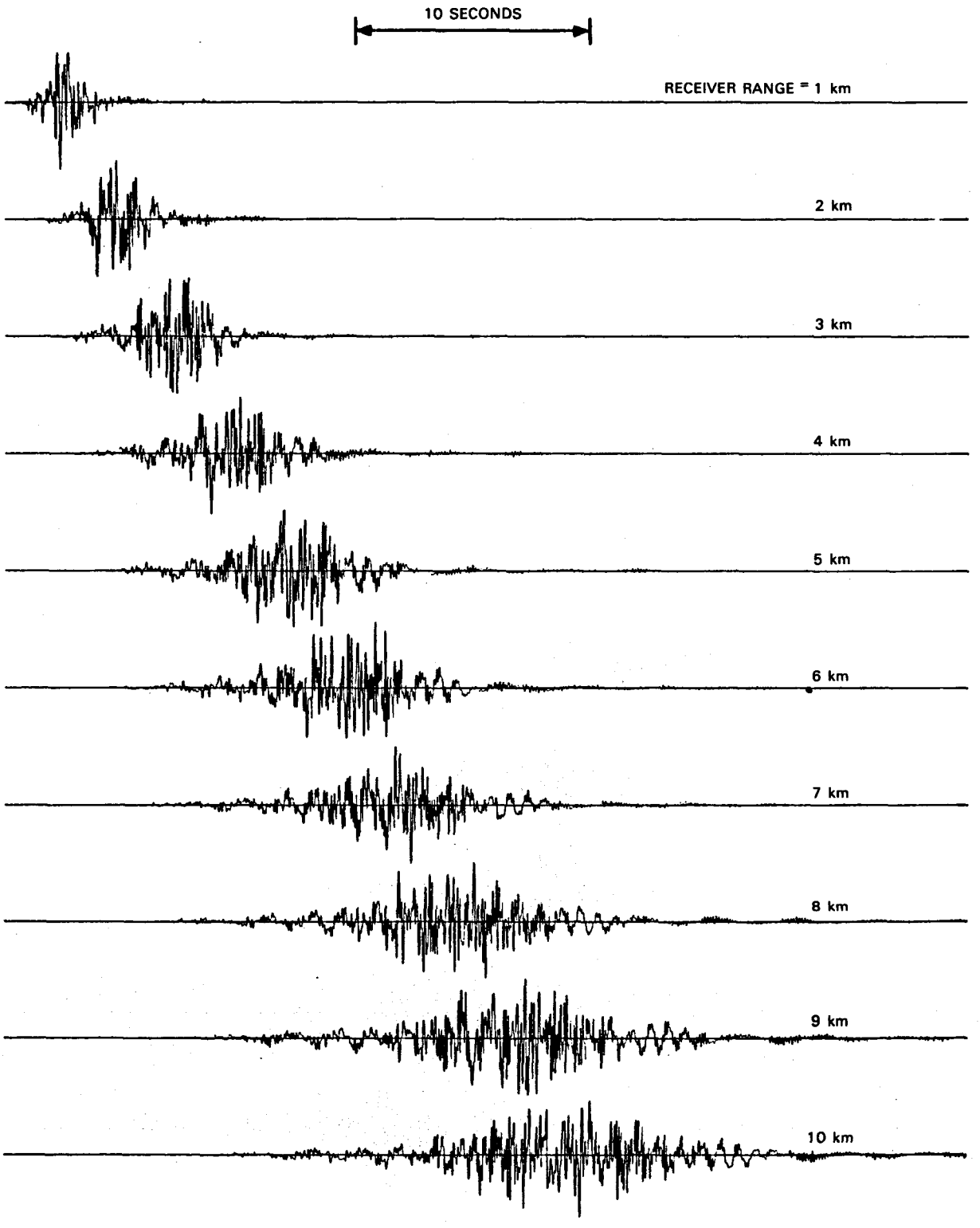

Figure B5. Synthetic seismogram calculated for source dip 45°, source depth 0.3 km.

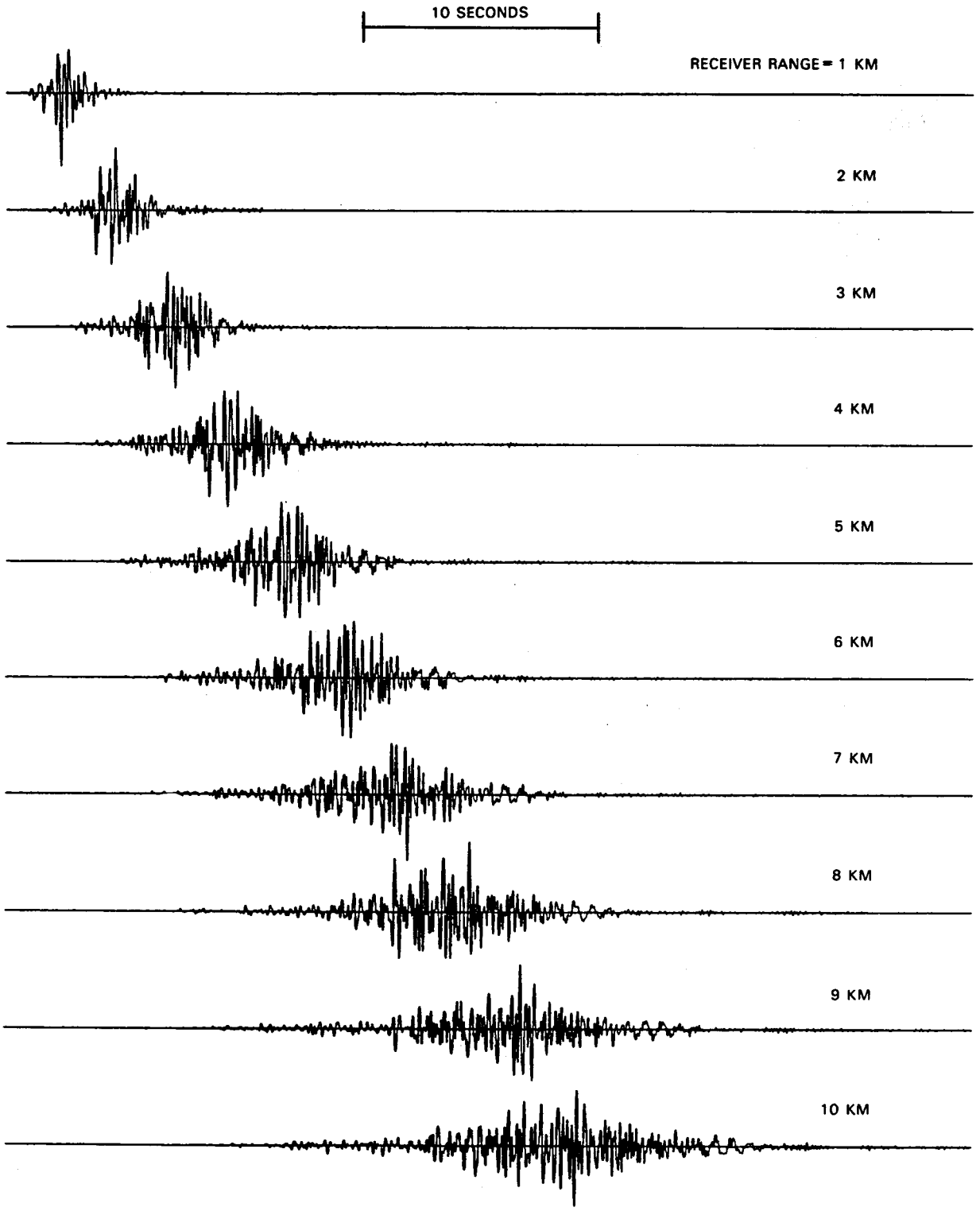

Figure B6. Synthetic seismogram calculated for source dip 45°, source depth 0.3 km and convolved with instrument transfer function.

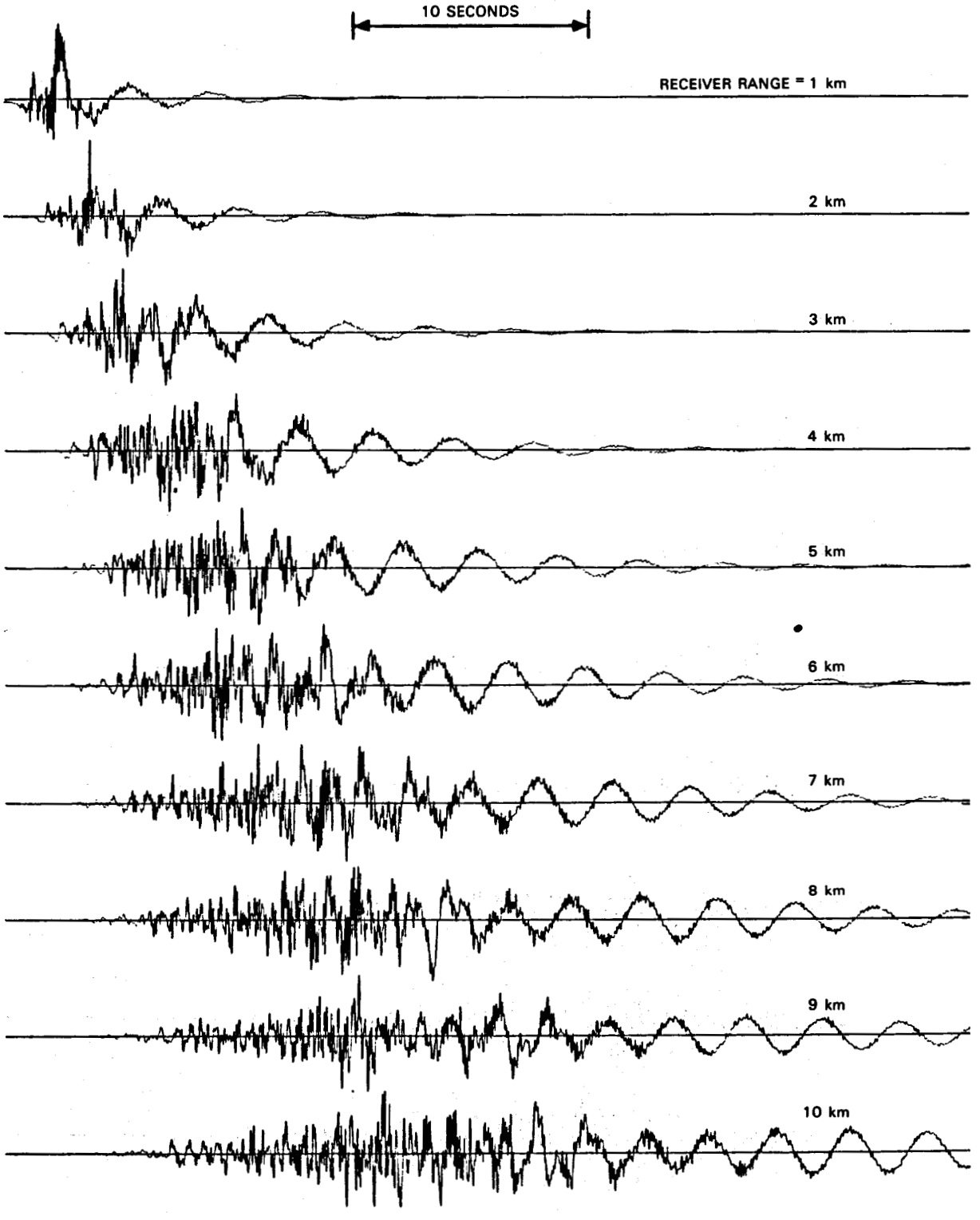

Figure B7. Synthetic seismogram calculated for source dip 45°, source depth 0.8 km.

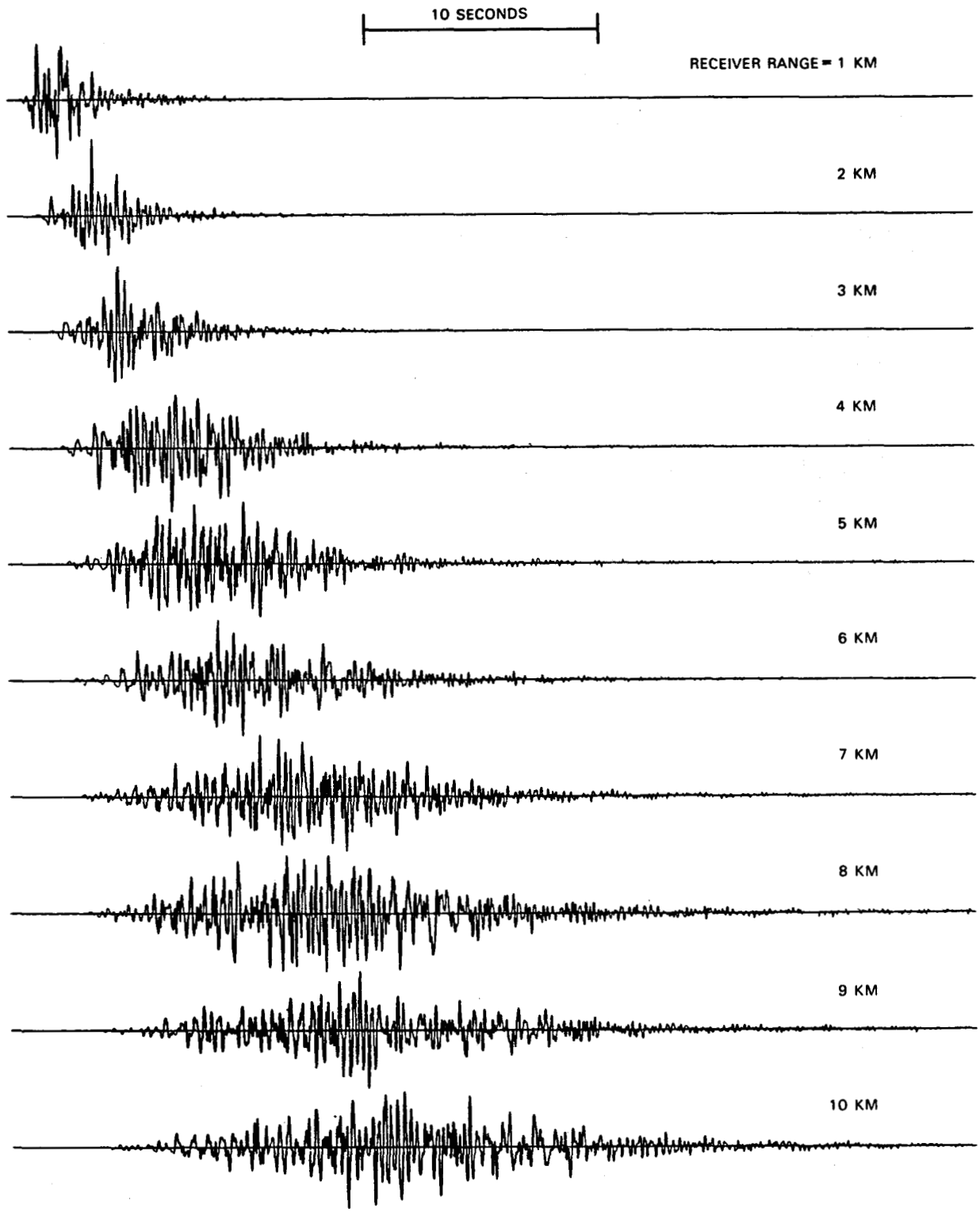

Figure B8. Synthetic seismogram calculated for source dip 45°, source depth 0.8 km, and convolved with instrument transfer function.

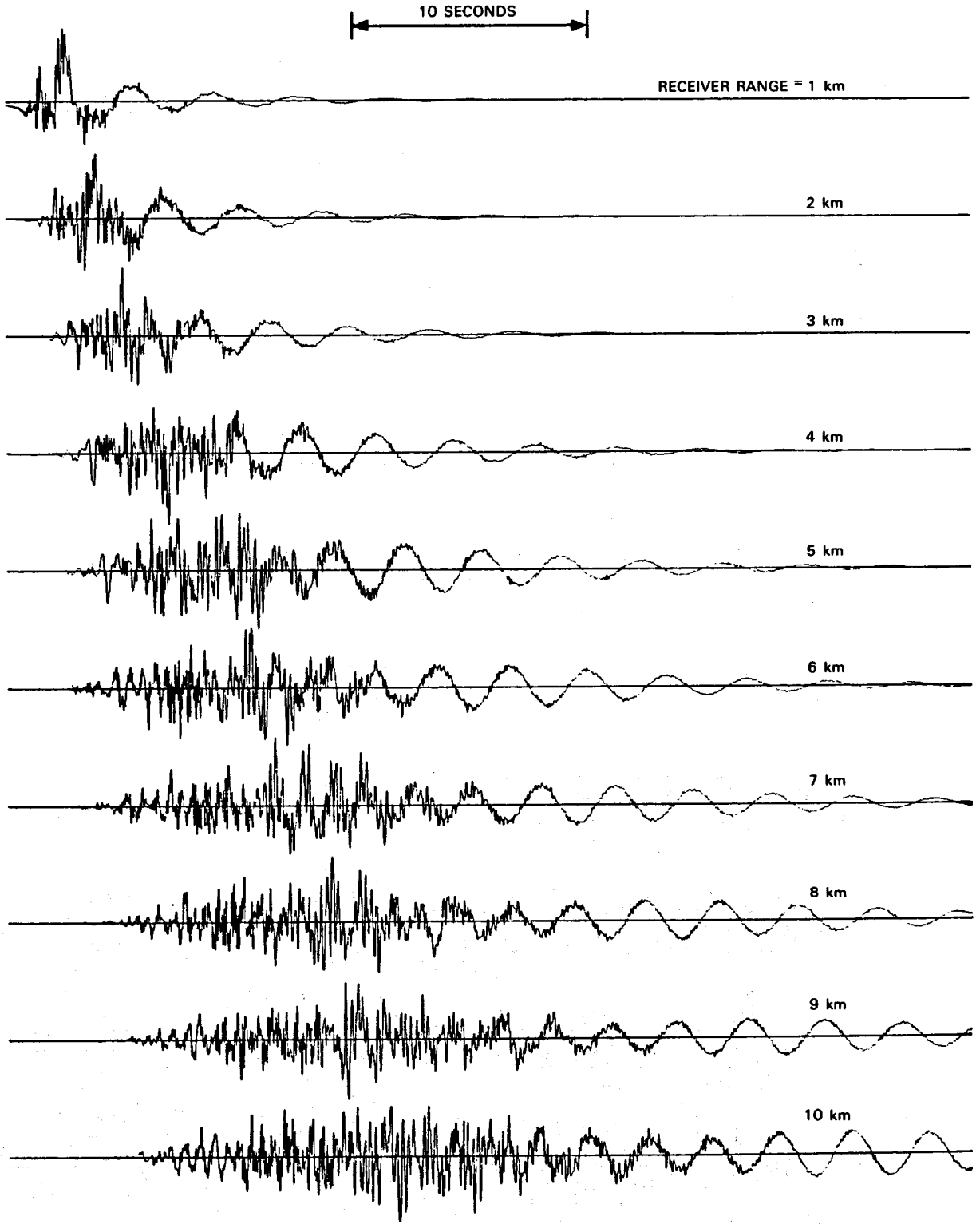

Figure B9. Synthetic seismogram calculated for source dip 45°, source depth 1.0 km.

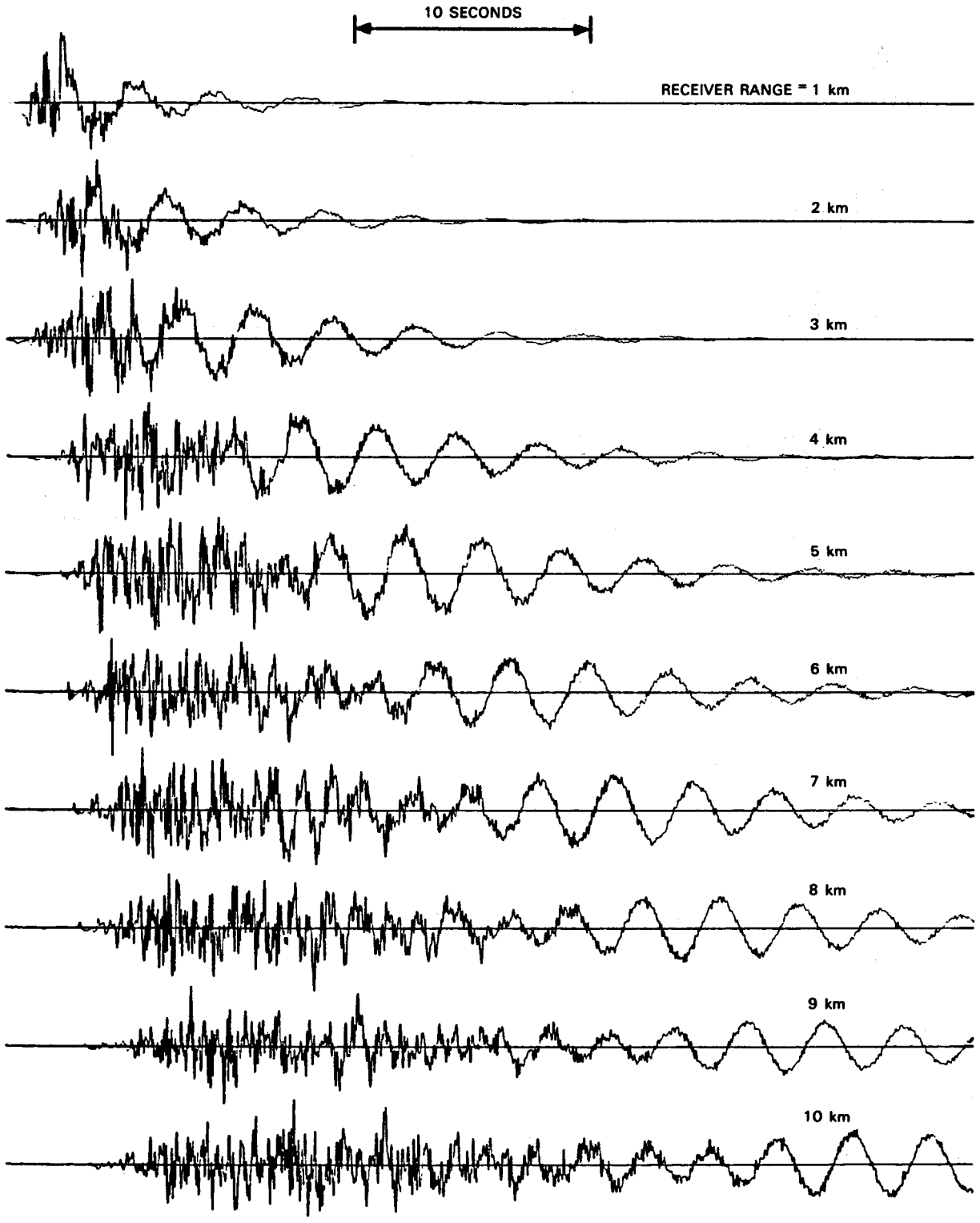

Figure B11. Synthetic seismogram calculated for source dip 45°, source depth 1.3 km.

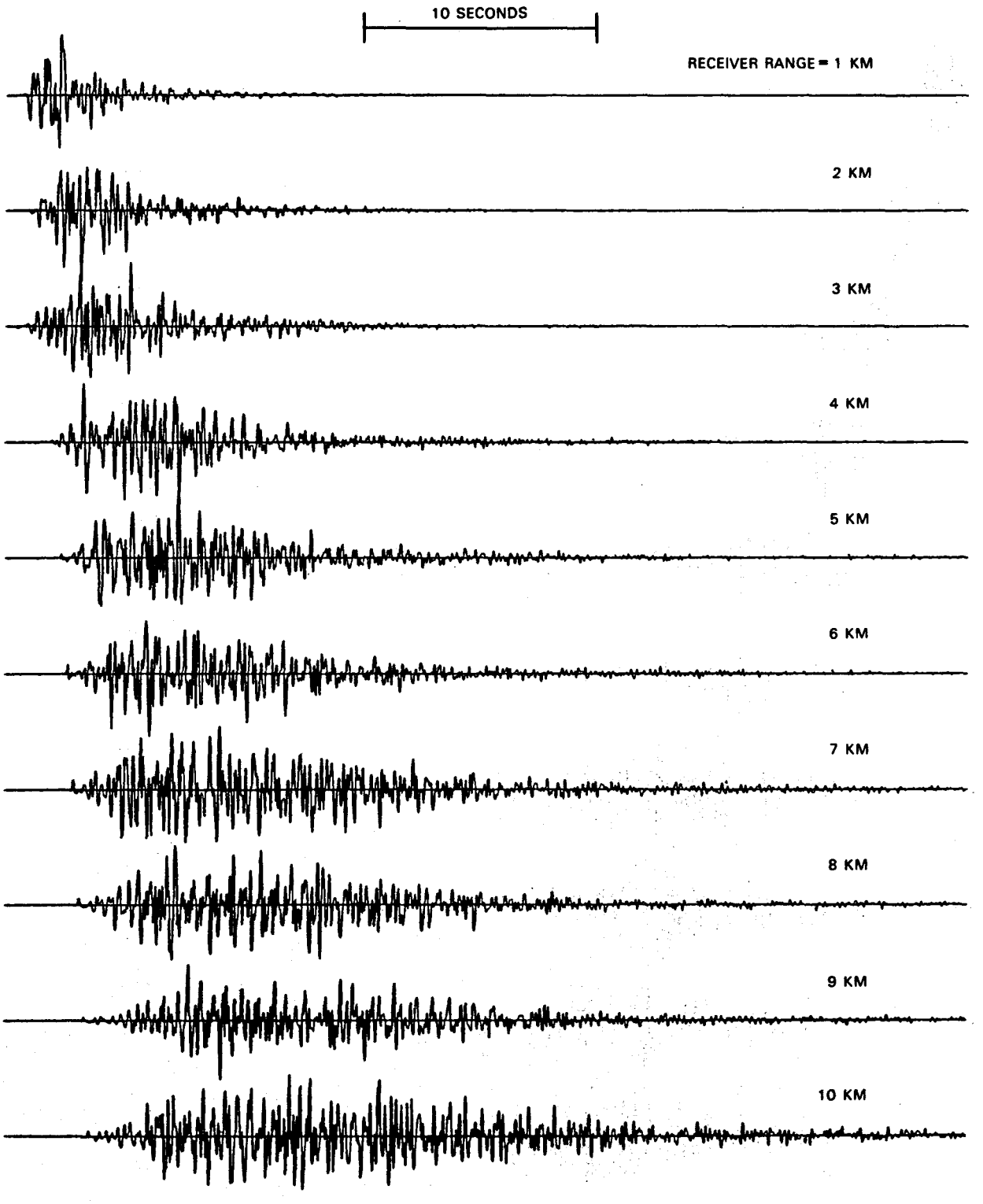

Figure B12. Synthetic seismogram calculated for source dip 45°, source depth 1.3 km, and convolved with instrument transfer function.

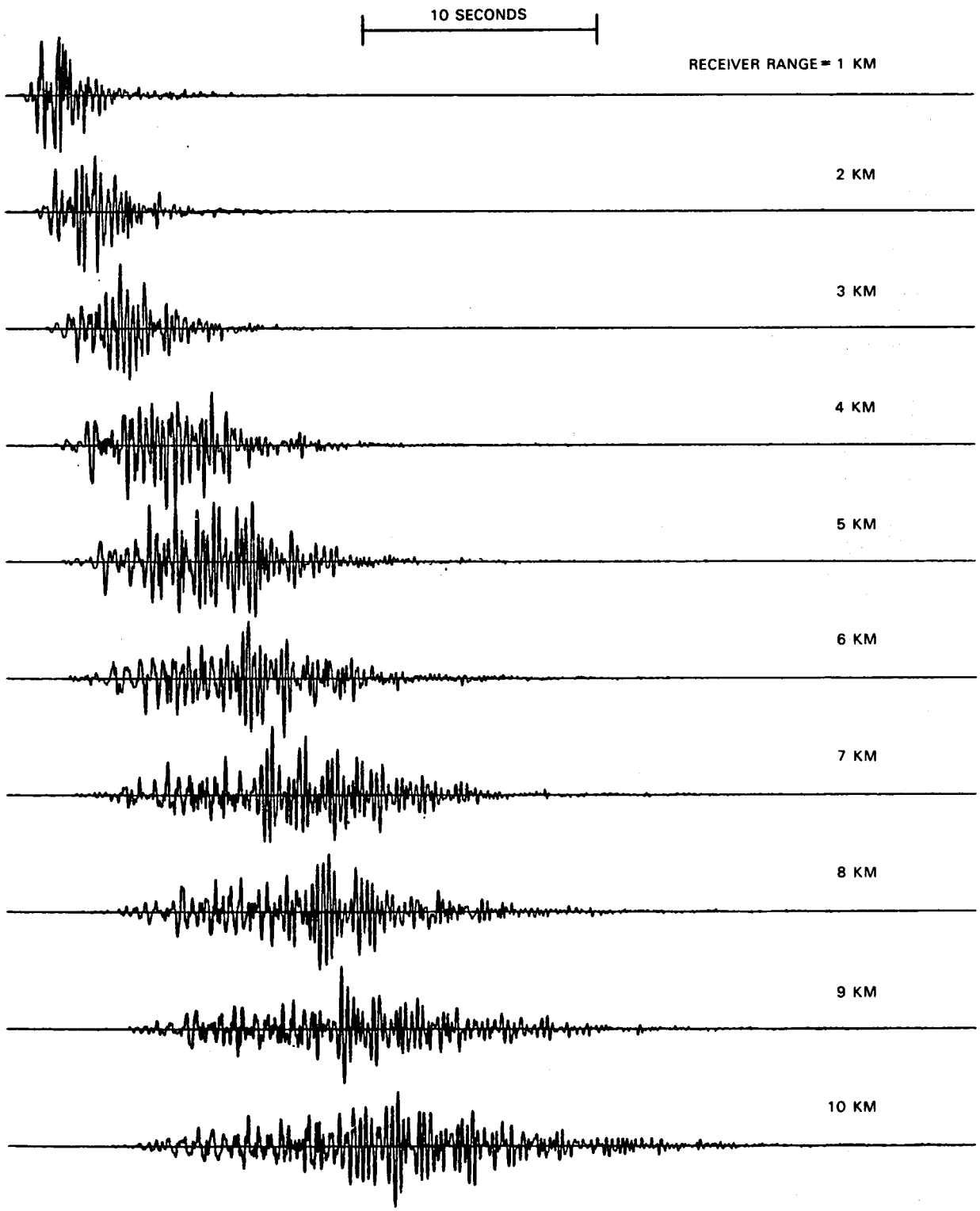

Figure B10. Synthetic seismogram calculated for source dip 45°, source depth 1.0 km, and convolved with instrument transfer function.

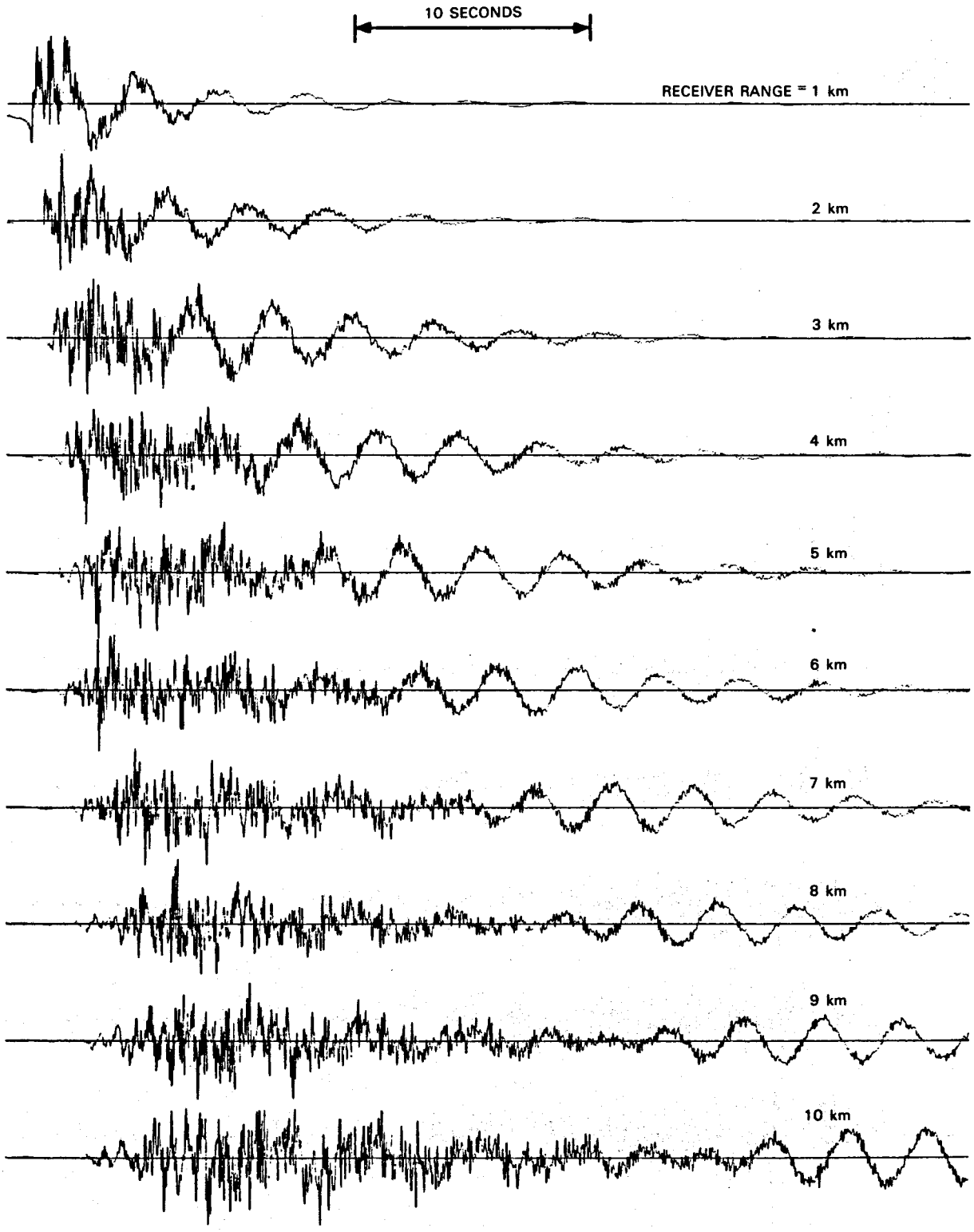

Figure B13. Synthetic seismogram calculated for source dip 45°, source depth 1.8 km.

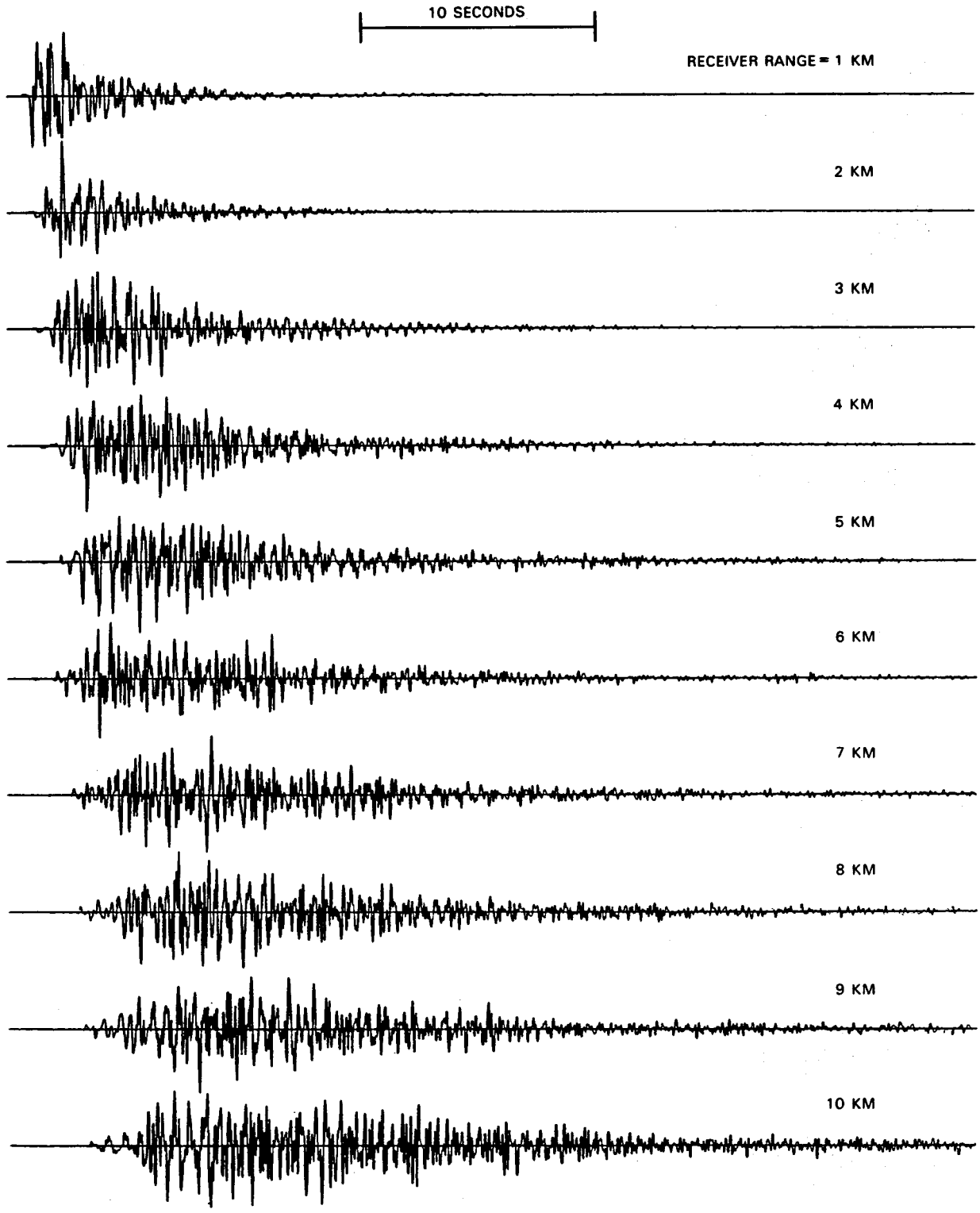

Figure B14. Synthetic seismogram calculated for source dip 45°, source depth 1.8 km, and convolved with instrument transfer function.

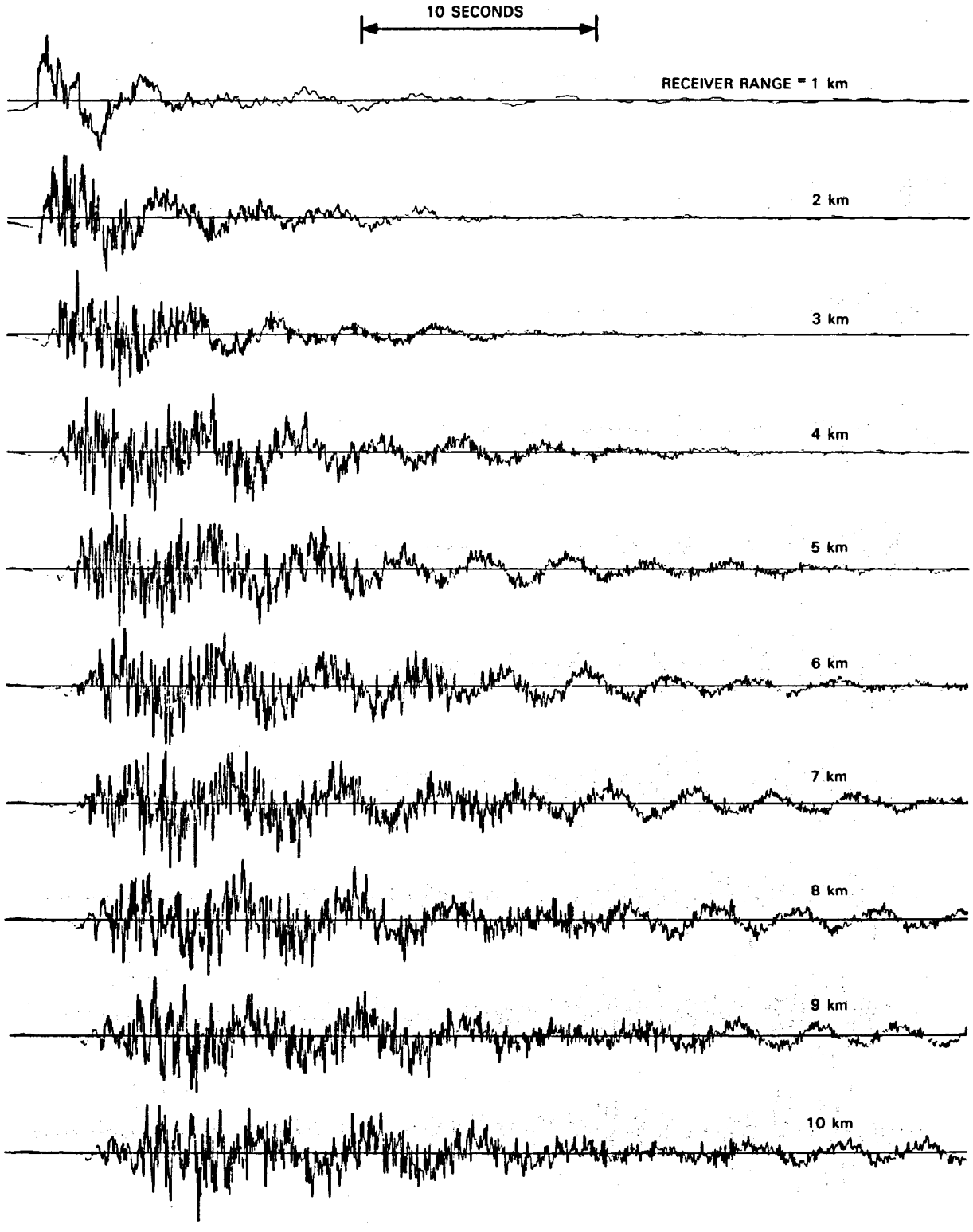

Figure B15. Synthetic seismogram calculated for source dip 45°, source depth 2.8 km.

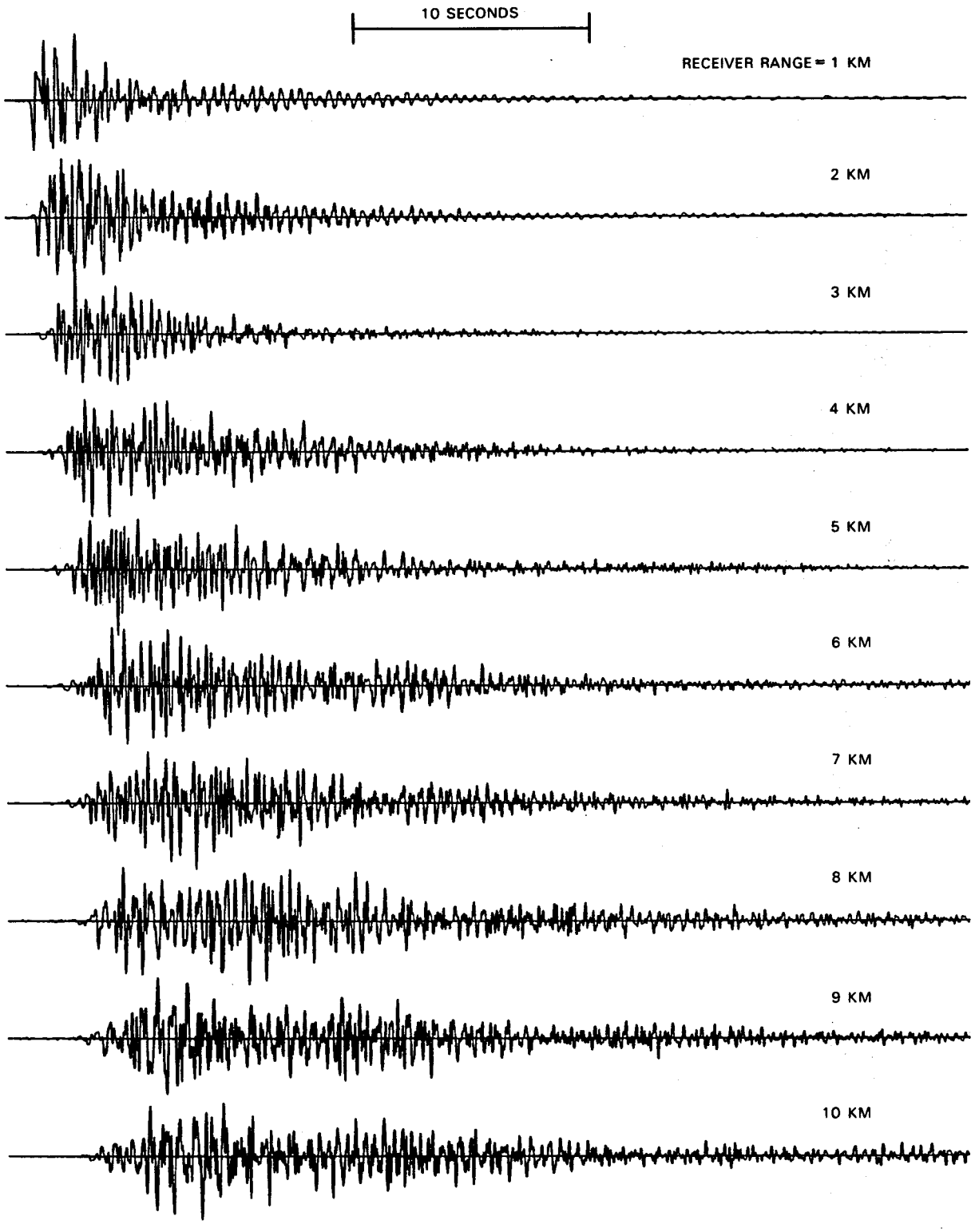

Figure B16. Synthetic seismogram calculated for source dip 45°, source depth 2.8 km, and convolved with instrument transfer function.

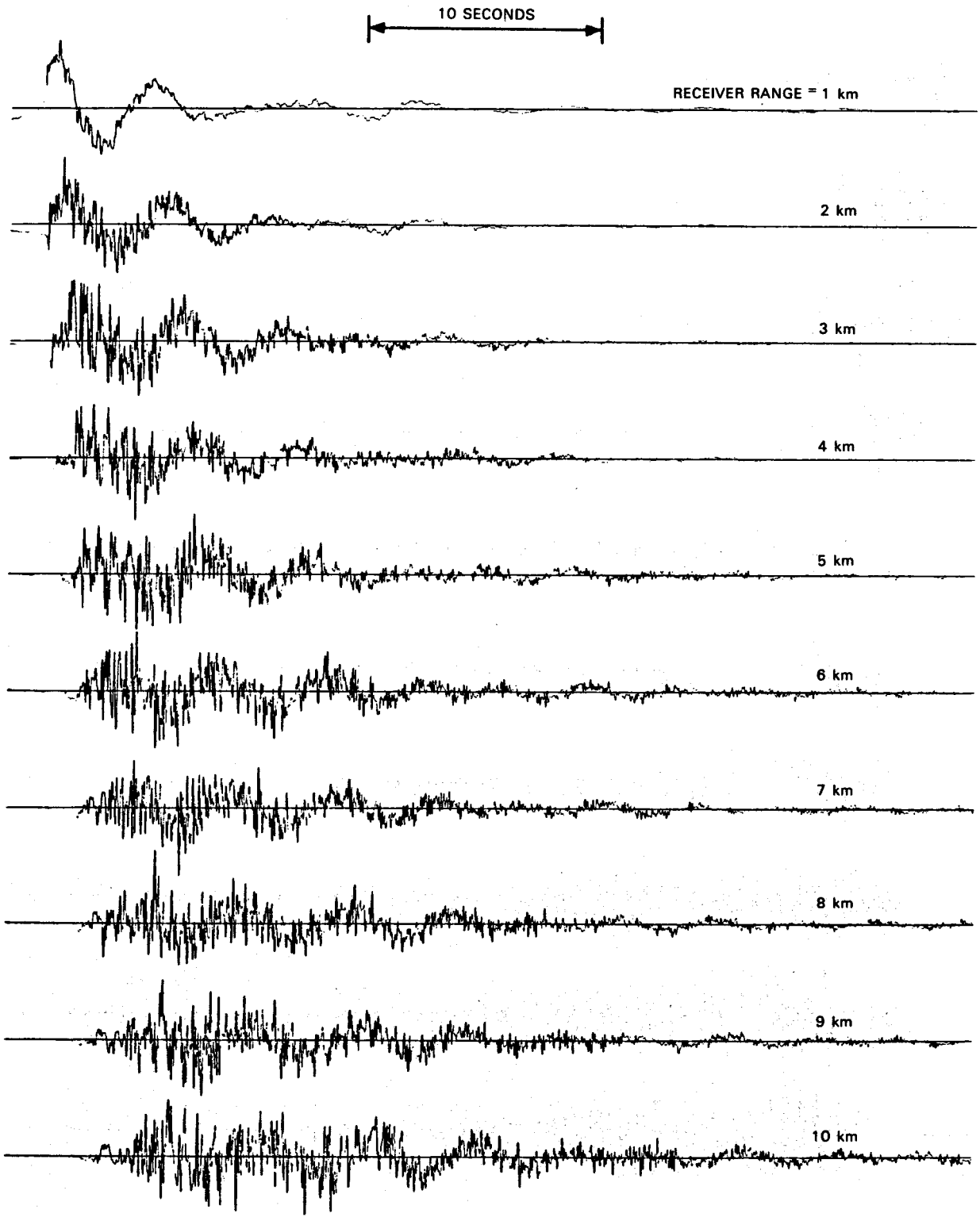

Figure B17. Synthetic seismogram calculated for source dip 45°, source depth 3.8 km.

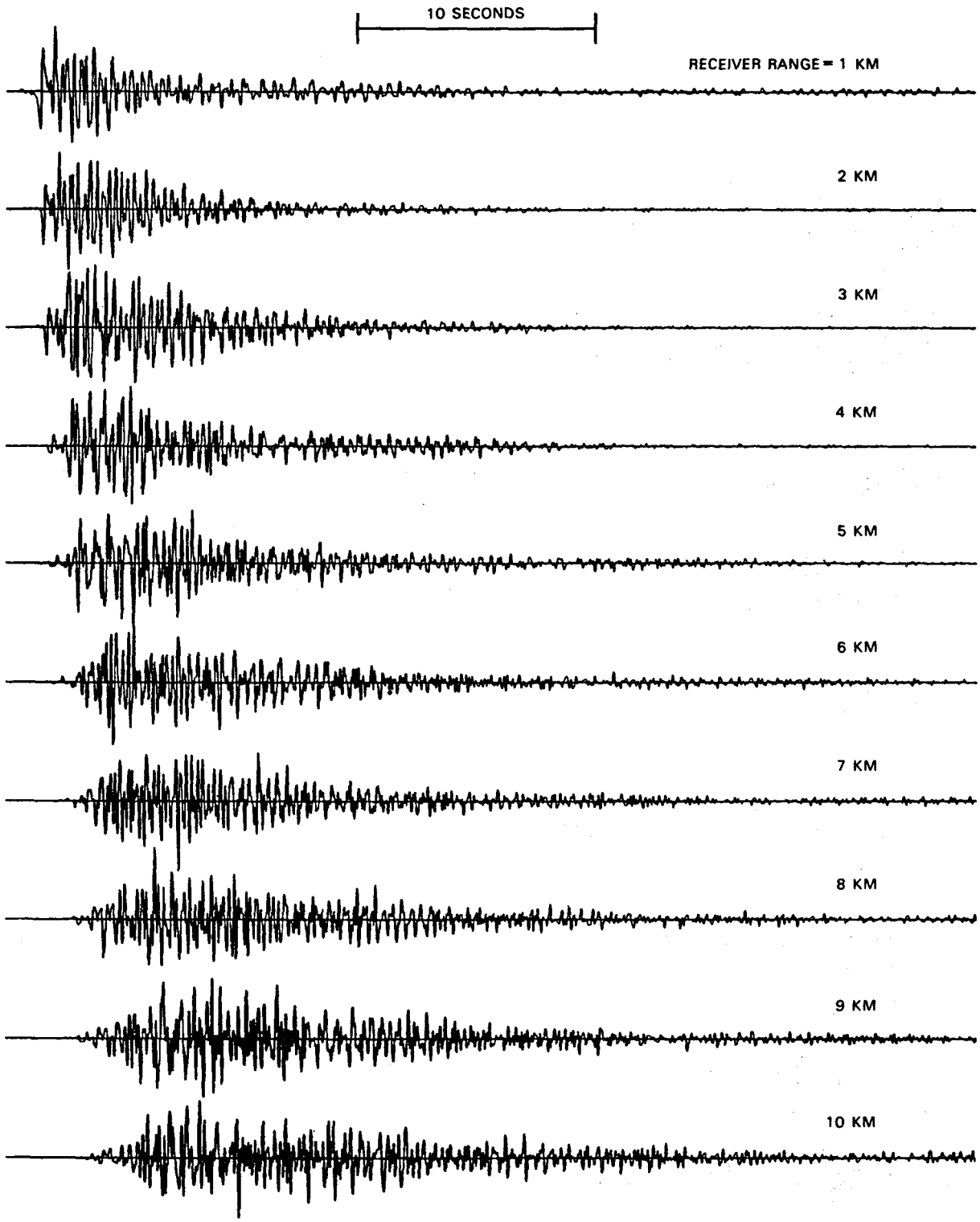

Figure B18. Synthetic seismogram calculated for source dip 45°, source depth 3.8 km, and convolved with instrument transfer function.

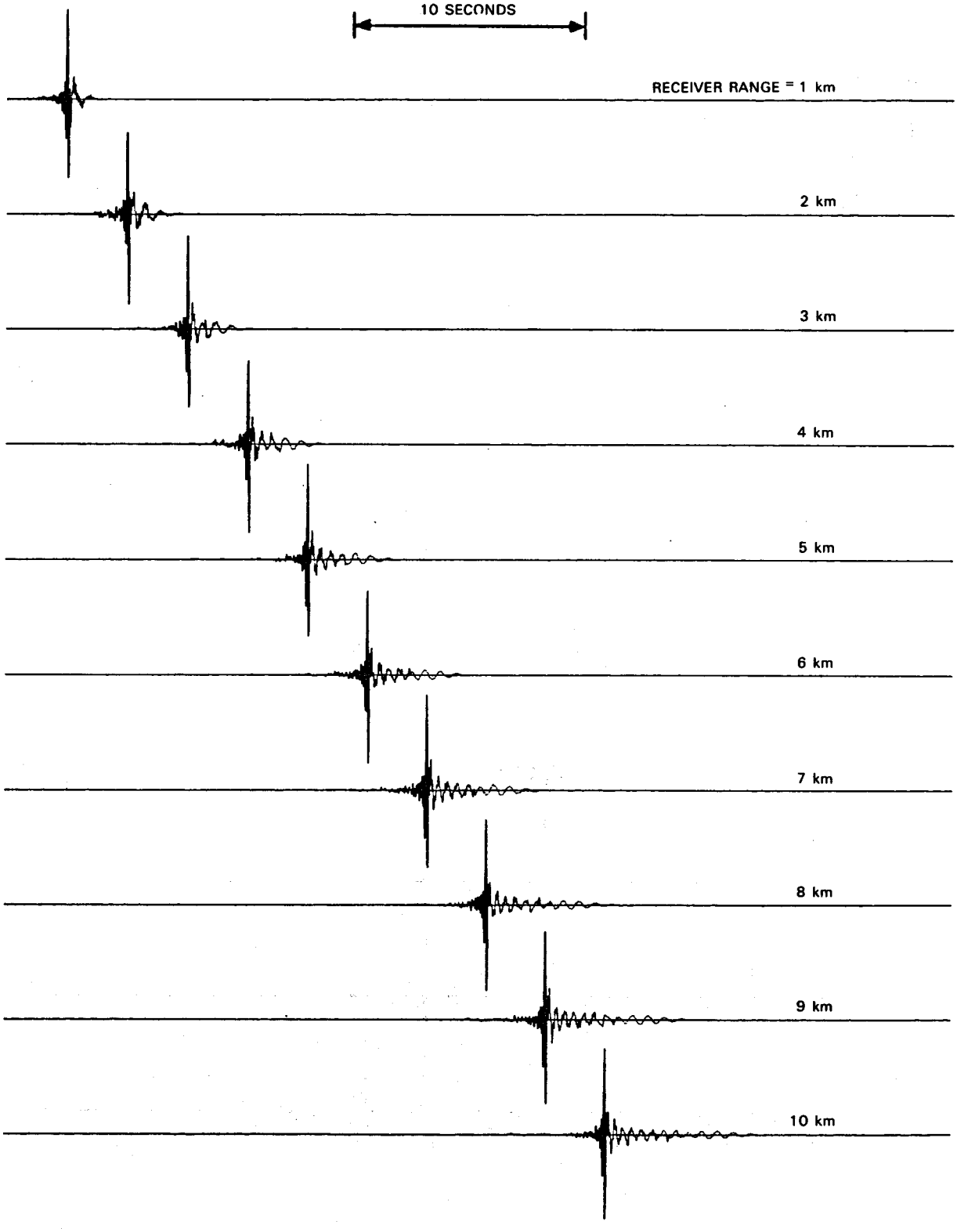

Figure B19. Synthetic seismogram calculated for source dip 90°, source depth 0.0 km.

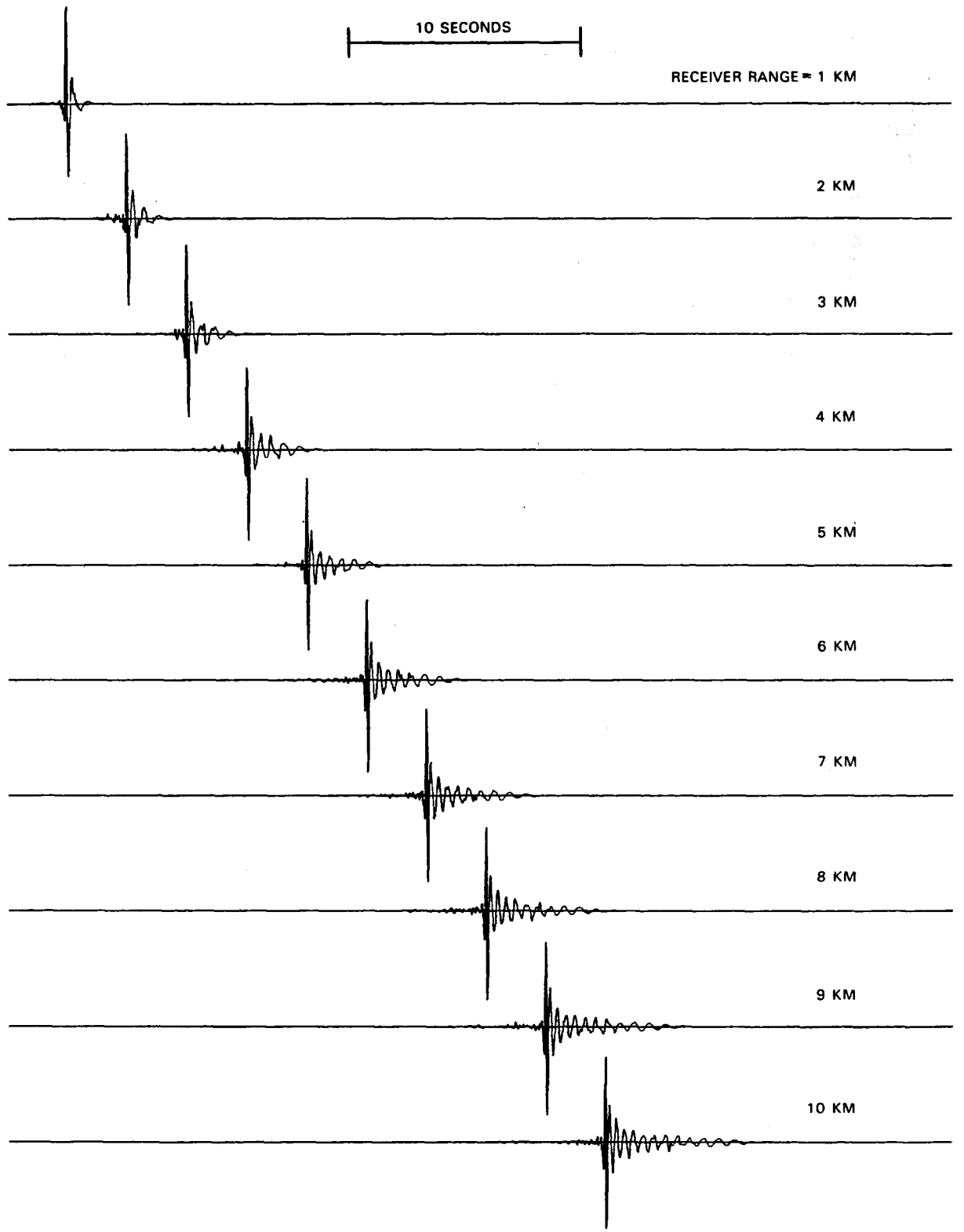

Figure B20. Synthetic seismogram calculated for source dip 90°, source depth 0.0 km, and convolved with instrument transfer function.

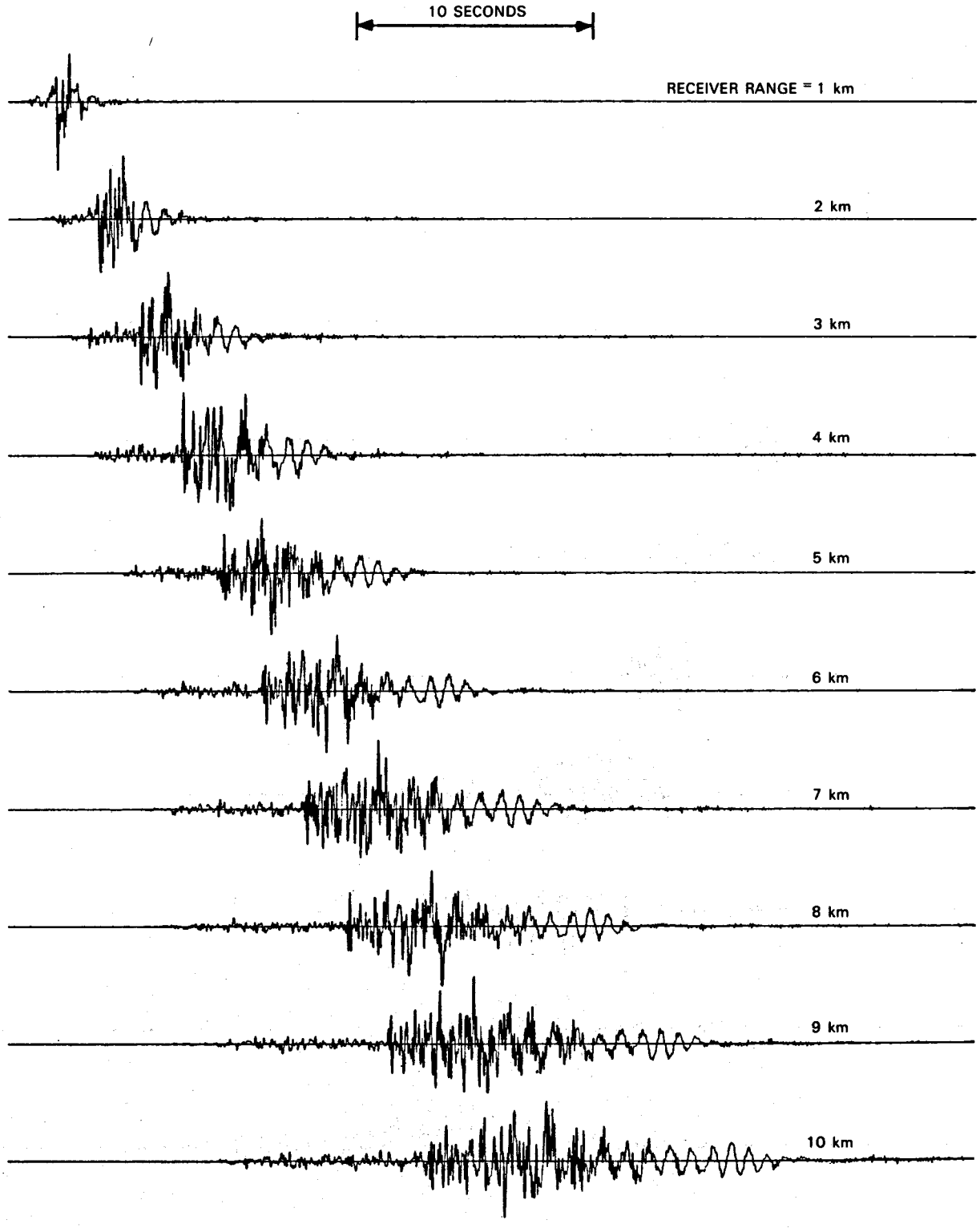

Figure B21. Synthetic seismogram calculated for source dip 90°, source depth 0.3 km.

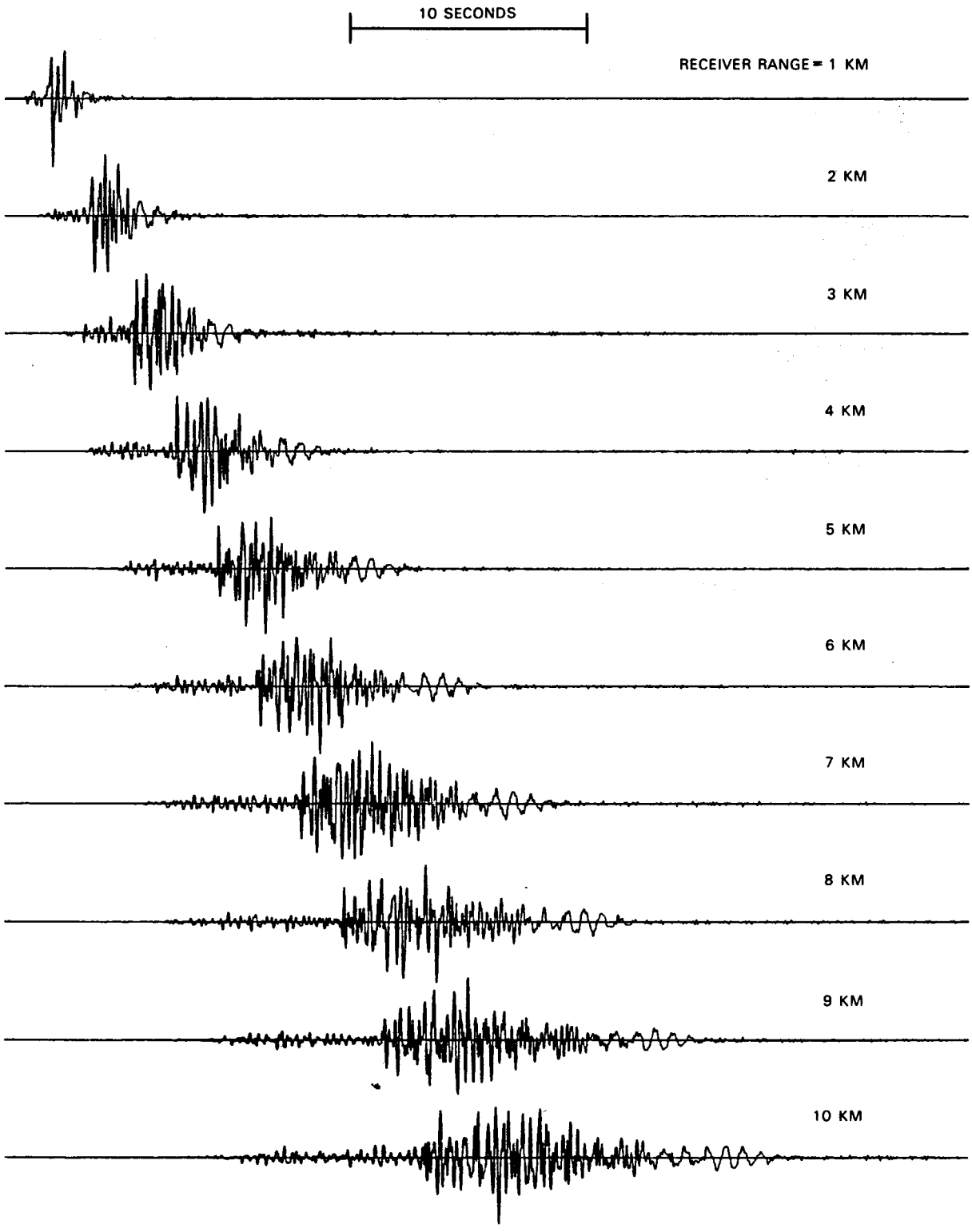

Figure B22. Synthetic seismogram calculated for source dip 90°, source depth 0.3 km, and convolved with instrument transfer function.

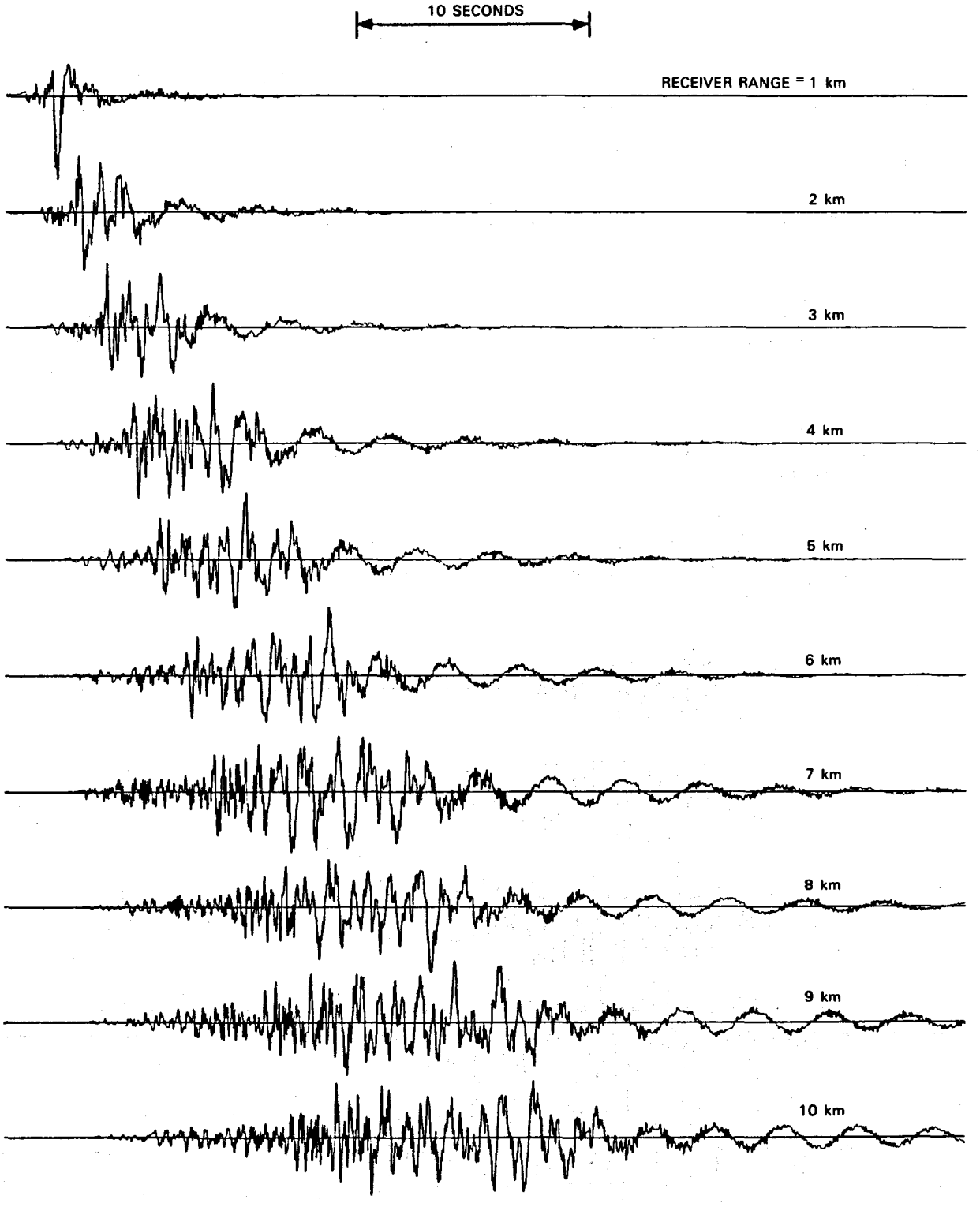

Figure B23. Synthetic seismogram calculated for source dip 90°, source depth 0.8 km.

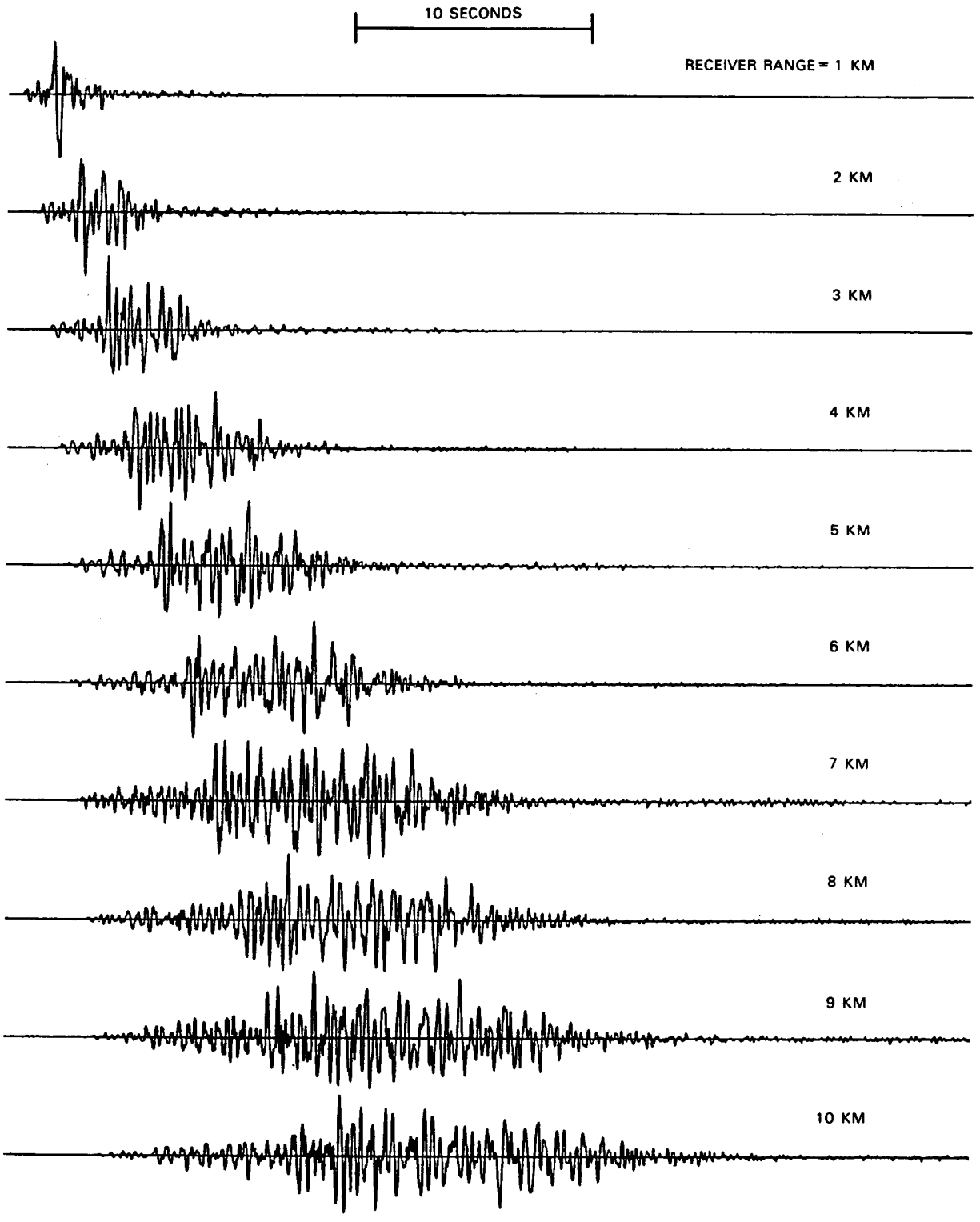

Figure B24. Synthetic seismogram calculated for source dip 90°, source depth 0.8 km, and convolved with instrument transfer function.

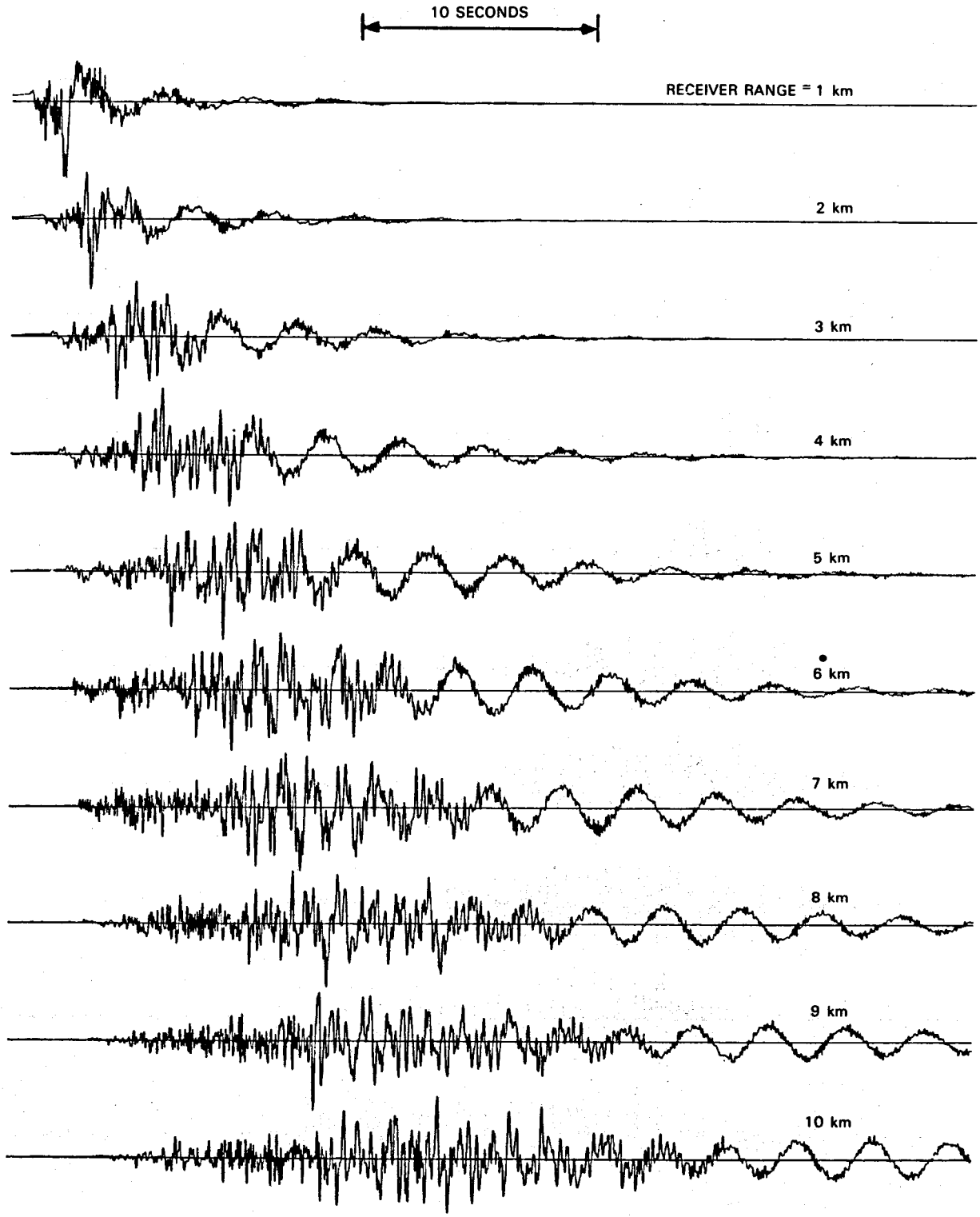

Figure B25. Synthetic seismogram calculated for source dip 90°, source depth 1.0 km.

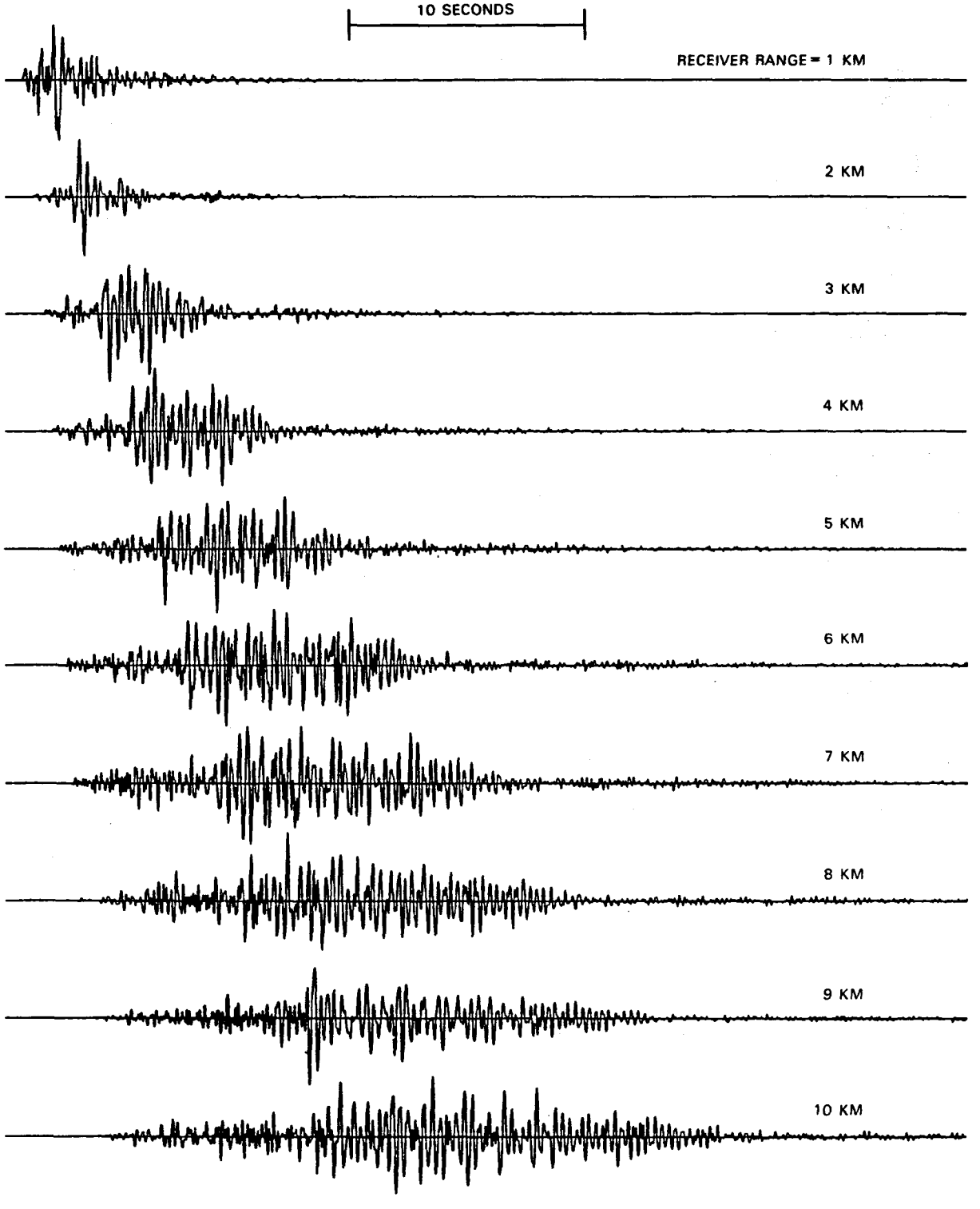

Figure B26. Synthetic seismogram calculated for source dip 90°, source depth 1.0 km, and convolved with instrument transfer function.

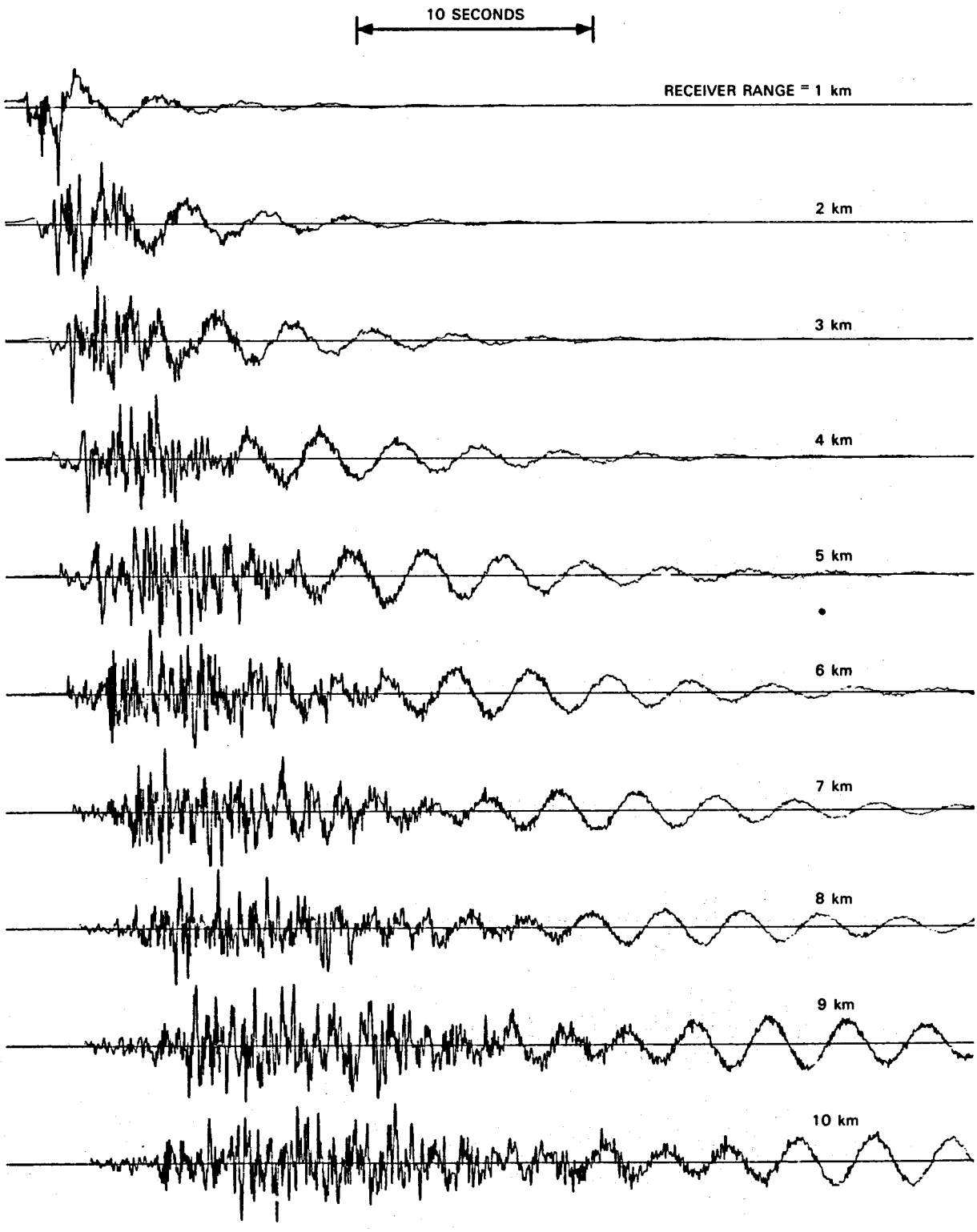

Figure B27. Synthetic seismogram calculated for source dip 90°, source depth 1.3 km.

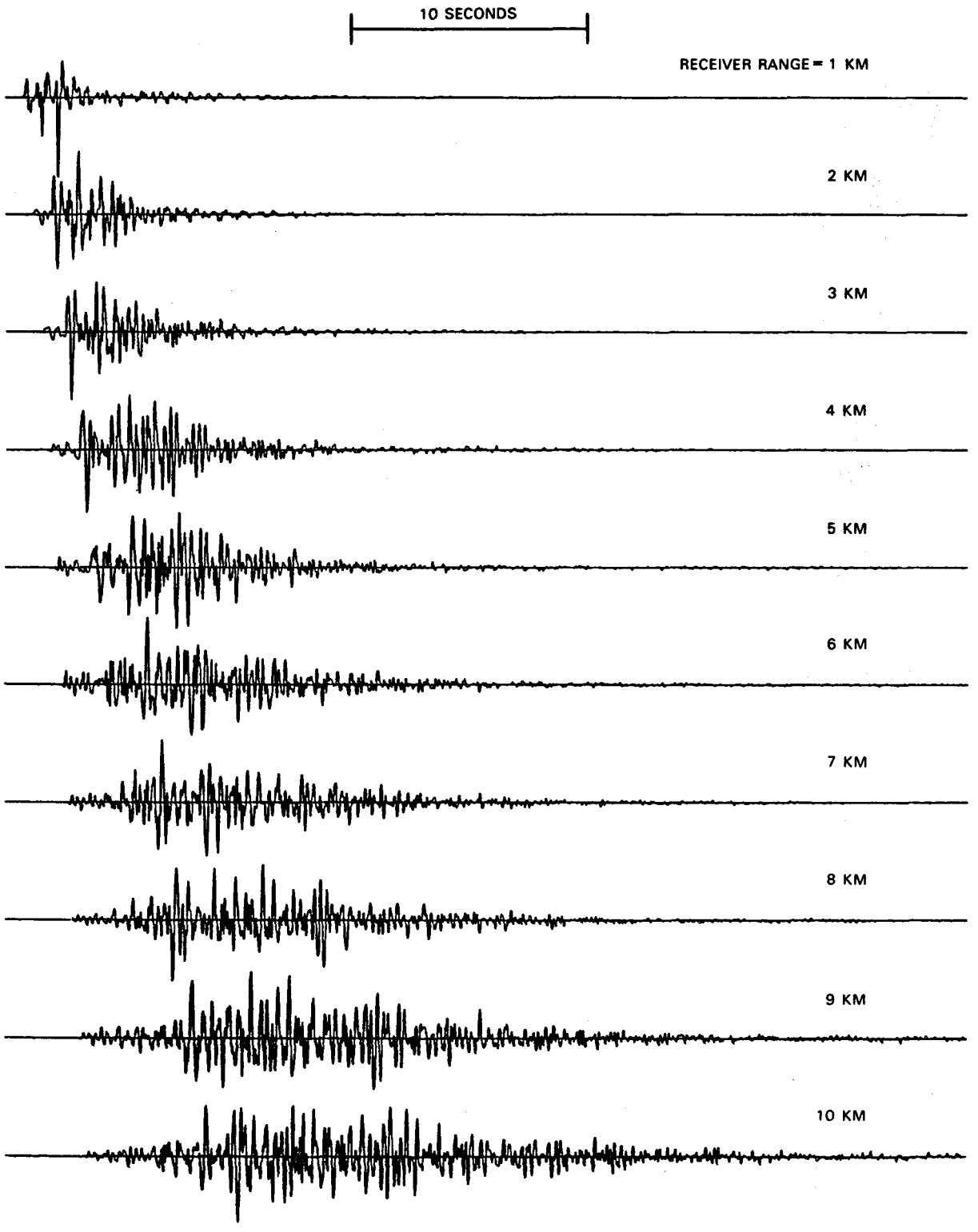

Figure B28. Synthetic seismogram calculated for source dip 90°, source depth 1.3 km, and convolved with instrument transfer function.

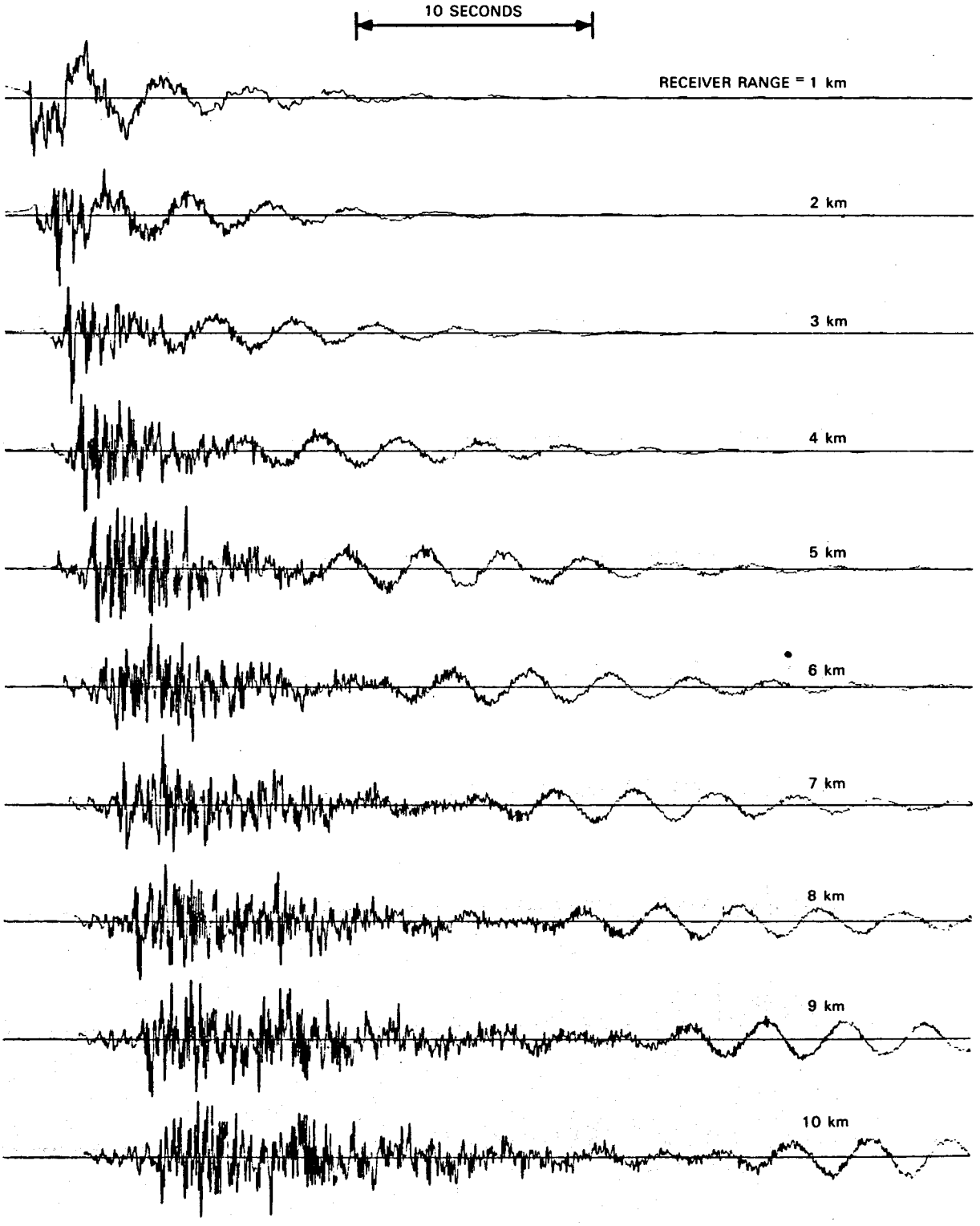

Figure B29. Synthetic seismogram calculated for source dip 90°, source depth 1.8 km.

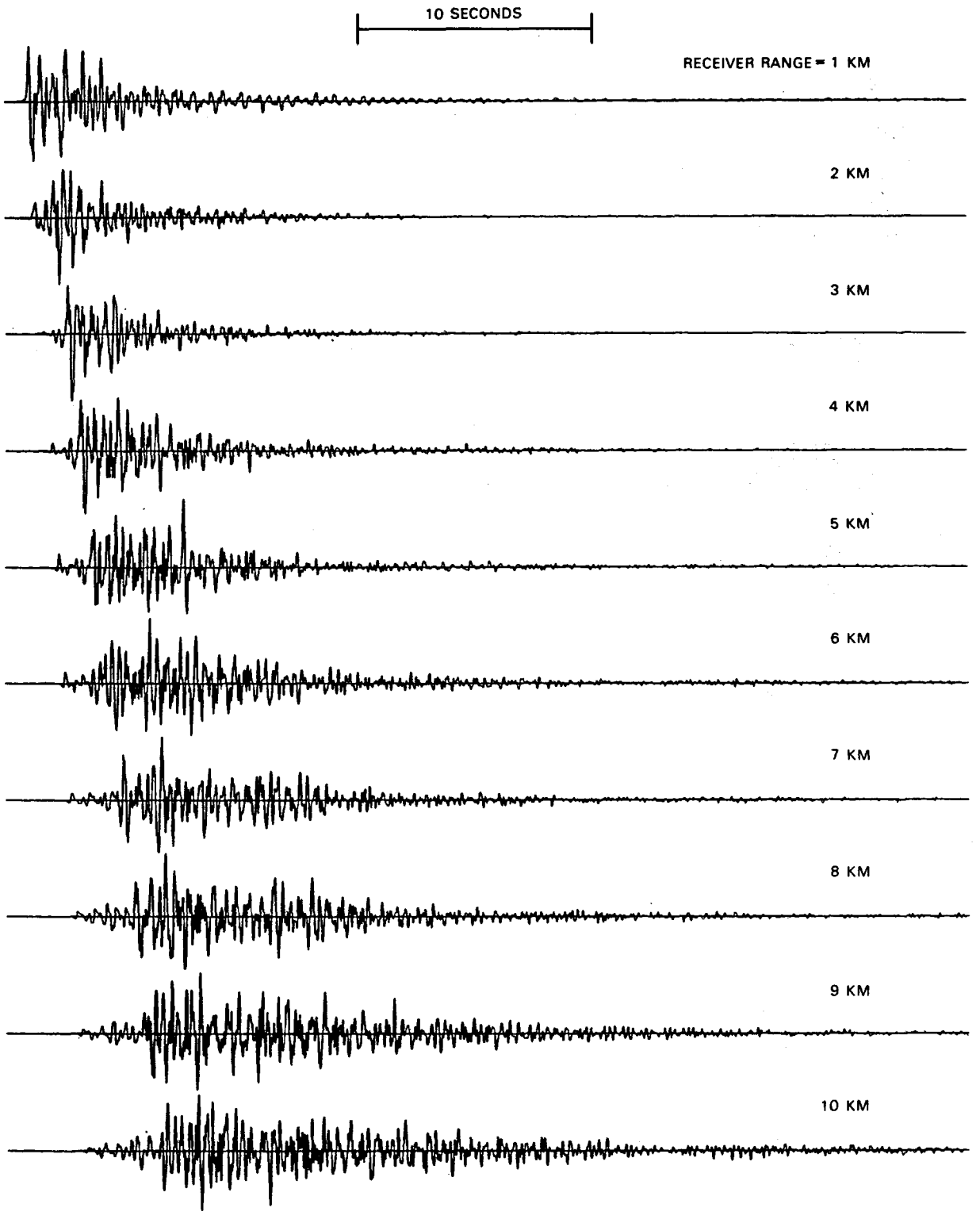

Figure B30. Synthetic seismogram calculated for source dip 90°, source depth 1.8 km, and convolved with instrument transfer function.

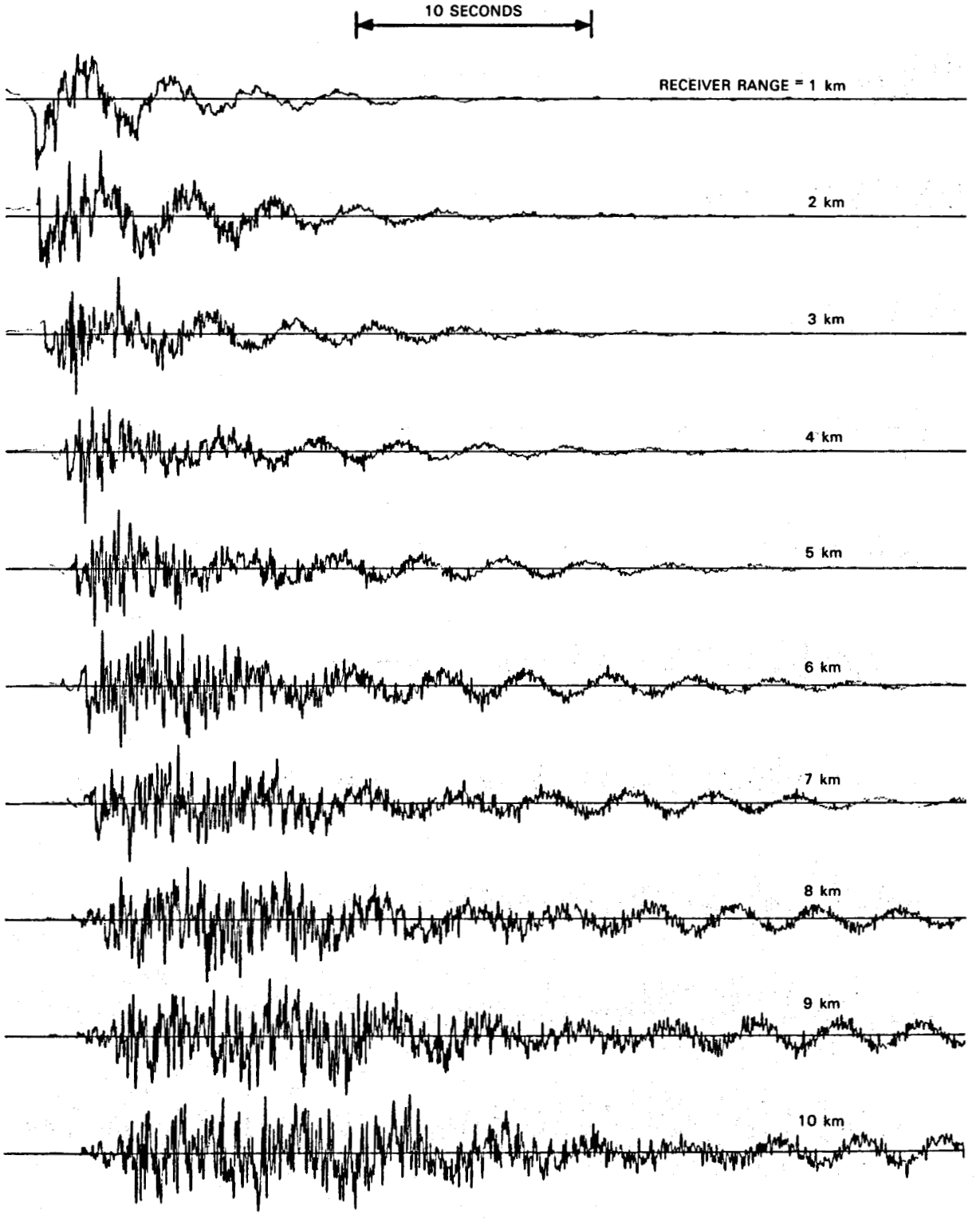

Figure B31. Synthetic seismogram calculated for source dip 90°, source depth 2.8 km.

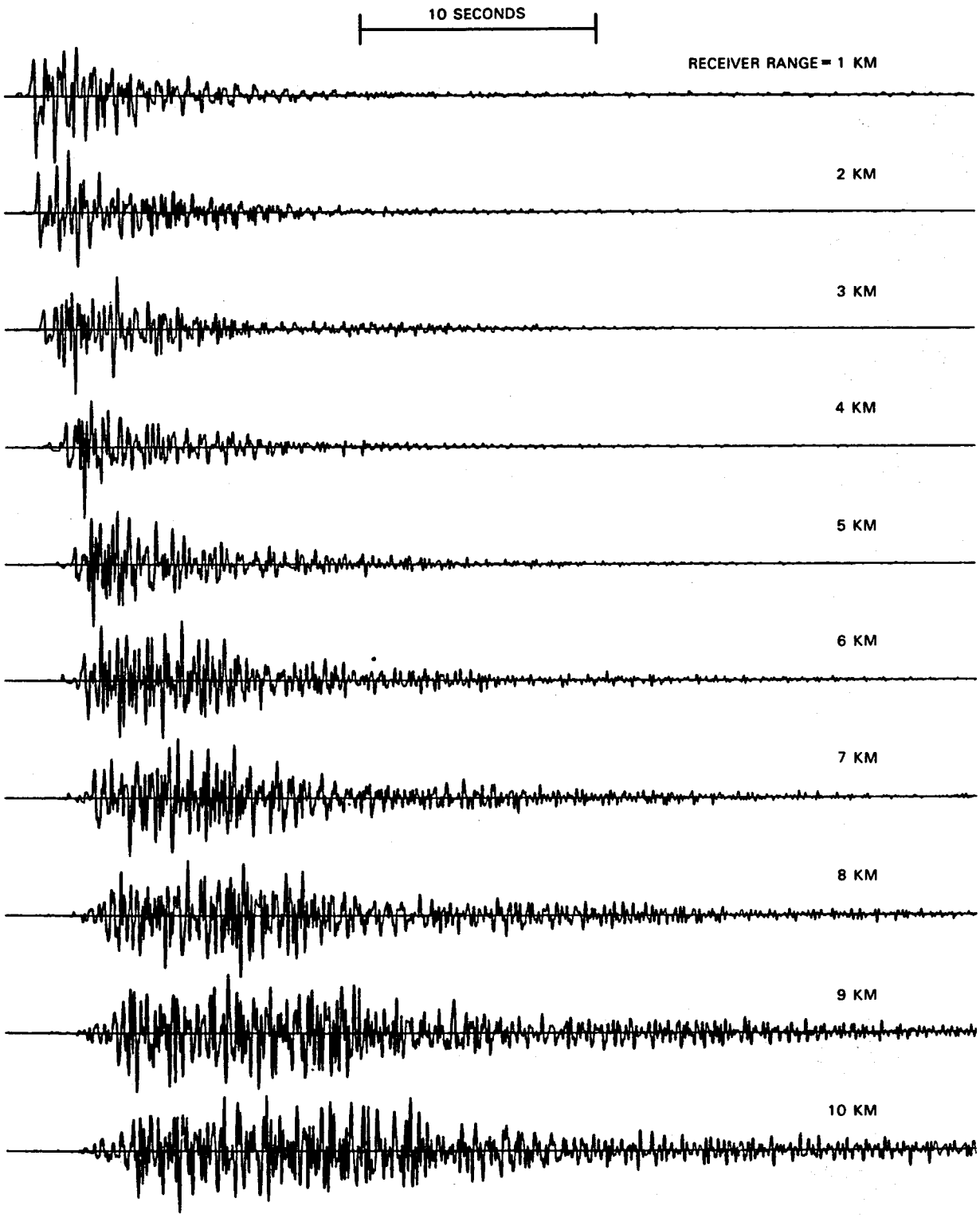

Figure B32. Synthetic seismogram calculated for source dip 90°, source depth 2.8 km, and convolved with instrument transfer function.

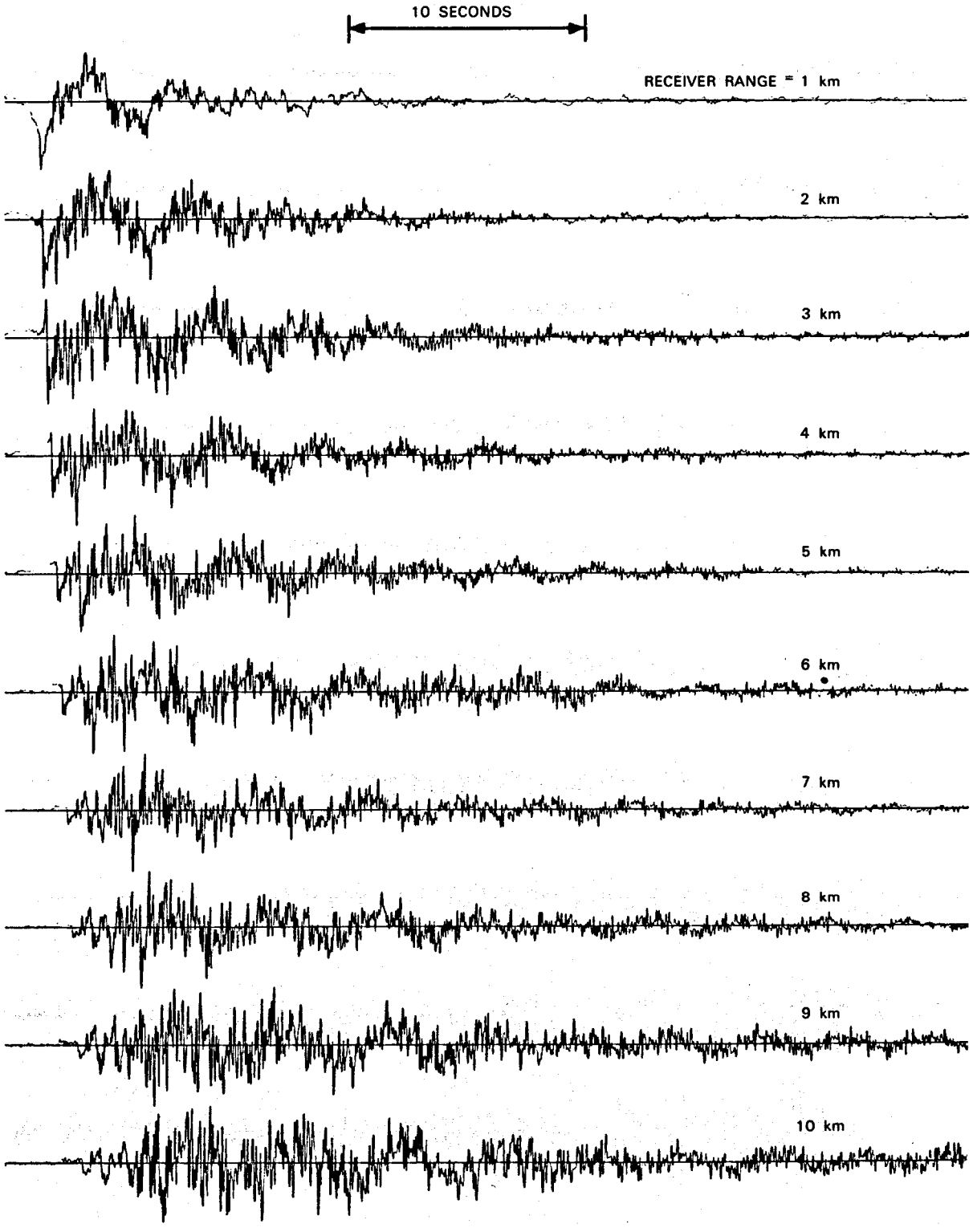

Figure B33. Synthetic seismogram calculated for source dip 90°, source depth 3.8 km.

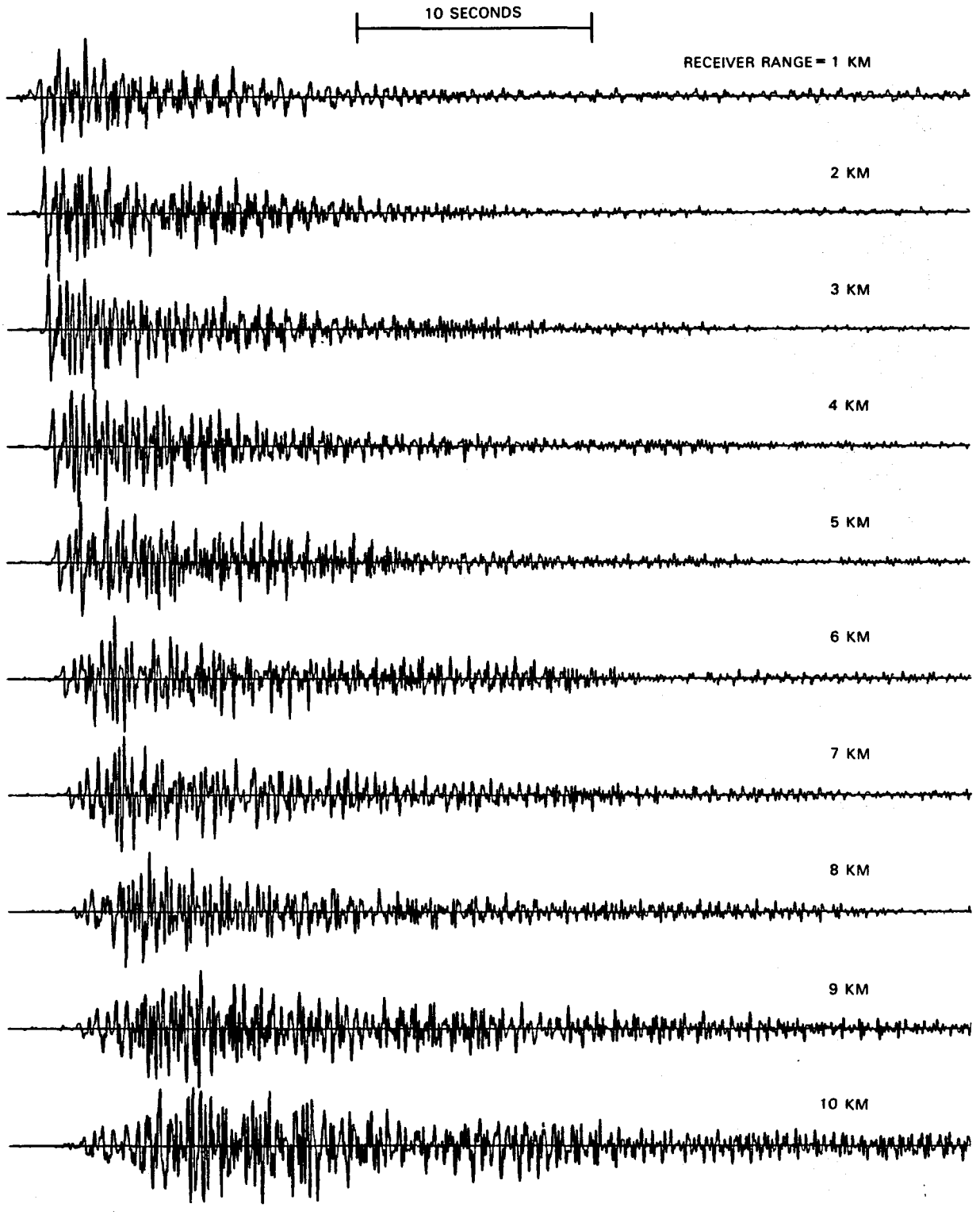

Figure B34. Synthetic seismogram calculated for source dip 90°, source depth 3.8 km, and convolved with instrument transfer function.

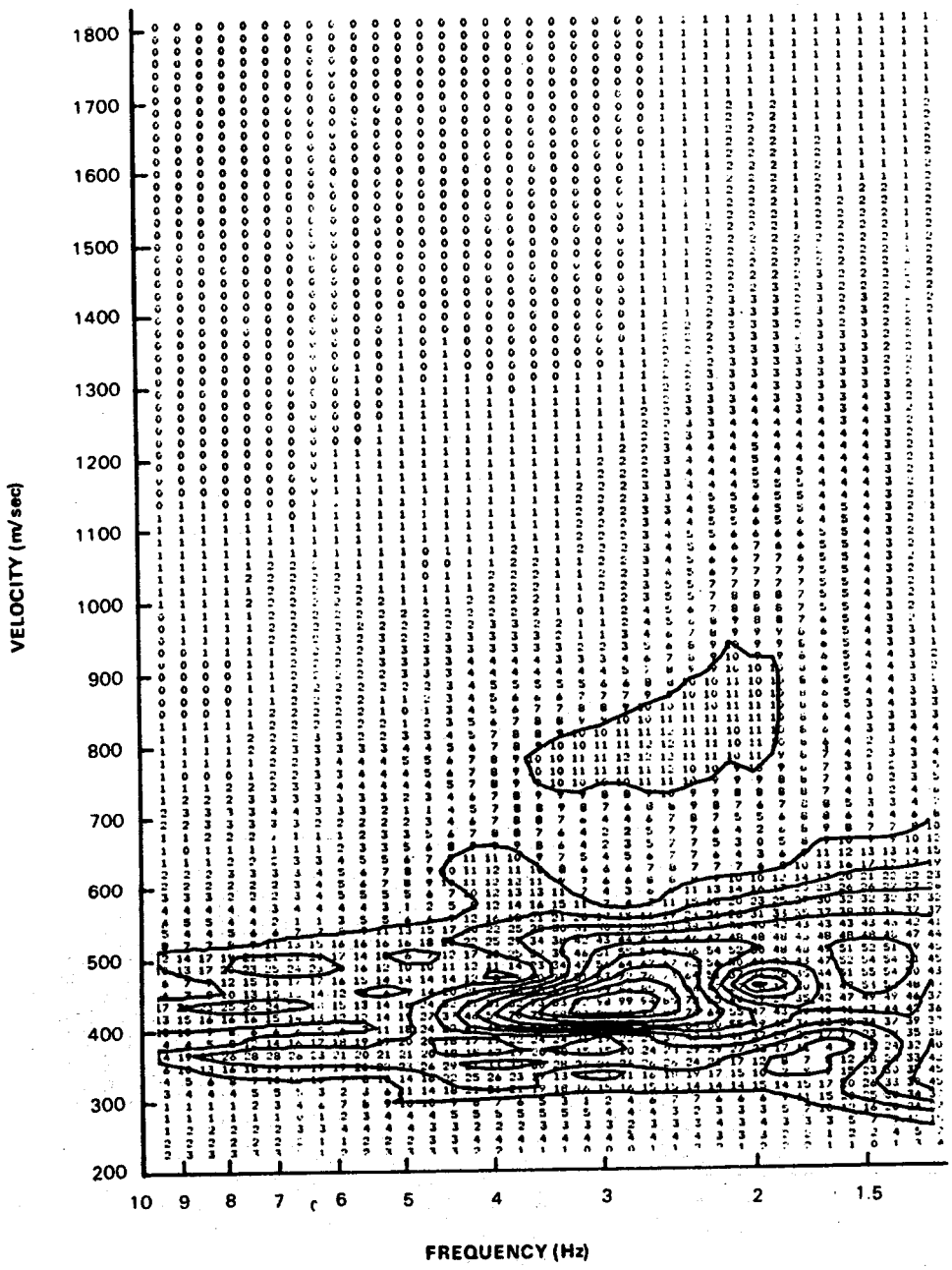

Figure B35. Multiple filter analysis of the synthetic seismogram calculated for source dip 45°, source depth 0.3 km, receiver range 2 km.

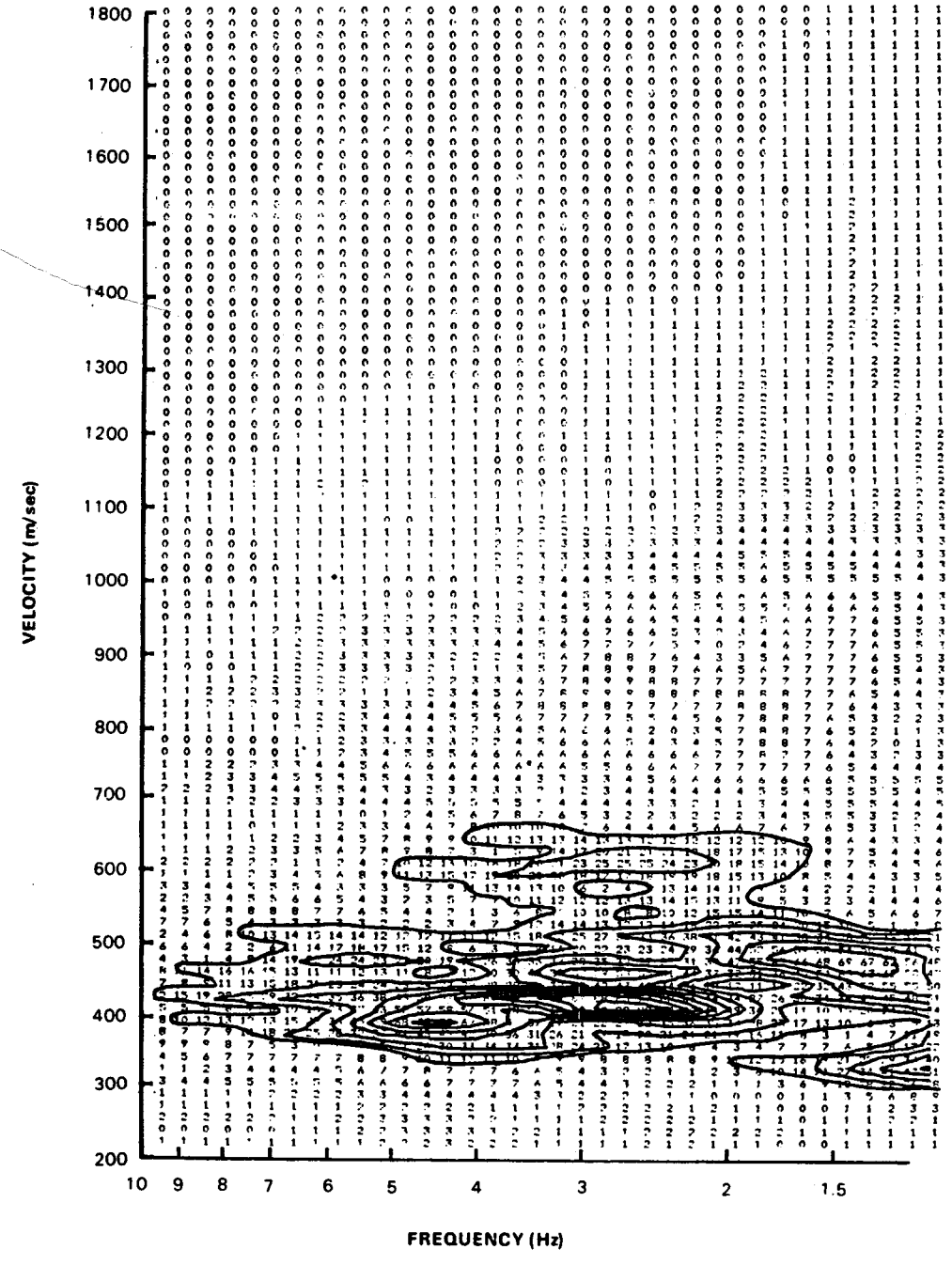

Figure B36. Multiple filter analysis of the synthetic seismogram calculated for source dip 45°, source depth 0.3 km, receiver range 5 km.

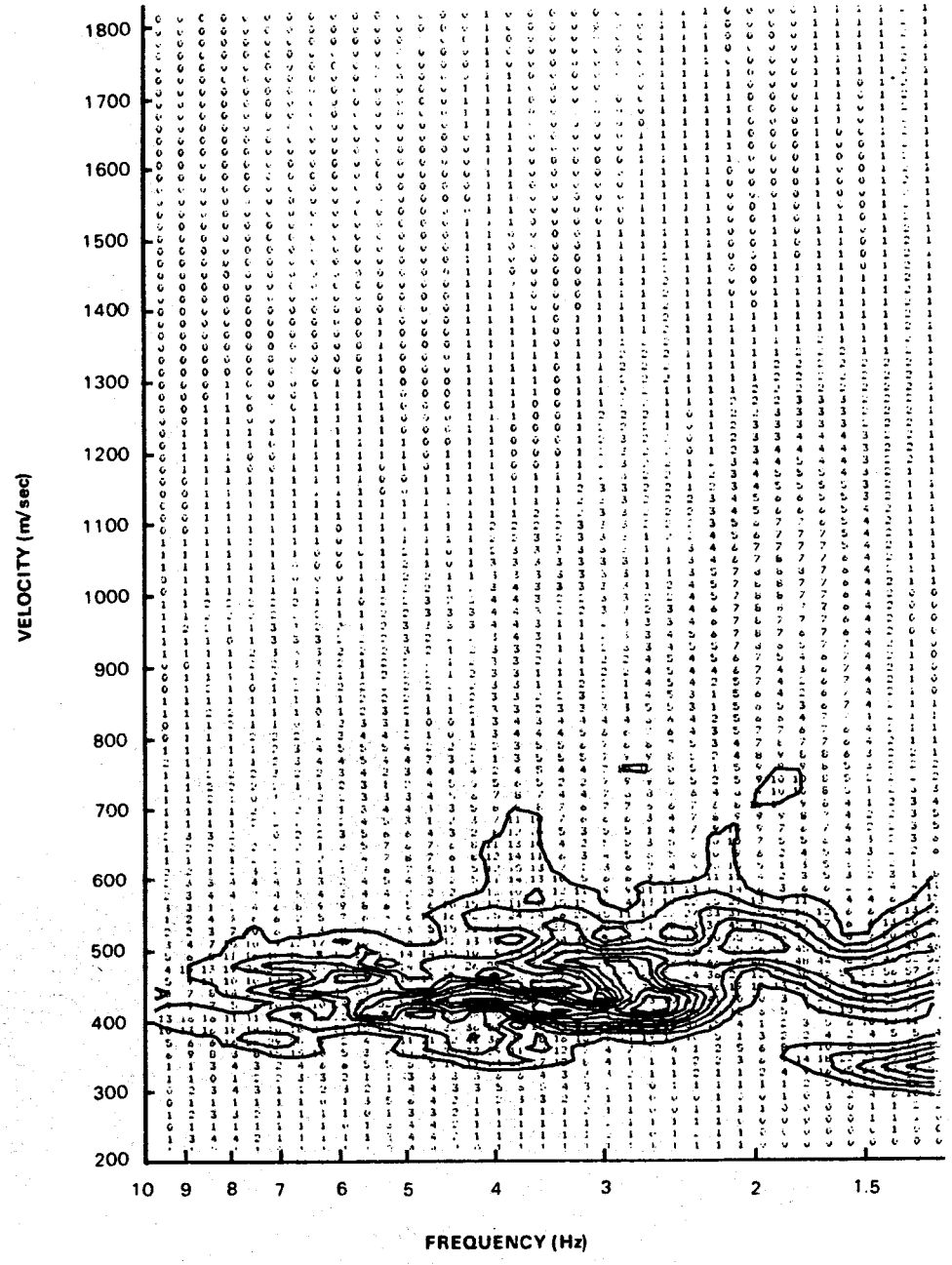

Figure B37. Multiple filter analysis of the synthetic seismogram calculated for source dip 45°, source depth 0.3 km, receiver range 8 km.

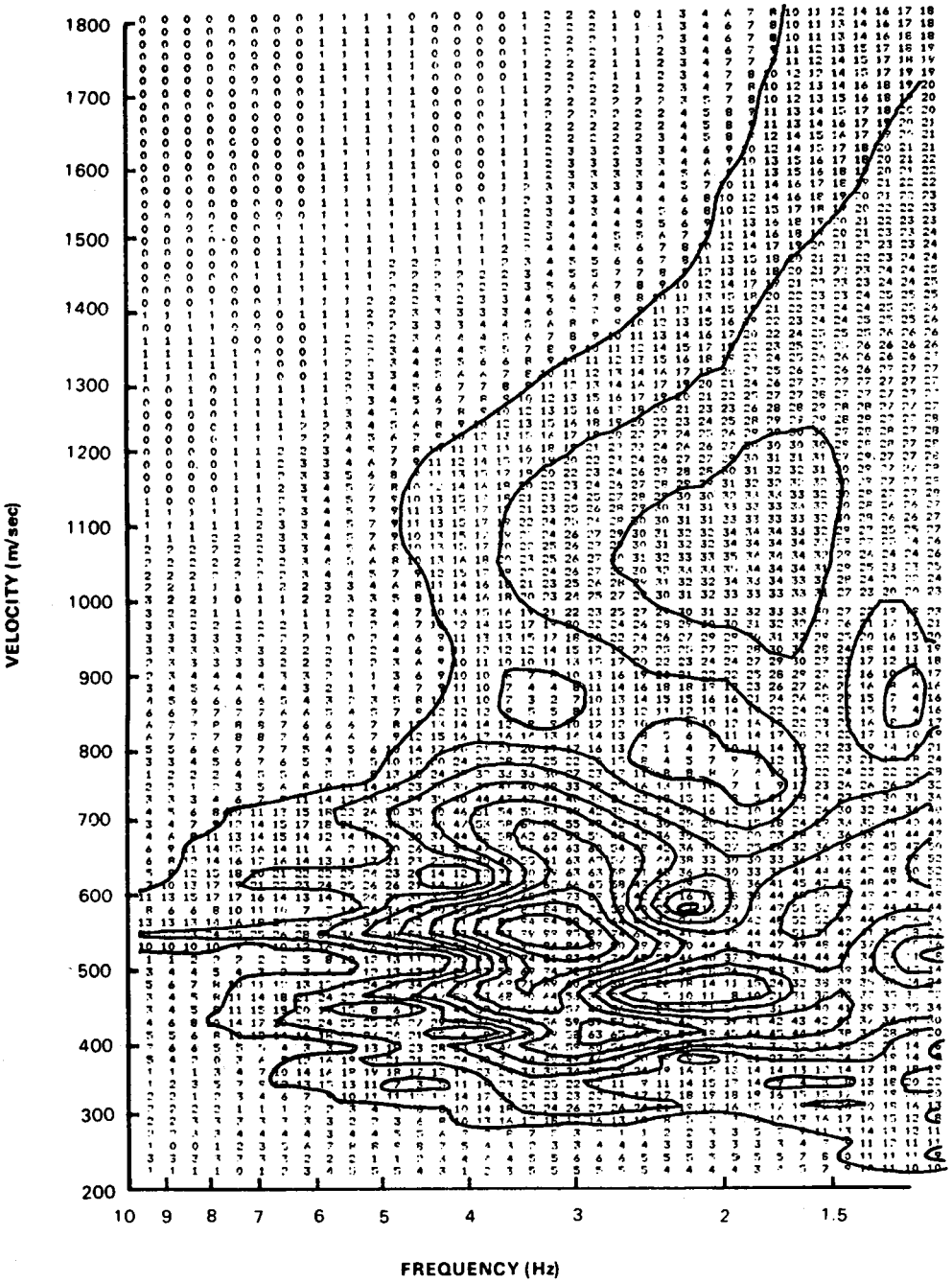

Figure B38. Multiple filter analysis of the synthetic seismogram calculated for source dip 45°, source depth 0.8 km, receiver range 2 km.

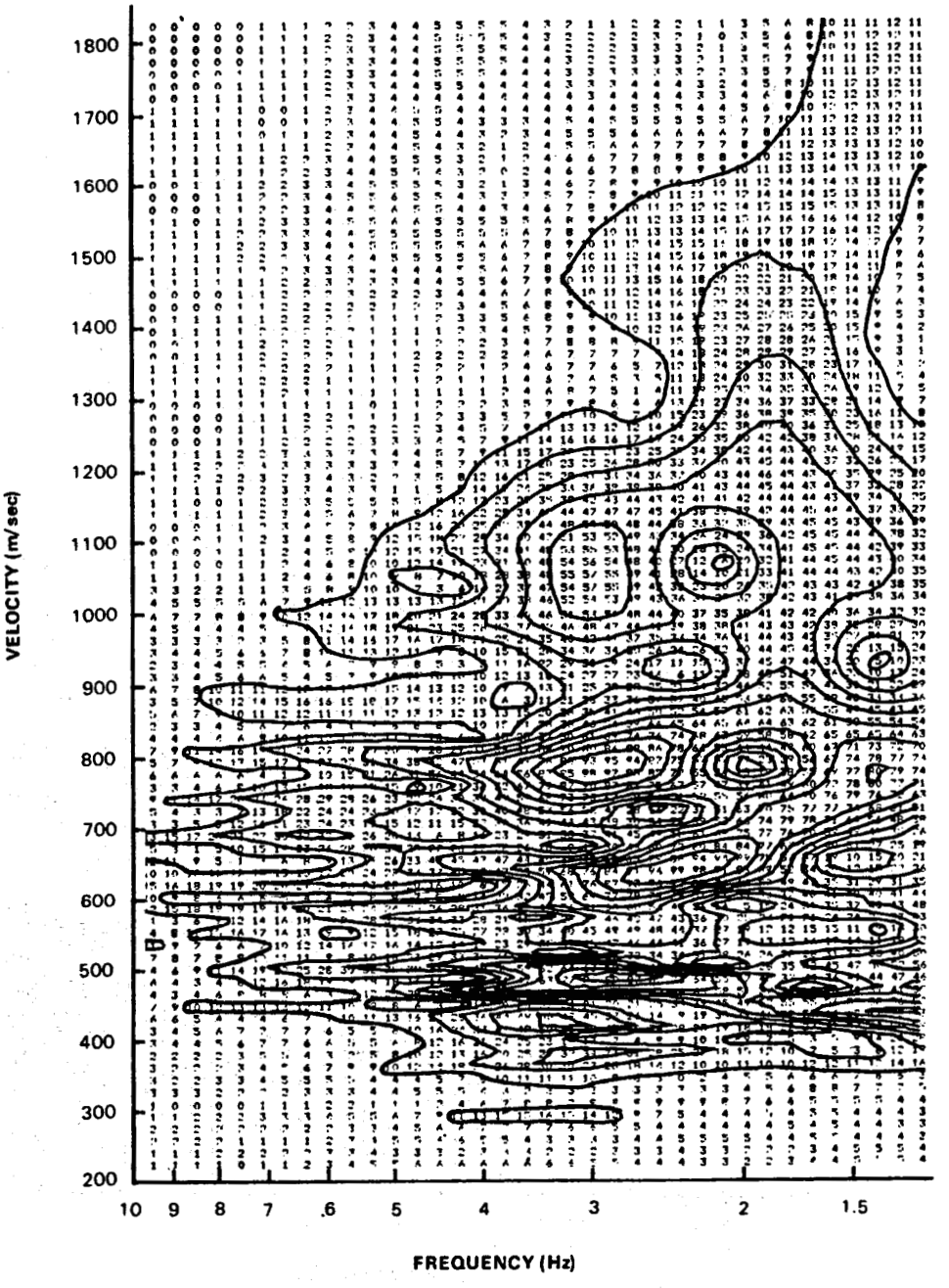

Figure B39. Multiple filter analysis of the synthetic seismogram calculated for source dip 45°, source depth 0.8 km, receiver range 5 km.

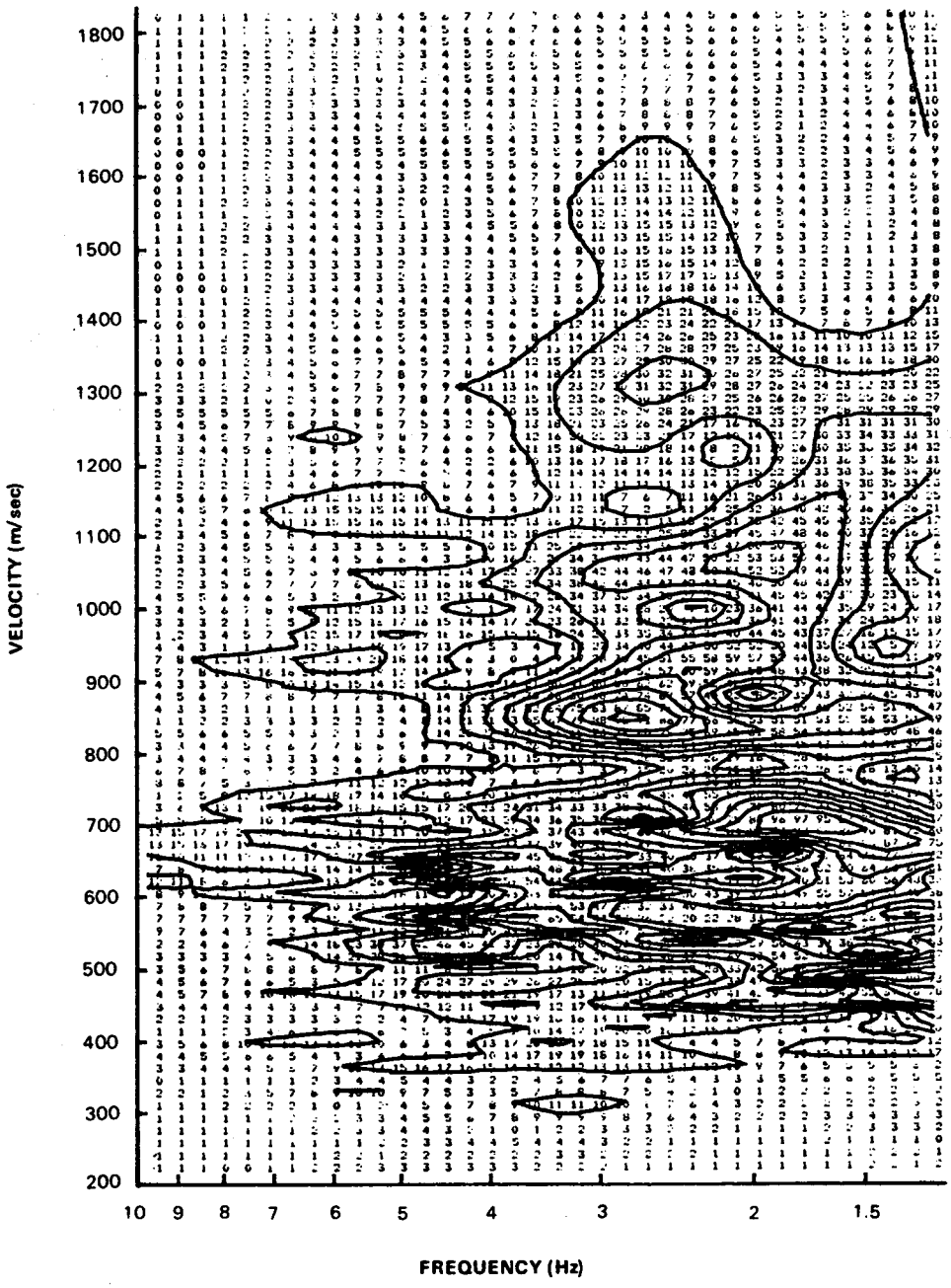

Figure B40. Multiple filter analysis of the synthetic seismogram calculated for source dip 45°, source depth 0.8 km, receiver range 8 km.

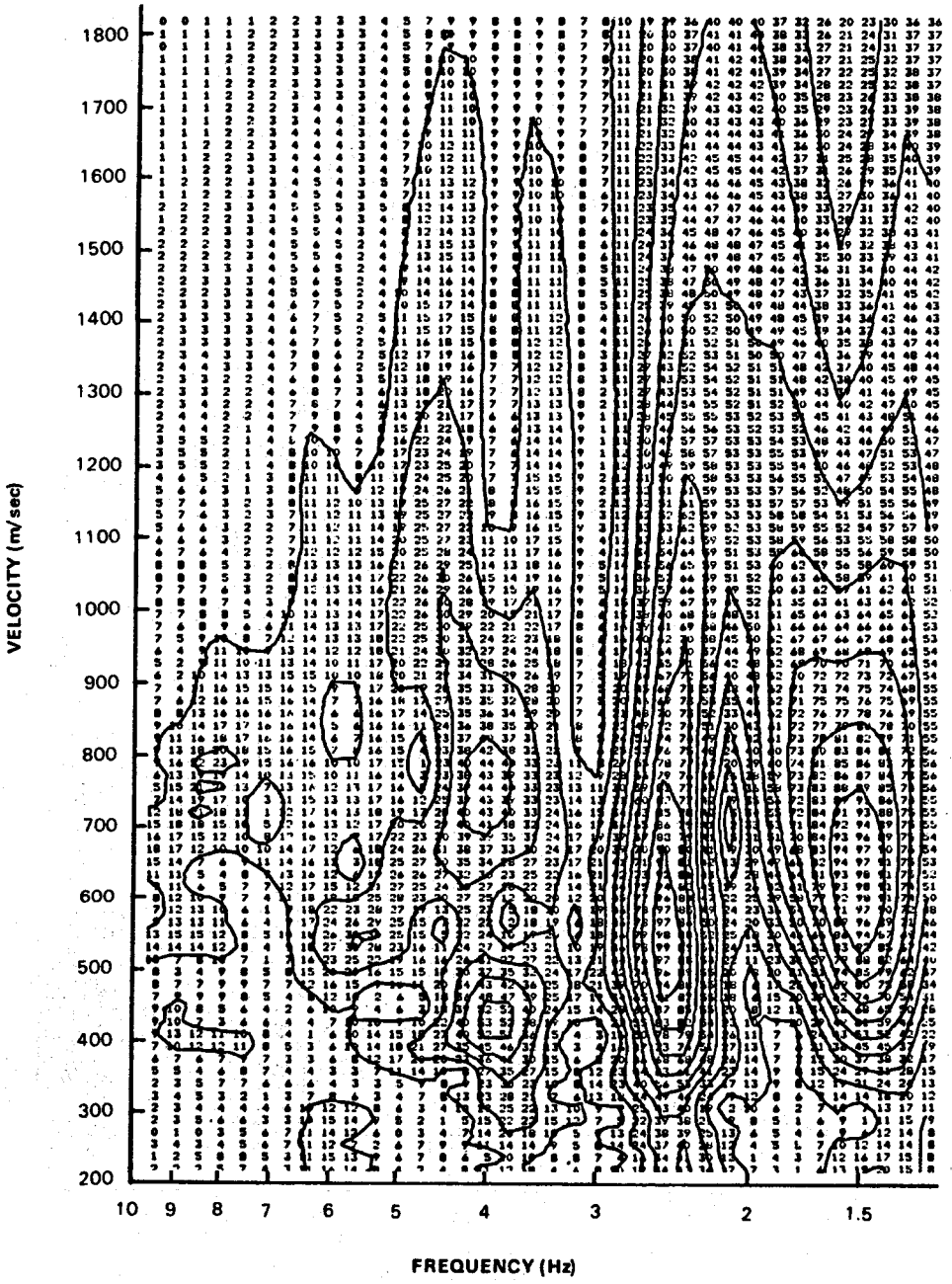

Figure B41. Multiple filter analysis of the synthetic seismogram calculated for source dip 45°, source depth 2.8 km, receiver range 2 km.

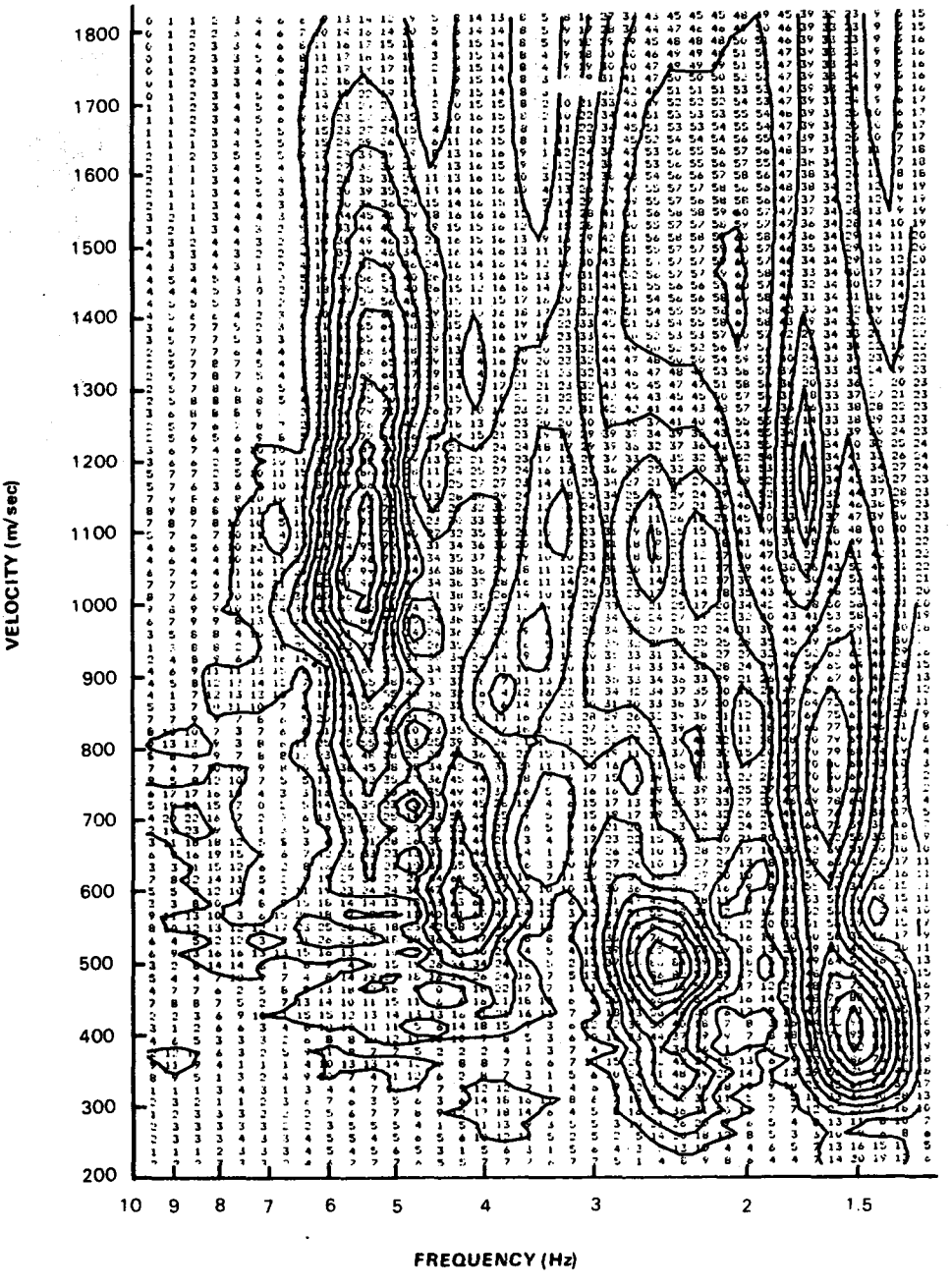

Figure B42. Multiple filter analysis of the synthetic seismogram calculated for source dip 45°, source depth 2.8 km, receiver range 5 km.

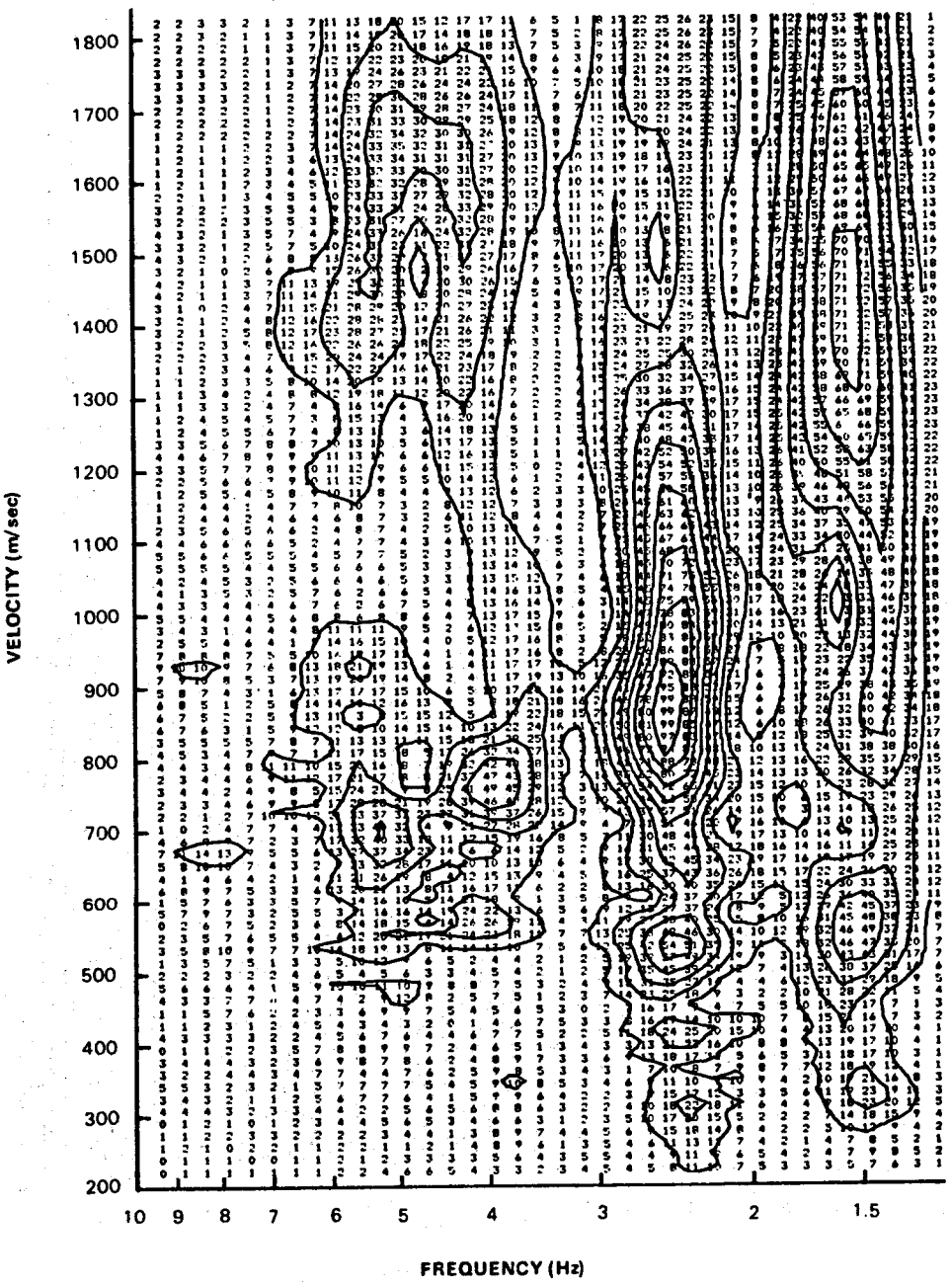

Figure B43. Multiple filter analysis of the synthetic seismogram calculated for source dip 45°, source depth 2.8 km, receiver range 8 km.

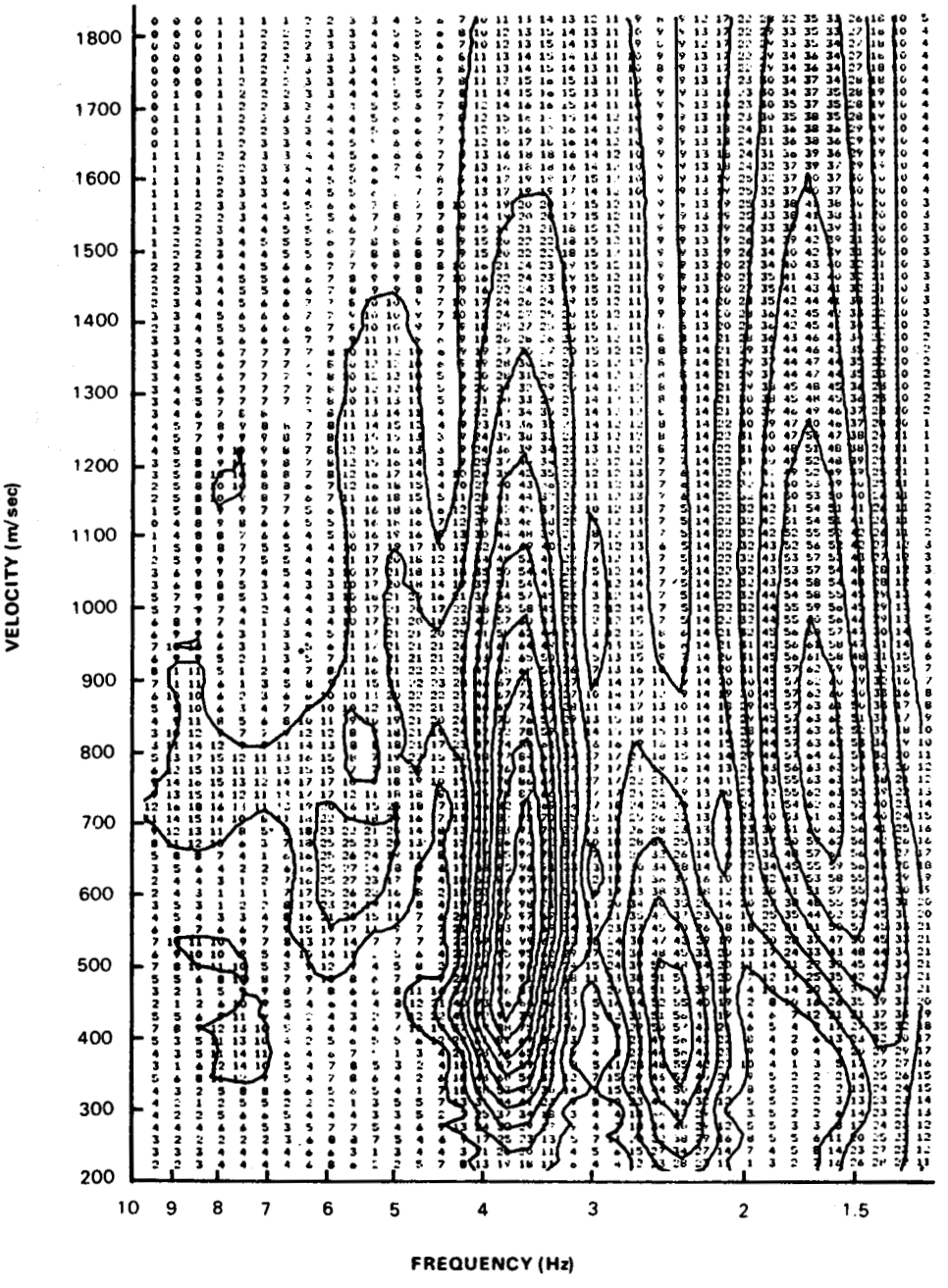

Figure B44. Multiple filter analysis of the synthetic seismogram calculated for source dip 45°, source depth 3.8 km, receiver range 2 km.

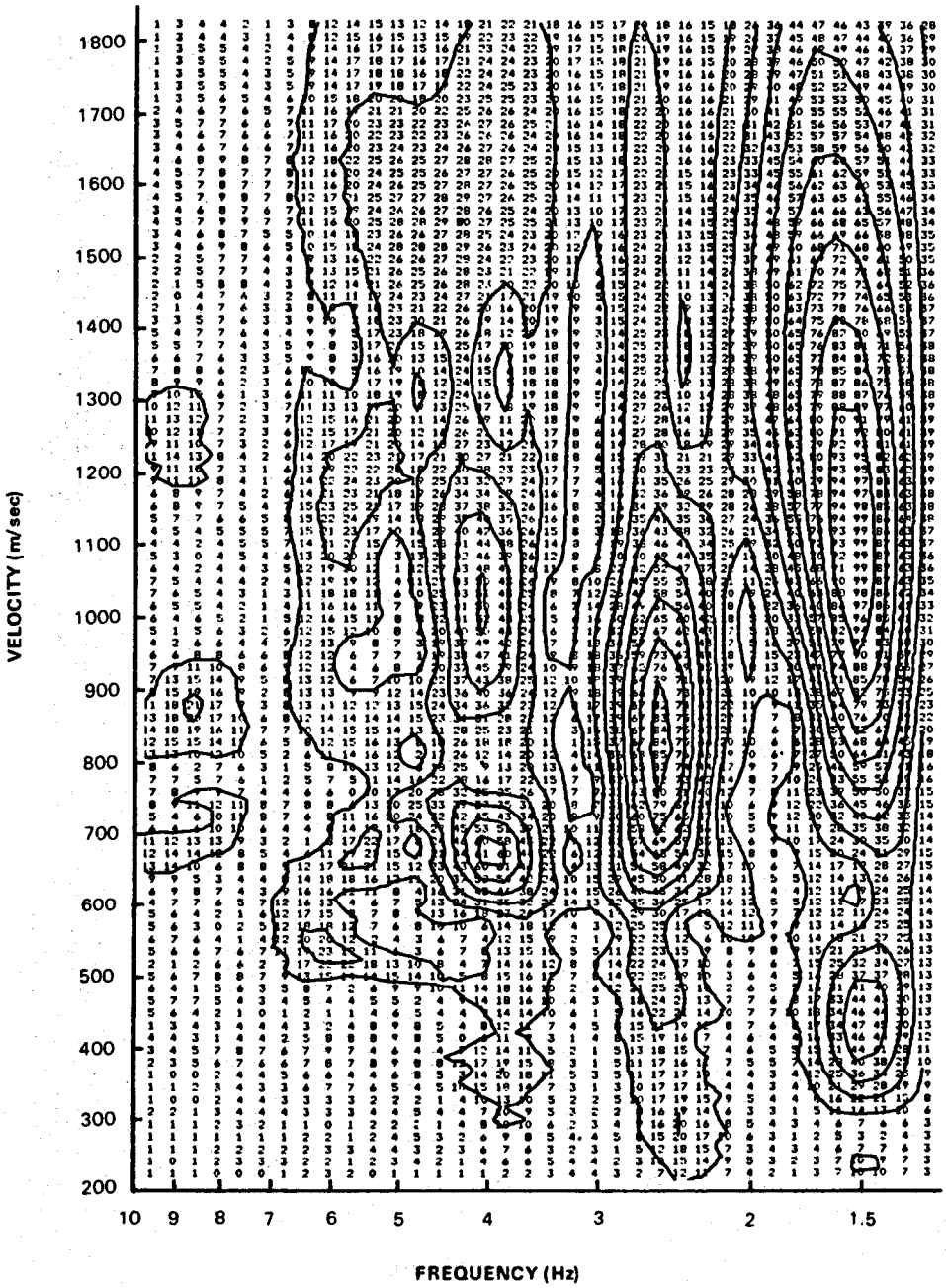

Figure B45. Multiple filter analysis of the synthetic seismogram calculated for source dip 45°, source depth 3.8 km, receiver range 5 km.

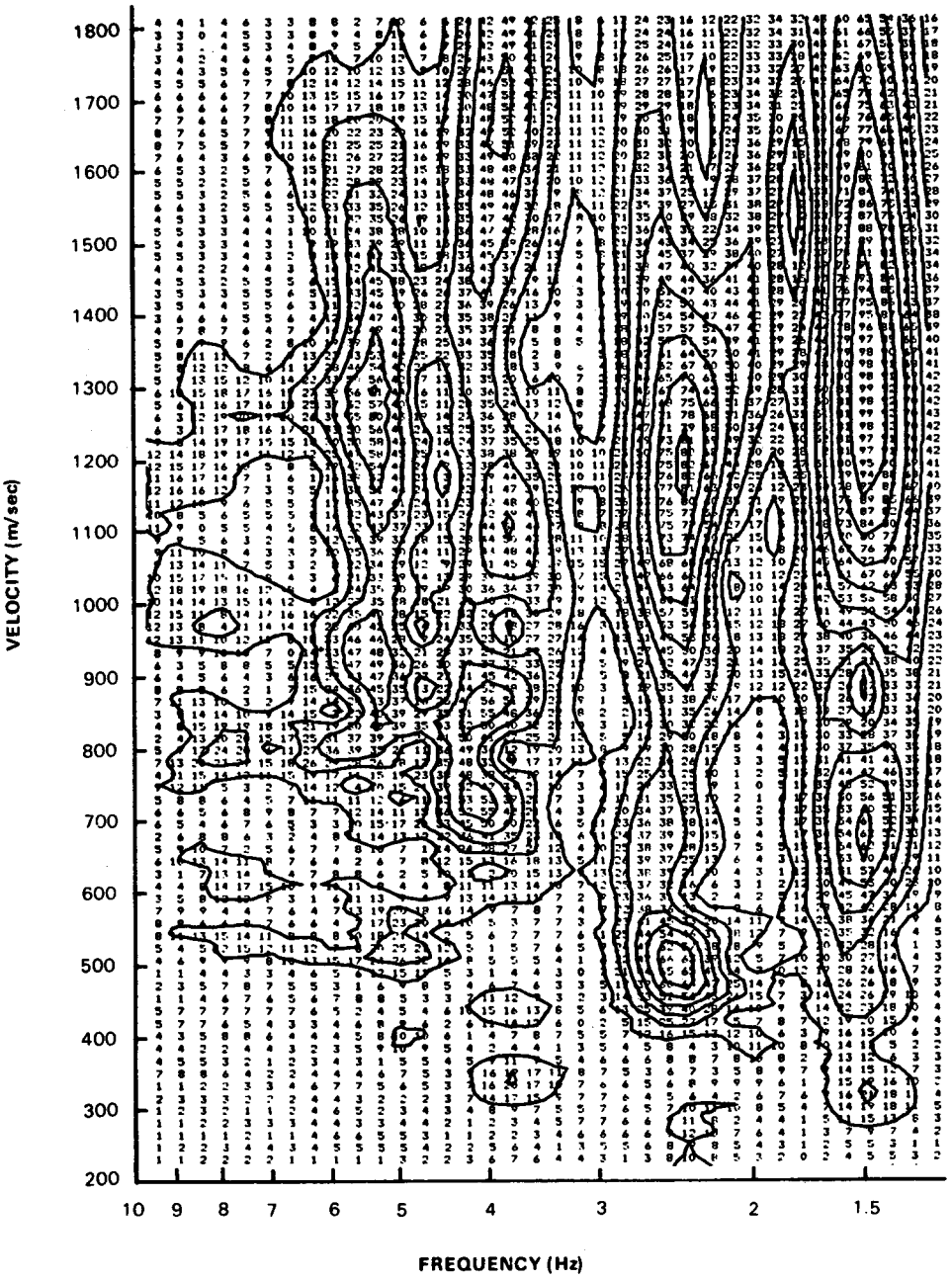

Figure B46. Multiple filter analysis of the synthetic seismogram calculated for source dip 45°, source depth 3.8 km, receiver range 8 km.

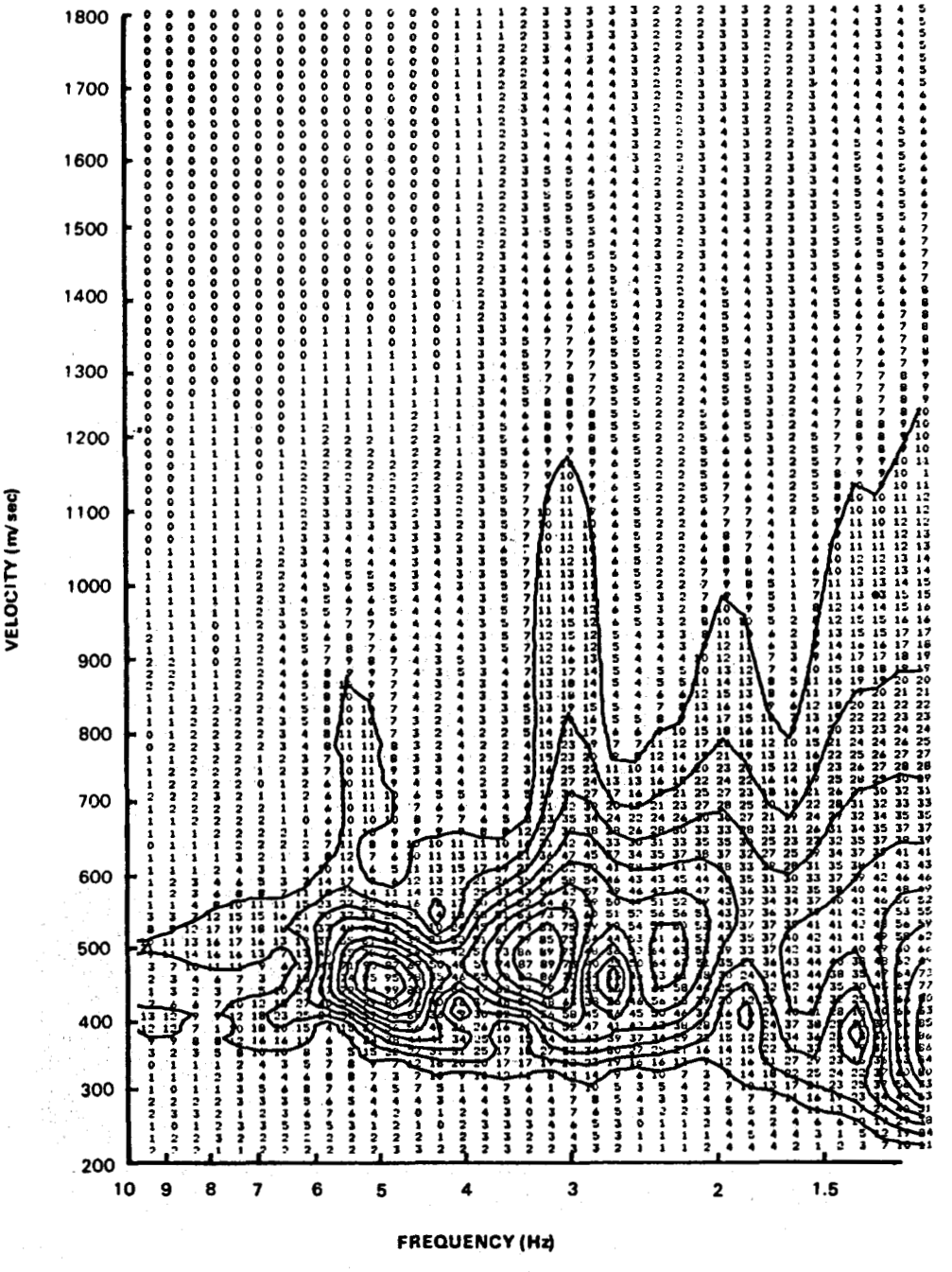

Figure B47. Multiple filter analysis of the synthetic seismogram calculated for source dip 90°, source depth 0.3 km, receiver range 2 km.

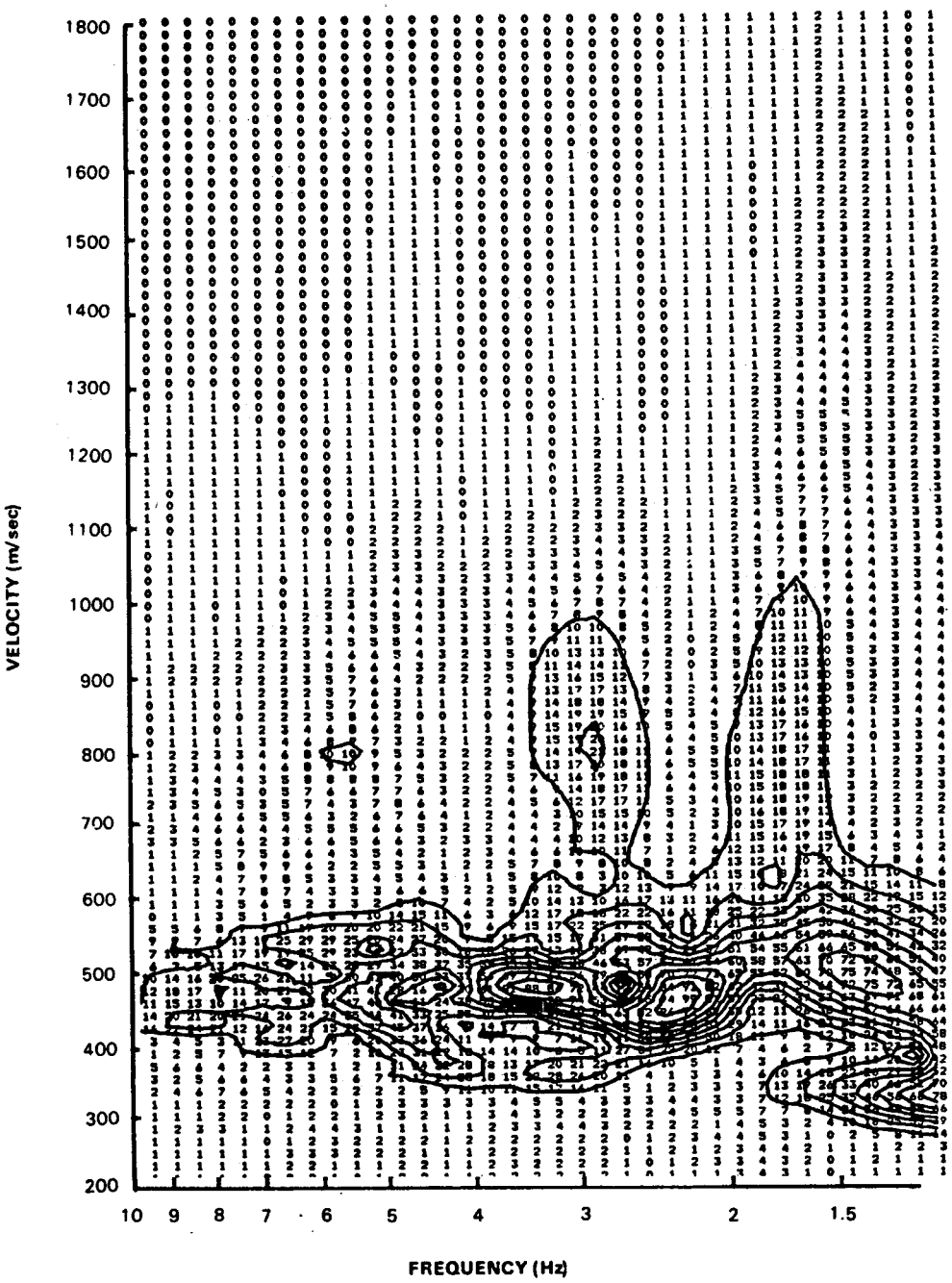

Figure B48. Multiple filter analysis of the synthetic seismogram calculated for source dip 90°, source depth 0.3 km, receiver range 5 km.

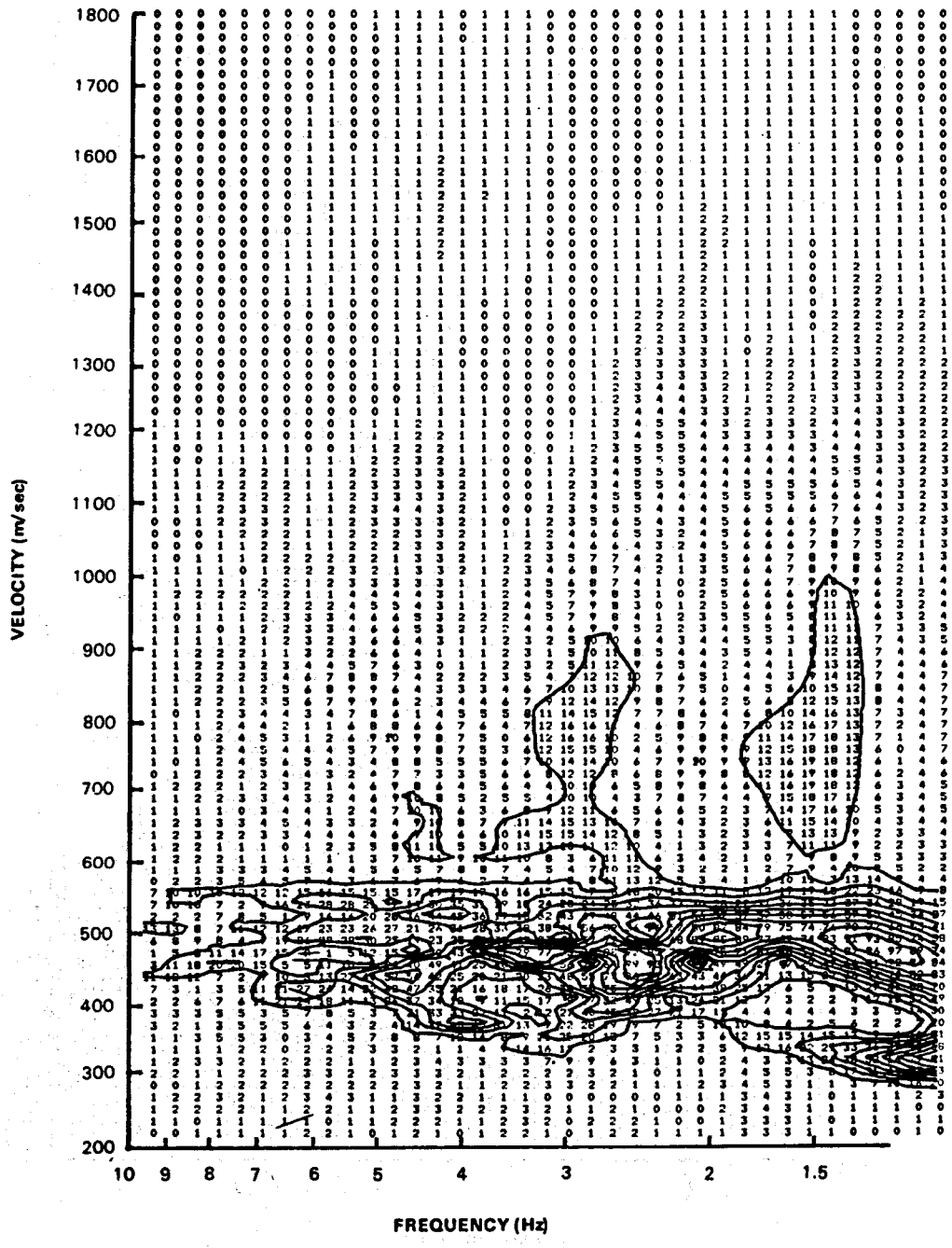

Figure B49. Multiple filter analysis of the synthetic seismogram calculated for source dip 90°, source depth 0.3 km, receiver range 8 km.

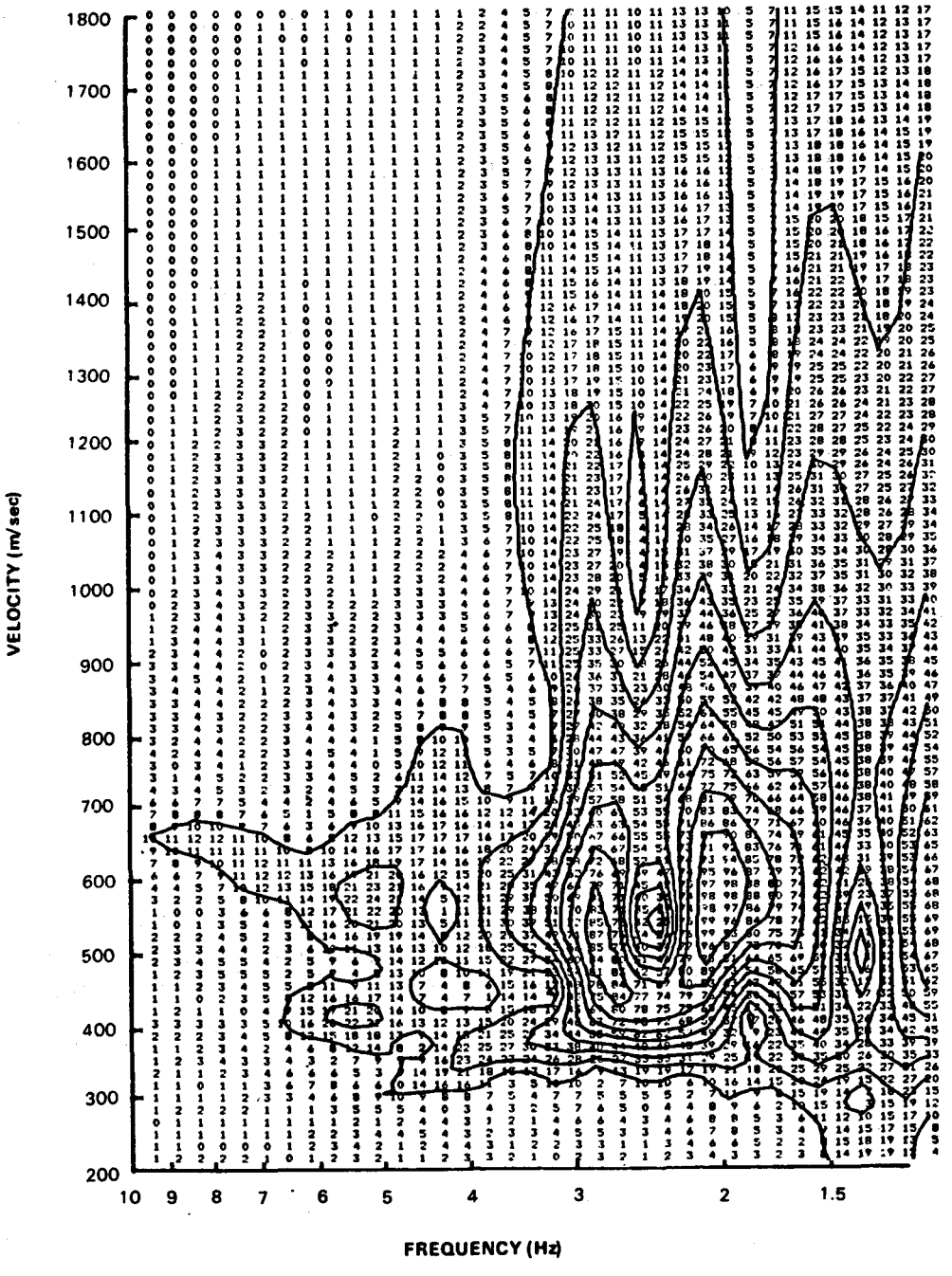

Figure B50. Multiple filter analysis of the synthetic seismogram calculated for source dip 90°, source depth 0.8 km, receiver range 2 km.

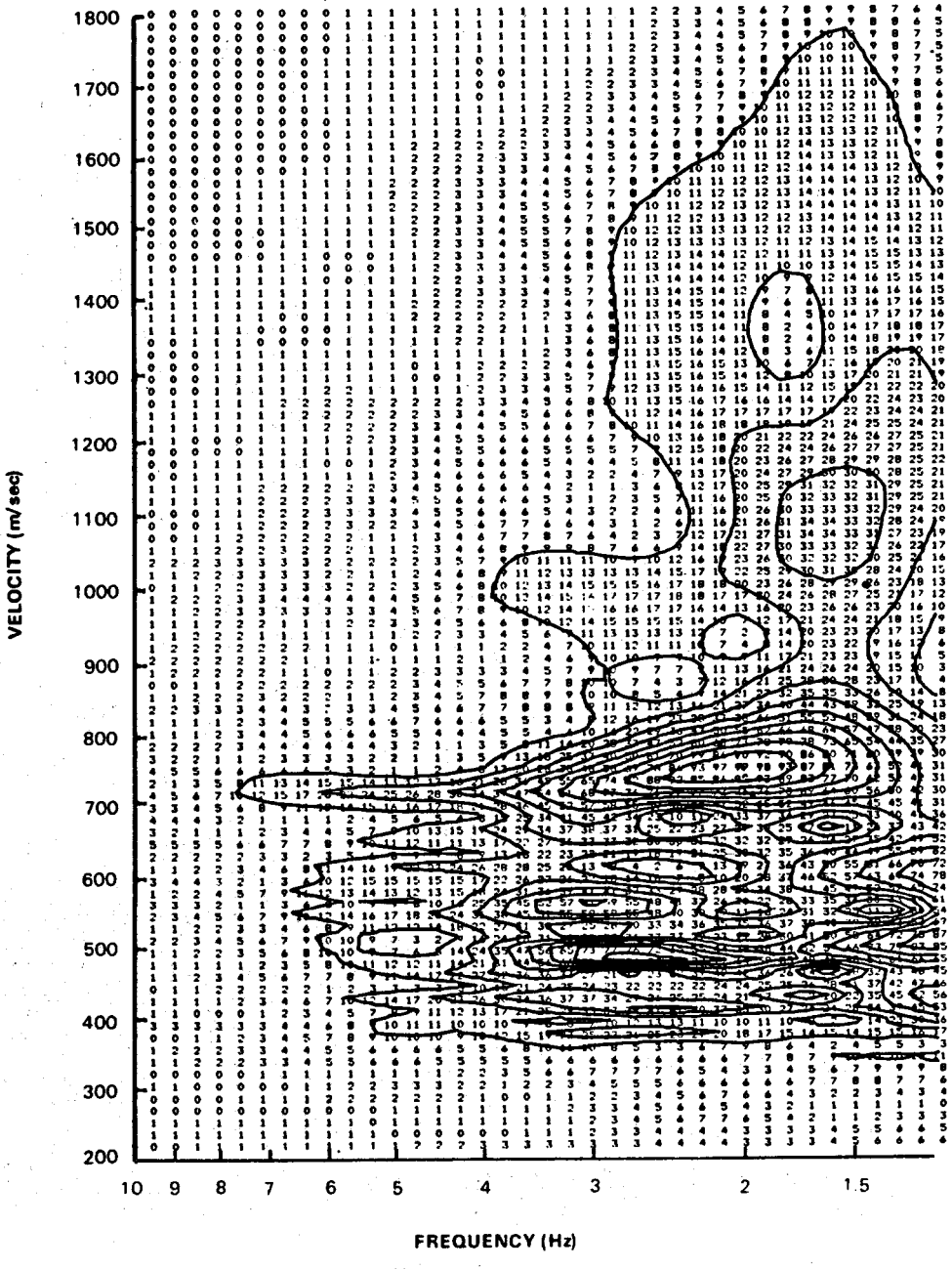

Figure B51. Multiple filter analysis of the synthetic seismogram calculated for source dip 90°, source depth 0.8 km, receiver range 5 km.

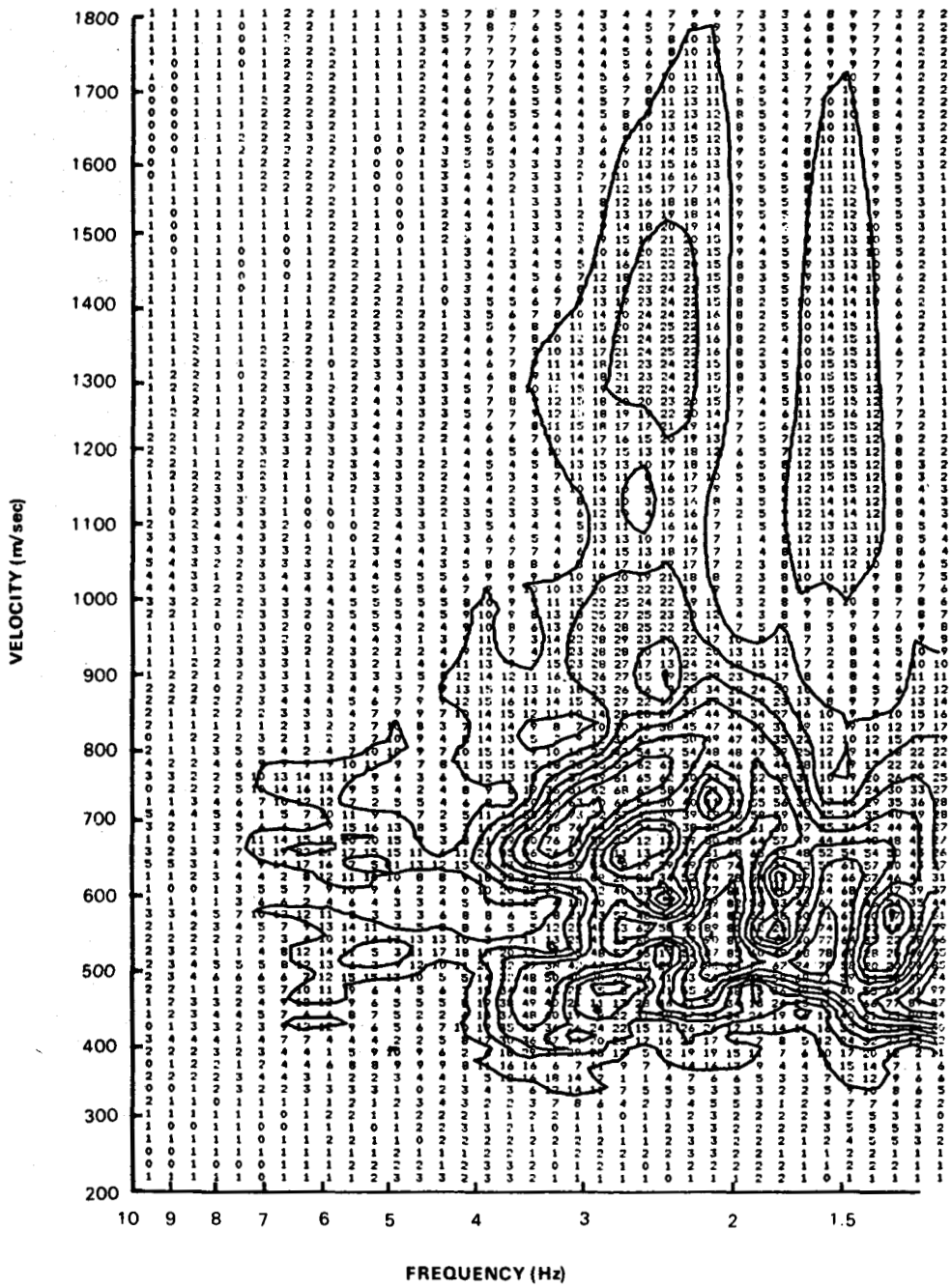

Figure B52. Multiple filter analysis of the synthetic seismogram calculated for source dip 90°, source depth 0.8 km, receiver range 8 km.

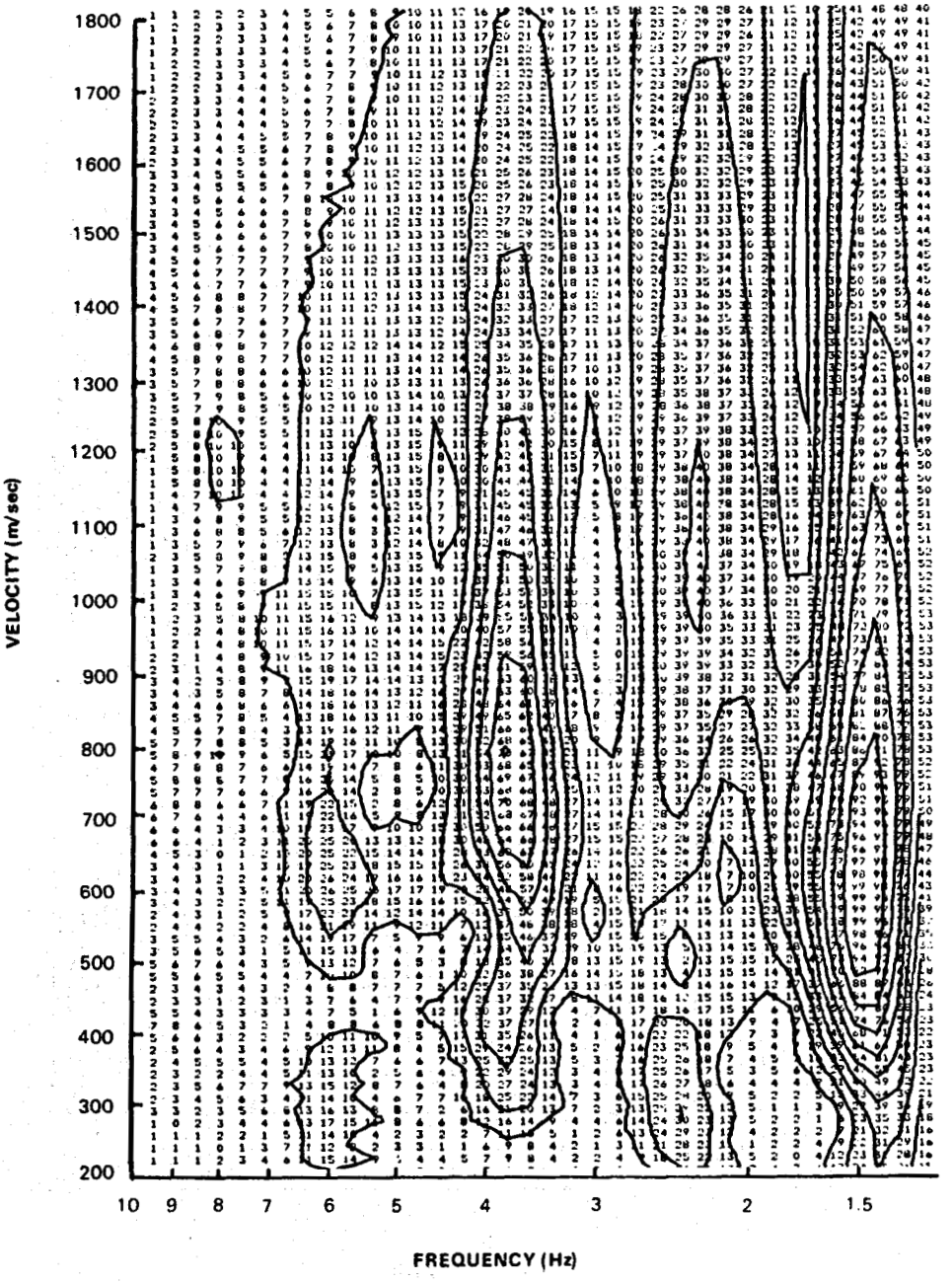

Figure B53. Multiple filter analysis of the synthetic seismogram calculated for source dip 90°, source depth 2.8 km, receiver range 2 km.

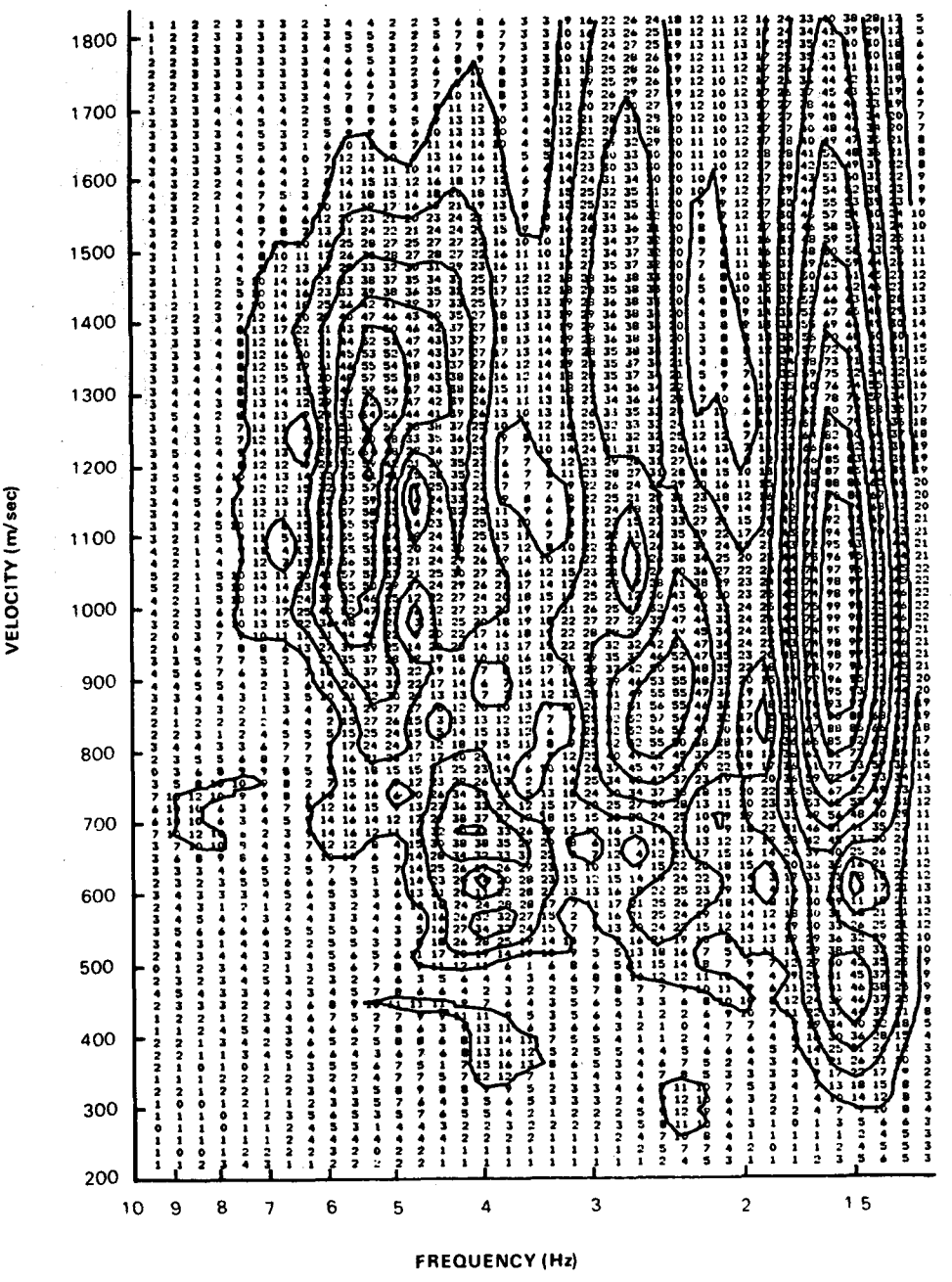

Figure B54. Multiple filter analysis of the synthetic seismogram calculated for source dip 90°, source depth 2.8 km, receiver range 5 km.

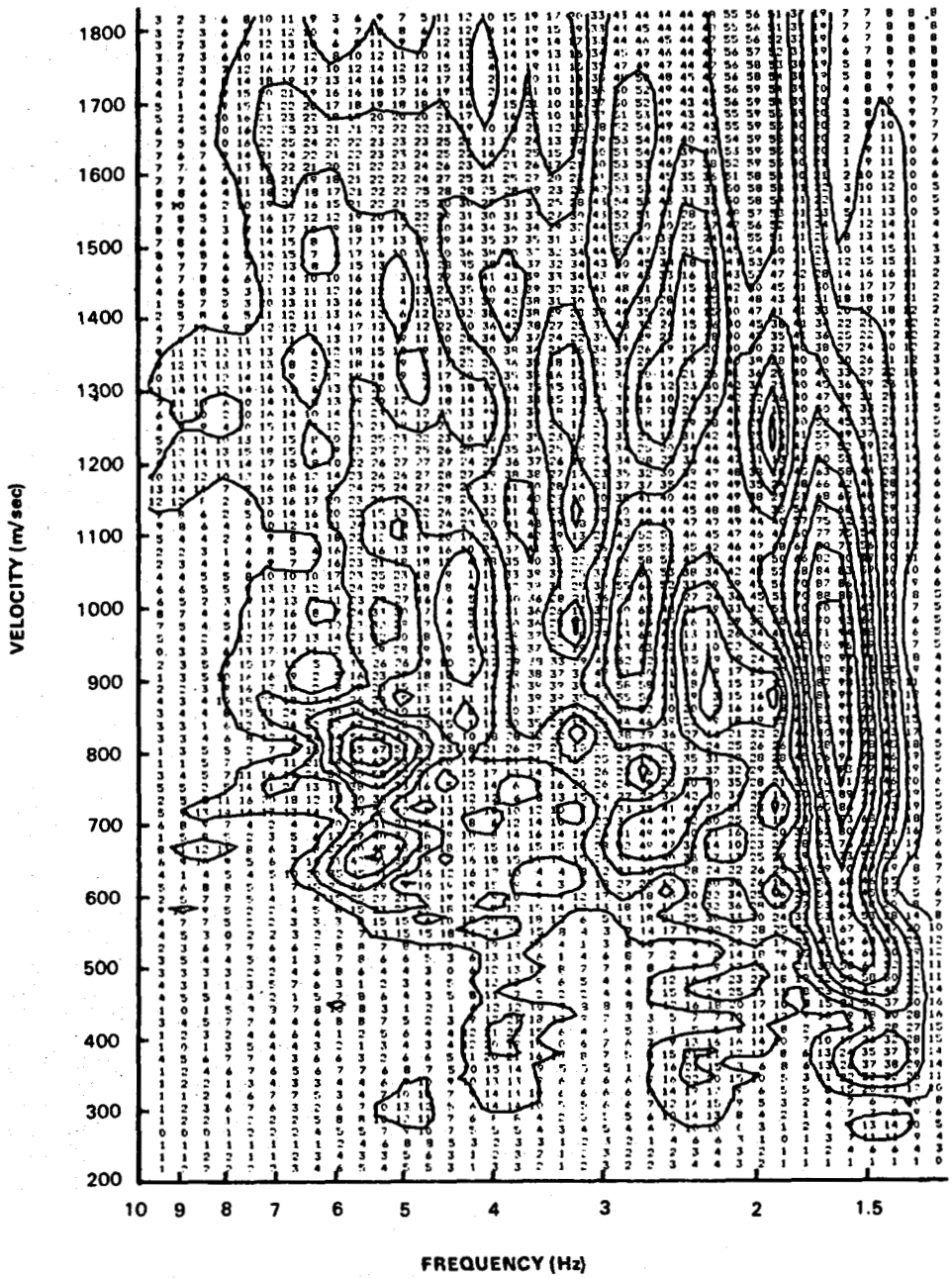

Figure B55. Multiple filter analysis of the synthetic seismogram calculated for source dip 90°, source depth 2.8 km, receiver range 8 km.

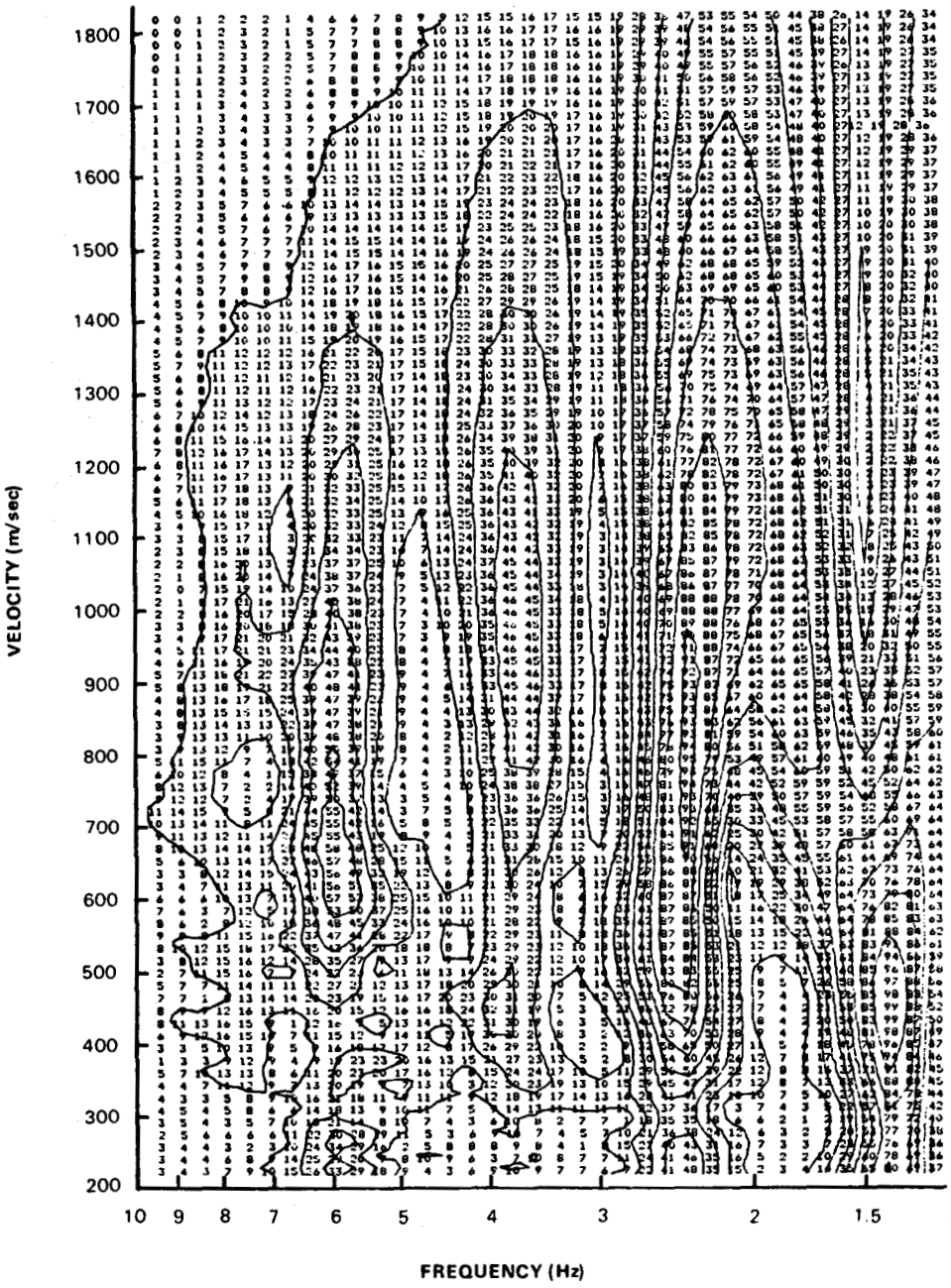

Figure B56. Multiple filter analysis of the synthetic seismogram calculated for source dip 90°, source depth 3.8 km, receiver range 2 km.

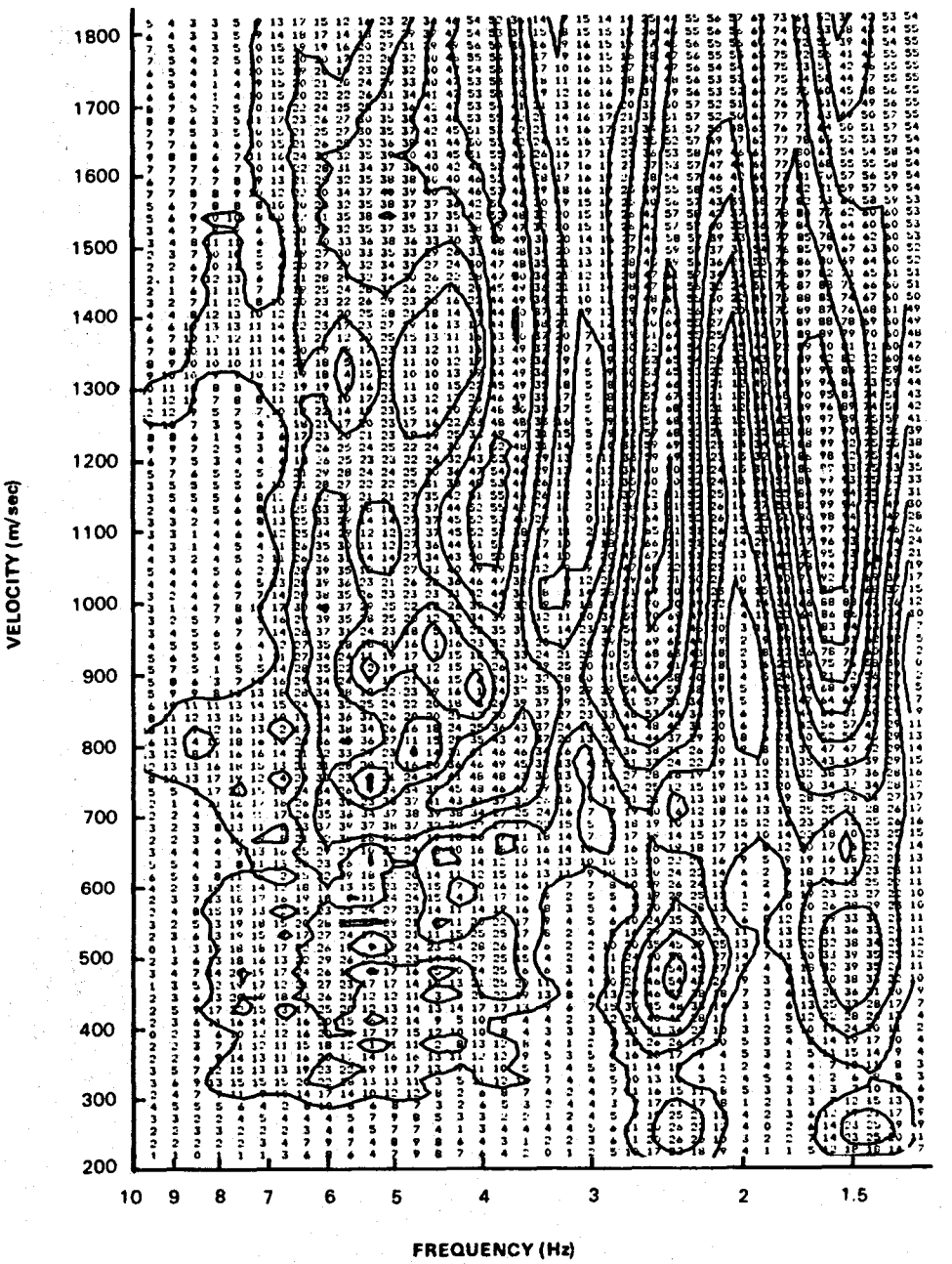

Figure B57. Multiple filter analysis of the synthetic seismogram calculated for source dip 90°, source depth 3.8 km, receiver range 5 km.

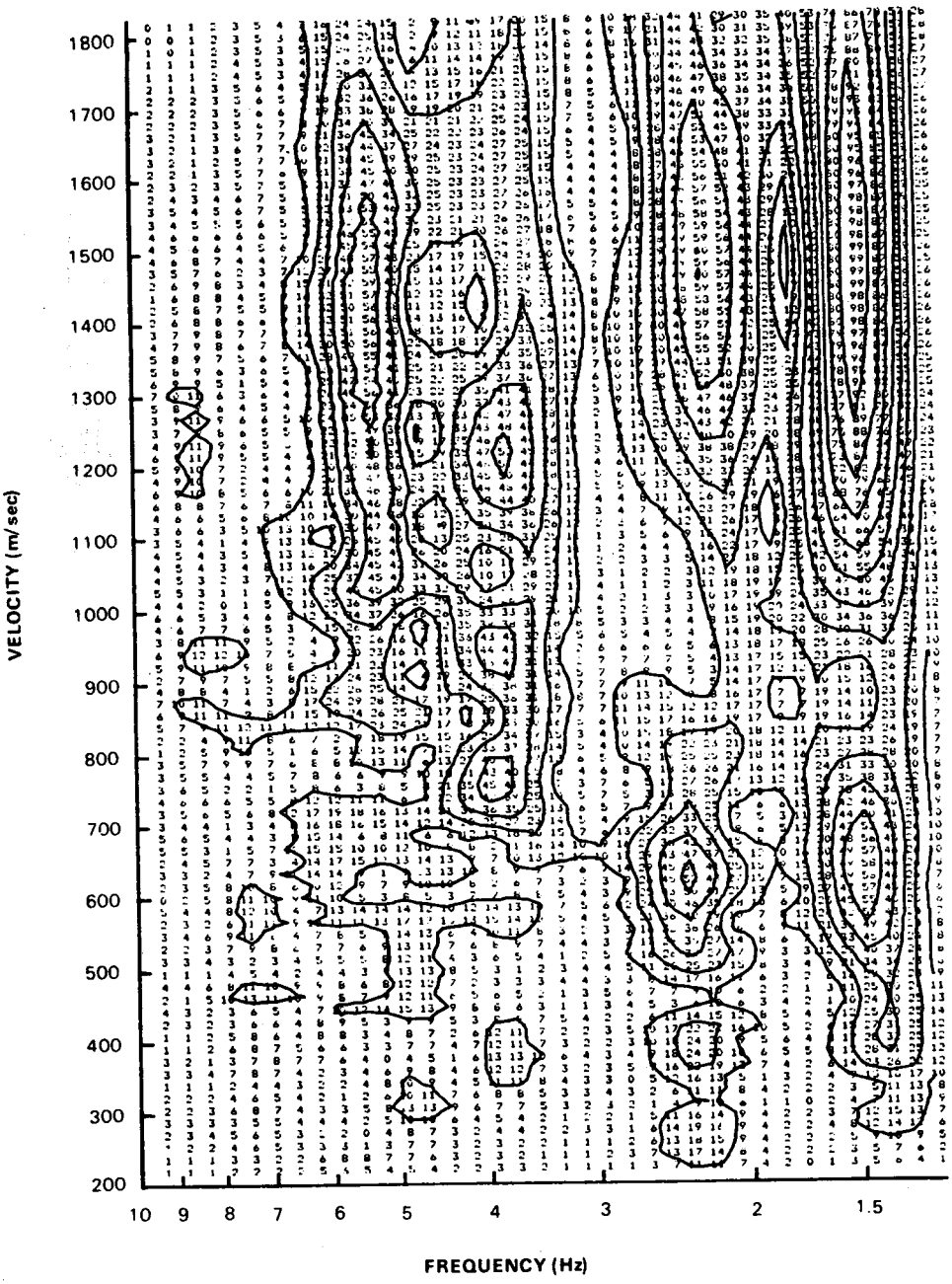

Figure B58. Multiple filter analysis of the synthetic seismogram calculated for source dip 90°, source depth 3.8 km, receiver range 8 km.

★U.S. GOVERNMENT PRINTING OFFICE: 1984-746-081/10150